Endometrial mucins and human embryo implantation.

Griffiths, Sean Gereint

Endometrial mucins and human embryo implantation

By
Sean Gereint Griffiths
BSc Genetics (1st class)

College of Medicine, Centre for NanoHealth,
Swansea University
September 2013

A thesis submitted to Swansea University in fulfilment of the requirements for the Degree of Doctor of Philosophy

Abstract

Summary

Failure of the embryo to implant into the uterine lining results in infertility and is also the rate limiting step in IVF. The tethered, glycoprotein MUC1 is a protective cell surface receptor that has been associated with infertility. Evidence suggests MUC1 and other endometrial mucins regulate embryo implantation. Endometrial epithelia must be shielded from infection whilst permitting the recognition and implantation of the embryo. The protein backbone of MUC1 is thought to act as a scaffold for L-selectin ligands and may be integral to the initial tethering of the embryo during early implantation.

Objectives

The remit of this thesis was to model the expression of MUC1 and other mucins in the human endometrium using endometrial cell lines and to use atomic force microscopy to understand the role played by these proteins in shaping the non-specific and embryo specific adhesive characteristics of endometrial monolayers. If possible the proposed L-selectin implantation mechanism was to be identified and functionally characterised.

Methodology

This project successfully married the traditional molecular tools of quantitative PCR and immunocytochemistry with novel application of INCELL analyzer high content screening protein analysis, peak force quantitative nano-mechanical mapping atomic force microscopy and single molecule force spectroscopy atomic force microscopy to characterise the specific and non-specific surface adhesion on live endometrial monolayers.

Results

Firstly, immunocytochemistry and qRTPCR revealed that basal MUC1 expression was significantly higher in Hec-1-B relative to Hec-1A, Ishikawa and Hec50. Secondly, INCELL analysis qualified a distinct heterogeneous expression of MUC1 across the endometrial monolayer and delineated altered patterning following treatment with estradiol and progestins. Thirdly, we have shown a direct and proportional correlation between MUC1 expression and adhesion in live Hec-1A and Hec-1B cell monolayers. Fourthly, this work has confirmed and characterised binding of recombinant L-selectin to the endometrial epithelial cell surface. Fifthly, it is shown that L-selectin surface binding decreases following a reduction in MUC1 surface presentation.

Conclusions

The results implicate MUC1 as a key component of endometrial adhesion and an initial mediator of implantation with a functional patterned expression suggesting areas of altered receptivity exist across endometrial monolayers. Abnormal MUC1 expression has been shown in endometrial pathologies and unexplained infertility. The current investigation suggests MUC1 protein may assist embryo attachment by retarding it sufficiently through mechanical impedance to allow specific L-selectin binding further securing the embryo. A non-receptive endometrium may contribute towards the infertile phenotype despite repeated IVF treatments, thus novel examination of potential embryo adhesion molecules such as MUC1 may aid understanding of endometrial characteristics which prevent embryo implantation and contribute towards IVF failure.

Declaration

This work has not previously been accepted in substance for any degree and is not currently submitted in candidature for any other degree.

Signed..... (Candidate)

Date 07.03.14

STATEMENT 1

This thesis is the result of my own investigations, except where otherwise stated. Where corrections services have been used, the extent and nature of the corrections are clearly marked in a footnote(s). Other sources are acknowledged by footnotes giving explicit references. A bibliography is appended.

Signed..... (Candidate)

Date 07.03.14

STATEMENT 2

I hereby give consent for my thesis, if accepted, to be available for photocopying and for inter-library loan, and for the title and summary to be made available to outside organisations.

Signed..... (Candidate)

Contents

Acknowledgements

The last four years have been non-stop challenge towards the completion of one goal and it is through the kindness and support of many people that I have been able to get to where I am today. Firstly I have been fortunate to have the peer-support of the students and post-docs at the Centre for NanoHealth and the Institute of Life Science at Swansea; the team spirit and comradeship between the students and the advice and guidance of the post-docs has helped me get through the last four years especially during times when I have been struggling. So thanks must go to Natalie, Ben, Beth, Lauren, Julia, Roberta, Matthew T, Matthew H, Abdullah, Helen and Georgina and others, I wish you all the best in your future endeavours.

Special thanks must go to my family; Mum, Dad and James. They have been unfaltering in their support and encouragement throughout this project. Whether it is as simple my Dad asking how the writing is going, making us both a curry so I don't starve up or advising me how to professionally deal with difficult situations and to structure and present my findings he always has had (and continues to have) the right answers. My Mum and James have both had spells in hospital during the course of this work so I wish you both a continued and speedy recovery. I must extend my gratitude to my supervisors Professor Steve Conlan and Dr Lewis Francis for all their help throughout this undertaking. Under their supervision I was encouraged to develop my own ideas which I feel has strengthened my skills as a developing scientist, the speed and attention they demonstrated towards the critical analysis of my writing was astounding. During difficult times I have walked out of both their offices encouraged and re-motivated (sometimes even smiling), a testament to their characters and management styles. Special thanks must go to Dr Alexandre Berquand for his friendship and support in Germany, he went above and beyond what was required of him to not only impart his substantial expertise in the field of AFM, but also to help me settle into life in Mannheim. I really enjoyed our working lunches and this project would not have been completed without you. Merci bien Alex.

Also of special mention is Dr Deya Gonzalez who was my supervisor during my undergraduate project in 2008, her training and expertise in all things molecular and reproductive biology led to this PhD and is still helping me to this day. She has always spared the time to check up on her old undergraduate student. Dr Paul Lewis has been a source of perspective during my studies and his likable persona has brightened many a dark day. I would like to thank my friends for sticking by me, despite my lack of social life; Adam, Adrian, Andy, Anthony, Haz, James, Stewart, Sam, I will endeavour to meet up with you all and make up for lost time.

Last but certainly not least I must say thank you to Karen, you been a steadfast support all the way through this undertaking and have buffered all the ups and downs of this thesis with your sound advice and encouragement which has been instrumental in getting me to the end of this PhD. You've been incredibly selfless in supporting my studies and now I look forward to this new chapter in which we can move forward with our future. Thank you.

Figure list

Abbreviations

A	
AML	Adhesive Mucus Layer
ATCC	American Type Culture Collection
AFM	Atomic Force Microscopy
AR	Androgen Receptor
ART	Assisted Reproductive Technologies
C	
CAM	Cell Adhesion Molecule
CDLD	Calcium Dependant Leptin Domain
CC	Clominphine citrate (Clomid)
CLA	Cutaneous Lymphocyte Antigen
CM	Contact Mode
CNS	Central Nervous System
COH	Controlled Ovarian Hyperstimulation
D	
DAPI	4',6-diamidino-2-phenylindole
DCC	Dextran Coated Charcoal
DMEM/F-12	Dulbecco's Modified Eagle Medium: Nutrient Mixture F-12
DNA	DeoxyRibonucleic Acid
E	
EEC	Endometrial Epithelial Cell
E1	Estrone
E2	Estradiol
E3	Estriol
ECM	Extra Cellular Matrix
EGF	Epidermal Growth Factor
ERα	Estrogen Receptor alpha
ERβ	Estrogen Receptor beta
F	
FBS	Fetal Bovine Serum
FD	Force Distance
FC	Force Curve
FSH	Follicle Stimulating Hormone
G	
GAPDH	Glyceraldehyde 3-phosphate dehydrogenase
GlcNAc	N-acetyl-D-glucosamine
GnRH	Gonadatrophin releasing hormone
GPI	Glycosylphosphatidylinositol
H	
HCG	Human Chorionic Gonadotrophin

HCS	High Content Screening
HGEx-ERdb	Human Gene Expression Endometrial Receptivity Database
HSDC	High Speed Data Capture
HPO	Hypothalmic Ovarian Pituitary (axis)
I	
ICAM	Intracellular Adhesion Molecule
IC	Intermittent Contact
ICC	ImmunoCytoChemistry
IHC	ImmunoHistoChemistry
IVF	*In Vitro* Fertilisation
IUI	Inter Uterine Insemination
L	
LBD	Ligand Binding Domain
M	
MIS	Minimal Invasive Surgury
MPA	MethoxyProgesterone-Acetate
MRNA	Messenger Ribo-Nucleic Acid
MUC1	Mucin -1
N	
nN	NanoNewtons
NICE	National Institute of Clincial Excellence
NHR	Nuclear Hormone Receptor
O	
OFN	Oncofetal Fibronection
OPN	Osteopontin
P	
PBS	Phospho-Buffered Saline
PCOS	PolyCystic Ovary Syndrome
PEG	Poly Ethylene Glycol
PFQNM	Peak Force Quantitative Nanomechanical Mapping
PFT	Peak Force Tapping
PPAR	Peroxisome Proliferator-Activated Receptor
PR	Progesterone Receptor
PUNIAS	Protein Unfolding and Nano-Indentation Analysis Software
Q	
QRTPCR	Quantitative Real Time Polymerase Chain Reaction
QNM	Quantitative Nanomechanical Mapping
R	
RNA	RiboNucleic Acid
RAR	Retenoic Acid Receptor
RIF	Recurrent implantation failure
S	
SA	Spiral Arteries

SEA	Sea urchin, Enterokinase, Agrin (domain)
SEM	Scanning Electron Microscope
SCR	Short Consensus Repeat
SMFS	Single Molecule Force Spectroscopy
T	
TEM	Transmission Electron Microscope
TM	TransMembrane
TR	Thyroid Receptor
U	
UIF	Unexplained InFertility
V	
VDWs	Van Der Walls
VNTR	Variable Number Tandem Repeat
W	
WOI	Window of Implantation

Chapter 1 Thesis Introduction

1.01 Infertility

The National Institute of Clinical Excellence (NICE) defines infertility as "A woman of reproductive age who has not conceived after 1 year of unprotected vaginal sexual intercourse" (NICE clinical guideline #156). Infertility is estimated to affect 14.3% of heterosexual couples in the UK, and prevalence has been revised upwards (from 9%) since the last NICE guidelines were issued in 2003. The causal factors behind infertility are numerous and include; uterine or endometrial factors (Strowitzki et al. 2006), gamete or embryo defects (S. Zhang et al. 2013), and pelvic conditions such as polycystic ovaries or endometriosis which can both dramatically impact fertility (Falconer 2013). These causes are summarised in Figure 1.

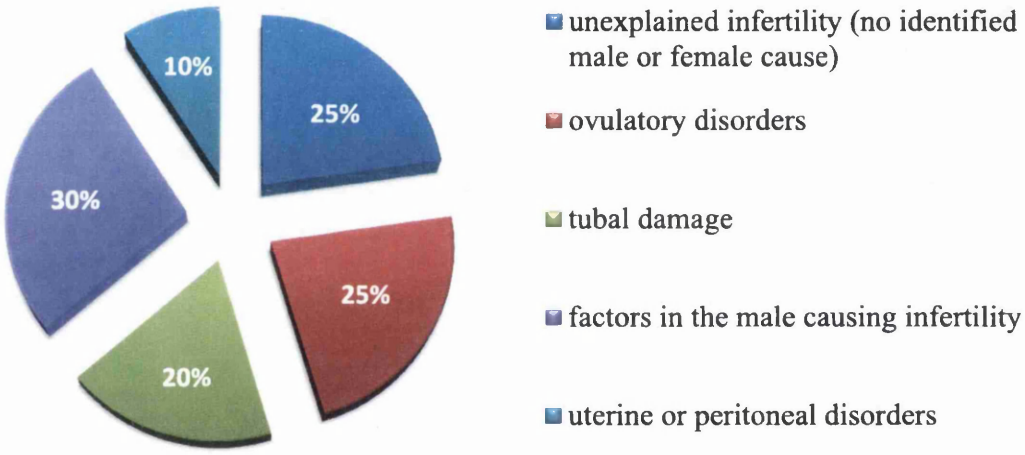

Figure 1: The aetiology of infertility. Recently revised NICE guidelines (Feb 2013) show the breakdown of the causes of infertility in the UK, 25% of all cases have no defined cause.

If the cause is known then specifically targeted medical treatments can be used to restore fertility such as the application of ovarian hormones to reverse anovulatory disorders, minimal invasive surgery (MIS) for treatment of endometriosis and assisted reproductive technology (ART). ART encompasses a broad spectrum of assisted conception techniques that do not require vaginal intercourse, such as *in vitro* fertilization (IVF), embryo cryopreservation, and intra-uterine insemination (IUI). One quarter of infertility cases have no defined cause, meaning it is difficult for clinicians to prescribe an appropriate course of action. It has been suggested that a defect in the lining of the uterus could be a silent contributing factor behind a large proportion of

unknown infertility cases (Graham et al. 1990; Diedrich et al. 2007; Sundqvist et al. 2012; Aplin et al. 1994; Carson et al. 2000).

1.02 The uterus and reproductive tract

The female reproductive tract is a multifunctional system evolved to support pregnancy (Figure 2). The ovaries produce the female reproductive cells (oocytes) and facilitate their transport through the fallopian tubes (oviduct) to the uterus for fertilisation/conception. Following conception the fertilised embryo travels to the uterus and implants into the uterine lining (endometrium), signalling the beginning of pregnancy. In the absence of fertilisation and/or implantation the uterine lining undergoes a cyclic shedding and regeneration termed the menstrual cycle. The ovaries are a key component of the female reproductive system and produce the requisite steroid hormones for the menstrual cycle control.

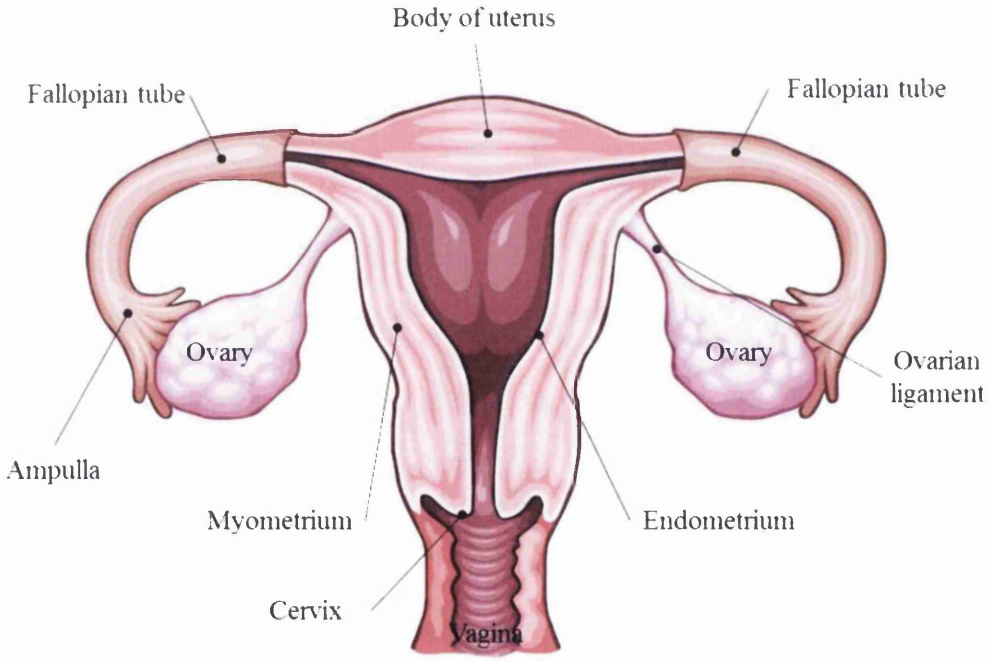

Figure 2: The structure of the female reproductive system. The female reproductive system principally consists of ovaries (small paired organs situated near the pelvis) and the uterus (a thick, pear shaped, muscular organ) interconnected by the fallopian tubes. Further down the cervix connects the uterus to the vagina, which allows passage of sperm during intercourse and also the release of menstrual fluid during menstruation.

1.021 The ovaries

The ovaries are small, round, paired organs that are covered by the mesovarium portion of the broad ovarian ligament and situated in the ovarian fossa, a shallow depression in

the pelvic wall adjacent to the uterus body. The central medulla is the central portion of the ovarian body and is surrounded by a tough connective tissue known as tunica albunginea. The major functions of the ovaries are the production of female germ cells (oocytes) which are released from a dominant ovarian follicle in a process known as oogenesis (Sánchez & Smitz 2012) and the generation of bioactive molecules, primarily steroids such as the estrogens and progestins. Such compounds are critical for ovarian function, regulation of the hypothalamic pituitary ovarian (HPO) axis (Figure 3), development of secondary sex characteristics and importantly regulation of endometrial receptivity to enable a fertilised embryo to implant and gestate (Ozturk & Demir 2010).

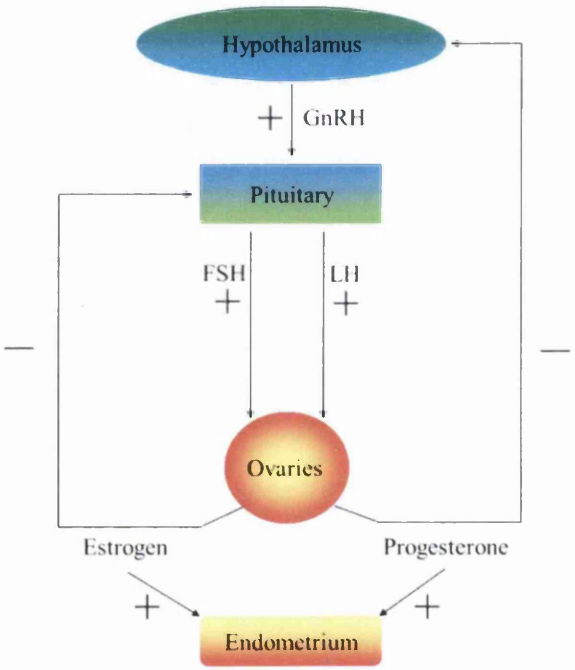

Figure 3: The hypothalmic-pituitary-ovarian axis. Gonadatrophin releasing hormone (GnRH) secreted from the hypothalamus acts on the pituitary gland causing it to secrete follicle stimulating hormone (FSH) and lutenizing hormone (LH). LH and FSH regulate the secretion of estrogen and progesterone from the ovaries, which in turn control endometrial receptivity and exert negative feedback control on the pituitary gland and hypothalamus.

1.022 The fallopian tubes

The fallopian tubes (oviducts) act as a conduit between the ovaries and the endometrium. The ampulla is the widest region of the oviduct and typically serves as the site of conception (the meeting of the sperm and the egg). Post-fertilisation, the oviduct facilitates the transfer the embryo to the site of implantation in a process known as gamete transfer.

1.023 The uterine cavity

The uterus has a small central cavity that serves to host the developing embryo from implantation stage to successful parturition over a 9 month gestational period. The uterus is located deep within the pelvic region suspended by cardinal, uterosacral and broad ligaments that allow for some movement. The uterus consists of three layered tissues, the outer peritoneum, the muscular myometrium and the inner mucosa, termed endometrium. The uterus is attached to the cervix, a hollow structure that adjoins the vagina and facilitates child-birth, sexual intercourse and passing of menstrual fluid.

1.024 The endometrium

The endometrium is a highly dynamic tissue lining the uterus that undergoes monthly cycles of growth, differentiation, shedding and regeneration between the years of menarche (age~12) and menopause (age 50+). Structurally it consists of a single-layered epithelium and its basal lamina, uterine glands, and a specialized, cell-rich connective tissue (stroma) containing a rich supply of blood vessels.

The endometrium functions to lubricate and thus prevent adhesion and abrasion between the opposing walls of the myometrium (sub-endometrial layer) and to provide a suitable surface for the fertilised embryo to implant into the uterine lining. The endometrial epithelium is the first point of contact between the maternal and embryonic tissues and thus must be receptive to the embryo. Like other epithelia, the endometrium possesses defence mechanisms to resist bacterial infection while allowing the recognition and adherence of an embryo. This adhesion/anti-adhesion balance is paramount and is addressed in detail later. This modulation of endometrial adhesion depends on the expression of cell surface proteins that are regulated by steroid hormones secreted by the ovaries (Maybin & Critchley 2012). The endometrial epithelium is the critical surface in establishing pregnancy and undergoes cellular and morphological changes in response to these steroid hormones that prepare the epithelium for implantation (Wang & Dey 2006). These morphological changes include the appearance of ciliated epithelial cells and flower-like projections called pinopods (Figure 4) that are thought to be indicative of suitable embryo implantation sites, referred to as nidation sites (Quinn & Casper 2009; Murphy 2006).

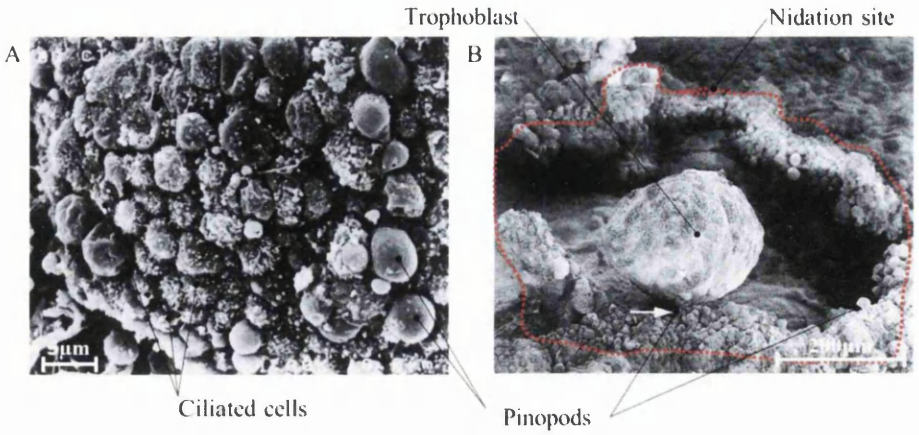

Figure 4: The surface of the endometrium. (A) Electron micrographs show cultured endometrial biopsy from woman who had undergone combined estrogen/progesterone treatment, replicating "receptive" conditions. Smooth epithelial projections termed pinopods and ciliated cells are shown. (B) The embryo adheres to the uterine epithelium. The nidation site where conditions are favourable for trophoblast attachment is shown in red. The defining characteristics of this site are unknown. Images reproduced from (Nardo et al. 2002) and (Petersen et al. 2005).

1.03 The ovarian hormones

The hormones that control the development and maintenance of endometrial receptivity are progestins and estrogens which are secreted by the ovaries (Dey et al. 2004). These ovarian secretions are in turn regulated by gonadatrophin releasing hormone (GnRH) secreted from the hypothalamus and luteinizing hormone (LH) and follicle stimulating hormone (FSH) secreted from the anterior pituitary gland. This co-ordinated regulation is the basis for the HPO axis (Figure 3) (Yen 1977). The primary female reproductive hormones are estrogen and progesterone, and are critical regulators of sexual differentiation, maturation, foetal growth, foetal development and endometrial receptivity (Królik & Milnerowicz 2012; Ozturk & Demir 2010).

The ovaries secrete progesterone and estrogen at varying concentrations throughout a monthly cycle known as the ovarian cycle (Figure 5). Estrogen is produced naturally in three closely related isoforms; estrone (E_1) estradiol (E_2) and estriol (E_3). E_2 is the primary estrogen produced between menarche and menopause, while in post-menopausal women estrone becomes dominant (Blair 2010). During the late follicular phase (days 9-14) of the ovarian cycle (ovarian cycle is shown in Figure 5), estrogen is the dominant hormone secreted. In the ovary, competitive follicular development begins due to an increase in FSH and a surge in LH secreted by the anterior pituitary gland occurs mid-cycle; 24-36 hours post-surge the oocyte is released from the dominant

follicle (Christensen et al. 2012). During the surge LH stimulates the dominant follicle to release high concentrations of E_2 (Baerwald et al. 2012). The outcompeted follicles undergo atrophy in a process known as ovarian follicle atresia.

After ovulation occurs the oocyte is swept down the oviduct by ciliated cells ready for potential fertilisation in the ampulla. The residual primary follicle is now transformed through the action of LH and FSH into the corpus luteum, a post ovulatory body that secretes modest concentrations of E_2 and greatly increased progesterone (P_4). The luteal phase is characterised by elevated P_4 which primes the endometrium ready to receive the fertilised embryo. This priming of the endometrium is driven through the actions of E_2 and P_4 mediated by their respective receptors that are expressed in endometrial stromal and epithelial tissues.

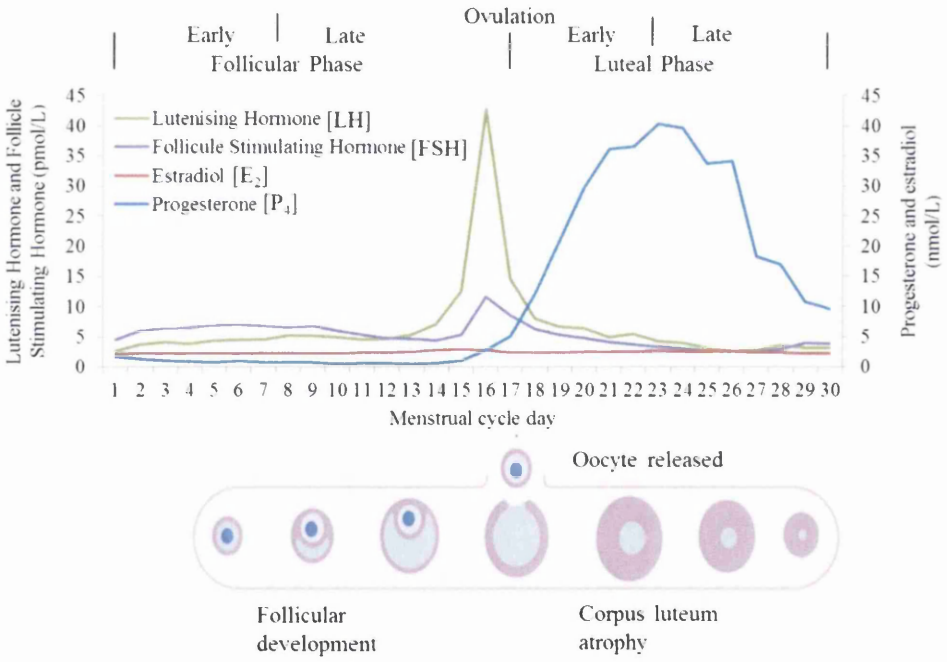

Figure 5: The ovarian cycle. During the follicular stage the secretion of LH by the anterior pituitary gland stimulates the primary follicle to produce E_2, which in turn exerts its effects on the endometrium. After ovulation the corpus luteum secretes P_4 that primes the endometrium for implantation. Chart reproduced from serum concentrations stated in (Stricker et al. 2006), data compiled from 20 women not in receipt of contraception.

1.04 The ovarian hormone receptors

Estrogen and progesterone receptors (ER, PR) belong to the nuclear hormone receptor (NHR) super-family (Mangelsdorf et al. 1995) which comprises 48+ transcription regulators and factors that are dependent on hormone ligand activation (Germain et al.

2006). In addition to ER and PR other examples of NHR include peroxisome proliferator-activated receptors (PPARs), thyroid receptors (TRs), androgen receptors (ARs) and retinoid acid receptors (RARs) (Lonard & O'Malley 2006; Lonard et al. 2007).

Estrogen action is mediated through 2 main receptor isoforms: ER alpha (ERα) and ER beta (ERβ) encoded by 2 genes ERS1 and ESR2 (Arnal et al. 2010; Nilsson 2002). These receptors localise to the plasma membrane of endometrial epithelial cells. Both estrogen receptors show overlapping expression in most tissues however distinct patterns of expression are found across gonadal tract, breast, testis, bone, skeletal muscle, liver, adipose tissue, central nervous system (CNS), vascular endothelium and bone marrow (Matthews & Gustafsson 2003). The ERα isoform is predominantly expressed in the endometrium of pre-menopausal women and has been shown to decrease post-menopause (Sakaguchi et al. 2003). Chapter 2 of this thesis describes two endometrial cell lines originating from women aged 39 (pre-menopause) and 72 (post menopause) and chapter 3 shows the relative expression levels of ERα and ERβ in these models cell lines, demonstrating experimentally the disparity of ER expression.

P_4 is the major progestin in animals and its effects are mediated through progesterone receptor (PR). P_4 is produced by the corpus luteum, the adrenal glands and the placenta, and plays a critical role in the regulation of the endometrium. During the first half of the ovarian cycle E_2 acts to expand the endometrial lining through stromal cell proliferation (Ozturk & Demir 2010). Post-ovulation P_4 serum levels increase over 40 fold (0.74-40.32) during the luteal phase (Figure 6) and this induces cellular differentiation of epithelial and stromal cells while antagonising the proliferative effect of E_2 through ER repression (Klaassens et al. 2006). The role of P_4 in inhibiting E_2 driven proliferation is vital in maintaining endometrial homeostasis and preventing excessive E_2 driven cell proliferation (Kim et al. 2013). This is the rationale behind the use of P_4 and the synthetic progestin medroxy-progesterone acetate (MPA) to treat ER-positive advanced endometrial carcinomas (Kim et al. 2013; Thigpen et al. 1999).

The action of P_4 is mediated through two isoform of PR that, unlike ER, are expressed from the same gene sequence but have different promoters (Kastner et al. 1990). The two isoforms PR-A and PR-B are structurally distinct and exert different genomic effects in response to ligand binding. This results in a system in which the expression of

progesterone target genes can be controlled by the ratio of PR-A:PR-B in specific tissues, and this has been shown to vary through the uterine cycle (Mote et al. 1999), and in endometrial cancers (Kumar et al. 1998).

1.05 The uterine cycle

The release of E_2 and P_4 during the follicular and luteal phases of the ovarian cycle results in ligand bound activation (or repression) of ER and PR target genes in the endometrium. Cyclic changes to these hormones thus regulate a corresponding series of physiological changes (mediated through ER and PR signalling cascades) to the lining of the uterus over the monthly cycle that prepare for embryo implantation.

Following successful implantation the embryo invades the uterine epithelium and the syncytiotrophoblast cells which line the trophoblast begin producing human chorionic gonadotrophin (hCG) (Handschuh et al. 2007). HCG stimulates the corpus lutem to continue secreting progesterone and thus prevents menstruation (see Figure 6 for menstruation)(Strott et al. 1969). HCG (referred to as the "pregnancy hormone") sustains pregnancy by promoting angiogenesis of the uterine lining (Berndt et al. 2009), suppression of maternal leukocyte migration (Akoum et al. 2005) and response and growth of the uterus in line with the developing embryo (Reshef et al. 1990).

In the absence of implantation the endometrium proliferates and degenerates over a 28 day cycle which is divided into three distinct stages; the menstrual, proliferative and the secretory phase (Figure 6). During the menstrual phase a decrease in serum levels of E_2 and P_4 cause the lining of the endometrium to be lost through menstruation with only the *stratum basale* (basal layer, 2-3 cells thick) being retained. This lost tissue is regenerated through the action of E_2 during the proliferative phase where the *stratum basale* serves as a source for regeneration of the *stratum functionale* (functional layer of the epithelium that faces the lumen)(King & Critchley 2010). The growth and regeneration of the stromal and epithelial layers appears to be interconnected as epithelial cells proliferation rates are reduced in co-culture with stomal cells (Arnold et al. 2001) suggesting that hormonal effects are exerted through paracrine signalling through the epithelial basement membrane. It is important to consider paracrine signals when devising cellular models of the endometrium as stromal signalling has been shown to influence endometrial epithelial cell proliferation and gene expression (Arnold et al. 2001). Finally, the secretory stage is marked by P_4 induced morphological changes

that prepare the epithelial layer for embryo implantation. This remodelling of the endometrium is termed decidualisation and involves a secretory transformation of the uterine glands, influx of maternal immune cells, thickening of the stromal layer and vascular remodelling of the stromal glands (Gellersen et al. 2007).

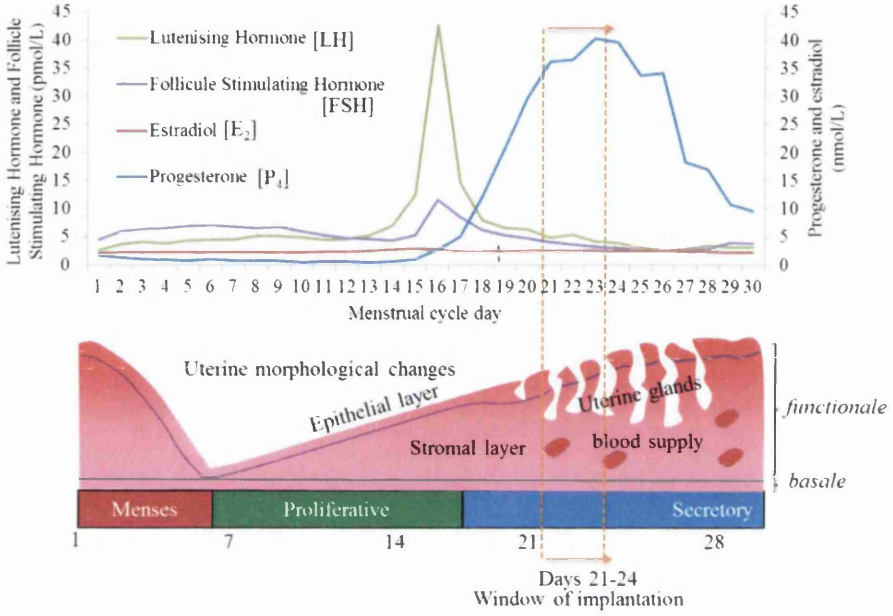

Figure 6: The uterine cycle. During the menstrual phase the lining of the endometrium is lost. The estrogen driven proliferative phase is characterized by cell growth and a thickening of the endometrium. The secretory phase is marked by vascularization, uterine gland development and a reduction in smooth muscle contractibility. The line graph is reproduced from serum concentrations stated in (Stricker et al. 2006), data compiled from 20 women not in receipt of contraception.

During the late secretory phase (day 21) the endometrium briefly becomes receptive to the fertilised embryo. This receptive state relies on chemokines (e.g. CCL14 which induces trophoblast migration) (Hannan et al. 2006), cytokines that regulate the maternal immune cell response to the semi foreign embryo (e.g leukemia inhibitory factor and interleukin-6) (Cork et al. 2002) and adhesion molecules (e.g. MUC1 and L-selectin)(Carson et al. 2006) that establish a physical attachment to the endometrial epithelium (van Mourik et al. 2009). After such a period (day 24) the endometrium becomes refractory to the embryo leading to the idea of an "implantation window".

This window of implantation (WOI) depends on the timely co-operation the three main systems that include cytokines, adhesion molecules, and immune cell suppression. Infertile pathologies can interfere with the this complex regulation required for

implantation but can also affect reproductive outcome by preventing ovulation or gamete transfer to the site of implantation.

1.06 Infertile pathologies

1.061 Endometriosis

Endometriosis is a common gynaecological disorder defined by the spreading of endometrial glands and stroma and lesions beyond the endometrium to extra-uterine locations, such as the ovaries, fallopian tubes or rectovaginal space (Olive & Schwartz 1993). Endometriosis affects around 6% of women who suffer from reduced fertility, pelvic pain and tubal dysfunction. The causative factors behind endometriosis are debated, it has been suggested that retrograde menstruation (reversal of menstrual flow) and failure of the immune system to remove resulting endometrial explants was first proposed (Sampson 1927) and is still the subject of debate (Redwine 2002; Bricou et al. 2008). Treatment can involve MIS to remove endometriotic tissue or hormonal therapies. As endometriosis is a proliferation of endometrial tissue specific targeting of ovarian E_2 production has had some success. However, endometriotic tissues have been shown to express 17-β-hydroxysteroid dehydrogenase (Zeitoun et al. 1998) which catalyses the local production of E_2 from E_1 (estrone). Recently it has been shown that this enzyme localises to endometrial lesions (Huhtinen et al. 2012) and that levels of E_1 and E_2 in endometriotic tissue are unrelated to circulating levels (secreted from the ovary) (Huhtinen et al. 2012). Thus future approaches that target localised E_2 are required.

1.062 Polycystic ovary syndrome

Polycystic ovary syndrome (PCOS) is a reproductive endocrine disorder defined by endocrine dysregulation (including elevated testosterone and early cycle LH), chronic anovulation and ovarian cysts that frequently results in infertility. PCOS is the most common endocrinopathy and affects 5-10% of reproductive age women (Krysiak et al. 2006). Treatment involves lifestyle changes such as weight loss and reduced alcohol intake before pharmacological intervention using metformin to restore menstrual cycling, reduce BMI and decrease testosterone (Velija-Ašimi 2013). Ovulation may be restored by the introduction of clomiphene citrate (CC) (Panidis et al. 2013). CC is a synthetic estrogen that antagonises ER and thus reduces the negative feedback of E_2 acting on the pituitary gland resulting removing the repression of LH and FSH which

can help produce high quality mature oocytes (see Figure 3 for the hypothalamic-pituitary-ovarian axis). Combined metformin-CC treatment increases ovulation and conception rates in a synergistic fashion (Ayaz et al. 2013)

1.063 Unexplained infertility

Women with unexplained infertility (UIF) are usually considered sub-fertile with no cause attributable using current diagnostic technology, but they may become pregnant after fertility treatments (Evers 2002). The normal treatments for UIF are (in order of application) timing therapy that coordinates the time of ovulation and coitus, controlled ovarian hyperstimulation (COH) (to induce ovulation), IUI, diagnostic MIS (to inspect the endometrium) and finally IVF (Tsuji et al. 2009). The combination of COH and IUI results in a meeting of oocyte and sperm in the ampulla and maximises the chance of successful fertilisation (Tsuji et al. 2009), however this does not always result in clinical pregnancy (a pregnancy confirmed by high levels of hCG and ultrasound imaging).

1.064 Limiting factors for receptivity

The hormonal regulation of the ovarian and uterine cycles through the HPO axis has been extensively studied and application of this knowledge has resulted in clinical outcomes for reproductive pathologies, such as the use of CC to artificially raise FSH and induce ovulation in women with anovulatory polycystic ovaries or UIF (Casper 2007). While the induced ovulation success of CC is high, typically 60-90% the overall pregnancy rate following treatment is still low (Neveu et al. 2007) suggesting an as yet unknown rate limiting step in achieving fertility. Furthermore, a recent study investigated the rate of clinical pregnancy in UIF women following COH and IUI and found this to be 466 out of 2929 individuals (15.6%) (Wolff et al. 2013). Despite successful ovulation and the artificial introduction of sperm clinical pregnancy is still infrequent which has led to the notion that an endometrial factor may be responsible for UIF (Wolff et al. 2013). This notion is supported by the low success rate of IVF which is between 20.7% (natural cycle) (Pelinck et al. 2007) and 30.0% (COH) per treatment and by the relatively high occurrence of miscarriage in both natural and assisted contraception.

Advances in reproductive medicine mean ovulation and fertilisation can be induced and embryos can be screened for defects, however pregnancy is still not established

suggesting a failure of fertilised embryo to implant to the uterine epithelium due to a lack of endometrial receptivity. Endometrial factors such as thickness (Hawkins et al. 2013), and expression of adhesion proteins (Liu et al. 2013) contribute to this receptive phenotype. The decoration of the endometrial epithelium with adhesion proteins during the WOI and the relevance of the patterned expression on the endometrial surface is not fully understood but it has been suggested that this facilitates embryo implantation and thus contributes to the receptive phenotype (Sharma and Kumar 2012; Rashid et al. 2011; Domínguez et al. 2010)

1.07 Endometrial receptivity

Endometrial receptivity refers to the physiological state in which the endometrium epithelium is able to facilitate embryo attachment, adhesion and subsequent penetration into the underlying stroma. The human embryo implants 7-10 days after the LH peak (Bergh et al. 1992), 9 days after ovulation. This implantation cascade is a linear process that requires a viable embryo at the correct developmental stage, a receptive endometrium and a subtle dialogue or crosstalk between the embryo and the endometrial surfaces (Rashid et al. 2011; Valles & Domínguez 2006; Carson et al. 2000). Adhesion across the endometrial monolayer is of paramount importance during the initial stage of the implantation cascade and crucial for establishment of clinical pregnancy.

Human implantation can be separated 3 main phases (Bentin-Ley & Lopata 2000; Schlafke & Enders 1967). The first phase is termed *apposition*, during which the trophoblast moves into close proximity of the uterine epithelium allowing initial tethering to the uterine epithelium. The second stage is known as *adhesion* in which the embryo firmly anchors to the epithelial basal lamina and at this point cannot be removed by uterine flushing. Finally, the embryo trophoectoderm forms a penetration cone that infiltrates through the epithelial layer and underlying basal lamina displacing cells of the stromal compartment (Bentin-Ley et al. 2000), a process known as *invasion* (Figure 7). The initial apposition stage and subsequent cell adhesion between the trophoectoderm and endometrial epithelium depends on a complex expression of adhesion molecules at their respective apical cell surfaces (Pafilis et al. 2007). This occurs despite the generally non-adherent nature of the apical epithelial cell surface, and as such embryo implantation is characterised as cell biological paradox.

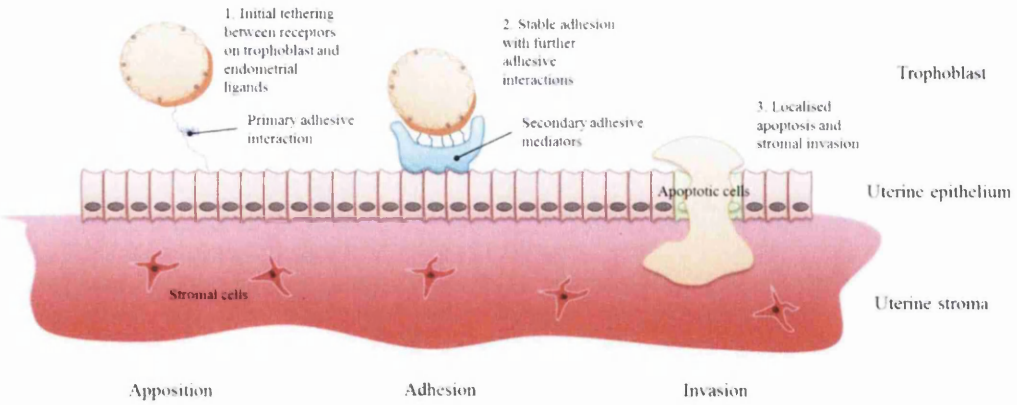

Figure 7: The three phases of human implantation. Embryo implantation occurs in three phases; apposition, adhesion and invasion. The endometrial physiology changes throughout the menstrual cycle and is receptive to the embryo in the late secretory phase. The trophoblast approaches the uterus wall and initial tethering secures the trophoectoderm to the apical epithelium to allow stable adhesion and invasion of the stromal layer following the localised degeneration of the epithelium.

There is debate in the literature as to whether human implantation fails primarily due to poor embryo quality or molecular aspects resulting in poor uterine receptivity (Koot et al. 2012). Implantation failure due to embryo genetic and metabolic abnormalities has been be proposed (Pellicer et al. 1999; Quenby et al. 2002), but it is strongly suggested that an unreceptive epithelium may contribute (Cameo et al. 2004).

1.08 Endometrial adhesion proteins and uterine receptivity

Intracellular recognition and attachment of the embryo involves classes of proteins localised to the apical endometrial membrane, including but not limited to; mucins (Horne et al. 2001), cadherins (Riethmacher et al. 1995), immunoglobulins (Defrère et al. 2005; Chae et al. 2010), integrins (Lessey 1998; Lessey et al. 1992) and selectins (Genbacev et al. 2003). Interestingly, examples from each of these classes of protein have been shown to influence endometrial receptivity (Horne et al. 2001; Riethmacher et al. 1995; Defrère et al. 2005; Lessey 1998; Genbacev et al. 2003). It is likely that the expression and post-translational modification of these proteins is able to alter membrane adhesion function (Pinho et al. 2011). Moreover, it is N-linked glycosylation of key transmembrane proteins such as the mucins that is believed to aid initial embryo recognition (Margarit et al. 2009). The function of each class of proteins during the WOI is outlined below and illustrated in Figure 11.

1.081 Cadherins

Cadherins are glyco-proteins that specialise in cell-cell adhesion. The family is subdivided into E-, P-, and N- cadherins on the basis of tissue localisation and immunological activity. E-cadherin localises to adherent junctions on the lateral side of epithelial cells and has established roles in cell-cell adhesion (Gumbiner 1996), and maintenance of cell polarity (Nelson et al. 2013). The E-cadherin interaction is homophilic and dependent on Ca^{2+}. In the reproductive setting, E-cadherin has roles in embryogenesis where it is involved in gastrulation, neuralation and organogenesis (Barth et al. 1997). E-cadherin dysfunction due to mutations in the E-cadherin gene can result in defective embryo development and subsequent implantation failure in mice (Riethmacher et al. 1995). In the human endometrium there is conflicting evidence surrounding E-cadherin regulation. E-cadherin mRNA is up-regulated during the window of implantation (Fujimoto et al. 1996), but several studies have shown E-cadherin protein expression remains stable during the menstrual cycle (Béliard et al. 1997; Poncelet et al. 2002; Dawood et al. 1998). However, more recently the cellular distribution of E-cadherin has been shown to change from lateral to apically polarised during the window of implantation (Buck et al. 2012). Cellular Ca^{2+} is a critical regulator of E-cadherin, increasing concentrations of Ca^{2+} stimulate E-cadherin disassembly at lateral adherent junctions (Li et al. 2002) providing a rationale for this change in cellular distribution. Moreover, calcitonin (a regulator of serum Ca^{2+}) has been shown to be up-regulated in the mid-secretory phase under P_4 stimulation (Kumar et al. 1998). Thus during the WOI progesterone may regulate E-cadherin via calcitonin release. It is possible that expression of E-cadherin in the apposition phase of implantation could play a role in embryo adhesion because it is expressed on the trophoblast (Coutifaris et al. 1991), the endometrium (Shirane et al. 2012) and is a homophilic binding protein (Chappuis-Flament 2001). It is also possible that E-cadherin depolarisation during the invasion stage of implantation allows for trophoblast penetration through the luminal epithelium by weakening epithelial cell junctions. E-cadherin up-regulation has been observed at implantation sites (Jha et al. 2006) which suggests the protein has a role to play.

1.082 Immunoglobulins

Intercellular adhesion molecule 1 (ICAM-1) belongs to the immunoglobulin class of proteins and is expressed on the surface of fibroblasts, leukocytes, endothelial and epithelial cells. ICAM-1 mediates cell-cell adhesion through its interaction with

integrins (Oberyszyn et al. 1998), which are widely expressed on the membranes of many cell types. ICAM-1 is known to be involved in leukocyte trans-epithelial migration (Hubbard & Rothlein 2000) through and interaction with endothelial β2 integrin which results in the stable attachment of the leukocyte to the epithelium. Leukocyte migration has other molecular parallels with embryo implantation such as the use of L-selectin and its ligands to initiate adhesion of leukocyte and trophoblast (Dominguez et al. 2005), thus ICAM1 potentially has shared role in these processes. ICAM-1 is expressed on endometrial stromal and epithelial cells where it is localised to the apical surface. Interestingly, expression in the apical epithelial layer (where it is placed to interact with the trophoblast) is higher than in the stroma but both cell types have strong expression suggesting an inherent role for ICAM-1 in endometrial physiology (Defrère et al. 2005) and possible recognition of the embryo through integrins, which have been shown to be expressed on the trophoblast (Shu et al. 2013).

1.083 Integrins

Integrins are transmembrane heterodimeric proteins consisting of α and β subunits linked by non-convalent bonds. In total 18 α and 8 β subunits have been identified in humans, which can combine to form 24 distinct integrin molecules. A diverse variety of integrins have been described within the endometrium (Lessey et al. 1994; Coughlan et al. 2013) and most endometrial integrins display constant expression throughout the menstrual cycle, however some have been shown to increase in the secretory phase, and could serve as markers of receptivity (Lessey et al. 2000). The integrins α1β1, α4β1 and αVβ3 are all expressed during the WOI, but of this group only the β3 subunit shows increased mRNA expression after day 19, and is undetectable beforehand. Immunohistochemistry (IHC) has revealed the presence of αVβ3 in luminal epithelium in the endometrium together with one of its ligands osteopontin (OPN), during the WOI (Apparao et al. 2001). The localisation to the apical epithelial surface, and the tightly regulated window of expression suggest αVβ3 is a potential receptor involved in mediating embryo adhesion. The expression of integrins is not limited to the uterine epithelium, the trophoectoderm has been shown to express integrins at the time of implantation (Wang & Armant 2002). One possibility is that integrins on the uterine epithelium and trophoblast bind to common ligands present in extra cellular matrix (ECM) of the trophoblast and epithelium respectively, thus resulting in the sandwich model of trophoblast adhesion. Examples of αVβ3 ligands are epithelium secreted OPN

and trophoblast secreted oncofetal fibronectin (OFN). Integrin β3 has been shown to be required for embryo adhesion as siRNA treatment of β3 in Ishikawa cells reduced attachment of rat trophoblasts (Kaneko et al. 2011). These experiments revealed β3 expression on the trophoblast and on the apical uterine epithelium; trophoblast local expression was up-regulated by close endometrial proximity (Kaneko et al. 2011).

The αVβ3 and OPN adhesion mechanism is very likely to be intricately involved in the later stages of embryo adhesion as knocking down αVβ3 expression reduces trophoblast attachment. The distribution of integrin β3 in trophoblast cells polarises to the apical surface following attachment (Kaneko et al. 2011) suggesting that limited attachment occurs before activation of the integrin adhesion mechanism and it has been suggested that "juxtacrine" signalling is required for integrin activation (Armant 2005). Moreover, αVβ3 and OPN are relatively small proteins at 90KDa and 70KDa respectively and are dwarfed by other components of the endometrial epithelium and as such unlikely to be the first (and most critical) point of contact for the approaching embryo.

1.084 Selectins

The selectin family consists of a group of three closely related cell adhesion molecules (CAMS), P-selectin (140kDa), L-selectin (74-100 kDa) and E-selectin (120kDa). Each selectin has been well conserved during mammalian evolution as human, mouse, rat, and bovine share a high degree of amino acid sequence homology (Jebali et al. 2011). The selectin family share a unique, characteristic and highly conserved N-terminal calcium dependent lectin domain (Lasky 1995), a regulatory epidermal growth factor (EGF)-like domain which is 47% conserved, and 2-9 short consensus repeats (SCR) domains that are 35% conserved (Figure 8) (Kansas 1996; Tedder 1995; Ley 2003). However, the transmembrane (Barthel et al. 2008) and cytoplasmic domains are not conserved at all between groups. The similarity in the lectin and EGF domains suggests overlapping affinity for ligands such as tetrasaccharide carbohydrate moieties like sialyl lewis x (sLe^x) and sialyl lewis a (sLe^a) (Rosen 2004; McEver 2002). Mucins are often decorated with these carbohydrate groups allowing them to present ligands to selectins.

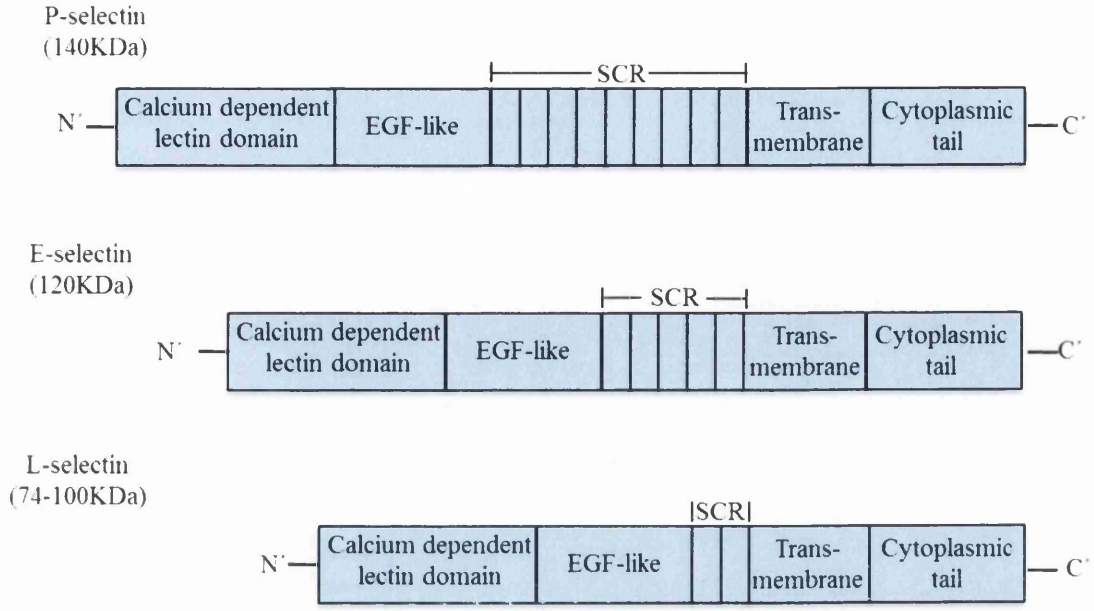

Figure 8: The structure of P, E and L-selectin. All selectins contain a calcium dependent lectin domain~120aa, an EGF-like domain~36aa, a short consensus repeat region (which differs between selectins)~63aa, a transmembrane~23aa and cytoplasmic region 17-35aa. The lectin domain is associated with carbohydrate binding and can interact with a diverse range of ligands.

Prior to hatching from the zona pellucida [glycoprotein coat], embryo L-selectin expression was found to be weak and diffuse or absent, whereas after hatching strong staining was observed over the entire embryo surface and with particular association to the trophectoderm (Genbacev et al. 2003). Increased expression the sLe^x L-selectin ligand (specifically) has been shown on the surface of pinopods, which are markers of fertility (Nejatbakhsh et al. 2012), and up-regulation *in vitro* of these ligands increases trophoblast attachment (Liu et al. 2011). Moreover, decreased expression of these ligands has been shown in infertile pathologies PCOS and endometriosis compared to fertile controls, and absence of these ligands associated with recurrent implantation failure (RIF) (Foulk et al. 2007) leading to the suggestion that they are required for successful implantation and may be markers of fertility (Foulk et al. 2007).

1.085 L-selectin and sialyl lewis x ligands

The interaction between selectins and their ligands has long been established in the process of leuckocyte rolling (Alon et al. 1996; Alon & Feigelson 2002; Rosen 2004). Both the capture and rolling of leuckocytes is mediated by endothelial selectins that are able to form transient, low affinity contacts with selectin ligands on leuckocytes. This

slows the leuckocyte allowing it to sense signals on the inflamed endothelium and facilitates integrin activation leading to consequent leuckocyte arrest (Bianchi et al. 2013). Limited parallels have been drawn with the initial stages of embryo attachment to the uterine epithelium (Dominguez et al. 2005), where L-selectin may interact with ligands known to be expressed on the endometrial surface during the WOI (Lai et al. 2006; Lai et al. 2005) to secure the initial attachment of the embryo (Figure 9). Binding of L-selectin to its glycoprotein ligands occurs by the N-terminal lectin domain that recognizes the tetrasaccharide sLe^x, its isomer sLe^a and other related oligosaccharides (Foxall et al. 1992).

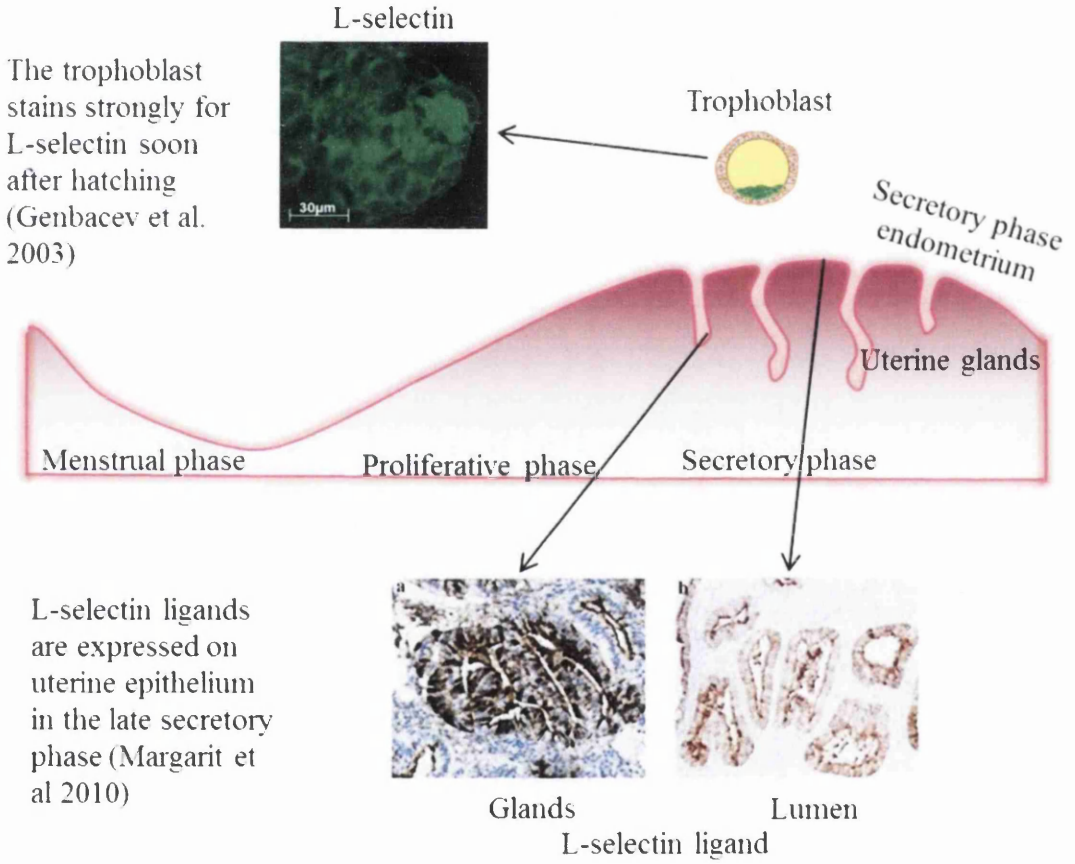

Figure 9: Localisation of L-selectin and its ligands. Immunostaining has shown that L-selectin is strongly expressed on the blastocyst prior to hatching (Genbacev et al. 2003) and that L-selectin ligand is expressed on the uterine epitheium. Images reproduced from (Genbacev et al. 2003; Margarit et al. 2010)

Beads coated with 6-sulfo sLe^x, the recognition determinant moiety for L-selectin, were introduced to placental tissue explants under flow conditions to assess the interaction with L-selectin (Genbacev et al. 2003). The beads bound to cytotrophoblast cells and to the syncytiotrophoblast surface, the cells that express L-selectin *in situ* and *in vitro*. Pre-

incubating cytotrophoblast cells with blocking antibody to L-selectin [DREG-56 mAb] abolished most of the binding to 6-sulfo sLe^x conjugated beads. This suggests that L-selectin on the trophoblast and sLe^x carbohydrate ligand motifs on the uterine epithelium could be potential mediators of embryo adhesion (Genbacev et al. 2003; Minas et al. 2005; Kim et al. 1999). A number of physiological ligands including mucins, have the ability to host sLe^x type tetrasaccharides and it has been shown with purified mucins and selectin affinity chromatography that sialic acid dependent mucin affinity occurs for all three selectins (Kim et al. 1999).

1.086 Mucins

Mucins are large (250KDa-2.5MDa), extensively glycosylated proteins present on the apical surface of endometrial epithelial cells (Hey et al. 1995; Lagow et al. 1999). Many mucins have been identified and have been sub-classified into secreted or gel forming (MUC2, MUC3, MUC5AC, MUC5B and MUC6) and membrane tethered or cell surface (MUC1, MUC3, MUC4, MUC12, MUC13, MUC16 and MUC17). The secreted mucins form a gel layer termed the adhesive mucus layer (AML) that provides the respiratory, gastrointestinal and reproductive epithelia with a degree of protection against bacterial and (in the case of the intestine) enzymatic insults (Lamont 1992; Gum 1995). The secretory surfaces of the liver, pancreas and gall bladder are also protected by this gel layer and the membrane tethered mucins consolidate this gel like defence. Strict classification of the membrane tethered forms is clouded by the occurrence of splice variants that generate secreted forms (Choudhury et al. 2001; Zaretsky et al. 1990) and the spontaneous shedding and continual regeneration of some mucins at the cell surface (Thathiah et al. 2003; Thathiah & Carson 2004).

Mucins are characterised by a highly variable tandem repeat (VNTR) domain (also known as the mucin domain). The VNTR region contains sites for addition of sialic acid residues that imbue mucins with a net negative charge and has been shown to be a determining factor in the ability of mucins to protect epithelia from microbes such as plasmodium (Kato et al. 2013), bacteria (Martín-Sosa et al. 2002; Derrien et al. 2010) and rotovirus (Yolken et al. 1992). The VNTR domain may play a significant role in embryo recognition and this concept is explored in chapter 5 of this thesis. The tethered mucins known to be expressed in the endometrium are MUC1, MUC4 and MUC16

(Figure 10) (Brayman et al. 2004) and these are the subject of the mucin component of this thesis.

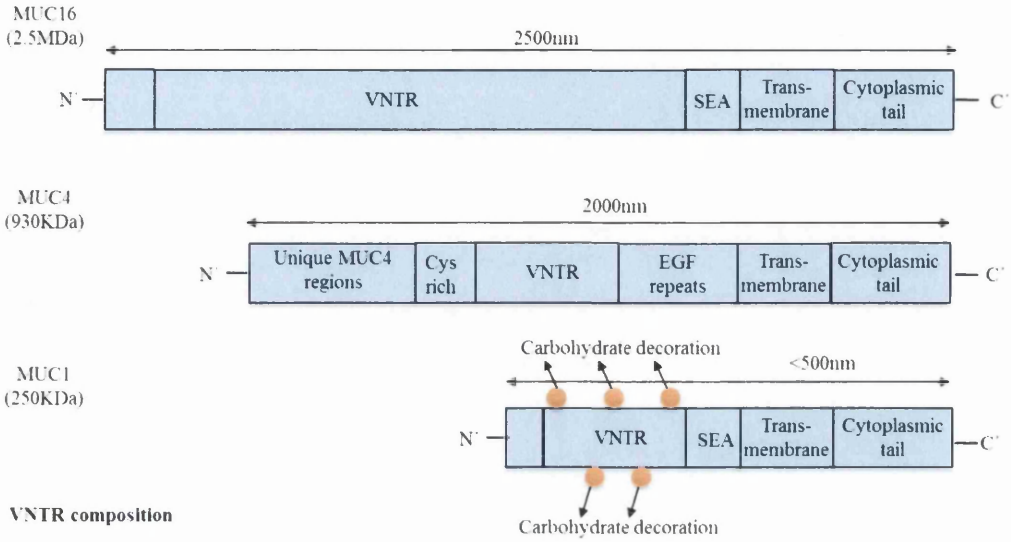

Figure 10: The structure of endometrial mucins. All three mucins share small cytoplasmic and transmembrane domains and a large extracellular domain containing the VNTR that is subjected to extensive glycosylation. Due to the large number of proline residues and O-linked glycans in this region, the extracellular domain is proposed to have a very rigid structure extending out from the membrane (sizes indicated here). The VNTR region dominates the extracellular domain while the SEA (sea urchin, enterokinase, agrin) domain is a target for cleavage. The relatively small cytoplasmic tail is subject to phosphorylation and can act as a transcription factor. All mucins have a VNTR repeating sequence which differs in primary amino acid sequence and repeat number. The amino acid sequence of MUC1,4 and 16 VNTRs is shown.

The tethered mucins contain a small cytoplasmic domain, a transmembrane region and a large extracellular domain that contains the VNTR region (Figure 10). A sea urchin, enterokinase, agrin (SEA) domain is a site for mucin cleavage (Wreschner et al. 2002) and is thought to facilitate shedding of mucins from the epithelium using proteolysis enzymes such as tumor necrosis factor-α converting enzyme/ADAM 17 (Thathiah et al. 2003) and membrane-type matrix metalloprotease (Thathiah & Carson 2004). It has been suggested that the large size of the mucins and glycosylation state of the VNTR region provides steric-hindrance by masking other adhesion proteins such as E-cadherin and integrins from recognising the approaching embryo thus modulating their activity

(Hilkens et al. 1992). The branched and rigid structural properties of mucins are likely to dictate the biomechanical (adhesive) properties of endometrial monolayers, a characteristic explored in chapter 4.

This thesis focuses on investigating whether MUC1 is the major determinant of embryo epitope recognition, while not overlooking the potential overlapping functions of MUC4 and MUC16. MUC1 is abundantly expressed at the apical surface of both luminal and glandular epithelia of the uterus in various species (Hoffman et al. 1998; Hey et al. 1994; Hild-petito et al. 1996; Surveyor et al. 1995; Julian et al. 2005). Down-regulation of MUC1 during the WOI or at nidation sites is a requisite for uterine receptivity in a wide variety of large animal models (Hild-petito et al. 1996; Surveyor et al. 1995; Julian et al. 2005; DeSouza et al. 1998; Bowen et al. 1996). In humans MUC1 is retained during the window of implantation (Hey et al. 1994; DeLoia et al. 1998; Hey et al. 1995), which distinguishes humans from other species. This suggests that although differentially regulated, MUC1 is related to fertility in humans. The glycosylation status of MUC1 has been linked to endometrial receptivity (Hey et al. 1995; Margarit et al. 2010), and it is known to host carbohydrate ligands recognised by L-selectin. The adhesive interaction between MUC1 and L-selectin expressed on the embryo is therefore one of the core threads of investigation throughout this thesis.

1.09 MUC1 hosts sialyl lewis x ligands

The sLe^x moiety and its positional isomer sLe^a have been associated with endometrial MUC1 protein in the EEC cell lines Hec-1-A and Hec-1-B (Hey & Aplin 1996). Further experiments showed that Hec-1-A expressed both sLe^x and sLe^a while Hec-1-B expressed only sLe^a. Moreover, immunoprecipitation has demonstrated that sLe^a is associated with MUC1 in Hec-1-B cells, and both sLe^x and sLe^a are associated with MUC1 in Hec-1-A cells (Hey & Aplin 1996), suggesting that MUC1 may be a potential mediator in embryo adhesion.

MUC1 glycosylation and generation of sLe^x and sLe^a depends initially on terminal N-Acetylglucosamine (GlcNAc) carbohydrate residues attached to the VNTR region in the core extracellular domain of the molecule. The VNTR consists of a tandem repeating 20-amino acid sequence –Pro-Pro-Ala-His-Gly-Val-Thr-Ser-Ala-Pro-Asp-Thr-Arg-Pro-Ala-Pro-Gly-Ser-Thr-Ala (Hattrup & Gendler 2008; Tarp & Clausen 2008). Formation

of GlcNAc can occur at five potential O-glycosylation sites in the repeat (Figure 13). GalNAc formation through α-O-glycosidic linkage to Ser/Thr residues in the VNTR region is dependent on the glycosyltransferase enzyme, GlcNAc6ST-2

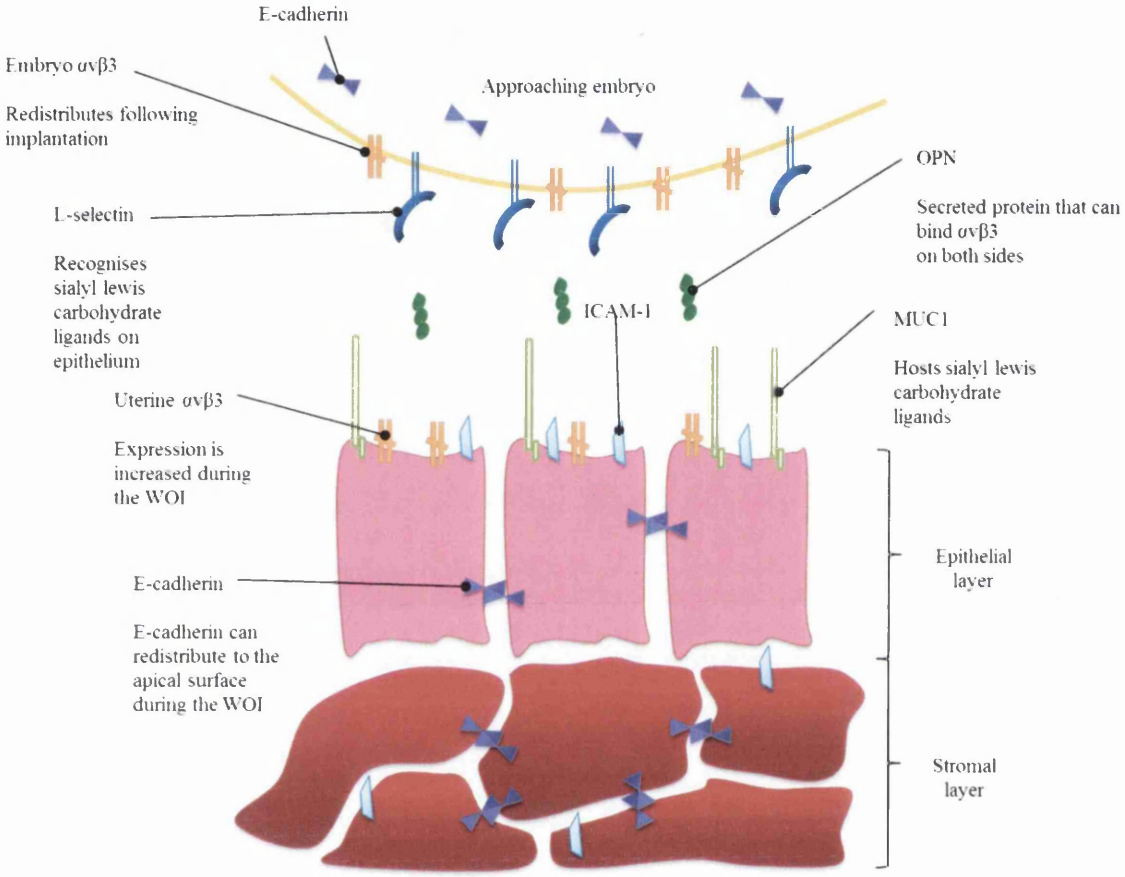

Figure 11: Mechanisms of human implantation. The endometrial epithelium is decorated with a range of adhesion molecules that mediate embryo implantation. E-cadherin homophilic junctions are present in the epithelial and stromal layers, but can redistribute to the apical epithelial surface during the WOI. ICAM-1 is expressed on the stromal and the epithelial layers and may recognize integrins on the approaching tropoblast. Integrin αvβ3 is expressed on the epithelium and trophoectoderm and recognizes secreted OPN, a linker molecule that is up-regulated during the WOI. MUC1 is large protein that supports carbohydrate ligands for L-selectin that is expressed on the trophoblast.

After attachment of the initial GlcNAc residue other glycotransferase enzymes catalyse the formation of the functional sialyl lewis epitopes. In the case of sLe^x, β4-Gal-transferase, α3-sialyltransferase and α3-Fuc-transferase sequentially attach β4-Galactose, α3-sialic acid and α3-Fucose to GlcNAc. SLe^a chains are synthesized by β3-Gal-transferase, α3-sialyltransferase and α4-Fuc-transferase (Brockhausen 2006) (Figure 12).

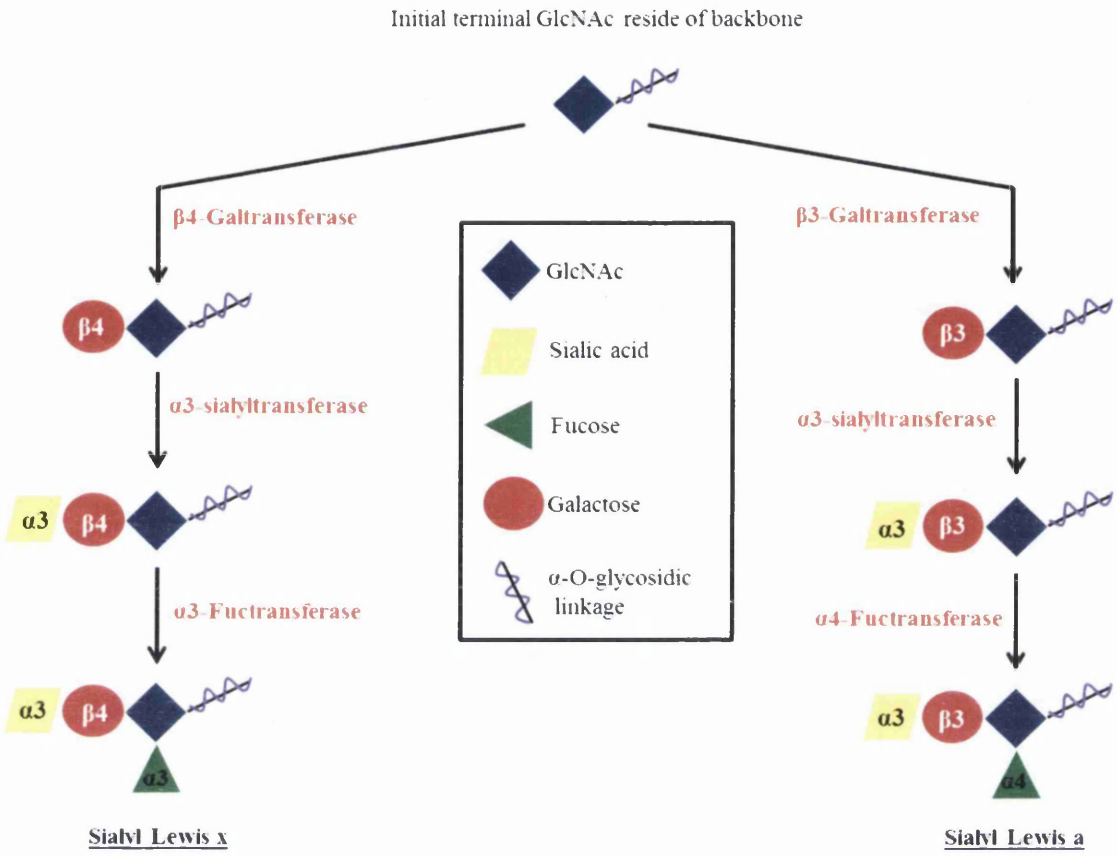

Figure 12: Generation of sLe^x and sLe^a antigen assembly begins with terminal N-acetylglucosamine (GlcNAc) residues found on endometrial glycoproteins. The sLe^x structure is synthesised by the addition of a β4-Galactose to GlcNAc by β4-Galtransferase (β4-GalT), followed by the addition of α3-sialic acid to Galactose by α3-sialyltransferase (ST3Gal) and of α3-Fucose to GlcNAc by α3-Fuctransferase (α3-FucT). SLe^a antigen is assembled by β3-Gal-transferase (β3-GalT), ST3Gal and α4-Fuc-transferase (α4-FucT). (diagram reproduced from 'Brockhausen 2006').

1.10 Sialyl lewis ligands and endometrial receptivity

SLe^x and sLe^a are both recognised by all three selectins (Galustian et al. 2002), however L-selectin is thought to have the highest affinity for the sLe^x isoform (Silva et al. 2011), and it is sLe^x not sLe^a that has been proposed to mediate adhesion during implantation (Liu et al. 2011). The anti-Human Cutaneous Lymphocyte Antigen (CLA) monoclonal antibody (HECA-452) recognises sLe^x and requires both the presence of α3 sialylation and α3 fucosylation for epitope recognition (Toppila et al. 1999). MECA-79 is an anti-sLe^x mAb that requires the presence of 6-sulfo sLe^x, a sulfation dependent determinant on L-selectin ligands that overlaps with the ligands' recognition epitope (Pablos et al. 2005).

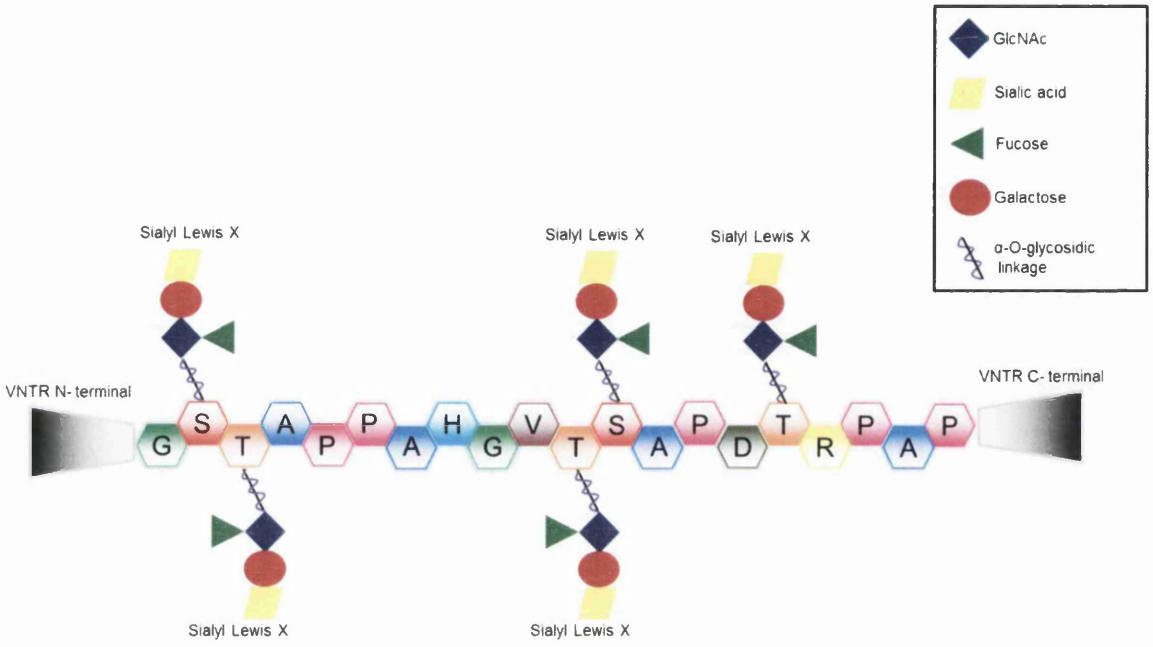

Figure 13: Each VNTR motif is able to host five glycans. The VNTR domain of MUC1 is a 20aa sequence that is repeated 20-125 times. Each repeat is able to host 5 glycans via serine and threonine residues in the protein core. The construction of sialyl lewis antigen begins with the attachment of GlcNAc to the VNTR core via an α-O-glycosidic linkage and requires β4-galtransferase, α3-sialyltransferase and α3-fuctransferase for addition of β4-galatose, α3-sialic acid and α3-fucose thus completing the sLe^x epitope.

It has been shown that sLe^x is elevated when the endometrium becomes receptive during the WOI (Genbacev et al. 2003), and that elevated sLe^x has been associated with improved implantation (Wang et al. 2008). Moreover, suppression of the fucosyltransferase α3-FucT, which catalyzes the final stage synthesis of sLe^X, both reduces sLe^X and decreases implantation in an *in vitro* model (Liu et al. 2008).

The expression of the sulfo-transferase enzyme, GlcNAc6ST-2 (N-acetylglucosamine-6-O-sulfotransferase), a has been shown to be a requisite for the generation of 6-sulfo sLe^x in the non-endometrial tissues (Hiraoka et al. 1999), and knocking down GlcNAc6ST-2 gene expression in mice models reduced sLe^x highlighting the importance of GlcNAc6ST-2 in sLe^x generation (Hemmerich & Rosen 2000; Tangemann et al. 1999). It has also been shown siRNA treatment of GlcNAc6ST-2 readily reduced sLe^a generation (Okayama et al. 2011) highlighting the important role of this enzyme.

Studies in our group have used endometrial biopsy material and have reported a reduction in GlcNAc6ST-2 expression, correlating with reduced MECA-79 expression

in infertile patients (Margarit et al. 2010). The GlcNAc6ST-2 enzyme catalyses the very first step in the generation of both sLe^x and sLe^a, and as such is a crucial factor in the establishment of these moieties (Figure 12).

1.11 Endometrial pathologies and L-selectin ligands

Previous publications from our group have reported significant decreases in 6-sulfo sLe^x (as recognised by MECA-79 mAb) in patients presenting with infertile pathologies such as UIF, PCOS and endometriosis compared to the fertile controls (Margarit et al. 2010). MUC1 may carry sLe^x L-selectin ligands throughout the secretory phase of the menstrual cycle, which gives MUC1 the potential to interact with L-selectin expressed by the trophoblast at the time of implantation (Carson et al. 2006). As MUC1 structure affects the extent of glycosylation (there are 5 potential sites per VNTR repeat) (Figure 13) this may link MUC1 length with the ability of the molecule to present L-selectin ligands to the trophoblast. Horne and colleagues reported that MUC1 isoforms with shorter VNTR regions correlated with an unexplained infertile phenotype, while the longer VNTR isoforms appeared more frequently in fertile women (Horne et al. 2001). The presentation of sLe^x L-selectin ligand at the endometrial surface is a potential marker for fertility and is likely dependent on a multitude of factors such as expression of scaffold proteins (of which MUC1 is a prime candidate), the expression of structural isoforms of such proteins and expression of a host of glycotransferase enzymes such as GlcNAc.

1.12 Current approaches to modeling implantation *in vitro*

Despite continued and intense biochemical investigations into potential receptivity markers such as the human gene expression endometrial receptivity database (HGEx-ERdb) (Bhagwat et al. 2013) the process of human implantation is not fully understood. Functional models of implantation offer an alternative to biochemical screening but are subject to their own limitations. It is not possible to study the mechanism of human implantation *in vivo* and even *ex vivo* models present many difficulties (Hannan et al. 2010). Very few laboratories have access to human embryos which must be specifically donated for the purpose of research and consent obtained. It is somewhat easier to obtain biopsy material through endometrial pipelle extraction, and whilst primary endometrial stromal cells are relatively easy to prepare from endometrial biopsy epithelial cells are very difficult to isolate and it is not possible to maintain these cells indefinitely in culture.

Animal models are routinely used for the study of early implantation events and rodents are still the most commonly used (Ye et al. 2012; Grzmil et al. 2013), but larger primates such as baboons (Fazleabas et al. 1999) and monkeys (Enders & Lopata 1999) are also subjects of study. However, animal models all have limitations as substitutes for human implantation. Primates (in particular the baboon) and guinea pigs are most similar to humans, however primates are costly, impractical and produce few offspring (Lee & DeMayo 2004; Enders et al. 1983; Enders et al. 1989; Enders & Lopata 1999; Tarantal & Hendrickx 1988) and guinea pig blastocysts implant with the zona pellucida intact (a glycoprotein coat from which human embryos "hatch") (Enders 2000; Enders & Schlafke 1969). Mice, rats, and rabbits are the easiest to sustain and most well defined, but do not exhibit interstitial implantation (the complete embedding of the blastocyst within the endometrium of the uterine wall) (Dey et al. 2004; Dey 2006; Hoffman et al. 1998) and have short uterine cycle lengths; 4-5 days in rodents compared to 28 in humans (Caligioni 2009). Pigs, sheep, and cows have prolonged implantation events but also do not exhibit interstitial implantation (Gray et al. 2002; Gray et al. 2001; Wooding 1984; Wooding 1992). Moreover, MUC1 is down-regulated during the WOI of most animals (Surveyor et al. 1995; Julian et al. 2005; DeSouza et al. 1998) compared to humans where it is retained (DeLoia et al. 1998) and crucially the role of L-selectin and sLe^x ligands in animals is still undetermined.

Therefore, use of appropriate cell lines, particularly for functional studies of implantation offers an alternative model. Use of cell lines derived from endometrial cancers such as Hec-1, Ishikawa, EEC-1, and RL95 and trophoblast choriocarcinomas (trophoblastic, placental cancer) such as JAR, JEG-3 and BeWo is established (Teklenburg & Macklon 2009; Hannan et al. 2010). These cell lines are often used for attachment models that involve a co-culture of endometrial epithelial cells and trophoblast spheroids. Typically, the epithelial cells are grown in monolayer configuration which is used to mimic the endometrial epithelium, where they are subjected to various hormonal or biochemical stimulation and then spheroids are introduced. This co-culture is subjected to physical agitation (rocker machine) and attachment (or detachment) rates are used as a measure of endometrial receptivity (Figure 14). Spheroids are generated by the accumulation of trophoblastic cells by rocking in culture until the reach the size of the pre-implantation embryo (~105μm) at which point they are selected for co-culture (Ho et al. 2012).

This model of implantation has been widely used (Hohn et al. 2000; John et al. 1993; Kosaka et al. 2003; Li et al. 2002; Rahnama et al. 2009; Thie & Denker 2002; Tinel et al. 2000; Kaneko et al. 2013; So et al. 2012). However, experiments such as these are time consuming and result in low sample numbers because spheroids are selected microscopically and their attachment is quantified by manual counting. More recently Ho and colleagues refined this system by introducing a sieve between 70-100μm allowing more rapid collection of trophoblast spheroids. They also fluorescently stained spheroids so attachment rates could be calculated using a fluorescent signal from a plate reader (Ho et al. 2012).

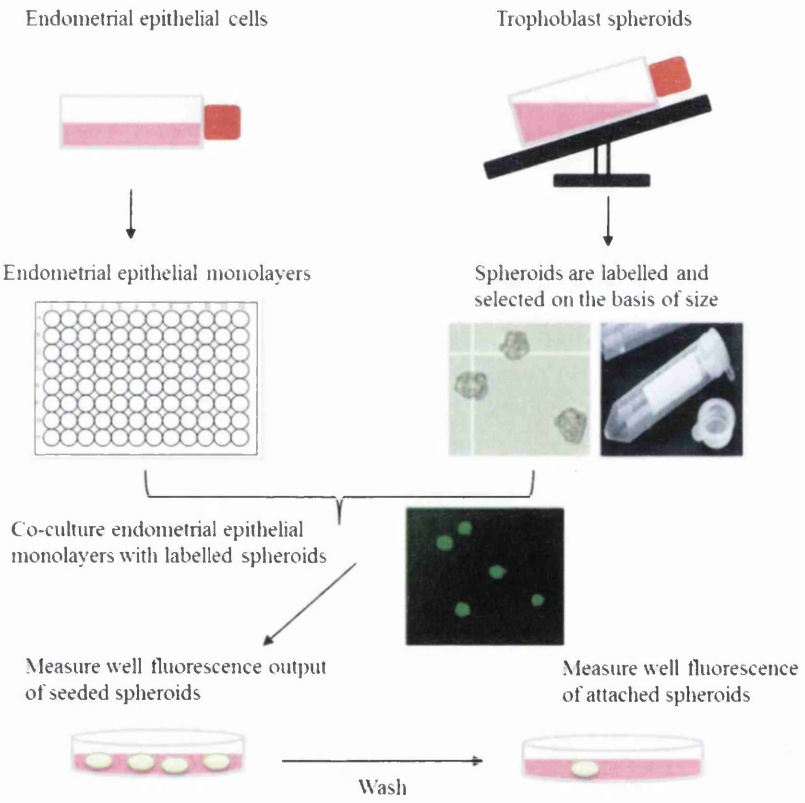

Figure 14: Methodology of automated adhesion assays. Endometrial epithelial cells are grown in flasks, trypsinized, and seeded onto 96-well plates to form monolayers. Trophoblast spheroids are generated by rocking trophoblast cell lines until the resulting aggregated spheroids are between 70-100μm, they are then stained and selected for co-culture. Spheroids are allowed to incubate on top of endometrial monolayers and then subjected to washing. Remaining spheroids are used as a measure of attachment (Ho et al. 2012).

The application of the above methodology has generated functional data on endometrial receptivity and embryo implantation. It has been demonstrated *in vitro* that sex steroids E_2 and MPA facilitate trophoblast attachment and invasion by inducing decidualisation

in a epithelial-stromal 3D co-culture system (Wang et al. 2013). Furthermore, the importance of stromal cells and PR-B presence on epithelial cell receptivity has been shown by co-culturing stromal cells from endometrial biopsy with the endometrial epithelial cell line RL95. A correlation between spheroid attachment rate and PR-B protein was observed, that depended on the stromal layer (Evron et al. 2011). The effect COH on trophoblast attachment in infertile women under-going IVF has been investigated, while COH is used successfully to induce ovulation in IVF these experiments show the negative effect of high serum E_2 on endometrial epithelial cells is to reduce spheroid attachment (Chai et al. 2011). The effects of environmental toxicants such as the herbicide 2,3,7,8-Tetrachlorodibenzo-p-dioxin (TCDD, "Agent Orange") on implantation and infertility has been examined using monolayers of RL95 and Ishikawa cells (Tsang et al. 2012).

The effect of menstrual cycle regulated adhesion proteins on spheroid attachment has been investigated. Increased spheroid attachment has been seen reported following induction of integrin αVβ3 in Ishikawa cells (Xiong et al. 2012) and the difucosylated oligosaccharide Lewis y contained within integrin αVβ3 has been shown to be required for endometrial receptivity on RL95-2 cells (Zhang et al. 2011). These experiments can also eliminate potential receptivity markers, for example experiments using the endometrial cell line Hec-1-A showed trophoblast adhesion is not affected by endometrial leptin receptor gene silencing (Cervero et al. 2007).

While there is room for further refinement such as the automated acquisition and counting of fluorescent spheroids using high content screening, and dual colour stains to aid counting epithelial and trophoblast co-cultures (Holmberg et al. 2012) some of the limitations of this strategy are insurmountable. The data generated from such experiments reveals only the number of bound spheroids, and no information is gained on the strength or number of molecular interactions underpinning the trophoblast adhesion. Furthermore, it is unclear how representative artificial trophoblast spheroids are as very little data involving human embryos is forthcoming; whether the rocking action employed to dislodge said spheroids is in any way akin to the forces experienced by the embryo in the human endometrium is also unknown.

A developing strategy is to use co-cultures under-flow conditions to quantify the micro-biomechanics of implantation. This involves some variation of a sealed flow system

containing confluent monolayers of endometrial cells. In these experiments trophoblastic cells are introduced into the system under flow and attachment rates are counted. This model has been used to implicate L-selectin binding to sLe^x in the initial stages of implantation (Yucha et al. 2013), but most shear stress studies of trophoblast adhesion to date centre on the action of early human pregnancy placental trophoblasts as they migrate along uterine spiral arteries (SAs) during placental development (James et al. 2012; James et al. 2011; Liu et al. 2010; Cao et al. 2008). This approach is advantageous compared to the spheroid adhesion assays because the shear stress experienced by the adhering cells can be calculated as a co-efficient of flow rate. The limitations of this system are the monolayers of endometrial epithelial cells are exposed to un-natural forces (the pressure in the uterus has been estimated 5-25 mmHg based on secretory phase uterine contractions) (Eytan et al. 1999) and flow rate must be high enough to dislodge trophoblast cells while not removing the adherent monolayer (as shown in Figure 15C). Moreover, these experiments are technically demanding, requiring understanding of fluid flow dynamics to calculate the flow rate and therefore the force required for detachment.

While these studies have added knowledge to the complex process of implantation, their focus was not to specifically investigate the L-selectin binding process; there is no data showing in specific targeted quantification of the L-selectin-sLe^x forces involved in embryo attachment. When we consider the scale of the forces occurring across the maternal-embryo interface are likely to be in the pico-newton scale (Zhang, Bogorin, et al. 2004) then trophoblast attachment assays appear crude and the requirement for a more sensitive technology becomes apparent. The atomic force microscope allows us to investigate and quantify the nano-mechanical forces occurring across endometrial monolayers and relate these to implantation.

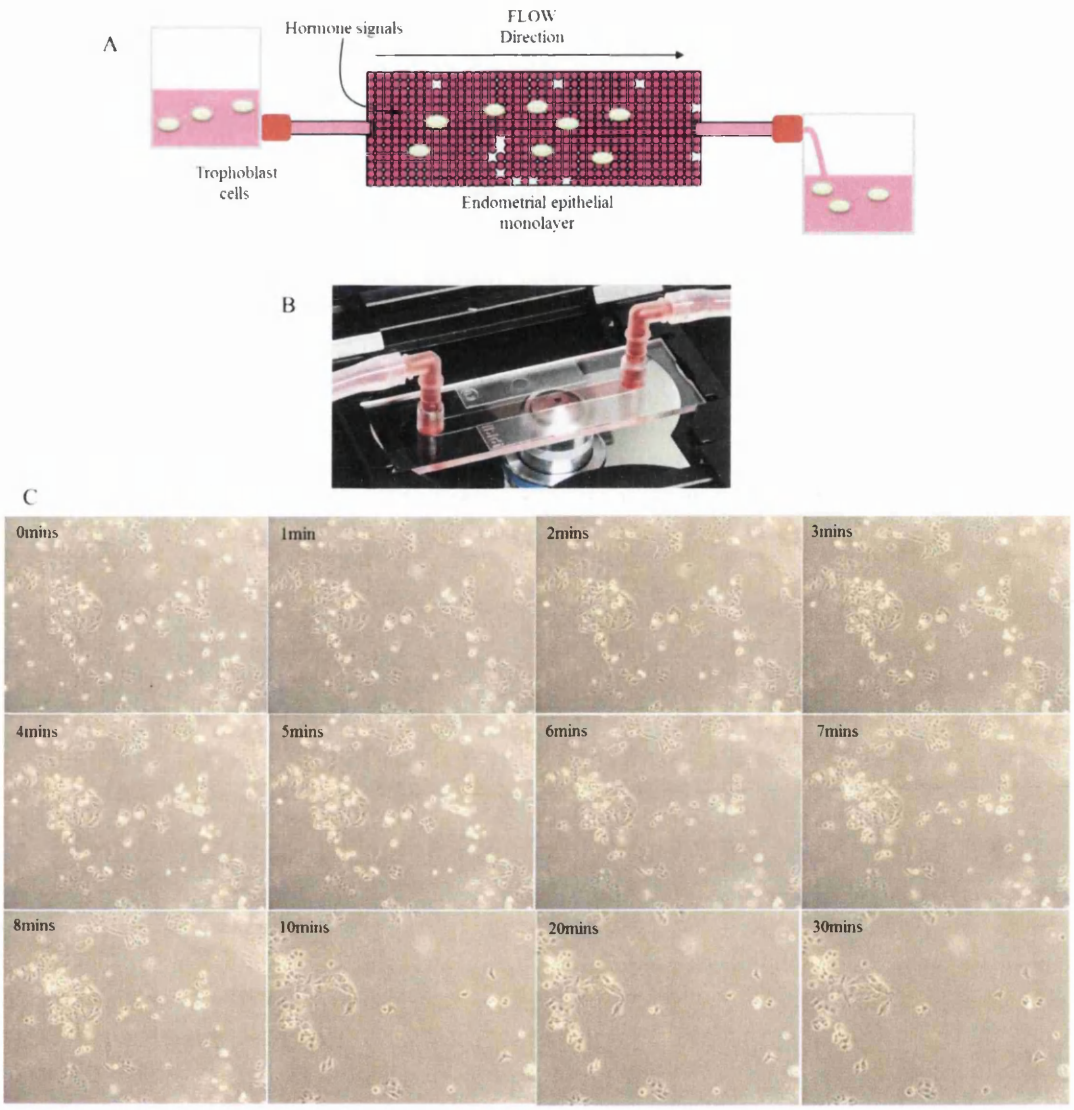

Figure 15: Flowing trophoblast cells over endometrial monolayers. (A) Schematic representation of a lamina flow system used to measure the force of detachment. Trophoblast cells in media are introduced to a laminar flow slide and allowed to adhere. A shear stress is applied and the detachment rates of trophoblastic cells are measured. (B) An example of one such slide in combination with optical microscopy. (C) The effect of 10ml/hour flow rate over 30mins on endometrial monolayers showing shear stress also affects the monolayer of epithelial cells (images from author's data).

1.13 Atomic force microscopy

Classical microscopy techniques such as scanning electron microscopy (SEM) and transmission electron microscopy (TEM) can be used to detect the position, distribution and the dynamics of biomolecules and to visualise and characterise cellular morphology at the sub-nanometer scale (Riva et al. 2010) thanks largely to improvements in chemical fixation (Wierzbicki et al. 2013). Atomic force microscopy (AFM) is a mechanical profiling technique complementary to SEM and TEM that generates 3D

maps of surfaces at cellular, molecular or atomic resolution (Giessibl 2005). AFM typically involves an interaction between a sharp tip (radius~10nm) made from silicon or silicon nitride and a surface. The tip is located on the end of a micro-fabricated cantilever around 200µm in length which is scanned across the sample. The forces that act between the tip and the surface are measureable with sub pico-newton sensitivity allowing calculation of the nano-mechanical surface properties such as topography (height), adhesion, deformation, energy dissipation and stiffness by observing the cantilever deflections resulting from tip–sample interaction (Song & Bhushan 2008).

Figure 16 shows a schematic diagram of an AFM tip–cantilever assembly interacting with an endometrial epithelial cell. The relative movement of the tip across the sample results from a cylindrical piezoelectric actuator which positions the AFM tip in the *x,y* and *z* direction and can act as the holder of either the cantilever or the sample depending on the system design. The deflection of the cantilever is measured using the optical lever method. A laser beam is projected onto the upper surface of the cantilever close to the tip (laser spot). The reflected beam is reflected by a mirror (not shown here) into a four-segment photo-diode. The distance from the cantilever to the photodiode is hundreds of times the length of the cantilever, therefore extremely small deflections in cantilever position are multiplied many times, making AFM a very sensitive technique.

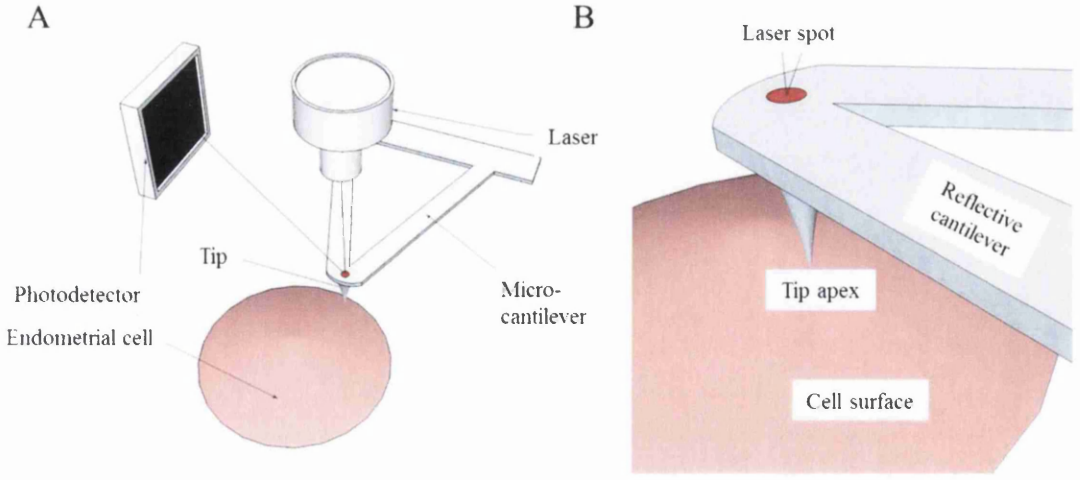

Figure 16: Schematic representation of AFM apparatus. (A) laser beam is reflected off the reflective back of a micro-fabricated cantilever to a photodiode. (B) The tip apex is brought into contact with the cell surface and any cantilever deflections are recorded by

the change in position of the laser spot multiplied using an optical lever and recorded on a photodetector.

1.131 Attractive and repulsive regimes

AFM is a described as a contact probe technique; however this "contact" is the interplay between forces on the tip and the surface substrate. Experiments using intermittent contact AFM (see below) have revealed the existence of two force regimes that the tip encounters on approach (Figure 17). The attractive regime is dominated by van der Walls (VDWs) (Wang et al. 2004), casimir (a quantum force between two polarizable atoms) (Lin & Zhao 2005) and electrostatic (Zhang et al. 2007) long range, non-linear, forces of attraction that pull the cantilever towards the cell (Giessibl 1997; Gotsmann et al. 1999; Hölscher & Schwarz 2007). This may result in a "jump to contact" phenomenon as the tip snaps towards the sample surface on approach (Figure 17). As the inter-atomic distance decreases the net force becomes more repulsive, and once the atoms of the tip and surface are in contact the net force is completely repulsive. The repulsive interaction regime is dominated by a net repulsive force caused by this atomic contact. This repulsion is made up of inter-atomic forces that affect the cantilever by deflecting it or dampening its oscillation depending on the AFM mode used (García & San Paulo 1999), and are largely responsible for the topographical measurements generated. The term atomic force microscopy is derived from the inter-atomic forces experienced within the repulsive regime used for topographical measurements (Binnig 1986). In order to study biological surfaces, the AFM may be operated in several modes that monitor these forces through deflection of the cantilever (Moreno-Herrero et al. 2004; Zhang et al. 2012).

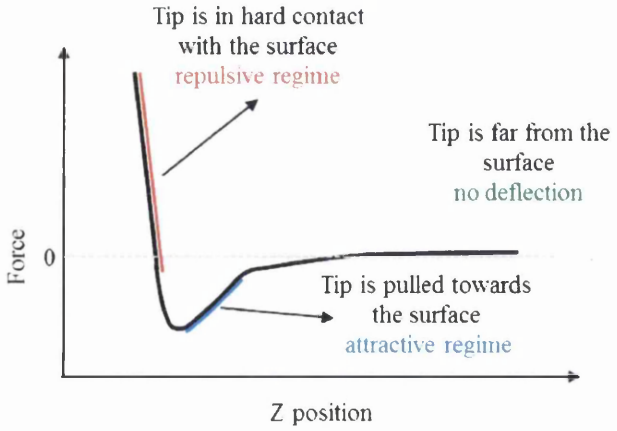

Figure 17: As the tip approaches the surface it encounters two non-linear force regimes. The attractive regime pulls the tip towards the surface; at a certain point the net force becomes repulsive owing to the short range strong forces in the repulsive regime.

1.132 Contact mode

In contact mode the tip is lowered toward the surface by piezoelectric actuator constricting in the *Z* direction, as it enters the repulsive regime the force on the tip increases causing the cantilever to deflect until a pre-determined level of cantilever deflection is reached, known as the set point. When the set point is reached a feedback loop maintains the voltage at the piezo and ensures that the tip is held at this force. The piezo now constricts in the *x* and *y* direction causing the tip to be line-scanned across the surface and the tip is deflected as it encounters surface corrugation. The actual deflection is compared to the desired deflection (the set point) and the piezo exerts force on the cantilever to maintain the tip sample distance and therefore constant height above the surface. The force (measured in volts or newtons) required by the piezo to maintain constant tip-surface separation is used to calculate surface topography, which can be viewed as a 3D map by imaging software.

Although it has very high resolution (~ 0.1nm), contact mode can damage biological samples because it generates frictional (lateral) forces that tear soft surfaces such as cell membranes (Müller & Dufrêne 2011). There have been some attempts to mediate these effects such as the electrostatic dampening of the lateral force between the tip and the sample by altering the pH and electrolyte concentrations of imaging buffers (Muller et al. 1999) and use of low set point forces (<1nN) (Neuman & Nagy 2008). Low force contact mode has been used image glutaraldehyde fixed alveolar epithelial cell layers and has complementary image resolution to SEM and CM (Hecht et al. 2011). However, the most effective way is to reduce the lateral forces and therefore sample degradation is by using an intermittent-contact AFM mode.

1.133 Intermittent contact mode

Where live (or fixed) cell membranes are to be investigated then intermittent-contact/tapping/alternating current (Zhong et al. 1993; Morita 2002) emerges as the preferred mode. Intermittent-contact (IC) mode is a high-amplitude (100-200nm) (Gross et al. 2009) mode in which the cantilever is oscillated at high frequency, close to its natural resonance frequency. At this resonance frequency even a small driving force imparted by the piezo actuator will produce large amplitude oscillations of the cantilever and the vibrating system as a whole stores more energy. The propensity for

an oscillating system to retain energy is referred to as the Q-factor of the system (Bhiladvala & Wang 2004) and is defined as the ratio of the energy stored in an oscillatory system to the energy lost from the system during one oscillation cycle. When imaging cells in aqueous conditions the Q-factor is reduced 10-20 fold (Frederix et al. 2009) so sufficiently stiff cantilevers (having a spring constant, $\underline{k}$ of 10-100Nm^{-1}) must be used to ensure the forces of adhesion and friction associated with cells in aqueous conditions do not overcome the force required to oscillate the cantilever (Putman et al. 1994). As the oscillating tip scans across the sample, changes in surface topography modulate this oscillation. Areas of increasing elevation act to reduce oscillating amplitude, while depressions cause it to increase. Rather than relying on a deflection set point as in contact mode, IC mode (and non-contact mode) monitors the change in the resonance amplitude (or frequency) of the cantilever. The resulting change in amplitude is compared with the amplitude set point and the piezo voltage is adjusted to maintain a constant amplitude and therefore tip-sample separation. While the short range repulsive forces are widely assumed to be responsible for dampening the oscillation, the VDWs forces of attraction also contribute to this effect (Garcia & San Paulo 2000). Moreover, the feedback loop is unable to determine whether reduction in oscillating amplitude is the result of attractive, repulsive or a combination of both forces (Garcia & San Paulo 2000).

As the cantilever is oscillating at high frequency the surface contact time is reduced and thus lateral forces between the tip and the surface are greatly reduced; IC mode is excellent for soft biological samples, such as cell membranes which are frequently damaged by contact mode (Howard et al. 1996). The data provided by IC mode includes topography (generated by the amplitude feedback signal) and phase (Tamayo & Garca 1997). Phase imaging measures the phase lag of the cantilever oscillation relative to the piezo drive amplitude (Babcock & Prater 1995). Deviations in surface properties induce shifts in the phase of the two waves, which are mapped to produce phase images and can reveal fine cellular structures in high contrast which are not visible in topographical imaging (Babcock & Prater 1995). Phase imaging is able to identify boundaries between regions with altered surface properties that are not related to height, such as surface viscous damping, adhesion and membrane stiffness (Liu et al. 2009). IC mode has been used to successfully image moving DNA molecules (Argaman et al. 1997), cell

membranes in liquid (Kamruzzahan et al. 2004) and dynamic morphological changes to membrane structure over time using live cells (Li et al. 2013).

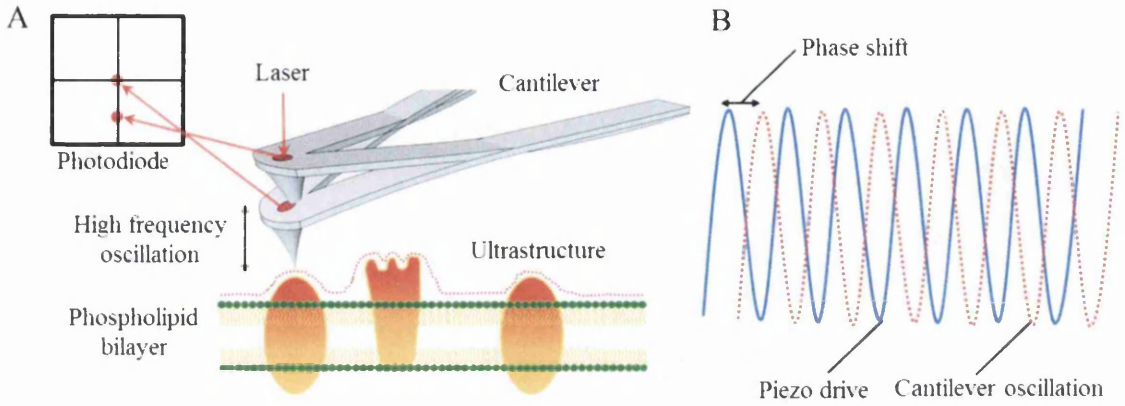

Figure 18: Intermittent contact mode AFM. (A) The cantilever is oscillated at high frequency across the sample. Surface forces affect oscillation amplitude and are recorded by the laser deflection. (B) Surface properties not related to height (such as stiffness, which compresses the shift) induce a phase shift between the piezo drive frequency and the cantilever oscillation frequency. This can be used to generate high contrast images of the cell surface ultrastructure.

IC mode has been established as an imaging tool comparable with SEM (Hecht et al. 2011), however the resonant oscillation of the tip that is integral to IC mode masks the force curves making extraction of nano-mechanical information impractical (Stark et al. 2002; Legleiter et al. 2006).

1.134 Force distance mode

Force distance curve based AFM (FD-AFM) is a nano-indentation technique that measures the force on the tip against the z-position to ascertain properties about the material (Müller et al. 2009). In imaging mode the AFM generates high resolution topographical data based on tip sample interactions. In contrast, FD-AFM can be used to measure the surface nano-mechanical properties (Alsteens et al. 2012) of living (and non-living) systems at high sensitivity (Hugel & Seitz 2001; Kirmizis & Logothetidis 2010). As the tip is brought towards the surface it interacts with the sample, and forces acting on the tip cause the cantilever to deflect facilitating detection of interaction forces. When maximum indentation is reached the force set point (a user controlled parameter) triggers a feedback loop that instructs the piezo to withdraw the probe to the starting position thus controlling indentation. The tip moves in the lateral direction and the process is repeated (Figure 19A), resulting in a grid of sample points across the

surface that is termed a 'force map'. The force on the tip against vertical distance from the sample is displayed using a graphical output termed a force distance curve (Figure 19B). FD curve AFM can reveal physical surface properties of biological surfaces such as stiffness, adhesion, indentation (deformation), energy dissipation (Heinz & Hoh 1999). These properties are calculated by fitting mathematical models of contact mechanics to the FD curves using open source, proprietary or home written software environments. In contrast to IC mode, FD AFM requires the use of soft cantilevers (k = 0.01-0.5Nm^{-1}) to detect minute forces on biological membranes which can be as low as 50 piconewtons (Müller et al. 2009).

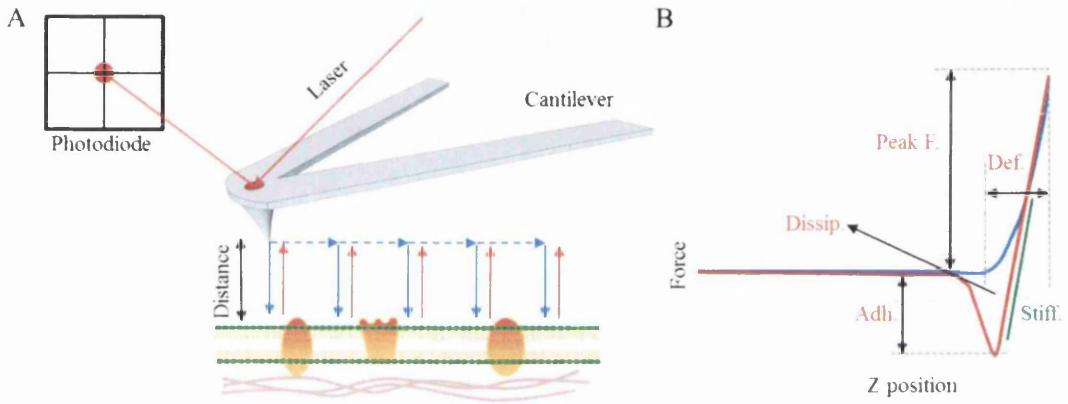

Figure 19: Force Distance AFM. (A) The AFM probe is indented into a biological surface and withdrawn; the interaction with surface forces is recorded by the deflection on a cantilever. (B) The data is outputted in a graph of force against distance; models of contact mechanics applied to these 'force curves' permits calculation of mechanical properties such as adhesion, stiffness, deformation and energy dissipation.

1.135 Single molecule force spectroscopy

A significant development in FD-AFM has been the separation of specific interactions from non-specific interactions on biological surfaces. Biological membranes are no longer considered to be homogeneous fluids, instead they are composed of mobile lipid rafts associated with varied and dynamic expression of surface glycoproteins, receptors and glycolipids (Simons & Vaz 2004). For identification and characterisation of specific interactions across these heterogeneous surfaces a single functionalization molecule may be attached via a flexible linker to the AFM tip (Zimmermann et al. 2010), a derivation termed single molecule force spectroscopy. Nano-indentation is performed as in FD AFM however, when the tip is withdrawn from the sample any specific bonds between the functionalization molecule and the surface stretch and then rupture (Figure 20A). The rupture event can be characterised by the rupture force and the distance the

rupture occurs from the surface (Figure 20B). The force required for bond rupture (the bond strength) is dependent on bond loading rate (Evans & Ritchie 1997) and thus is a dynamic force (Evans & Calderwood 2007). The dynamic rupturing of molecular bonds can be described as a transition between bound and unbound energy states, and external force applied to the bond increases the chance of a transition to the unbound state, a probability which increases with bond loading rate (Dufrene et al. 2013). The retraction FD curves are analysed using specialist software such as Open Fovea (Roduit et al. 2012), Hooke (Sandal et al. 2009), PUNIAS and JPK DP (JPK Instruments AG 2012) to detect step changes in force that represent separation of molecular bonds.

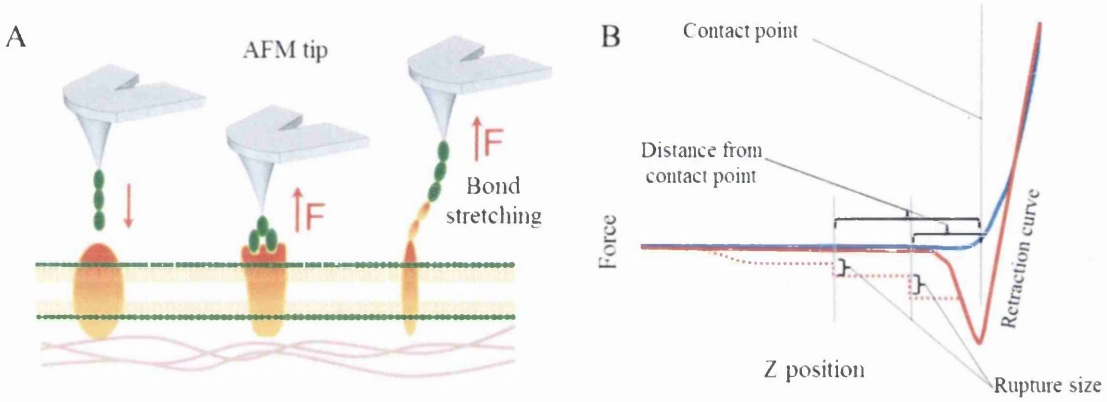

Figure 20: Single Molecule Force Spectroscopy AFM. (A) The tip is functionalized with a biomolecule and indented into the cell membrane, the bond is loaded as the tip withdraws from the surface resulting in bond stretching and then bond rupture. (B) Force curves are analysed for bond ruptures on the retraction part of the force curve. Such ruptures appear as "steps" on the retraction curve (dashed red line).

Early characterisation of bio-intermolecular bonds began with large bio-molecules immobilised on atomically flat substrates such as dextran polysaccharides on gold (Rief et al. 1997) and LexA protein on mica (Kühner et al. 2004). The intermolecular homophilic bond strength of adhesion proteins such as E-cadherin has been investigated (Baumgartner et al. 2000; Perret et al. 2004) but these studies utilised recombinant protein fragments attached to a mica substrate. More recent developments in functionalised force mapping have investigated the bond strength of rituximab (an anti-CD20 monoclonal antibody targeted drug) to receptors on lymphoma cells (Li et al. 2013), the affinity of anti-cancer peptides to HeLa cell membranes (Shan et al. 2012), location (Ahmad et al. 2011) and binding affinities (Li et al. 2013) of Fc gamma receptors on macrophage cells providing information about the mechanism behind

macrophage binding to target cells coated in antibody. These experiments were all conducted using intact fixed cells. Using intact cells rather than immobilised substrates ensures the natural orientation of cell receptors within the membrane and any post-translational modifications (such as glycosylation) of the proteins are preserved. This is especially important in the endometrium when we consider that these modifications are critical to function (for example the addition of sLe^x tetrasaccharides to MUC1). Furthermore, using intact cells retains the functionality of the cytoskeletion so that transmembrane receptors (such as mucins, integrins) can still interact with the cytoskeleton through their cytoplasmic domains.

However, fixing the cells with protein cross-linking agents such as glutaraldehyde and paraformaldehyde may reduce the functionality of transmembrane receptors due to crosslinking inducing conformational changes in functional N-terminal domains (Migneault et al. 2004). Moreover, cell signalling pathways of live cells can regulate receptor action and therefore bond characteristics, this has been demonstrated experimentally; ICAM-1 bonds with β2 integrin on live neutrophils displayed longer lifetimes and increased bond strength compared to ICAM-1 bonds with α2β2 integrin coated glass beads (Kinoshita et al. 2010).

1.136 High resolution force distance mode

Conventional FD-AFM is slow, requiring around 30 minutes to record high resolution (<10nm), multiparameter force maps (Dufrene et al. 2013) which is a limitation of traditional force mapping in live cell systems. Recent advances in AFM technology (Berquand 2011; JPK instruments 2012) have enabled the capturing of arrays of FD curves with much improved speed (7-10minutes for 512x512 pixel images) while still recording viable force curves. These advances in instrumentation allow extraction of quantitative information from high resolution images at speeds comparable to IC mode (Dufrene et al. 2013). The high resolution FD mode 'Peak Force Tapping' (PFT) was used for the experiments in this thesis. When in PFT mode the piezo oscillates the base of the cantilever in a similar fashion to IC mode, however the probe moves in a sigmoidal sweep compared to linear as in traditional FD-AFM. The *z*-piezo is modulated far below the cantilever resonance frequency (150kHz in this case), typically 1-2kHz (Berquand 2011) and the tip scans across the image and performs a rapid force curve at each pixel. The sinusoidal waveform causes the tip velocity to approach zero as

the tip approaches the surface which allows quantification of very small forces (<10nN) (Pittenger et al. 2013). Peak force mode is similar to IC mode in that fact that the tip only contacts the sample for a small proportion of the time, however unlike IC mode where the amplitude set point is used to modulate the amplitude signal PFT measures the peak force experienced by the tip (typically during the repulsive regime) and feeds back this parameter in order to maintain a constant peak force. The peak force is defined as the force difference between the contact point and point of maximum indentation on the approach to the sample. Figure 21 shows the periodic interaction with the probe and the surface. The dashed line shows the z position of the tip as one period interaction is completed. As the modulation frequency is between 1-2kHz in the current form, elapsed time from point A to E is 0.5-1s^{-3}. This results in a periodic interaction many orders of magnitude faster than the traditional quantitative AFM mode; force spectroscopy where modulation frequency is 1-5Hz resulting in an interaction typically lasting 0.5-1s^{-1}.

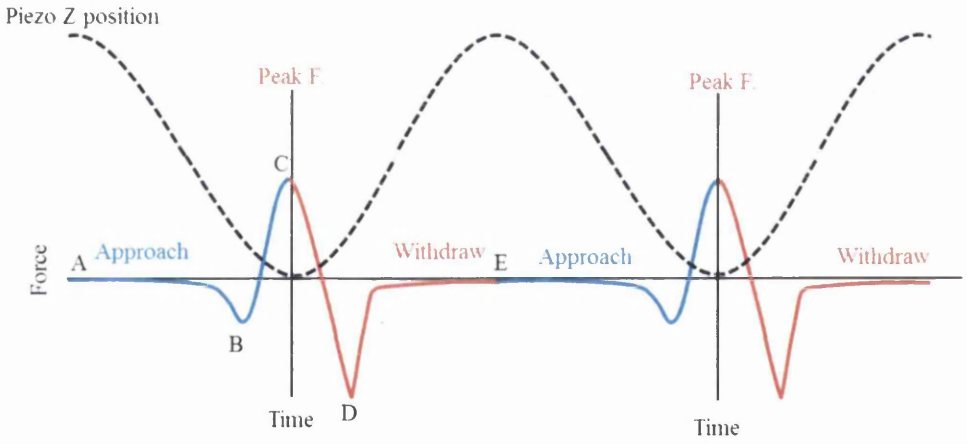

Figure 21: Peak Force Tapping AFM. Diagram shows two indentations of the tip during PFT. The dotted line represents the position of the tip through each oscillation, the red and blue lines show the force acting on the tip as a function of time. The peak force occurs when the tip contacts the surface and is used to feedback to the piezo. Conventional force curves analysis is used to obtain the desired nano-mechanical properties of surfaces. Points A-E are areas of maximal or minimal force that correspond with tip position.

In order to quantify the surface properties, calibration of cantilever normal elastic constant (k_n) (also known as spring constant) is conducted prior to experimentation. Although probes have a nominal k_n from manufacture this can vary up to 200% from actual k_n (Hazel & Tsukruk 1999) so experimental determination of this value is conducted using the accepted thermal tune method (Sader et al. 2012).

Deflection sensitivity (D_{sens}) is a crucial parameter that is also calibrated prior to imaging. A PFT force curve is a measure of tip position against the output voltage of a position sensitive photodiode detector. The displacement of the cantilever is measured using the optical lever, however when the laser is aligned, the relative positions of the cantilever and the laser spot can affect the displacement calibration, and therefore the output voltage. Usually the cantilever is indented into a non-deforming surface, therefore the deflection of the cantilever is directly equivalent to the piezo position (Tranchida et al. 2007). Once these calibrations have been completed PFT mode allows extraction of quantifiable data for topography, peak-force error (phase signal), adhesion, stiffness (using DMT model), deformation and dissipation per pixel of the AFM image. This derivation is termed Peak Force Quantitative Nanomechanical Mapping (PFQNM), which is faster than force spectroscopy and provides more information than IC mode (Berquand 2011).

PFQNM has been widely used on hard surfaces (Dunér et al. 2012; Trtik et al. 2012; Chafidz et al. 2012; Panaitescu et al. 2012; Kaplova et al. 2012) but publications showing quantitative maps of eukaryotes (Pletikapić et al. 2012) microbal and yeast systems are emerging (Alsteens et al. 2012). One notable live cell study characterised the *in vitro* hardening of keratinocyte cells in response to the herbicide glyphosate (Heu et al. 2012). To my knowledge PFQNM has never been used to characterise endometrial cells before. FD-AFM and PFQNM are complementary modes, as PFQNM performs a high frequency sinusoidal sweep making calculation of the tip velocity is difficult and thus is not applicable for cases where the loading rate (tip velocity) dependence of the measurement is important, such as bond rupture events. For this application traditional FD mode is still preferred.

1.137 AFM to study endometrial adhesion

Despite the advancements in technology platforms such as live cell AFM, there is a lack of uptake of these technologies in the field of reproductive biology. Previous publications from our group correlated changes in endometrial cell height and surface roughness to a hormonal environment replicating that of the WOI (Francis et al. 2009) suggesting that the AFM can detect nano-scale changes to endometrial cell surfacess. *In vivo* the endometrium exists as a flat layer with varying degrees of adhesion across the apical surface; the development of PFQNM combined with advanced molecular biology techniques provided an opportunity to characterise this adhesion and investigate the role

played by key proteins. The endometrium is a key interface in human fertility, it is the site of embryo attachment, yet the vagaries of the molecular interactions which occur between embryonic and maternal cells following fertilisation, and the unique process of endometrial receptivity and implantation represent an obvious target for single molecule force spectroscopy.

1.14 Aims and objectives

This thesis constitutes a systemic study of the role played by MUC1 and L-selectin in trophoblast-endometrial interactions during the apposition phase of implantation. The main aim of this thesis is to investigate the proposed L-selectin/sLe^x adhesion mechanism involved in embryo attachment and the role of MUC1 in L-selectin adhesion. My secondary aim was to assess the patterning of endometrial adhesion mediators and their functional significance utilising the novel application of two advanced quantitative tools, the INCELL Analyzer and AFM. In chapter 3 my objective was to build an *in vitro* model of mucin expression during the WOI which is characterised by high and low expression at the EEC surface and secondly develop the use of INCELL technology as a high content, quantitative mapping tool capable of delineating the complex staining pattern of adhesion proteins and providing novel insights into the effect of steroid hormones on EEC lines. In chapter 4 my objective was to explore the use of PFQNM on EEC lines as a tool comparable to force distance AFM which is capable of characterising the nano-mechanical and topographical properties of cells which express varying levels of mucins using an *in vitro* model allowing direct correlation of the quantitative QNM data with advanced molecular biology (siRNA) to fully delineate the role of MUC1 at the EEC surface. The final aim of this thesis was to develop SMFS strategies to interrogate MUC1 as a scaffold for L-selectin ligands and assess its suitability for further understanding this adhesion system and its role in endometrium receptivity and embryo implantation

Chapter 2 Materials and Methods

2.01 Endometrial epithelial cancer cell lines (EEC)

Hec-1-A cells were first derived from explants of a moderately differentiated endometrial adenocarcinoma of a 71 year old woman over 40 years ago (Kuramoto et al. 1972). They are the most widely used cell line in implantation research (Hannan et al. 2010) and are considered poorly adhesive to trophoblast cells. Hec-1-B cells were acquired from a sub-population of Hec-1-A cultures that sustained a stationary growth period from 135-190 days (Kuramoto 1972). The original cell line Hec-1-A and sub-strain Hec-1-B exhibit morphological and karyotypic differences. Hec-1-B cells have a raised morphology (Kuramoto et al. 1972) and are predominantly tetraploid, whilst Hec-1-A are flatter and predominantly diploid (Satyaswaroop et al. 1978). Additionally, the cell lines differ on the expression of nuclear receptors and adhesion proteins and thus must be characterised individually prior to use in research experiments.

Ishikawa cells were derived from a well differentiated endometrial adenocarcinoma of a 39 year old woman (Nishida et al.1985) and are the best characterised of the all endometrial cell lines. Ishikawa cells have small vacuoles that produce mucus, irregular nuclei and a doubling time of up to 36hrs (Albitar et al. 2007). They display mixed characteristics of glandular and luminal epithelium and express functional steroid receptors for progesterone and estrogen (Croxtall et al. 1990; Boehme et al. 2009). Ishikawa is considered a good model for receptive human endometria and has been shown to facilitate adhesion of embryo derived cells (Heneweer et al. 2005).

Hec50 cells were isolated from a metastatic lesion in the peritoneal cavity in a patient with advanced disease. Hec50 forms sheets of undifferentiated cells and does not develop glands or produce secretions, compared to Ishikawa cells they have many more chromosomal rearrangements (29 versus 7) and the doubling time is much more rapid (Albitar et al. 2007). Hec50 cells have been shown to be negative for PR (Davies et al. 2004) and while some studies shown Hec50 cells to be positive for ER they lack an estrogen response. This may be due to structural or functional alterations in the ER protein resulting in a loss of its capability to undergo the estrogen-directed conformational changes required for biological activity (Kassan et al. 1989).

2.011 EEC cell lines in culture

Commercially available Hec-1-A, Hec-1-B, Ishikawa and Hec50 EEC cell lines were obtained from the American Type Culture Collection (ATCC). All cell culture work was undertaken utilising appropriate aseptic techniques in ventilated tissue culture

hoods. Cell lines were maintained in commercially available DMEM/F-12 + Glutamax™ full media (GIBCO) supplemented with 10% foetal bovine serum (FBS), sodium bicarbonate 1mM, sodium pyruvate 1mM and 1% antibiotic-antimycotic solution in plastic culture vessels ($25cm^2$, $75cm^2$, $125cm^2$) at 37.0 ^0C and 5% CO_2 incubator (Nuaire). Cells were supplemented with free, full serum media every 2 days and passaged when confluent. Only cells passaged 2 or more times were used for experiments.

2.012 Passage of EEC cell lines in culture

Cells were passaged when confluent. Media was removed and cells were washed with phospho-buffered saline (PBS) (-Mg^{2+},-Ca^{2+}) (GIBCO) to remove residual medium. PBS and residual media was then aspirated and cells were incubated in PBS at 37.0 ^0C and 5% CO_2 for 5 minutes. Following further aspiration the cells were incubated in 1ml Trypsin-EDTA (0.25%) at 37.0 ^0C and 5% CO_2 for 5 minutes (or until the cells appeared rounded and detached). Trypsin cleaves E-cadherin and other adhesion proteins freeing the cells from plastic surface of the culture flask. 10ml of media was added to neutralise the trypsin and the resulting cell suspension was split into two centrifuge tubes and centrifuged at 1500rpm for 5 minutes. The pellet was re-suspended in 10ml of DMEM/F-12 + Glutamax™ media (GIBCO) and the cell suspension was added to a fresh culture vessel for incubation.

Cell growth dynamics were characterised using a high content screening (HCS) system to rapidly count large numbers of cells and assess their level of confluence at any given stage. EEC cells were grown in a T125 cell culture flasks (Greiner bio-one #660175) until confluence ($10x10^6$ cells), trypsinised as above and serially diluted to the following concentrations (units are cells/ml); $2x10^4$, $5x10^4$, $1x10^5$, $2x10^5$, $3x10^5$ and $5x10^5$. 1ml of each dilution was added to one well of a 6 well plate (Greiner bio-one #657160), the cells allowed to adhere and then another 1ml of DMEM/F-12 + Glutamax™ media was added to each well. This was repeated with four 6-well plates for each cell line, resulting in a total of 16 plates. All plates were incubated at 37.0°C and 5% CO_2. Every 24hrs four plates were removed (one from each cell line), media aspirated from all wells and the cells rinsed with PBS. Nuclei were stained with NucBlue™ (Life technologies # R37605) 4',6-diamidino-2-phenylindole (DAPI) preparation (2 drops/ ml PBS for 25 minutes at 25°C). The INCELL analyzer 2000 (GE Healthcare) was used to image 15 randomly selected fields (random selection is a

When not in use all hormone stocks were maintained at -20°C in glass vials. Fresh stocks were made up periodically to counter the effects of ethanol evaporation when in use, ensuring consistent cell exposure to correct concentrations.

Hormones in combination - Preparations of hormones were combined in an extended treatment regime that lasted for 72hrs. Media was aspirated and cells were incubated in serum stripped media containing 10nM E_2 at 37.0°C and 5% CO_2 for 24hrs. This treatment was then removed and the cells were washed once with hormone free serum media before being incubated in varying combinations of hormones for 48hrs summarised inTable 2.

Treatment	1	2	3	4	5
Shorthand	Control	E→P	E→P+E	E→MPA	E→MPA+E
First 24hrs	Ethanol	E_2 (10nM)	E_2 (10nM)	E_2 (10nM)	E_2 (10nM)
Last 48hrs	Ethanol	P_4 (100nM)	P4 (100nM) E2 (10nM)	MPA (100nM)	MPA (100nM) E2 (10nM)

Table 2: Combined hormone stimulations. In order to mimic the combination of E_2 and P_4 exposure of the luminal epithelial cells during the secretory phase of the menstrual cycle, multiple combination treatments were employed in this study to test for their effect on mucin expression during an *in vitro* model of the WOI.

2.03 RNA interference

Specific gene silencing was conducted with MUC1 and MUC16 siRNA (Santa Cruz Biotechnology [sc-37266 and sc-44971 respectively]). For each siRNA used a control siRNA-A (Santa Cruz Biotechnology [sc-37007]) that is not complementary to any known human transcript was used. Lyophilised siRNAs were reconstituted in 330µl ddH_20 to a stock concentration of 10µM and aliquoted into 10µl vials before being stored at -20°C as per manufacturer's guidelines.

Gene silencing was optimised by testing multiple concentrations of MUC1 siRNA on Hec-1-A and Hec-1-B cell monolayers and assessing gene knockdown by using qRTPCR. The cells were sub-cultured and prepared as outlined above. $5x10^4$ cells in suspension were aspirated onto the appropriate culture vessel for the endpoint assay (Figure 22) and allowed to attach for 5 minutes. Antibiotic free media was added and cells incubated in a controlled atmosphere of 5% CO_2 at 37°C for a minimum of 24hrs. When the cells reached the 40% confluence, the culture medium was aspirated and replaced with pre-incubated in reduced serum OPTI-C medium (Invitrogen #31985-062) containing 25, 50 or 75nM siRNA and 0.0375% RNAi MAX (Invitrogen #13778030) ensuring full coverage of the monolayer. 1.5ml of antibiotic free medium

software feature) in the DAPI channel at low magnification (10x objective) across each well. These 15 images (per well) were post processed (see section 2.062 HCS Image analysis for INCELL image processing) and nuclei were counted, the average number of nuclei per field was divided by the number of nuclei in a field of confluent monolayer of that cell line (typically around 2000) generating a percentage for cell confluence. Table 1 shows the confluence calculation of Hec-1-A cells at various seeding densities at the 24hr end point. Nuclei were counted after 24, 48, 72 and 96hrs for each cell line tested.

End point	24hrs											
No. Seeded	20000		50000		100000		200000		300000		500000	
Well (field)	Nuc. Count	Well (field)	Nuc. Count	Well (field)	Nuc. Count	Well (field)	Nuc. Count	Well (field)	Nuc. Count	Well (field)	Nuc. Count
A - 1 (fld 1)	31	A - 2 (fld 1)	68	A - 3 (fld 1)	48	B - 1 (fld 1)	326	B - 2 (fld 1)	259	B - 3 (fld 1)	327
A - 1 (fld 2)	119	A - 2 (fld 2)	76	A - 3 (fld 2)	142	B - 1 (fld 2)	116	B - 2 (fld 2)	200	B - 3 (fld 2)	310
A - 1 (fld 3)	40	A - 2 (fld 3)	83	A - 3 (fld 3)	102	B - 1 (fld 3)	247	B - 2 (fld 3)	580	B - 3 (fld 3)	620
A - 1 (fld 4)	49	A - 2 (fld 4)	47	A - 3 (fld 4)	74	B - 1 (fld 4)	209	B - 2 (fld 4)	549	B - 3 (fld 4)	354
A - 1 (fld 5)	22	A - 2 (fld 5)	75	A - 3 (fld 5)	89	B - 1 (fld 5)	296	B - 2 (fld 5)	248	B - 3 (fld 5)	341
A - 1 (fld 6)	89	A - 2 (fld 6)	91	A - 3 (fld 6)	229	B - 1 (fld 6)	216	B - 2 (fld 6)	225	B - 3 (fld 6)	381
A - 1 (fld 7)	16	A - 2 (fld 7)	73	A - 3 (fld 7)	144	B - 1 (fld 7)	183	B - 2 (fld 7)	255	B - 3 (fld 7)	1023
A - 1 (fld 8)	42	A - 2 (fld 8)	142	A - 3 (fld 8)	240	B - 1 (fld 8)	189	B - 2 (fld 8)	586	B - 3 (fld 8)	716
A - 1 (fld 9)	57	A - 2 (fld 9)	84	A - 3 (fld 9)	82	B - 1 (fld 9)	258	B - 2 (fld 9)	510	B - 3 (fld 9)	393
A - 1 (fld 10)	50	A - 2 (fld 10)	111	A - 3 (fld 10)	188	B - 1 (fld 10)	176	B - 2 (fld 10)	215	B - 3 (fld 10)	426
A - 1 (fld 11)	68	A - 2 (fld 11)	91	A - 3 (fld 11)	158	B - 1 (fld 11)	548	B - 2 (fld 11)	681	B - 3 (fld 11)	773
A - 1 (fld 12)	106	A - 2 (fld 12)	133	A - 3 (fld 12)	161	B - 1 (fld 12)	197	B - 2 (fld 12)	183	B - 3 (fld 12)	353
A - 1 (fld 13)	15	A - 2 (fld 13)	125	A - 3 (fld 13)	226	B - 1 (fld 13)	182	B - 2 (fld 13)	606	B - 3 (fld 13)	1426
A - 1 (fld 14)	41	A - 2 (fld 14)	63	A - 3 (fld 14)	85	B - 1 (fld 14)	327	B - 2 (fld 14)	503	B - 3 (fld 14)	589
A - 1 (fld 15)	41	A - 2 (fld 15)	44	A - 3 (fld 15)	81	B - 1 (fld 15)	315	B - 2 (fld 15)	239	B - 3 (fld 15)	338
Average	52		87		137		252		389		558
Confluence %	2.6		4.4		6.8		12.6		19.5		27.9

Table 1: Calculating Hec-1-A growth characteristics. Each column contains the number of nuclei counted in each field, of which there are 15 per well. Each well had a different initial seeding density ranging from 20000 cells to 500000 cells.

This simple experiment counted large numbers of cells, randomly sampled across the well ensuring that the growth rate of any one of the four cell lines in culture could be predicted accurately.

2.02 Hormone treatments

All cell treatments were conducted in appropriate culture vessels for their downstream assay (Figure 22). Cells were seeded at the correct density to ensure 80-100% confluence at the end of the culture period and grown in the presence of FBS supplemented serum for a minimum of 24hrs. 24hrs prior to treatment, the culture media was replaced with stripped serum to ensure the removal of all large molecular weight proteins and steroids from the cell medium.

Stripped serum media was made up with hormone stripped FBS. Dextran coated charcoal treatment of FBS was carried out in order to remove any naturally occurring steroid hormones from the serum. This was achieved by adding 1.0g of dextran coated activated charcoal (SIGMA-ALDRICH [C-6241] 5g) to 500ml of FBS (GIBCO [10437028] 500ml). The solution was incubated at 56°C for 2hrs, filter sterilized and stored in 50ml Falcon tubes at -20°C prior to use. Hec-1-A and Hec-1-B cell monolayers were removed with 0.25% trypsin-EDTA (Life Technologies [25200-072]) and re-suspended in fresh culture media (detailed above). 1.0ml of cell suspension (containing $5x10^4$ cells) was aspirated onto appropriate dishes (Figure 22) and allowed to attach for 5 minutes. 2.0mls appropriate media was added and cells incubated in a controlled atmosphere of 5% CO_2 at 37°C for 24hrs. Stock solution consisting of 2µl of P_4, E_2 or MPA in ethanol was combined with 2ml of hormone stripped serum media. Culture medium was aspirated and cells covered with this preparation and incubated in a controlled atmosphere of 5% CO_2 at 37°C for 48hrs.

Progesterone (P_4) - 0.314g of progesterone (SIGMA-ALDRICH; P-0130 [>99%]) was added to 10ml absolute ethanol (Fisher-Scientific) to a concentration of 1mM. This stock was diluted 1/10 resulting in a 100µM working stock and when required, 2µl of the working stock was added to 2ml hormone stripped serum media resulting in a final treatment concentration of 100nM.

Estradiol (E_2) - 0.272g of estradiol (SIGMA-ALDRICH; E-8875 [>98%]) was added to 10ml absolute ethanol (Fisher-Scientific) to a concentration of 1mM. This stock was diluted 1/100 resulting in a 10µM working stock and when required 2µl of this working stock was added to 2ml hormone stripped serum media resulting in a final treatment concentration of 10nM.

Methoxyprogesterone acetate (MPA) - 0.386g of MPA (SIGMA-ALDRICH; P-0130 [>99%]) was added to 10mL absolute ethanol (Fisher-Scientific) to a concentration of 1mM. This stock was diluted 1/10 resulting in a 100µM working stock and when needed 2µl working stock was added to 2ml hormone stripped serum media resulting in a final treatment concentration of 100nM.

was added and cells incubated in 5% CO_2 at 37°C for 48hrs. All subsequent silencing of MUC1 and MUC16 gene expression was conducted with 50nM siRNA and 0.0375% Lipofectamine RNAi MAX (as per manufacturer's guidelines) for 48hrs.

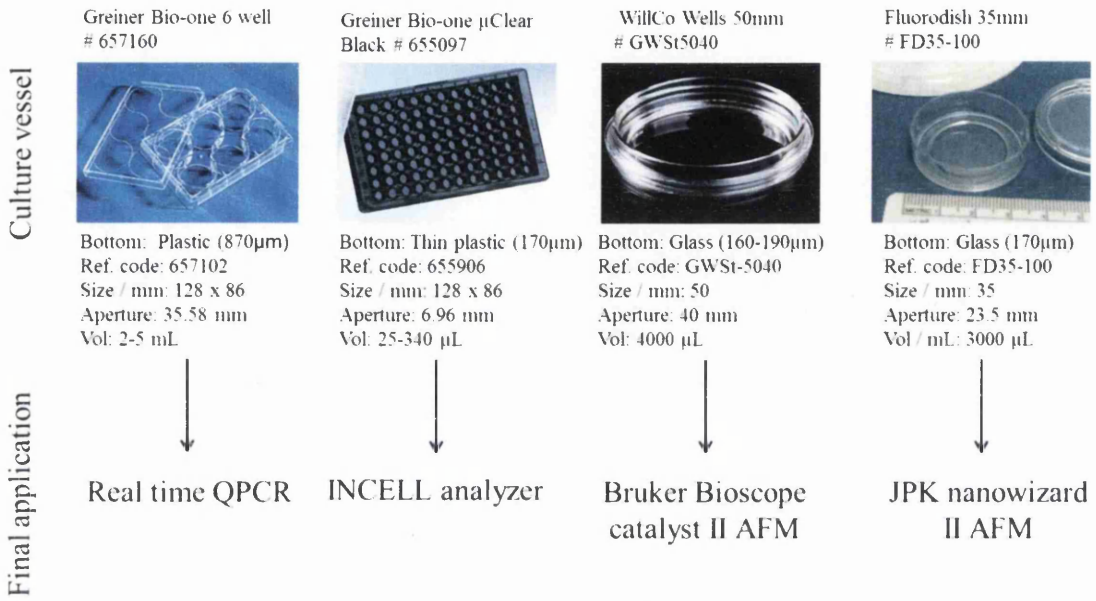

Figure 22: Cell culture vessels used for qRTPCR, INCELL analyzer based HCS, and AFM. Depending on the final endpoint assay the culture vessels for the cells and all appropriate treatments varied. All are outlined here.

2.04 Quantitative Real Time Polymerase Chain Reaction (QRTPCR)

RNA extraction -Total RNA was isolated from confluent monolayers using the RNeasy mini kit and DNAseI kit (Qiagen [74106 and 79254]), following the manufacturer's instructions. Total RNA captured on the column was eluted into 90µl of RNAse free water (Qiagen #129112).

Reverse Transcription -The concentration of total RNA extracted was determined using a Nano-drop ND-1000 spectrophotometer and all samples were adjusted to a concentration of 100µg/ml using RNAse free H_2O (Qiagen #129112). Total RNA was reverse transcribed to produce cDNA using the high capacity cDNA kit (Applied Biosystems [4387406]). The reaction master mix consisted of 2.0µl 10x RT buffer, 0.8µl 25x dNTP mix, 2.0µl 10x random decamer primers, 1 µl of reverse transcriptase enzyme 1.0 µl of RNAse inhibitor, and 1.2 µl of dH_2O. The kit was supplemented with 2.0 µl of oligo-dT primers (Ambion [AM5730G]) to ensure a preference for mRNA in the reverse transcription reaction. 10µl RNA (100µg/ml) was combined with 10µl reaction master mix resulting in a 20µL final volume and placed in a T-100

thermocycler (Biorad [186-1096]). The reaction mix was incubated at 25°C for 10mins, 37°C for 120mins, 85°C for 10mins and 4°C for 10mins.

QRTPCR - cDNA was amplified using gene specific primer pairs (Table 4) to obtain a PCR product between 75-263bp for each of the genes under study. RP-L19 was used as a housekeeping gene, and genomic DNA and RNA were used as positive and negative controls respectively. Amplification reactions of volume of 10µL were prepared by adding 5 µL of SsoFast™ EvaGreen® Supermix containing the *Pyrococcus furiosus* (Pfu) DNA polymerase (Bio-Rad #1725200), 1.25µL of each primer (4µM concentration) and 2.5µl of cDNA (1/10 dilution). QRTPCR amplifications were conducted in triplicate in 96-well optical reaction plates and run on the CfX-96 PCR detection system (Biorad). Plates were heated first to 95°C for 5min to activate the DNA polymerase enzyme and run for 40 cycles of 1s at 95°C, 5s at the optimal annealing temperature for each primer pair and 5s at 72°C to allow extension. To obtain the melting curves for each sample a final step of 40 cycles was performed for 5s at 53°C, increasing the set point temperature by 0.5°C per cycle up to a maximum temperature of 95°C. No amplicons were obtained using RNA directly in the QRTPCR reaction.

Relative quantification of gene expression data was determined from quantification cycle (C_q) values for each sample using the standard curve method (Karlen et al. 2007). Each plate included a standard curve of known concentration, serial dilutions of cDNA 1/5, 1/10, 1/100 and 1/1000 (Table 3) that were converted into common logarithm (log base 10) values and plotted against the respective C_q. A trend line was fitted to the resulting calibration curve (Figure 23) and the equation of the line ($y=mx+c$) used to calculate the log dilution from samples of unknown cDNA starting quantity.

$$y = mx + c$$

equation of the line, where (m) represents the gradient and (c); represents the point at which the line intercepts the y axis, (y) represents the C_q and (x) the common logarithm of the starting quantity can then be re-arranged to find (x). The common logarithm values were converted to nominal values by taking the result and making it the power of the base [$10^{\wedge result}$].

The co-efficient of determination (R^2) was then calculated in Excel to determine how closely the points from different cDNA dilutions adhere to the standard curve, and this

value used as a determination of PCR efficiency. An R^2 value >0.99 provides good confidence in correlating two values and shows the reaction was very efficient. All standard curves had an R2 value of >0.98 (Summarised in Figure 23).

All expression levels were normalised with values obtained for the internal reference gene RP-L19. Once normalised, expression was calculated as a relative value of transcript levels between treated and control or individual cell line samples for each gene. Normalised starting quantity (SQ) values from triplicate wells were combined to give an average SQ per repeat. Significance was tested using a two-tailed Student's T-test conducted on average values from three independent repeats. Treated samples were compared against the untreated controls where P values ≤0.05, ≤0.01 and ≤0.001 were considered statistically significant and denoted with a: *, ** and *** respectively.

Well ID	Dilution	Log dilution	Quantification Cycle (Cq)	Avg. Cq	Log diultion	Starting quantity	Relative factor
Standard 1/5	0.2	-0.699	18.14				
Standard 1/10	0.1	-1	18.67	18.68	0.97	9.27	
Standard 1/10	0.1	-1	18.73				
Standard 1/10	0.1	-1	18.65				
Standard 1/100	0.01	-2	21.91				
Standard 1/1000	0.001	-3	25.37				
Hec1A			18.91	18.83	1.01	10.31	1
Hec1A			18.81				
Hec1A			18.77				

Table 3: Data analysis of raw quantification cycle data. Standard curves ranging between 1/5 and 1/1000 dilutions of cDNA were converted into natural logarithms. The Log dilutions are then plotted against the C_q values. The equation of the line for this plot is re-arranged to yield log dilutions of unknown triplicate samples (Hec-1-A shown here). Log dilutions are converted back to starting quantities by making the log the power of the base 10.

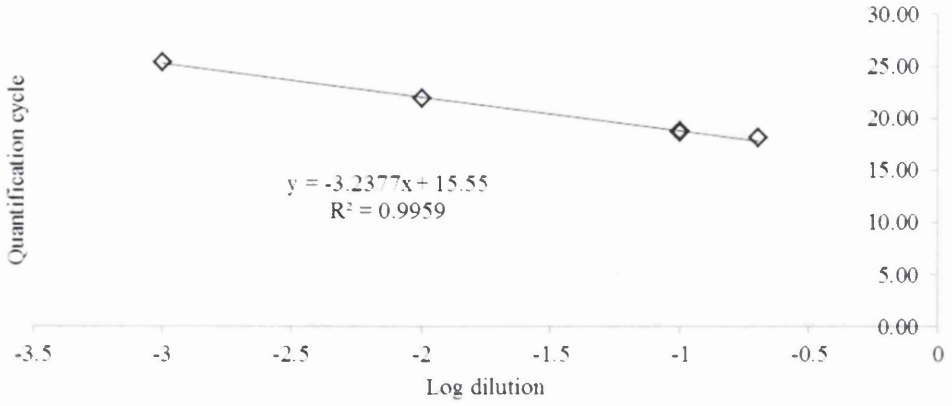

Figure 23: qRTPCR standard curve analysis. The standard curve is plotted using the log standard dilutions of 1/5, 3(1/10), 1/100 and 1/1000 against their respective C_q. Log quantities of unknowns may be fitted to this standard curve using the equation of the line. The R^2 value shows the efficiency of the reaction.

Primers for use in qRTPCR were designed using the National Centre for Biotechnology Information (NCBI) "PRIMER BLAST" against the nucleotide sequences of: ribosomal protein L19 (RPL19), mucin 1 (MUC1), mucin 4 (MUC4), mucin 16 (MUC16), progesterone receptor (PR), estrogen receptor α (ESR1), estrogen receptor β (ESR2) and N-acetylglucosamine-6-O-sulfotransferase (GlcNAc6ST). The forwards and reverse primer sequences, the temperature required for template annealing (calculated using Biorad CFX software), and amplicon length are shown in Table 4.

Gene	NCBI acsension	Primer direction	Oligo-nucleotide sequence	Annealing temp. (C)	Amplicon length (bp)
RPL-19	NM_000981.3	F	5'-CCTGTACGGTCCATTC-3'	54.3	144
		R	5'-AATCCTCATTCTCCTCATCC-3'		
Mucin-1	NM_002456.5	F	5'-TGGTGCTGGTCTGTGTTCTG-3'	54.2	233
		R	5'-CTCGCTCATAGGATGGTAGGTA-3'		
Mucin-4	AF522055.1	F	5'-CTCTGCCTCCTTCCGCATGT-3'	56.2	145
		R	5'-TCCCTCTAGTGTCGCTGTTGT-3'		
Mucin-16	AF361486	F	5'-TTCGCCTGCCAGTCCTAAAG-3'	55.0	283
		R	5'-GTGCTGGCCATTTGCATTGA-3'		
PR	M15716	F	5'-CTGCACTCGGCCTCAACGGG-3'	53.5	119
		R	5'-TGTGGGCTCTGGCTGGCTTC-3'		
ERα	NM_000125	F	5'-CCTCATCCTCTCCCACATCAG-3'	53.5	240
		R	5'-GGCGTCCAGCATCTCCAG-3'		
Erβ	DQ838583	F	5'-TGCTGAACGCCGTGACCGATG-3'	54.2	167
		R	5'-ATGGATTGCTGCTGGGAGGAGA-3'		
GLcNAcST	AB014680	F	5'-ATCCGTGAGAGCCTACAGGT-3'	59.5	382
		R	5'-CATTGCGTGCAGATACCACG-3'		

Table 4: Primer sequences. The nucleotide sequence of each gene was acquired using a NCBI nucleotide search. Ascension numbers are shown. Primers were designed using

the "Pick Primers" function and annealing temperatures and amplicon lengths are shown.

2.05 Immunocytochemistry (ICC)

Confluent monolayers for each cell line were trypsinised and re-suspended in fresh DMEM-F12 media. Cells were adjusted to a seeding concentration of $8x10^4$ cells/ml and seeded onto slides within quadriperm vessels (Nunc), allowed to attach for 5 mins before flooding with 5ml of media and left to grow for a minimum of 24hrs or until they were 80-100% confluent.

Each slide was labelled with mouse VU4H5 anti-MUC1 antibody (Santa Cruz Biotechnology) at a 1:50 dilution. A positive control section of colon adenocarcinoma was used. Primary antibody incubation was for 36 minutes at 37°C. Positive immunostaining was detected through interaction of avidin-biotin peroxidise (ABP) complex with biotin conjugated secondary antibody using a ventana I view DAB detection kit (Ventana Biotek Solutions [760-500]). The slides were subsequently counter stained with haemotoxylin, dehydrated and mounted to be examined under light microscopy. An immunocytochemical scoring system was used in which the same observers examined a designated representative area for each of the immunocytochemical slides prepared. The observers were blinded to the origin of the slides and cell type before scoring. The endometrial epithelial cells were assessed for stain intensity throughout the cell. The intensity of the staining was assessed as follows: (0) – absent, (1) – less than 25%, (2) - 25-50%, (3) - 50-75% and (4)-75-100% of the cell surface stained.

Two observers scored 20 cells independently from each slide area (triplicate slides for each treatment and cell line sample) and scores were collated into a single data set giving 120 cells for each steroid receptor in each cell line. Significance was tested using the Kruskal-Wallis one-way analysis of variance for non-parametric data. This test detected whether at least one of the samples was significantly different from the group. Where a significant difference between groups was detected then Mann-Whitney U test was used to analyse specific sample pairs for significant differences. All cell lines were compared using Kruskal-Wallis and then Hec-1-B was compared to Hec-1-A, Ishikawa and Hec50 using Mann-Whitney. P values ≤ 0.05, ≤ 0.01 and ≤ 0.001 were considered statistically significant and denoted with a: *, ** and *** respectively.

2.06 High Content Screening (HCS) of MUC1 and sLe^x using INCELL technology

The cells were cultured as previously described. Cell monolayers were fixed with paraformaldehyde (4% w/v for 10min at 4°C), and permeablised with Triton X-100 (0.01% v/v for 5min at 25°C). Cells were incubated in blocking buffer (5% goat serum + 1% BSA in PBS) for 1hr at 25°C. Next, cells were incubated in either mouse VU4H5 anti-MUC1 antibody (Santa Cruz Biotechnology #sc-7313) at a final concentration 2ug/ml or CTAGE1 Antibody-FITC (MECA-79) (Santa Cruz Biotechnology #sc-53514) for 1hr at 25°C. For fluorescent detection, the VU4H5 antibody required the addition of anti-mouse Texas-Red conjugated secondary antibody (Molecular Probes #T-6390) at a final concentration 2ug/ml in PBS for 1hr at 25°C. For MECA-79, Texas-red conjugated secondary antibody was omitted because the primary antibody was conjugated to a FITC reporter element. The cell nuclei in both preparations were counter stained with NucBlue™ (Life technologies # R37605) 4',6-diamidino-2-phenylindole (DAPI) preparation (2 drops/ ml PBS for 25 minutes at 25°C). 5x 5min washes in PBS followed each incubation step and the cells were imaged in excess PBS.

2.061 HCS Image acquisition

HCS of MUC1 and sLe^x using immuno-fluorescence was undertaken using the INCELL Analyzer 2000 (GE healthcare). Image data was recorded in two emission spectra channels; DAPI nuclear staining (Channel 1 λ 470nm for 0.0150s) and Texas Red MUC1 staining (Channel 2: λ 620nm for 5.000s) or FITC MECA-79 staining (Channel 2: λ 521nm for 5.000s). The nuclear stain was a requirement to separate individual cells in subsequent analysis. Thirty low magnification images (10 x objective) were obtained for control and treated. These images contained a total of ~15000 cells (30 images of approx. 500 cells).

The INCELL analyzer acquisition software allows for a random distribution of fields across the well surface and regions of the centre or edge of the well may be excluded from field selection. The regions close to the well boundary were excluded from field selection as they were not representative of other areas of the well. The exposure time for each channel was kept constant across all experiments, therefore changes in fluorescence were directly attributable to protein expression levels. The output file is termed XDCE, which is a folder containing compiled images from all channels and all fields of view screened.

2.062 HCS Image analysis

XDCE files were analysed by using INCELL investigator software suite (GE Healthcare Analysis) to quantify MUC1/sLe^x immune-fluorescence. Briefly, an object segmentation feature masked the nuclei by segmenting on the basis of intensity in the DAPI channel. The high contrast in fluorescence output between the nuclear material and background facilitated efficient separation of nuclei against background. The masked bitmap was eroded in order to separate clumped nuclei prevalent in the monolayer. The initial segmentation was then repeated as above and nuclei in close proximity were separated as individual objects using the eroded mask from the previous step. A 10μm collar drawn around the nuclear mask isolated the cytoplasmic region of each cell (see Figure 24, Figure 25 –*Nuclei identification*). Fluorescence output in absolute grey levels was recorded pixel by pixel across the cell area mask and each cell was assigned a value for MUC1 expression based upon area the average pixel fluorescence. The software allows for calculation of total cellular fluorescence but this meant cell size would be a conflicting factor and thus was not desirable.

Depending on the output parameters specified, average fluorescence output per cell, that is across the pixels over the cell body or a mean output for the cell population was generated. This mean output for the population is denoted "average well intensity" and displayed in the form of a bar graph normalised against negative control. This normalisation process involved subtracting the average well intensity from a no antibody negative control from the experimental value to account for any background staining meaning the remaining signal was due to specific bound primary antibody. This was repeated with three independent repeats and the well values were tested for significance using a two-tailed Student's T-test conducted on average values from three independent repeats. Treated samples were compared against the untreated controls where P values ≤ 0.05, ≤ 0.01 and ≤ 0.001 were considered statistically significant and denoted with a: *, ** and *** respectively.

In some instances (e.g. Figure 42, Chapter 3) the spread of the data is best illustrated with a histogram. This time the individual fluorescence output values per cell were sorted on the basis of intensity to look for subtle changes in the distribution of protein expression, cells comprising these histogram data sets are compiled from three repeats and total cells sorted.

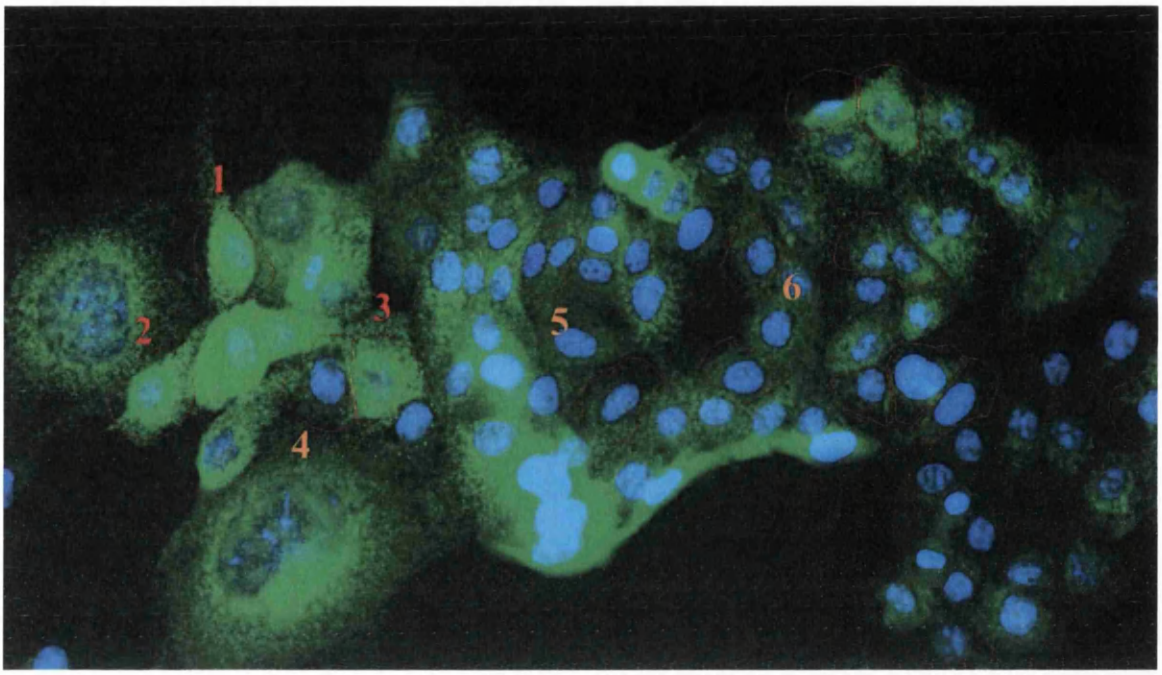

Figure 24: Analysing image data using HCS. Image shows analysis of EEC cells stained for MUC1 (green). Nuclei were counter stained (blue) in order to separate clumped cells. Red outlines denote estimated cell boundaries. Values for MC1 expression are average fluorescence per pixel inside marked area. This analysis helped identification of high expressing cells (1,2,3) compared to lower expressers (4,5,6).

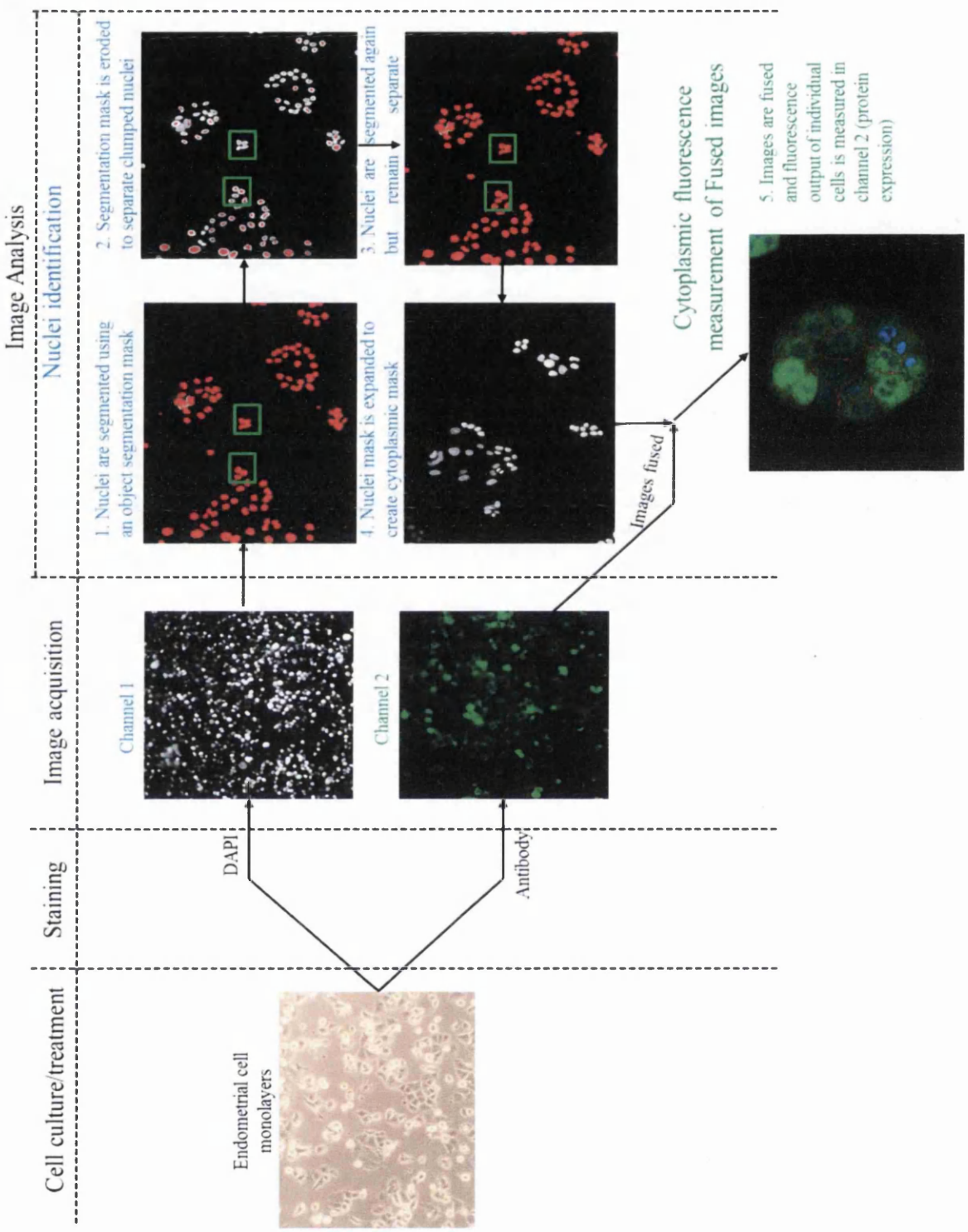

Figure 25: Overview of HCS. Endometrial monolayers are grown to 40-60% confluence (shown here) and treated with ovarian hormones or siRNA. Cells are then fixed and media removed. From here the analysis is conducted in two channels. First cells are stained with DAPI to identify the nuclear region while a single (MECA-79) or dual (MUC1) antibody stain is used for identification of expressed proteins. The INCELL analyzer 2000 captures two superimposed images, one in the DAPI emission wavelength and one in the Texas-red (MUC1) or FITC (MECA-79) emission spectrum.

These images are post-processed separately, nuclei are used to identify individual cells and the resulting mask is expanded to encompass the cytoplasmic region. At the final stage the images are fused and fluorescence signal within the cytoplasmic region is assessed in the protein channel. This results in a fluorescence value per cell, relating to the expression of protein in that cell.

2.07 Atomic force microscopy

During my project I undertook an industrial placement at Bruker nano in Mannheim, Germany. The imaging and QNM data presented in this thesis was acquired using a Bioscope catalyst II AFM (BRUKER Nano) equipped with a Nanoscope V controller and coupled to a DMI6000 (Leica, Mannheim, Germany). Upon my return to Swansea, I trained to use a Nanowizard II AFM (JPK, Berlin, Germany) mounted on a Zeiss LSM510 confocal microscope. All SMFS data presented was conducted on this instrument.

2.071 Sample preparation for AFM imaging

Fixed cell imaging in liquid - Cell lines were cultured as outlined in the appropriate section above (2.012 Passage of EEC cell lines in culture) in 50mm diameter glass dishes (WillCo Wells #GWSt5040) until 80-100% confluent. After 48hrs or the after the desired treatment regime was complete, the culture media was removed and the cells washed in 3mls PBS for 5mins, before being fixed with 4% paraformaldehyde at 4°C for 10mins. Cells were then rinsed in PBS to remove excess fixative and taken to the AFM for fixed cell imaging in fresh PBS at room temperature (RT).

Live cell imaging - cell lines were cultured as outlined in the appropriate section above (2.012 Passage of EEC cell lines in culture) in 50mm diameter glass dishes (WillCo Wells #GWSt5040) for use on the Bruker Bioscope Catalyst II AFM or 35mm diameter glass dishes (Fluorodish #FD35) for use on the JPK Nanowizard II AFM. After 48hrs or the culmination of the desired treatment regime, the culture media was replaced with 2ml of pre-warmed DMEM/F-12 phenol red free media (GIBCO # 21041-025) prior to live cell imaging. Application of fresh phenol red free media removed any accumulated floating cell debris from the sample which could interfere with the AFM probe and the lack of phenol red enabled easy alignment of the laser spot on the upper reflective surface of the cantilever. Cells were imaged over a maximum time of 90 minutes and maintained at 37°C using the stage heater system to ensure cells remained adherent and viable.

For all imaging in liquid, tapping mode was employed utilising the flexibility of the ScanAsyst Fluid cantilevers which had a nominal spring constant of 0.7N/m and a tip apex radius of 20-60nm. These probes have an intentionally dull tip ideal for force measurements and imaging extremely delicate cell surfacess in fluid. Care was taken to avoid the generation of imaging artefacts throughout.

2.072 Surface roughness

Mean surface roughness (Ra) is defined as the arithmetic mean of the deviations in height from the line mean value. Analysis of surface roughness used 10 randomly selected 3μm^2 square areas of each monolayer image in the height channel of peak force QNM. Three areas of monolayer were analysed for roughness from Hec-1-A and Hec-1-B cells to determine the effect of mucin protein expression on surface roughness (Figure 26). Significant difference between the two data sets was assessed using the Kruskal-Wallis one-way analysis of variance for non-parametric data. P values ≤0.05, ≤0.01 and ≤0.001 were considered statistically significant and denoted with a: *, ** and *** respectively.

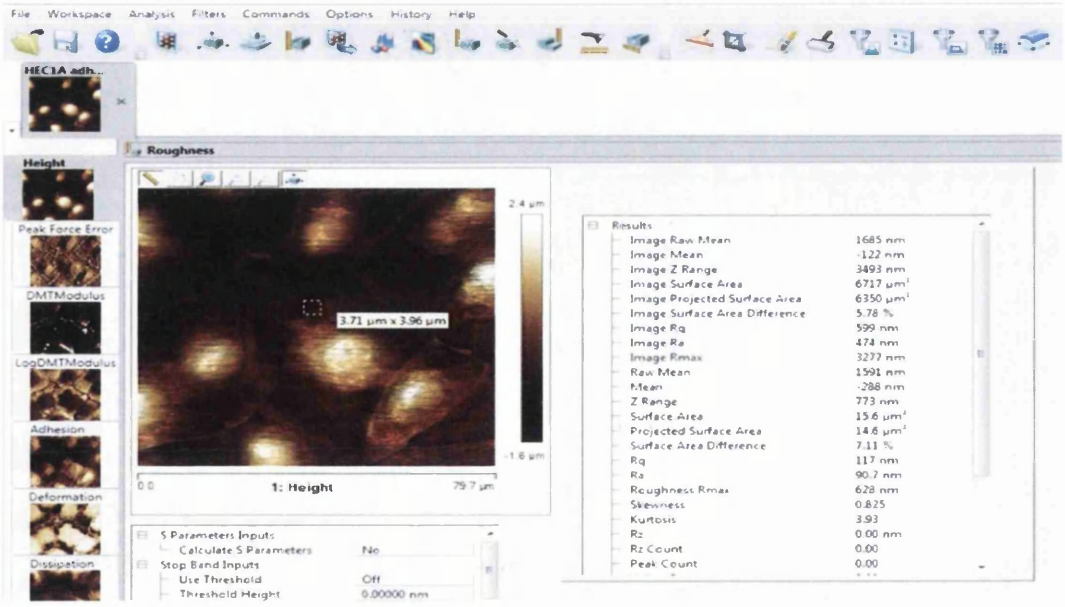

Figure 26: Analysis of surface roughness within the Nanoscope analysis software. Surface roughness was measure by selecting 30 3μm^2 areas across the monolayer for Hec-1-A and Hec-1-B.

2.073 Peak Force Quantitative Nano-mechanical Mapping (PFQNM)

2.0731 PFQNM Image acquisition

All PFQNM measurements were performed in aqueous solution; either on fixed cells in PBS or at near physiological conditions in media by using a Bioscope catalyst II AFM (BRUKER Nano) equipped with a Nanoscope V controller and coupled to a DMI6000 (Leica, Mannheim, Germany). Nano-meter scale images of surface topography and other surface properties were recorded in peak force tapping (PFT) mode using ScanAsyst fluid probes (Bruker Nano). Prior to experimentation the spring constant was calibrated using thermal tune sweep (300hz to 500hz) and found to be within 0.1 and 0.3 N/m. The cantilever deflection sensitivity was calculated using the in built Nanoscope software, by ramping into a non-compliant surface (glass) and fitting a trend line to the indentation curve, allowing the direct quantification of nano-mechanical surface properties using Peak Force QNM.

ScanAsyst fluid probes featured a triangular cantilever (k = 0.35-1.5N/m, resonance frequency 100Khz, LxWxH 70x10x0.6μm) coated with 45+/-5nm Ti/Au reflective layer and a sharp tip of height 2-6.5μm and nominal radius 20nm. Scanning parameters were maintained around 0.1Hz and 128 samples/line, corresponding to 16384 force curves per area. The scan area typically encompassed 50-150μm^2 regions of monolayer depending on topographical limitations and the peak-force amplitude was 300nm. Typically a frequency of oscillation of 1kHz was used and the z-range set to the maximum 27.1μm. The indentation force was kept as low as possible to preserve the live cell membrane and did not exceed 3nN. Each time the tip contacted the surface a force curve was recorded from which several parameters like topography, adhesion, dissipation and deformation were monitored and calculated using the in built nanoscope analysis software.

Nanoscope v8.2 software (Bruker Analysis software) allows capture of a single very high resolution (5000 samples/line) scan line. Termed High Speed Data Capture (HSDC) this feature allows 5000+ force curves to be recorded independent of the PFQNM image. These force curves can be exported for subsequent post processing using advanced models of elastic interaction in third party software. For every PFQNM image a corresponding HSDC file was captured.

2.0732 PFQNM image analysis

Nano-mechanical data presented in chapter 4 was generated using the Bioscope catalyst II AFM operating in peak force QNM imaging and high speed data capture (HSDC) modes. The fixed cell images were post-processed for adhesion, deformation, dissipation and height using the ''bearing analysis'' function of Nanoscope analysis v1.42r02 (Bruker Analysis Software). The returned value is an average of 262144 force curves. Three images were processed from one biological repeat thus returning a total of 786432 force curves.

The live cell images were processed for adhesion and deformation again using "bearing analysis". The returned value is an average of 16384 force curves, however this time three images were processed from each of three biological repeats thus contributing to a total of 147456 force curves for each condition.

Grouping	Number of biological repeats	Number of areas per repeat	Range of scan sizes (μm)	Image resolution (samples/line)	Image aspect ratio	Number of force curves per image	Total number of force curves per group
Hec-1-A [FIXED]	1	3	30-70	512	1	262144	786432
Hec-1-B [FIXED]	1	3	30-50	512	1	262144	786432
Hec-1-A	3	3	65-100	128	1	16384	147465
Hec-1-B	3	3	50-100	128	1	16384	147465
Hec-1-A MUC1 siRNA	3	3	100-150	128	1	16384	147465
Hec-1-B MUC1 siRNA	3	3	50-73	128	1	16384	147465

Table 5: The experimental design of fixed and live cell PFQNM studies. The preliminary fixed cell data set was obtained from 3 areas of the fixed cell monolayer from Hec-1-A and Hec-1-B cells. High resolution quantitative maps resulted in a large number of force curves per data set. The subsequent live cell investigation used lower resolution images but an increased number of independent repeats ensuring the biological robustness of the approach.

During the timeframe of this study the current AFM software (Nanoscope v8.2) by default calculated elastic modulus using DMT (Derjaguin et al. 1975) which assumes that adhesion forces occur outside the contact area and takes no account for adhesion between the tip and surface. In addition, DMT also requires the sample thickness to be many times thicker than the indentation depth. This model is suitable for high-density polymers or other such non-compliant samples but it is not particularly suitable for biological samples as the indentation depth into cells can be hundreds of nanometers. Therefore, force curve analysis for elastic modulus was conducted outside of the provided Nanoscope analysis v1.42r02 software using the Sneddon model (Sneddon 1965; Belikov et al. 2009), which takes the deformation induced by the indenter into account, considering the AFM tip as an infinite cone, and is well adapted to biological samples (Berquand et al. 2013; Kuznetsova et al. 2007; Lombardo et al. 2012).

As Sneddon was not native to the Bioscope Catalyst II Nanoscope software, for each image, a single HSDC file containing 5000 force curves was recorded for each image. The raw force curves were exported for analysis in custom software environment, Rainbow (Belikov et al. 2009), which gives the user the possibility to apply several different models, including Sneddon, to extract Young's modulus.

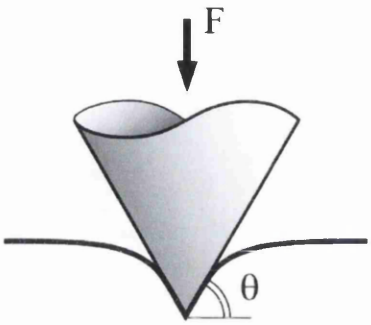

$$S = \frac{2}{\sqrt{\pi}} \frac{E}{(1-\nu^2)} \sqrt{A}$$

Figure 27: The indentation of a conical shape into a flat surface. Contact stiffness, S is related to the projected contact area A, and the elastic constants of the material, E and ν, Poisson's ratio.

The projected contact area, A can be calculated by:

$$\mathrm{A} = \tan\theta \, (s^1 - s^0)^2$$

Where θ is the angle of the cone and s^1 is the surface and s^0 is the indentation depth.

2.074 Single Molecule Force Spectroscopy (SMFS)

Cell monolayers were prepared and treated as desired, as described in section 2.012 Passage of EEC cell lines in culture.

2.0741 Functionalising the AFM probe

AFM probes were first cleaned by rinsing in deionised water and then immersed in HAPTES (SIGMA ALDRICH) buffer (0.1% v/v, pH 7.0) for 7mins at 25°C. The silanized probes were rinsed 5x in deionised H_2O then immersed in glutaraldehyde (0.5% w/v pH 7.0) for 7 mins at 25°C. The probes were again rinsed with water before being immersed in mouse VU4H5 anti-MUC1 antibody (Santa Cruz Biotechnology #sc-7313) at a concentration of 200µg /ml, for 7mins at 25°C. This antibody recognises the extracellular VNTR domain of MUC1 and is identical to that used for both ICC and HCS analysis. After this final incubation the AFM probes were rinsed 5x in Tris HCl (5% w/v pH 7.0). Probes were then immediately immersed in Tris HCl and were not allowed to dry out before taking measurements. This procedure was repeated with GAPDH antibody and recombinant human L-selectin protein fragments.

Recombinant L-selectin human L-selectin comprises a 294 amino acid fragment (39-332) out of a total length of 385 amino acids and corresponds to the mature L-Selectin extracellular (Tedder et al. 1990; Lasky et al. 1989). The recombinant protein is expressed in *E. coli* with an amino-terminal hexahistidine tag with metal affinity so allowing chromatography to isolate and concentrate L-selectin.

Functionalisation protein	Source	Applied Concentration	Target	Buffer
GAPDH antibody	Mouse	200 µg/1ml	Full length GAPDH	PBS
MUC1 antibody	Mouse	200 µg/1ml	MUC1 VNTR	PBS
L-selectin	E. coli	100 µg/0.5ml	LS ligands	1:1 Glycerol :PBS

Table 6: The Functionalisation tools used to probe endometrial cell surfacess. DNP-10 probes were functionalised with a range of binding proteins. All proteins were supplied at an effective concentration of 200µg/ml.

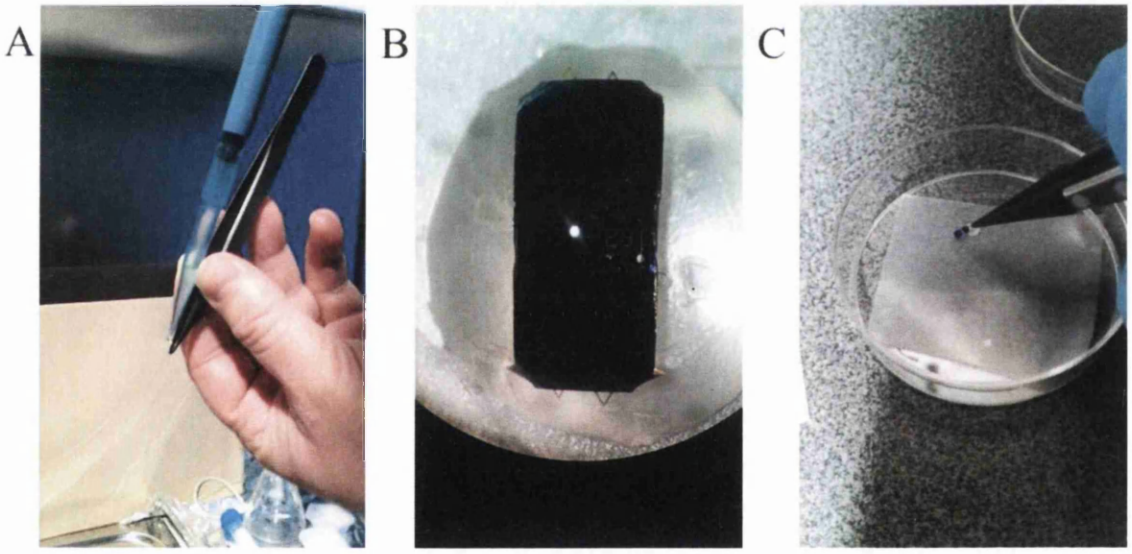

Figure 28: Functionalisation of DNP-10 probes. (A) A probe is washed with ddH_20 prior to functionalization, the water stream is run parallel to cantilevers C and D to ensure cantilevers are not damaged or bent. Carbon fibre tipped tweezers ensure a good grip on the probe during this process (B) A DNP-10 chip can be seen immersed in L-selectin allowing the formation of an imine bond to link the protein to the tip, all cantilevers are seen inundated in protein solution. (C) A probe is removed from parafilm substrate at the end of the final incubation, it was then washed with and used immediately.

Tips were functionalised fresh before every experiment and were never allowed to dry out. The silanization reagent APTES is hydrolytically unstable and has a half-life of 8.4 hrs in water pH 7 at 24°C. This compound hydrolyses generating ethanol and transient silanetriol derivatives, which will crosslink and prevent the silanization reaction

occurring on the AFM tip. The half-life may be extended to 56hrs by storing at 10°C but to ensure reproducibility APTES was made up fresh from concentrate and adjusted to pH 7 before every functionalization.

2.0742 Force mapping with the functionalised probe

The JPK Nanowizard II AFM was operated in force spectroscopy mode using silicon nitride DNP-10 probes (Bruker nano). Cell monolayers were probed near physiological conditions for single molecule force interactions by using cantilever D, a triangular cantilever (k = 0.06-0.12N/m, resonance frequency 18Khz, LxWxH 205x25x0.6μm) back coated with a 45+/-5nm Ti/Au reflective layer and a sharp tip of height 2.5-8μm and radius 20nm functionalised with mouse VU4H5 anti-MUC1 antibody (Santa Cruz Biotechnology #sc-7313). These cantilevers are very soft (nominal k 0.06N/m) and facilitate the detection of surface binding events. The functionalised probe was indented into $2\mu m^2$ area of the cell periphery allowed to rest for $100ms^{-1}$ to facilitate molecular binding and then withdrawn. The approach and retraction velocity of the tip was $3\mu m/s^{-1}$. Resolution was 16 samples/line and indentation force was between 2-3nN. Ramp size was maintained at 5.0μm in order to ensure that molecular binding occurred on the approach to the sample and the tip was withdrawn clear of the sample when retracted maximally. The number of event maps varied and for each cell line; there were 3 areas probed with GAPDH, 5 areas probed with anti-MUC1 and 9 areas probed with L-selectin. The negative control GAPDH consisted of one repeat, while anti-MUC1 and L-selectin maps consisted of 3 independent repeats, all data is shown. At least 256 force curves were obtained for each map.

The data presented in chapter 5 (-) consists of maps showing the location of steps on the retraction force curve, a percentage of positive curves (a curve with ≥1 step is considered positive) and histograms showing the spread of step sizes, which corresponds to the force required for tip/sample separation. The maps illustrate the spatial location and density of step occurrence, but additionally the colour of the pixel provides the number of steps on that single retraction curve resulting in a very informative visual illustration of binding. The percentage value revealed the frequency of surface binding, the percentage of positive curves was averaged across the number of maps and a Student's 2 tailed T.test was performed to assess whether the differences in positive curve number between the two cell lines on control vs siRNA were significant. P values ≤0.05, ≤0.01 and ≤0.001 were considered statistically significant and denoted

with a: *, ** and *** respectively. The step size histogram was a spread of all the measured step sizes to allow visualisation of the most common step size and therefore rupture force.

2.0743 Force curve processing and step fitting

JPK data processing software was used to fit steps to the retraction curves in order to detect specific surface interactions. Curves were analysed by force volume file, resulting in batches of 256 curves. Identical processing conditions were applied to all force volume files using a saved batch processing algorithm. Force curves were viewed in JPK data processing batch analysis (Figure 29A). Analysis was semi-automated as curves were checked manually before being accepted. Vertical deflection (baseline) correction was applied so the baseline was at 0nN, then a contact point correction was applied and adjusted the contact point to 0nm (Figure 29B). Next the curves were smoothed and steps were fitted to the curve using in built features of the software (Figure 29C). The step fitting algorithm provided data on the size of the step (pN) and the distance it occurred from the contact point.

The step fitting algorithm (JPK Software Analysis) represents the step signal as the sum of a slowly varying background signal (F_bg), a set of steps (i.e. a piecewise constant function)(F_step) and the background noise (F_noise). [The green curve displayed in the software represents F_bg + F_step]

To obtain F_step, we start with F_step = 0.

The software sweeps a reference step over the z range and look for the best overlap with F_noise. This gives one step, and accordingly F_step is updated. Applying the same procedure, the next step is identified, until the step height is smaller than the statistical noise level.

The two parameters to control the algorithm are "smoothing'' which defines how smooth the 'slowly varying background signal' is and 'significance' which sets the threshold below which steps are considered to be noise (and are thus discarded). A significance value of 0.001 means that the only step heights accepted have a probability of less than 1/1000 of being due to noise fluctuations (based on an estimate for the RMS of F_noise)

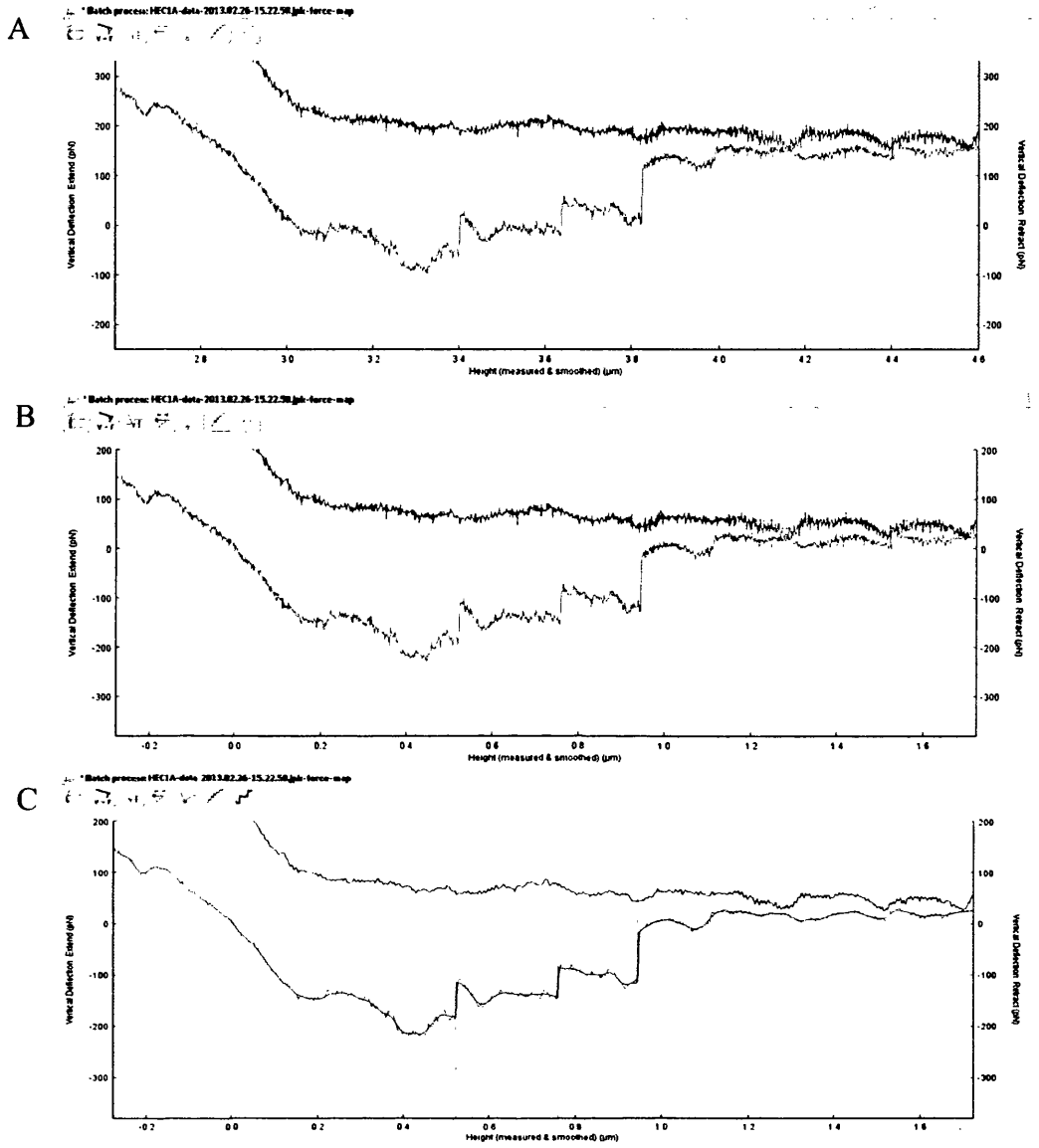

Figure 29: Force curve analysis and step fitting. JPK data processing software counted the number of steps in the force curve. Vertical lines running top to bottom are identified steps. Green line is the smoothed force retraction curve.

.

Chapter 3 An *in vitro* model for endometrial mucin expression

3.1 Introduction

If the endometrium is not receptive to the embryo, implantation does not occur. In humans, natural conception per cycle is poor (~30%), and 75% of failed pregnancies are considered to be due to implantation failure (Carson et al. 2000). The idea of a well-defined window of implantation is long established (Edwards 1988; Yoshinaga 1988) but after 25 years of intense biochemical analysis and implantation modelling in animals the molecular mediators of implantation remain elusive (Aplin 2006; Koot et al. 2012). Recurrent implantation failure (RIF) also remains the major limiting factor in assisted reproduction (Norwitz et al. 2001).

The phenotype of endometrium epithelium changes drastically from the proliferative to mid-secretory stages of the menstrual cycle, and only during a short period does the endometrium express the molecular requisites for successful implantation. The WOI is a limited period when blastocyst competency is superimposed on the receptive state of the uterus. Endometrial receptivity is achieved through the acquisition of adhesion ligands together with the loss of inhibitory components that act as a barrier to the approaching embryo (Aplin 2000). This receptive period occurs between days 21-24 of the menstrual cycle when the endometrium is primed for embryo attachment. The endometrium must acquire the morphological and molecular state for attachment and this development is driven by the ovarian hormones progesterone and estradiol, human chorionic gonadotrophin (hCG) from the trophoblast, growth factors and cytokines (Dey et al. 2004).

To date *in vivo* studies of implantation have used animal models. However, the regulation and expression of adhesive proteins during the WOI (such as MUC1) is not analogous between humans and commonly used animal models like rodents and rabbits (Dharmaraj et al. 2009). Larger primates such as the olive baboon (*Papio anubis anubis*) which is an excellent model for human implantation (Fazleabas et al. 1999), do express these proteins during the WOI (Hild-petito et al. 1996) and the size of these animals enables the use of endometrial biopsy, embryo flushing or transfer and hysteroscopy in a non-invasive way.

It is not possible to study this process of human implantation *in vivo* and even *ex vivo* models present difficulties. Very few laboratories have access to human embryos which must be specifically donated for the purpose of research and consent obtained. It is

somewhat easier to obtain biopsy material through endometrial pipelle biopsy, however whilst primary endometrial stromal cells are relatively easy to prepare from endometrial biopsy, epithelial cells are very difficult to isolate. Therefore, use of appropriate cell lines, particularly for functional studies of implantation is imperative. Use of cell lines derived from endometrial cancers such as Hec-1, Ishikawa, EEC-1, and RL95 and trophoblast (embryo) choriocarcinomas such as JAR, JEG-3 and BeWo is established (Teklenburg & Macklon 2009; Hannan et al. 2010).

This chapter required a model with which to manipulate expression of potential apposition stage adhesion proteins *in vitro* for functional studies using the AFM in chapters 4 and 5. To address such a requirement, the expression and regulation of selected potential tethering mucin proteins was examined using qRTPCR and high content analysis techniques across a range of EEC cell lines; Hec-1-A, Hec-1-B, Ishikawa and Hec50. Endometrial cell lines have been shown to vary in expression of (potential) adhesion molecules and have been used as models for receptive (Heneweer et al. 2005; Wang et al. 2012) and non-receptive (Thie et al. 1998) implantation surfaces. Thus, selection of an appropriate cell line that expresses suitable implantation markers was critical. Additionally, it has been shown that certain cell lines such as Ishikawa can display varying expression patterns of adhesion molecules and nuclear receptors in culture (Nishida 2002). This further highlighted the need to effectively and thoroughly characterise the cell lines available for this project before proceeding with a functional implantation model.

The endometrial epithelium must express molecules that allow the recognition and implantation of a blastocyst. It has been observed in endometrial cell lines (Meseguer et al. 2001) and in primary tissue (Horne et al. 2002) that the distribution of these molecules is not uniform across the endometrial monolayer, but little attempt has been made to explain these observations and the functional impact on the receptivity of this surface. Current data from *in vitro* models of implantation suggest the initial tethering of the embryo to a mucin on the apical glycocalyx via a carbohydrate mediated selectin interaction (Margarit et al. 2009; Genbacev et al. 2003; Carson et al. 2006), after which the uterine phenotype is modified by a medium- or short- range embryonic signal (Meseguer et al. 2001; Hey et al. 1994) allowing stable adhesion and then full trophoblast invasion to follow.

Mucins are a family of secreted and transmembrane >200KDa glycoproteins found on all epithelial cells, hematopoetic cells, activated T-cells and are secreted into gland lumens (Aplin et al. 1994). MUC1, MUC4 and MUC16 are present on the surface of human endometrial epithelial cells (Brayman et al. 2004) and typically extend away from the cell surface to a range of 300-2000nm, far beyond the range of other surface receptors which rarely extend greater than 50nm into the lumen (Bramwell et al. 1986). Mucins typically display a high degree of glycosylation, 50-90% by mass (Gendler 2001). A hallmark of the mucin family is a nucleotide tandem repeat domain that translates into a VNTR region encompassing a high proportion of serine and threonine residues (Moniaux et al. 2001). Functional carbohydrate epitopes are attached via an O-glycosidic-linkage formed through N-acetylgalactosamine (GalNAc) residues to serine or threonine on the VNTR protein core (Thathiah & Carson 2002). This domain is theorised to act as the scaffold for ligands that recognise the embryo and allow it to adhere and implant successfully (Margarit et al. 2009; Wang et al. 2008), a hypothesis that is tested thoroughly in chapter 5.

MUC1 is a major component of the endometrial epithelial glycocalyx expressed in both proliferative and secretory phases of many mammals (Hild-petito et al. 1996; Surveyor et al. 1995; Julian et al. 2005; DeSouza et al. 1998; Bowen et al. 1997) including humans (DeLoia et al. 1998; Aplin et al. 1994; Hey et al. 1994). MUC1 has a molecular weight of 200kD making it relatively small in comparison to other mucins such as MUC4 (930kD) and MUC16 (2000kD). However, the molecular mass of MUC1 can double due to VNTR length variations and altered glycosylation which have both been associated with infertility in humans (Horne et al. 2001; Margarit et al. 2009). MUC1 is believed to play host to ligands with embryo affinity and it is up-regulated during the window of implantation through the action of progesterone (Bergh PA 1992). MUC1 has been shown recently to be statistically significantly decrease in women with recurrent pregnancy loss (RPL) (Xu et al. 2012) whereas RPL patients had no altered integrin expression (Coughlan et al. 2013).

MUC4 is a 930KDa protein expressed in endometrial epithelium and theorised to extend 2000nm into the lumen (Koscinski et al. 2006). Like MUC1, MUC4 has a VNTR domain rich in serine and threonine residues comprising 145-395 repeats (Degand et al. 1998) and is theoretically capable of embryo affinity. In the pig endometrial MUC4 expression is up-regulated during the window of implantation

(Ferrell et al. 2003) while in the rat it is down-regulated (Idris & Carraway 2000) suggesting an anti-adhesive role. However unlike MUC1, MUC4 is not subject to hormonal regulation, and variations in the VNTR number do not correlate with implantation failure in humans (Koscinski et al. 2006).

MUC16 (2000kD) is the largest of the endometrial mucins. Although MUC16 has a larger glycosylated ectodomain than MUC1, and therefore could present embryo binding ligands, expression is reduced during the window of implantation in humans (Gipson et al. 2008). Adhesion assays using the human endometrial cell line EEC-1 which is positive for MUC1 and MUC16 showed that when MUC16 is targeted with siRNA embryo attachment increased (Gipson et al. 2008) suggesting the protein contributes to the non-receptive component of the endometrial surface.

Utereodomes (pinopods) are endometrial projections associated with implantation (Murphy 2006) and have been observed to correlate with the presence or absence of adhesion molecules such as MUC1 (Xu et al. 2012) and MUC16 (Gipson et al. 2008). Quenby et al used immunohistochemistry and H-score with frozen sections of primary biopsies for integrins ($\alpha1\beta1$, $\alpha4\beta1$, $\alpha V\beta3$), OPN and MUC1, and paraffin embedded sections for OPN and MUC1 to correlate distribution patterns of adhesion molecules with recurrent pregnancy loss (Quenby et al. 2007). Integrin patterning was highly variable and additional MUC1 reactivity was noted intra-cellularly and in gland secretions (Quenby et al. 2007). Patterning of adhesion molecules may create receptive areas of the endometrial surface but current approaches to investigate these observations such as ICC and confocal microscopy are limited by resolution or small sample sizes respectively.

The epithelial monolayer is an ideal model system with which to characterise the expression of mucin proteins at the epithelial interface. This thesis sets out to investigate endometrial adhesion molecules and their ligands as there is a need to understand their regulation and distribution across the endometrium. My hypothesis is that EEC cell lines are good models for adhesion protein presentation and that expression and patterning of such molecules is subject to ovarian hormone regulation. Endometrial cell lines have been shown to be representative of luminal and glandular epithelium and express a range of proteins that has allowed their use in adhesion experiments. The aim of this chapter is to explore and develop a model for regulation of

mucins and particularly MUC1 as a representative adhesion protein using EEC cell lines.

3.2 Results

In order to investigate the role of MUC1 at the surface of the endometrium, four EEC cell lines were characterized for their growth rate, expression of key functional adhesion protein candidates and steroid hormone receptor profiles. The Hec-1-A, Hec-1-B, Ishikawa and Hec50 cell lines were assessed for mRNA and expression of mucin proteins that could potentially act as the first point of contact for the embryo as it approaches the uterine epithelium. The cell lines were characterised for estrogen and progesterone receptors and regulation of endometrial mucins was explored using E_2, P_4 and MPA. The patterned expression of the endometrial mucin MUC1 was quantified using HCS and finally the effect of specific gene knockdown using mucin siRNA was explored as a method of regulating mucin presentation at the epithelial surface.

3.21 Growth rate of EEC cell lines in culture

The objective of this chapter was to develop an EEC cell line model for study of mucin glycoproteins that may be required for implantation. This model utilised several treatments requiring incubation for 24, 48 and 72hrs after which the monolayer was studied using ICC and HCS (this chapter) and atomic force microscopy (AFM) (chapters 4 and 5). The growth rates of all four cell lines were recorded over 96hrs so seeding density could be adjusted thus ensuring all cell lines reached the same state of confluence at the treatment end point. Maintaining the endometrial cells in monolayer conditions during HCS and AFM most resembled the continuing epithelial layer presented to the approaching trophoblast (*in vivo* morphology), allowed investigation of monolayer molecular patterning, and addressed the possibility of altered adhesion molecule expression resulting from variations in monolayer confluence.

Cells were seeded at varying concentrations ($2x10^4$ - $5x10^5$ cells/ml) and cultured under normal conditions (37°C 5% $C0_2$). At set time intervals (24-96 hrs) media was aspirated and cells were fixed using paraformaldehyde. Cells from each concentration were stained with 4',6-diamidino-2-phenylindole (DAPI) and counted using HCS. Absolute numbers of cells per $500\mu m^2$ field were divided by the number of cells in a 100% confluent monolayer of Hec-1-A cells thus producing a percentage of confluence for each cell line under different growth periods (Figure 30). This created a reference system for later experiments whereby a desired final concentration could be calculated

from the initial seeding concentration and required incubation time. This characterisation of varying grow rates was useful when working with four EEC cell lines simultaneously.

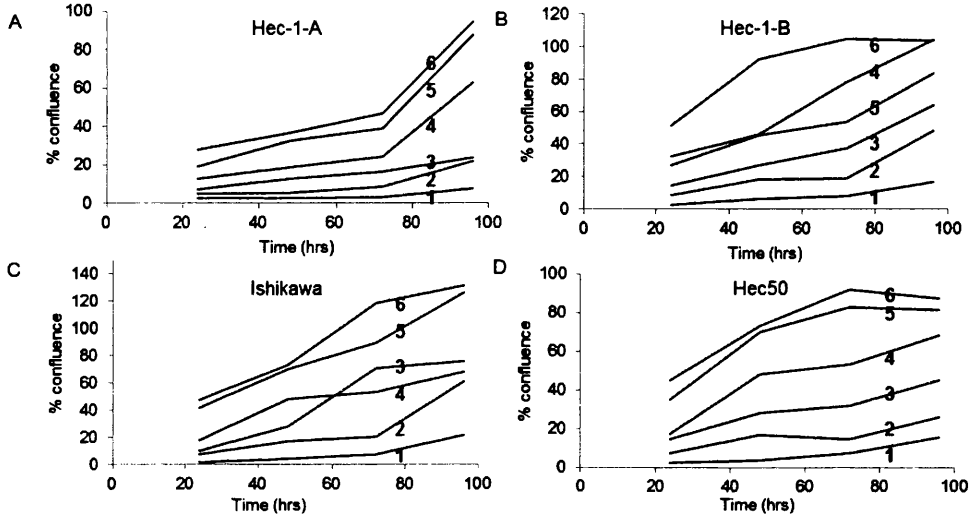

Figure 30: The growth characteristics of EEC cell lines in culture. Hec-1-A (A), Hec-1-B (B), Ishikawa (C), and Heraklio (D) were trypsinised and re-suspended in media. Cell suspensions underwent serial dilution to form seeding concentrations of $2x10^4$, $5x10^4$, $1x10^5$, $2x10^5$, $3x10^5$, $5x10^5$cells/ml represented by growth curves 1-6 respectively. Cell suspensions were seeded on 6 well plates and cultured for 24, 48, 72 and 96 hrs. Cells were fixed and stained with DAPI. The INCELL analyzer 2000 was used to image 10 $500\mu m^2$ fields and cells assessed for confluence using data generated by INCELL developer post acquisition analysis software platform.

3.22 Expression of steroid hormone receptor mRNA in EEC cell lines

The menstrual cycle is regulated through the actions of the ovarian steroid hormones E_2 and P_4 mediated through their respective nuclear receptors, the estrogen receptor (ER) and the progesterone receptor (PR). ER exists in two isoforms ERα and ERβ which are encoded by two different genes, ESR1 and ESR2. In contrast, the PR isoforms, PR-A and PR-B, are coded by the same gene (PGR) using different promoters. In order to test the hypothesis that ovarian hormones modulate mucin expression it was important investigate steroid receptor expression in the model cell lines to confirm that the receptors were present to modulate the effects of the hormones.

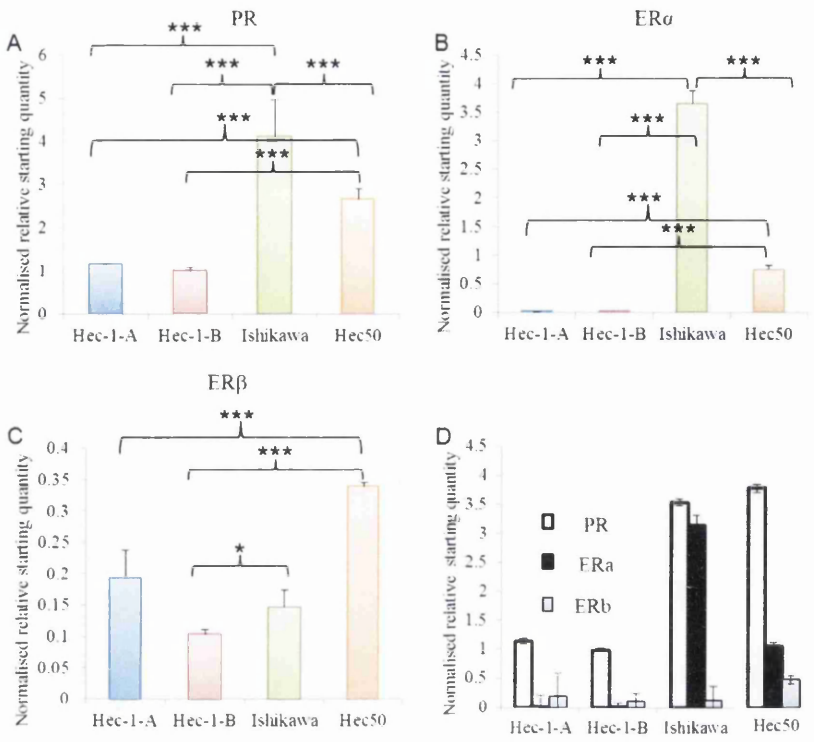

Figure 31: The expression of steroid hormone receptor mRNA in EEC cell lines. Bar graphs (A-C) show mRNA levels of Progesterone receptor (PR) Estrogen receptor alpha (ERα) and Estrogen Receptor beta (ERβ) in four EEC cell lines Hec-1-A, Hec-1-B, Ishikawa and Hec50 as assayed by real time quantitative PCR. (D) shows relative expression of all three steroid hormone receptors in the 4 cell lines. Data shown are average from three independent experiments. Values given are mean mRNA starting quantity normalised to RPL-19 ± STDEV from triplicates. Data was analysed using a two-tailed Student's T-test *p≤0.05, **p≤0.01, ***p≤0.001.

Figure 31A shows the expression of PR mRNA in Hec-1-A, Hec-1-B, Ishikawa and Hec50. PR mRNA was expressed in all the cell lines, Ishikawa was the highest expresser (4.11), 1.56 fold higher than the second highest expresser, Hec50 (2.65) (p≤0.001) and 3.57 fold and 4.11 fold greater than Hec-1-A and Hec-1-B respectively (p≤0.001).

Figure 31B shows ERα mRNA was expressed in Ishikawa and Hec50, as with PR Ishikawa expressed the highest levels of ERα in all the cell lines tested (3.65) displaying 4.90 fold higher levels than Hec50 (0.74) (p≤0.001). In contrast Hec-1-A and Hec-1-B could be considered negative for ERα transcript with values of 0.014 and 0.003 respectively which were 246 fold and 1019 fold less than Ishikawa (p≤0.001). 0.48).

Figure 31C shows ERβ mRNA expression in all the cell lines tested. The highest levels of expression were observed in Hec50 (0.34) which expressed 1.74 fold, 3.27 fold and 2.31 fold more ERβ transcript than Hec-1-A (0.19), Hec-1-B (0.10) and Ishikawa (0.15) respectively ($p \leq 0.001$).

These results demonstrate the positive expression of ERβ and PR in all the model cell lines. Ishikawa, often described as a useful model cell line because of a positive hormone receptor status (Nishida 2002) is shown here to express high levels of PR and ERα relative to the other cell lines tested.

3.23 Expression of mucin mRNA in EEC cell lines

The female reproductive tract has been characterised for the expression of mucins. Gipson et al used northern blot and IHC to show that the tethered mucins MUC1, MUC4 and MUC16, were expressed on endometrial epithelia (Gipson et al. 1997). A screen for the basal level of MUC1, 4 and 16 at the RNA level in each of the candidate cell lines was conducted in the first instance.

MUC1 transcript was expressed in the model cell lines. Hec-1-B (1.34) expressed 13.1 fold greater basal MUC1 mRNA compared to Hec-1-A (0.10) ($p \leq 0.01$) which was the second highest expresser (Figure 32). Ishikawa (0.044) and Hec50 (0.046) both expressed lower levels of MUC1 transcript. The highest and lowest expressers of MUC1 mRNA were Hec-1-B and Ishikawa.

MUC4 transcript was present in Hec-1-A and Ishikawa (Figure 32B). Hec-1-A (0.11) expressed the highest level of MUC4 mRNA, 4.58 fold greater than Ishikawa (0.023) ($p \leq 0.01$). Hec-1-B (0.000) and Hec50 (0.000) did not express MUC4 transcript.

MUC16 mRNA was present in Hec-1-A (0.09), Ishikawa (0.44) and Hec50 (0.03). Ishikawa expressed 4.68 fold greater MUC16 transcript than Hec-1-A ($p \leq 0.001$) and was the highest of all the cell lines tested. Hec50 expressed very low MUC16 transcript. Hec-1-B (0.000) was negative for MUC16 mRNA.

The Hec-1-B cell line expressed high levels of MUC1 mRNA but was negative for MUC4 and MUC16 transcript, thus highlighting itself as a useful tool with which to interrogate MUC1 function independently of related mucin proteins.

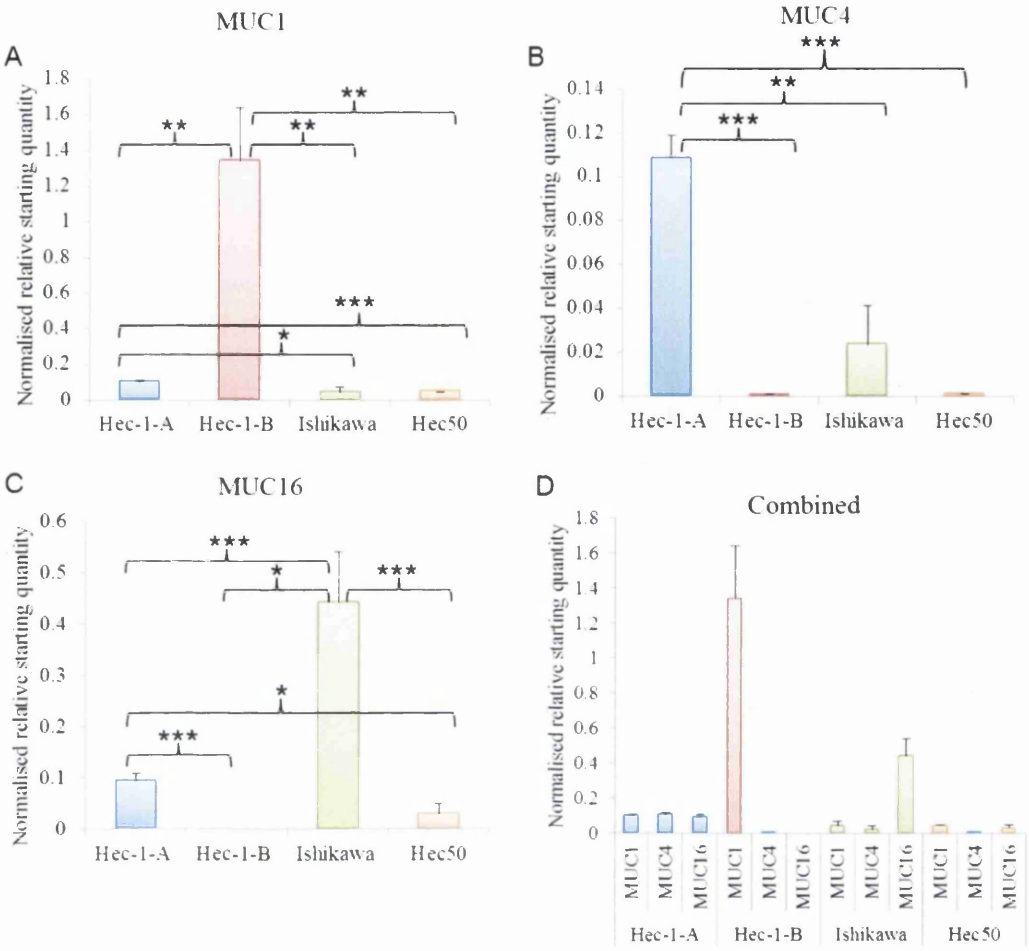

Figure 32: The expression of MUC1, MUC4 and MUC16 mRNA in EEC cell lines. Bar charts (A-C) show messenger transcript levels of MUC1, MUC4 and MUC16 in four EEC cell lines Hec-1-A (blue), Hec-1-B (red), Ishikawa (green) and Hec50 (orange) as assayed by real time quantitative PCR. Bar chart (D) shows combined expression of three epithelial mucins. Data shown are average from three independent experiments. Values given are mean mRNA starting quantity normalised to RPL-19 ± STDEV from triplicates. Data was analysed using a two-tailed Student's T-test *$p \leq 0.05$, **$p \leq 0.01$, ***$p \leq 0.001$ vs. control.

3.24 Hormonal regulation of mucin mRNA in EEC cell lines

P_4 induces physiological changes to the endometrium during the secretory phase and prepares the uterine for implantation. P_4 has been shown to increase MUC1 expression in EEC cell lines (Dharmaraj et al. 2010; Wang et al. 2010) but contrasting studies showed no MUC1 mRNA or protein response to P_4 (Tamm-Rosenstein et al. 2013). Hec-1-A, Hec-1-B, Ishikawa and Hec50 express varying levels of PR and ER mRNA, and in this section, the activity of the ligand signaling through these receptors and their effect on the expression of MUC1, 4 and 16 is monitored. Cell lines were treated with

P_4 at different concentrations in order to determine the concentration at which the receptor can be activated and induce transcription of mucin target genes.

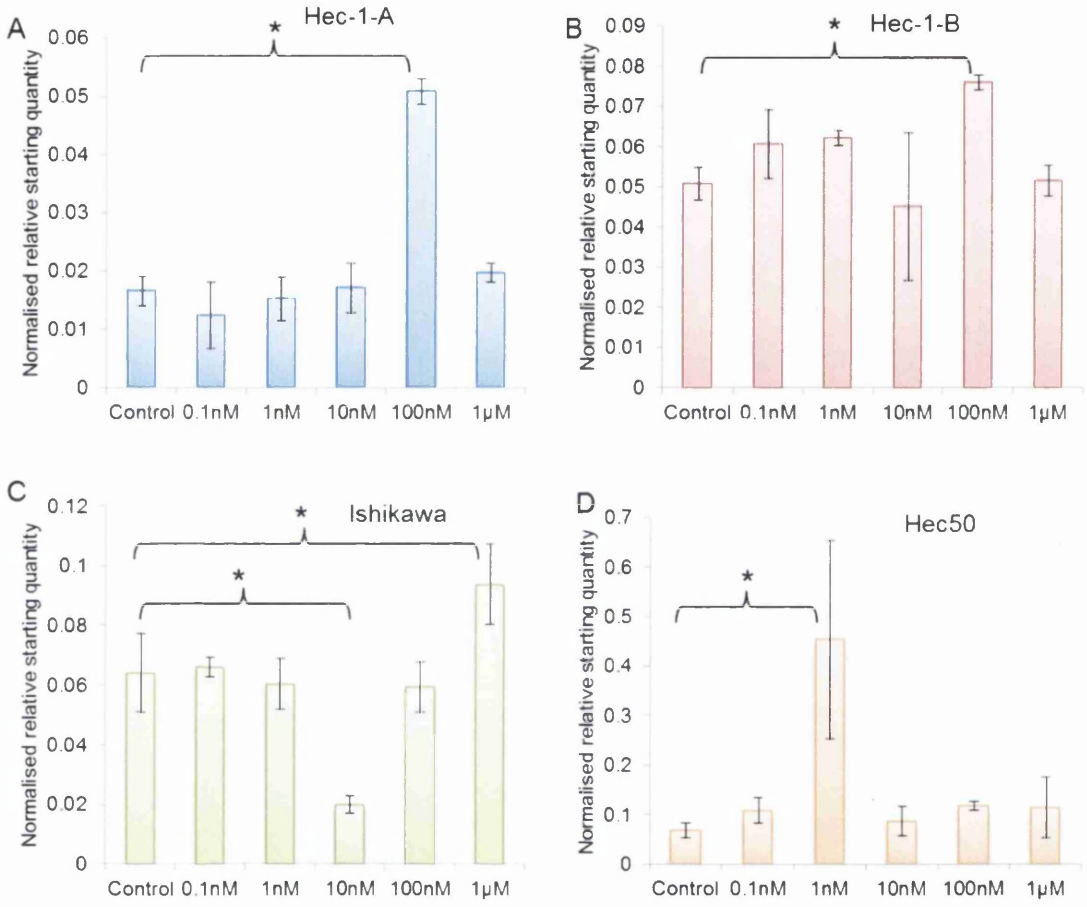

Figure 33: The effect of varying concentrations of progesterone on MUC1 mRNA expression in EEC cell lines Bar graphs show the effect of varying P_4 concentrations on MUC1 transcript levels in Hec-1-A (A), Hec-1-B (B), Ishikawa (C) and Hec50 (D) by real-time QRTPCR. Hec-1-A, Hec-1-B, Ishikawa and Hec50 cells were treated with 0.1nM, 1nM, 10nM, 100nM and 1μM progesterone for 48hrs. Data shown are average from three independent experiments. Values given are mean mRNA starting quantity normalised to RPL-19 ± STDEV from triplicates. Data was analysed using a two-tailed Student's T-test *$p \leq 0.05$ vs. control.

In Hec-1-A 100nM P_4 induced MUC1 transcript ~ 3.0 fold after 48hrs ($p \leq 0.05$) but no significant effect was seen with concentrations of 0.1nM, 1nM, 10nM or 1μM (Figure 33). MUC1 mRNA was also induced in Hec-1-B by 100nM P_4, but only a subtle 1.49 fold increase was observed after 48hrs ($p \leq 0.05$), as with Hec-1-A no significant differences in MUC1 transcript were observed with other P_4 concentrations. In contrast, treatment of Ishikawa cells with 10nM P_4 actually repressed MUC1 gene expression 3.2 fold ($p \leq 0.05$), while 1μM P_4 induced MUC1 transcript 1.66 fold compared to control

($p \leq 0.05$). Hec50 cells were generally unresponsive to P_4, however 1nM P_4 induced MUC1 mRNA 6.6 fold after 48hrs ($p \leq 0.05$). A large range of concentrations were investigated but no conventional positive or negative dose dependent response was seen in any of the tested cell lines.

3.241 The effect of progesterone and estradiol in isolation on mucin mRNA

The preliminary data in Figure 33 revealed that some cell lines appeared to be responsive to P_4 at 100nM concentration, however, the effect was subtle and/or highly variable. Treatment with P_4 appeared to up-regulate and down-regulate MUC1 mRNA in Hec-1-A and Ishikawa respectively.

At this stage mucin regulation with ovarian hormones showed some promise and warranted further investigation. 100nM P_4 appeared to induce MUC1 expression in Hec-1-A and Hec-1-B cells. The model cell lines were treated with 100nM P_4 or 10nM E_2 and gene expression of MUC1, MUC4 and MUC16 was quantified using qRTPCR.

MUC1 mRNA was expressed in all selected model cell lines (Figure 34A), and confirms previous experiments (Figure 4) showing Hec-1-B to be a relatively high expresser. In Hec-1-A cells treatment with P_4 and E_2 appeared to induce minor changes in MUC1 mRNA but they were not significant. In Hec-1-B cells the effect of P_4 and E_2 stimulation was a minor decrease in MUC1 transcript after 48hrs while Ishikawa cells showed no changes with the respective treatments. Hec50 cells showed no significant MUC1 response to E_2 or P_4 after 48hrs. Stimulation with ovarian hormones produced no change to MUC1 expression in any of the cell lines tested.

Hec-1-A expressed MUC4 transcript and stimulation with P_4 or E_2 for 48hrs resulted in a slight induction of MUC4 mRNA but this was not significant. Ishikawa was also shown to express MUC4 but stimulation with P_4 or E_2 showed no change relative to control. Hec-1-B and Hec50 cells were negative for MUC4 gene expression across all treatments (Figure 34B). Again, no significant changes were seen following any treatment.

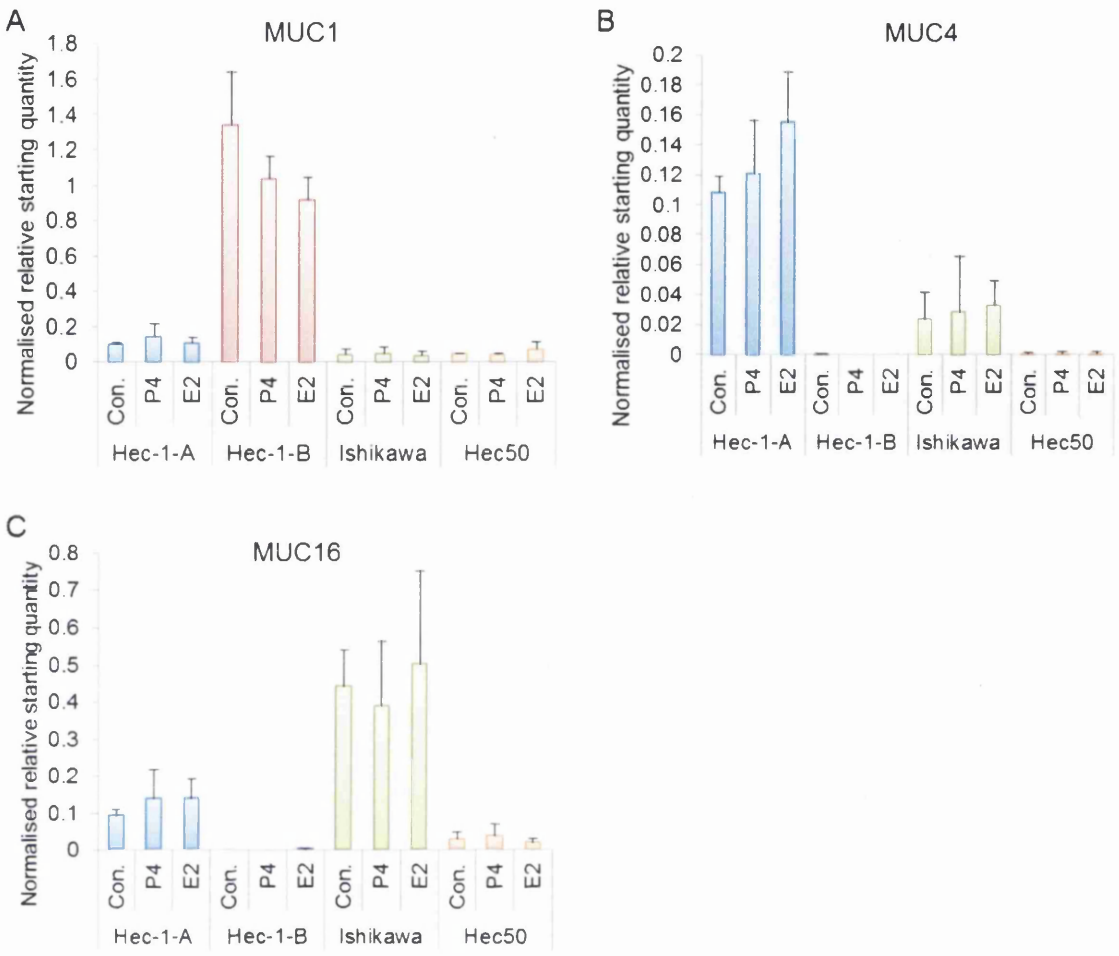

Figure 34: The effect of P_4 and E_2 on MUC1, MUC4 and MUC16 mRNA expression in EEC cell lines. P_4 and E_2 do not regulate endometrial mucin mRNA in EEC cell lines. Bar graphs show the effect of P_4 and E_2 on MUC1 (A), MUC4 (B) and MUC16 (C) transcript levels in Hec-1-A (blue), Hec-1-B (red), Ishikawa (green) and Hec50 (orange) by real-time QRTPCR. Hec-1-A, Hec-1-B, Ishikawa and Hec50 cells were treated with 100nM P_4 or 10nM E_2 for 48hrs. Data shown are average from three independent experiments. Values given are mean mRNA starting quantity normalised to RPL-19 ± STDEV from triplicates. Data was analysed using a two-tailed Student's T-test *p=<0.05, **p=<0.01 vs. control.

Figure 34C shows the MUC16 gene expression levels following treatment with P_4 and E_2 for 48hrs. Hec-1-A cell showed no change in MUC16 mRNA when treated with P_4 and E_2 respectively. MUC16 transcript in Ishikawa cells was not induced by P_4 and E_2. There was low level expression of MUC16 mRNA in Hec50 cells and this remained stable after stimulation with P_4 and E_2. Hec-1-B was negative for MUC16 gene expression and stimulation with P_4 and E_2 did not affect this. As with MUC1 and MUC4 no significant changes in MUC16 gene expression were observed.

MUC1, MUC4 and MUC16 all showed very little response to P_4 and E_2 stimulation. Any induction or repression of mucin transcript is masked at the mRNA level by variation between repeats. Quantification of the subtle changes in MUC1 protein expression observed here required a more elaborate approach and is re-visited later in this chapter.

3.2.4.2 The effect of progesterone and estradiol in combination on MUC1 mRNA

Whilst there was no consistent MUC1 mRNA response to P_4 or E_2 after 48hrs in any of the model cell lines, Hec-1-A and Ishikawa cells were shown to express similar levels of MUC1 mRNA under basal conditions and expressed both PR and ERβ making them the most suitable cell lines for a more elaborate treatment regime including 10nM E_2 pre-treatment for 24hrs and then a 100nM P_4 +/- E_2 incubation for 48hrs. This treatment regime represented hormonal conditions *in vivo* during the WOI as E_2 priming replicates the hormonal conditions during the proliferative and estrogen dominated phase of the menstrual cycle before the progesterone driven transition to the secretory phase endometrium.

Secondly, the progesterone metabolite methoxy-progesterone acetate (MPA) was introduced. This compound is a progesterone receptor agonist and has 2 fold higher affinity for binding compared to P_4 (Schindler et al. 2008), and provided the opportunity to investigate the effect of alternative (and more potent) progestin treatment on PR downstream targets.

Figure 35 shows the effect for P_4 and MPA on E_2 primed endometrial monolayers. In Hec-1-A cells. MUC1 transcript was induced 1.09 fold by E_2->P_4, 1.14 fold by E_2->P_4+E_2, almost no change after E_2->MPA treatment (1.02 fold increase) and a subtle 1.13 fold decrease due to E_2-> MPA+E_2. Ishikawa cells showed very small inductions of 1.05, 1.01, 1.16 and 1.18 fold following E_2->P_4, E_2->P_4+E_2, E_2->MPA and E_2-> MPA+E_2 respectively.

However, no statistically significant induction of MUC1 transcript in Hec-1-A or Ishikawa cells treated with P_4 or MPA after priming the tissue with E_2 was observed (Figure 35A+B) suggesting that MUC1 expression is not regulated by ovarian hormones in the selected model cell lines.

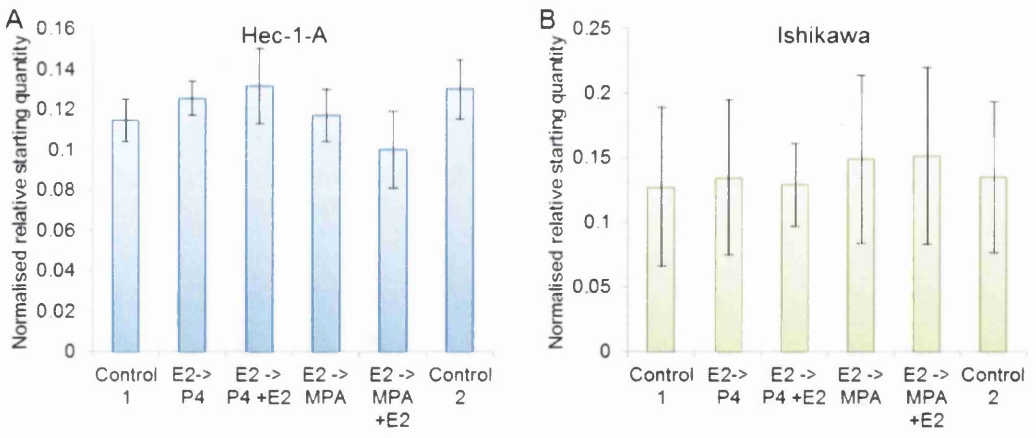

Figure 35: The effect of progestins and E_2 in combination on MUC1 mRNA expression in EEC cell lines. Combination treatments of P_4/MPA and E_2 do not regulate MUC1 transcript in EEC cell lines. Bar graphs show the effect of P_4, E_2 and MPA with E_2 pre-treatment on MUC1 transcript levels in Hec-1-A (A) (blue), and Ishikawa (B) (green) by qRTPCR. Hec-1-A and Ishikawa cells were primed with 10nM E_2 for 24hrs then treated with 100nM P_4 or 100nM MPA for 48hrs (with and without E_2). Data shown are average from three independent experiments. Values given are mean mRNA starting quantity normalised to RPL-19 ± STDEV from triplicates. Data was analysed using a two-tailed Student's T-test *p=<0.05, **p=<0.01 vs. control.

An aim of this chapter was to develop a model of mucin regulation. Treatment with varying concentrations of P_4, E_2 and MPA produced very little alteration in the expression of MUC1 at the mRNA level. Whilst there may be a hormone effect, it does not result in the significant changes in mucin expression, and as such was deemed and unsuitable model for investigating nano-mechanical properties of endometrial monolayers. The scope for MUC1 induction may be limited because the cell lines are already expressing high levels of MUC1 under basal conditions, thus an alternative approach was adopted to regulate MUC1 using an siRNA knockdown based approach.

3.25 RNA interference of mucin mRNA in EEC cell lines

Hec-1-A and Hec-1-B cells, both relatively high expressers of MUC1, made suitable candidates for gene knockdown and were treated with short interfering (si)RNAs of complementary sequence to MUC1 and MUC16 transcripts. SiRNAs are involved in RNA interference (RNAi), a process by which mRNA is targeted for post-translational degradation effectively silencing gene expression (see section 2.03 RNA interference). Two commercially available siRNA kits transfected into cells with lipofectamine RNAi Max were used to silence MUC1 and MUC16 expression. The effect typically lasts 5-7 days and as such is deemed a transient effect. A scrambled siRNA control, that has a

sequence not complementary to any known human gene transcript, was also used together with lipofectmine transfection reagent to evaluate any non-specific effects

The Hec-1-A and Hec-1-B cell lines were treated with 25nM, 50nM and 75nM siRNA for 48hrs (Figure 36). Expression of MUC1 transcript was reduced 7.38 fold, 25.45, fold and 21.37 fold respectively in Hec-1-A ($p=\leq 0.05$) and 26.47 fold, 29.04 fold, and 36.74 fold in Hec-1-B ($p=\leq 0.001$). The data showed no significant difference in expression between either of the two untreated controls and the scrambled siRNA transfection in either cell line, where the levels of MUC1 in Hec-1-A (low) and Hec-1-B (very high) were noted. The data showed that treatment with 50nM siRNA for 48hrs resulted in a knockdown efficiency of over 96% in both cell lines and that increasing the concentration of siRNA beyond 50nM did not increase the effectiveness of the treatment, therefore this concentration was selected for use in further experiments.

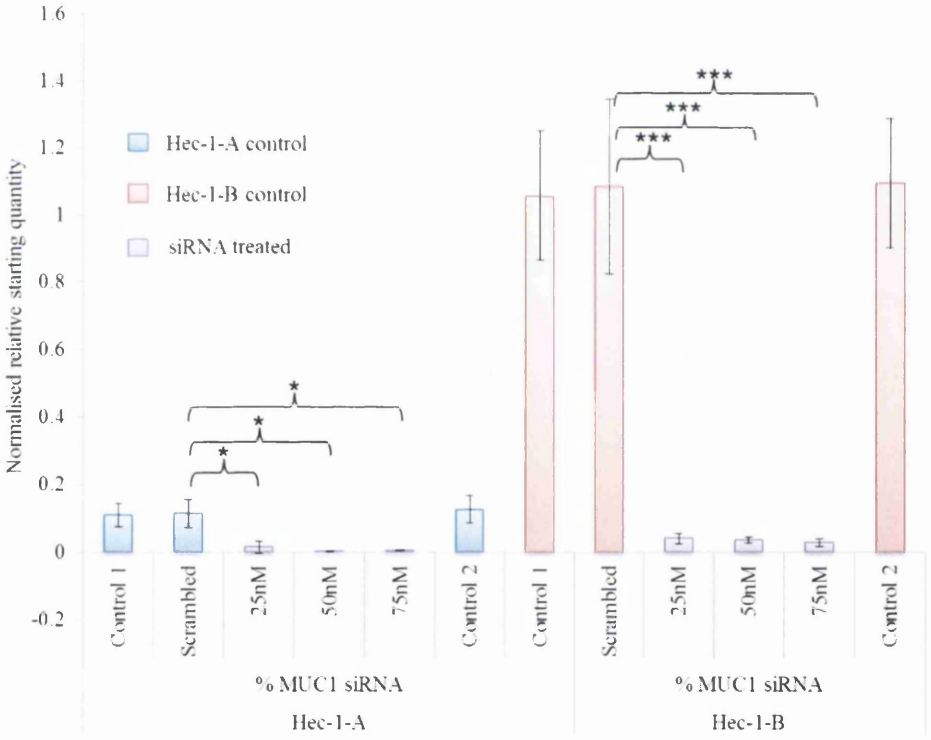

Figure 36: The effect of varying concentrations of MUC1 siRNA treatment on MUC1 mRNA expression in Hec-1-A and Hec-1-B EE cell lines. Bar graphs show the effect of varying concentrations of MUC1 siRNA (purple) on MUC1 transcript levels in Hec-1-A (blue) and Hec-1-B (red) at 48hrs. Hec-1 cells were treated with scrambled 50nM siRNA and 25nM, 50nM and 75nM MUC1 specific siRNA for 48hrs. Data shown are average from three independent experiments. Values given are mean mRNA starting quantity normalised to RPL-19 ± STDEV from triplicates. Data was analysed using a

two-tailed Student's T-test *p=<0.05, **p=<0.01, ***p=<0.001 vs. scrambled siRNA control.

Having optimised the treatment of siRNA to 50nM and 0.00375% lipofectamine for 48hrs, transient transfection was expanded to include MUC16 siRNA and performed on all four EEC cell lines (Figure 37).

Figure 37A shows the effect of specific gene silencing on the expression of MUC1 transcript after 48hrs. MUC1 mRNA was reduced 15.8 fold in Hec1-A ($p \leq 0.05$), 12.17 fold in Hec-1-B ($p \leq 0.01$), 11.0 fold in Ishikawa and 5.3 fold in Hec50 ($p \leq 0.05$). Treatment resulted in similar knockdown of MUC1 transcript in Ishikawa cells as the other model cell lines however due to the variability in Ishikawa samples this was not determined to be significant.

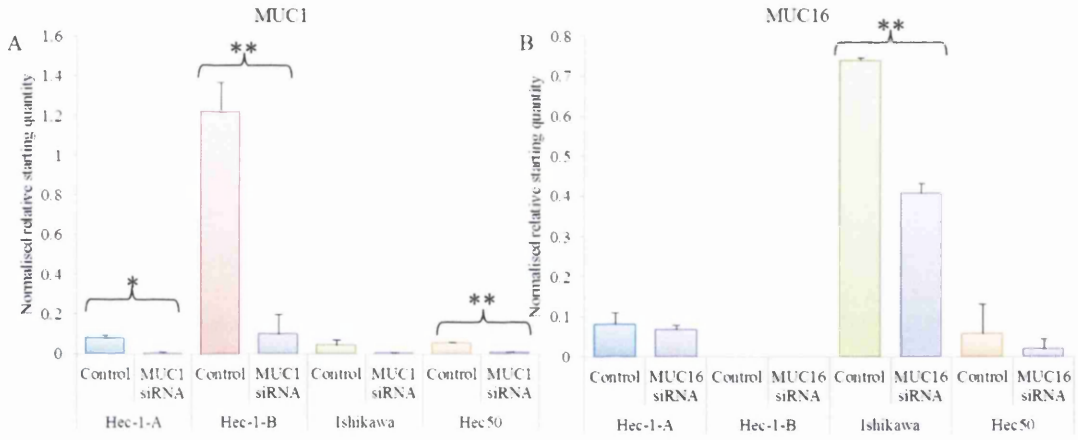

Figure 37: The effect of MUC1 and MUC16 specific siRNA on MUC1 and MUC16 mRNA expression in EEC cell lines. MUC1 and MUC16 gene expression is negatively affected by MUC1 and MUC16 siRNA. Bar graphs show the effect of (A) MUC1 siRNA (purple) and (B) MUC16 siRNA (purple) on MUC1 and MUC16 transcript levels in Hec-1-A (blue), Hec-1-B (red), Ishikawa (green) and Hec50 (orange) by qRTPCR. Endometrial epithelial cells were treated with scrambled 50nM siRNA and 50nM MUC1 specific siRNA and MUC16 specific siRNA for 48hrs. Data shown are average from three independent experiments. Values given are mean mRNA starting quantity normalised to RPL-19 ± STDEV from triplicates. Data was analysed using a two-tailed Student's T-test *p=<0.05, **p=<0.01 vs. scrambled siRNA control.

Figure 37B shows the effect of specific MUC16 gene silencing on the expression of MUC16 mRNA after 48hrs. MUC16 transcript was reduced 1.22 fold in Hec-1-A, 1.8 fold in Ishikawa ($p \leq 0.01$) and 2.9 fold in Hec50. However, out of all cell lines tested

only Ishikawa cells displayed significant knockdown of MUC16. The Hec-1-B cell line did not express MUC16.

Specific gene targeting resulted in efficient knockdown of mucins by siRNA, and therefore its effectiveness for interrogating the specific nano-mechanical properties of mucins. It seemed possible that a cell could adapt to loss of a particular mucin and compensate by increasing expression of other mucins making it difficult to determine whether changes to surface properties were the result of the specific targeting of MUC1. The turnover time for MUC1 (with GlcNAc modification) on epithelial surfaces is approximately 14hrs (Razawi et al. 2013) and the time taken for newly synthsised mucin proteins to reach the cell surface around 1hr (Hanisch et al. 2012; Kinlough et al. 2011) therefore any alterations in MUC4 or MUC16 expression would occur in the 48hr timeframe of this experiment. Mucin interplay was assessed by measuring any changes in MUC4 or MUC16 gene expression following MUC1 gene silencing, and any changes in MUC1 or MUC4 transcript levels following MUC16 gene silencing.

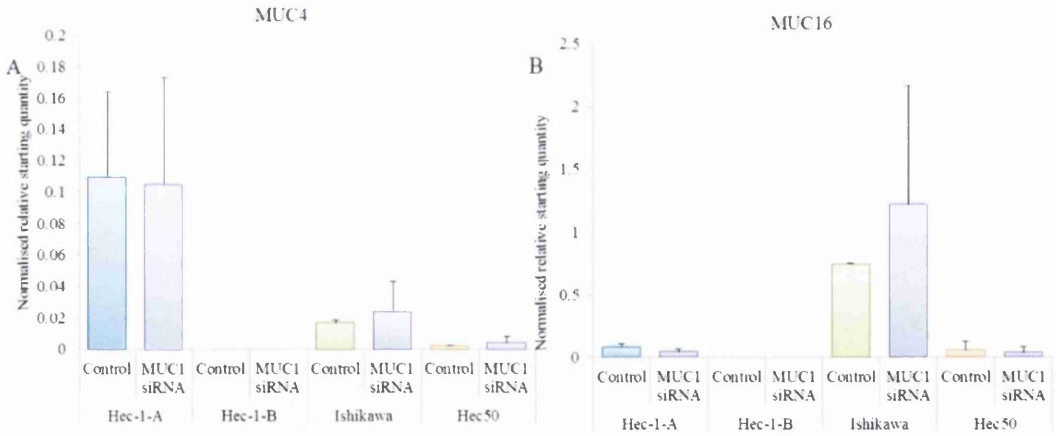

Figure 38: The effect of MUC1 specific siRNA on MUC4 and MUC16 mRNA expression in EEC cell lines. MUC4 and MUC16 gene expression is not affected by MUC1 knockdown. Bar graphs show the effect of MUC1 siRNA (purple) on MUC4 and MUC16 transcript levels in Hec-1-A (blue), Hec-1-B (red), Ishikawa (green) and Hec50 (orange) by qRTPCR. Endometrial epithelial cells were treated with scrambled 50nM siRNA and 50nM MUC1 specific siRNA for 48hrs. Data shown are average from three independent experiments. Values given are mean mRNA starting quantity normalised to RPL-19 ± STDEV from triplicates. Data was analysed using a two-tailed Student's T-test *p=<0.05, **p=<0.01 vs. scrambled siRNA control.

Figure 38A shows the effect of MUC1 specific gene silencing on MUC4 gene expression after 48hrs. MUC4 transcript levels were not significantly changed by

MUC1 siRNA in Hec-1-A, Ishikawa and Hec50. Hec-1-B showed no measureable levels of MUC4 mRNA and this was not changed by MUC1 siRNA treatment.

Figure 38B shows the effect of MUC1 specific gene silencing on the MUC16 mRNA levels in the cell lines after 48hrs. MUC16 mRNA was not induced or repressed by MUC1 gene knockdown in Hec-1-A, Ishikawa and Hec50. Hec-1-B again showed no measureable MUC16 transcript, and this was not affected by MUC1 knockdown.

Taken together the data shown in Figure 37 and Figure 38 demonstrates that MUC1 gene silencing using siRNA transfection in Hec-1-A, Hec-1-B and Ishikawa is very effective at down regulating MUC1 the mRNA level and that there were no measureable non-specific effects on MUC4 and MUC16 transcript.

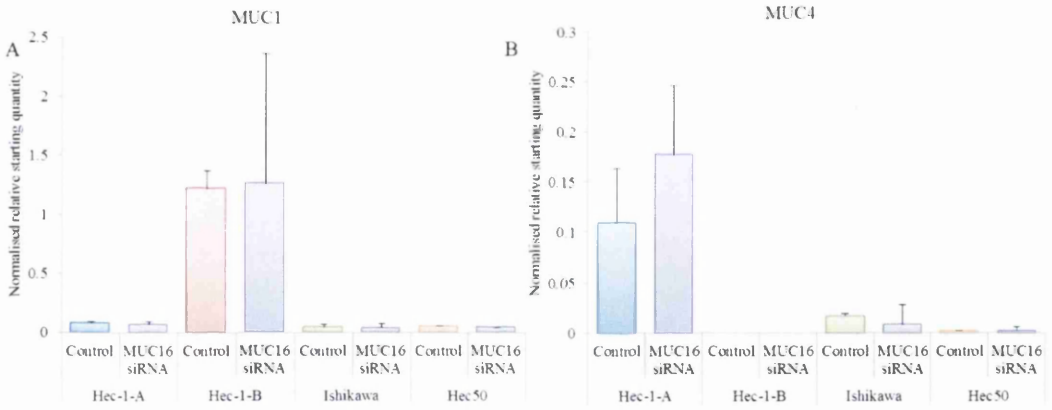

Figure 39: Effect of MUC16 specific siRNA on MUC1 and MUC4 mRNA expression in EEC cell lines. MUC1 and MUC4 gene expression is not affected by MUC16 knockdown. Bar graphs show the effect of MUC16 siRNA (purple) on MUC1 and MUC4 transcript levels in Hec-1-A (blue), Hec-1-B (red), Ishikawa (green) and Hec50 (orange) by qRTPCR. Endometrial epithelial cells were treated with scrambled 50nM siRNA and 50nM MUC16 specific siRNA for 48hrs. Data shown are average from three independent experiments. Values given are mean mRNA starting quantity normalised to RPL-19 ± STDEV from triplicates. Data was analysed using a two-tailed Student's T-test *p=<0.05, **p=<0.01 vs. scrambled siRNA control.

Figure 39A shows the effect of MUC16 siRNA treatment on MUC1 transcript in the model cell lines. There is no change to MUC1 expression in any of the cell lines tested after 48hrs of MUC16 siRNA.

Figure 39B shows the effect of specific MUC16 gene silencing on MUC4 mRNA levels after 48hrs. Again, there is no significant change in MUC4 transcript in Hec-1-A,

Ishikawa and Hec50 cells after MUC16 siRNA. Hec-1-B cells remained negative for MUC4 mRNA expression.

The data shown in figures 37, 38 and 39 suggests that MUC1 and MUC16 siRNAs are highly specific for MUC1 and MUC16 transcripts, and that silencing of any one mucin does not result in any compensatory up-regulation of other closely related mucin molecules.

3.26 Expression of MUC1 protein in endometrial EEC cell lines

3.261 Immunocytochemistry

Having determined mRNA expression levels of MUC1, MUC4 and MUC16, and demonstrated silencing of MUC1 expression while expression of other mucins was unaffected. MUC1 protein levels were investigated. Immunocytochemistry (ICC) was used to measure the intensity of MUC1 staining across all four cell lines.

Figure 40 shows ICC staining of Hec-1-A, Hec-1-B, Ishikawa and Hec-50 cells for MUC1 reactivity using the MUC1 VNTR antibody (Santa Cruz Biotechnology). Representative images show the characteristic MUC1 staining pattern in Hec-1-A, Hec-1-B and to a lesser extent Ishikawa and Hec50 cells. MUC1 reactivity was assigned an H-SCORE using a standardised ICC protocol. Mean expression of MUC1 in Hec-1-B (3.4) was 2.36 fold higher relative to Hec-1-A (1.44), Ishikawa (0.76) and Hec50 (1.56). Staining intensity variation between the model cell lines was assessed for significant differences using Kruskal-Wallis, and significant differences between groups were observed ($H=82.5$, $p\leq0.0001$). Subsequently, the Mann-Whitney-U test was used to compare groups and significant differences between Hec-1-A and Hec-1-B ($p\leq0.05$), Ishikawa and Hec-1-B ($p\leq0.01$) and Hec50 and Hec-1-B ($p\leq0.05$) were again observed demonstrating the differences in MUC1 protein expression between the cell lines.

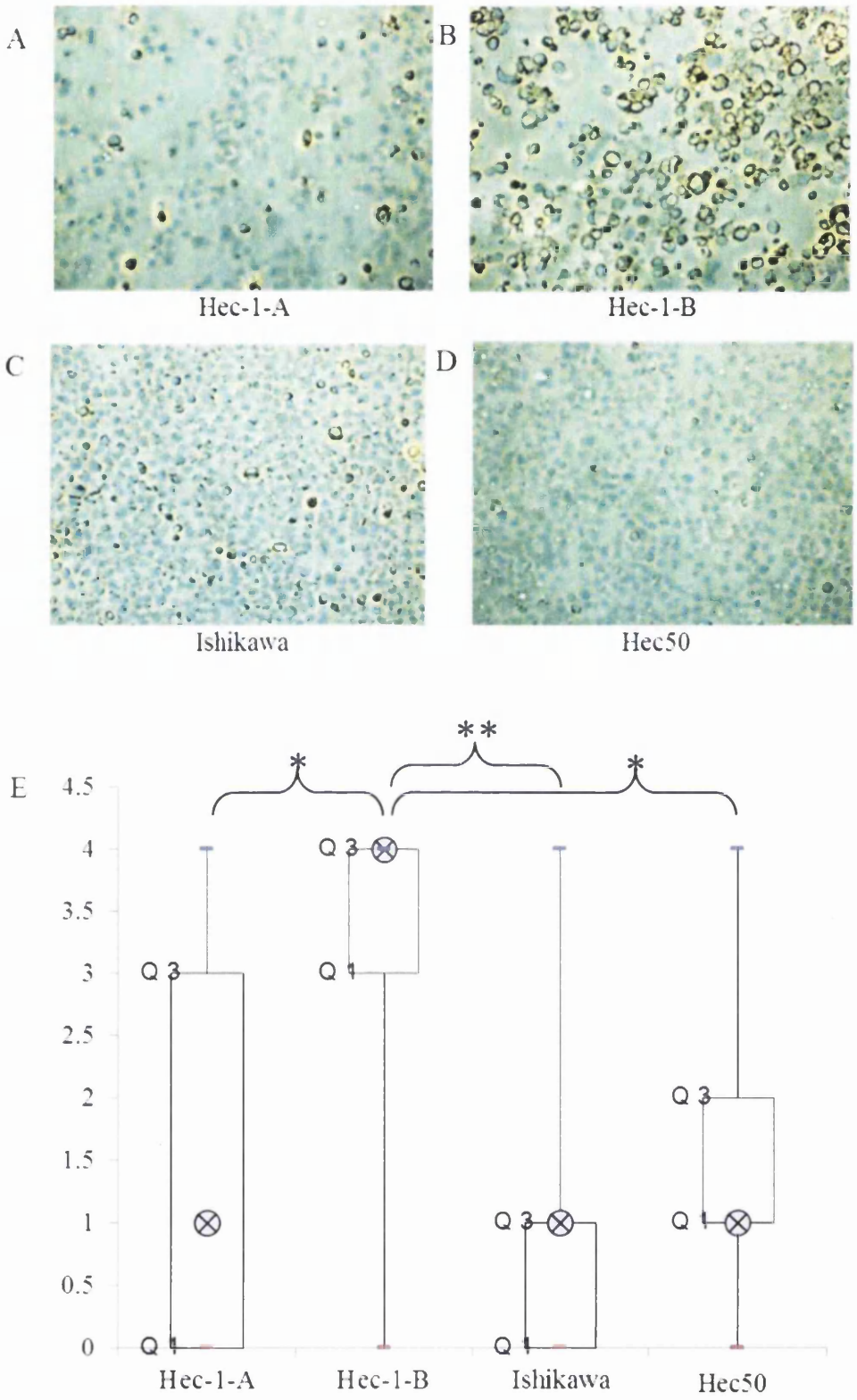

Figure 40: The expression of MUC1 protein in EEC cell lines: ICC
(A-D) Immuno-cytological staining showing intensity of MUC1 ND protein (brown staining) on Hec-1-A, Hec-1-B, Ishikawa and Hec50 cell monolayers. (E) H-SCORE for MUC1 protein staining.

Cells were antibody stained for MUC1 and nuclei were counter stained with Hematoxylin. Representative ICC images were taken using the Axio CamHRc colour camera (Zeiss) at 20x magnification. Cumulative scores for each cell line are plotted. Values are median (⊗) and inter-quartile range (Quartile 1 and Quartile 3). Statistical analysis was performed using the Kruskal-Wallis test followed by the Mann-Whitney test. *$p \leq 0.05$ and **$p \leq 0.01$ are considered significant. Kruskal-Wallis showed a very strong significant difference between groups ($p = 8.52^{-18}$)

3.262 High content screening

ICC (Figure 40) had demonstrated that MUC1 protein expression was variable across all four endometrial cell lines, and that Hec-1-B was a relatively high MUC1 expresser. Additionally, ICC revealed a heterogeneous, patterned, expression profile of MUC1 protein across the monolayer. This non-uniform distribution of MUC1 has been previously observed (Meseguer et al. 2001; Quenby et al. 2007) but the functional implications are still poorly understood. High content screening (HCS) was used to assess MUC1 staining distribution across large numbers of adherent cells. HCS was an improvement over ICC as it has the capability to conduct multiple target analysis algorithms on large cell numbers compared to tens of cells assessed subjectively during previously reported ICC. Cells were stained for MUC1 and counter stained with DAPI, and HCS was used to take 30 low magnification images randomly distributed across the cell culture plate. Image data was obtained in 2 image channels; (Figure 41A-D insert) nuclear using DAPI (emission λ=461 nm) and (Figure 41A-D) cellular using Texas-red conjugated anti-mouse secondary IgG that recognised the MUC1 primary antibody (emission λ=615 nm). INCELL analyzer 2000 developer proprietary software was used to generate average fluorescent output values (au) for all images.

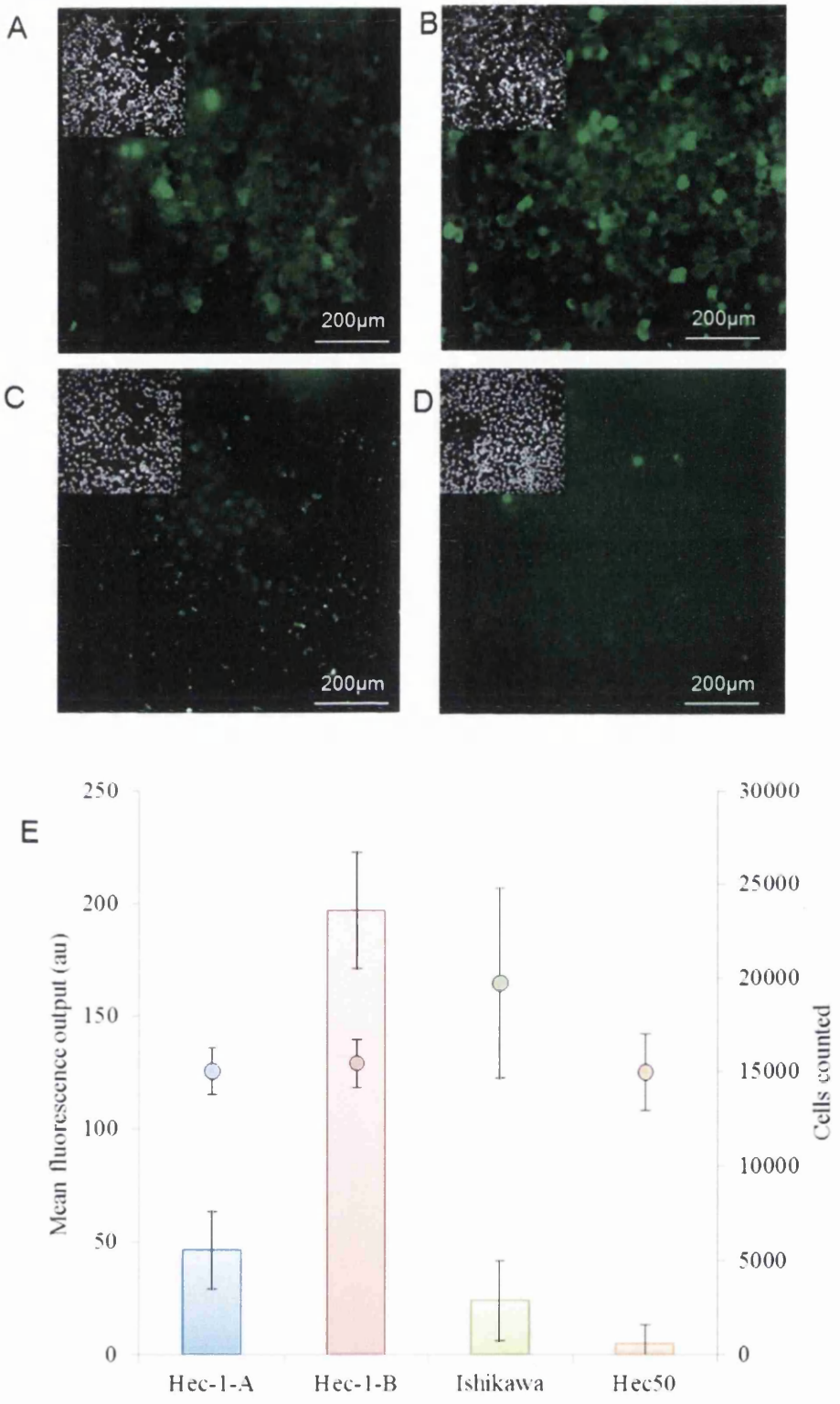

Figure 41: The expression of MUC1 protein in EEC cell lines: HCSHec-1-B is a relative high expresser of MUC1 at the protein level. Bar graphs show basal MUC1 protein expression in Hec-1-A (blue), Hec-1-B (red), Ishikawa (green) and Hec50 (orange). Scatter plot shows the number of cells from each cell line included in the analysis (colours are corresponding). Representative images were taken with the

INCELL analyzer 2000. Confluent cell monolayers were fixed and stained for MUC1 protein using Texas-red conjugated secondary antibody (Main window: false colour green shown here). Nuclei were counterstained with DAPI (Insert: false colour black and white shown here). Image data was acquired through automated high throughput bi-channel imaging using HCS. Images were post-processed within INCELL analyzer 2000 developer software. Individual cells were identified using a nuclear mask in the DAPI channel (nuclei). Subsequent analysis using a modified cytoplasmic mask assigned a relative value for cytoplasmic fluorescence to each cell (MUC1). Approximately 15000+ cells for each cell line.

Data shown are average from three independent experiments. Values given are mean fluorescent output from adherent cell populations, normalised to background ± STDEV from triplicates.

Figure 41 shows the expression of MUC1 protein as determined by INCELL total well fluorescence analysis and secondary axis shows the numbers of cells that were individual assessed. Following background correction, Hec-1-A, Hec-1-B, Ishikawa and Hec50 cell monolayers displayed fluorescence outputs of 46, 196, 24 and 5 AU calculated from 15052, 15472, 19739 and 14977 individual cells (Figure 41E). This data replicated the trend seen in previous ICC studies and confirmed Hec-1-B to be a high expresser of MUC1. Qualitative image analysis indicated presence of certain cells within the Hec-1-A and Hec-1-B population that displayed much higher staining denoting extremely high levels of MUC1 protein. This has been previously been observed (Harris et al. 2009) but no attempt has been made to characterise the function of this distribution. HCS provided a novel opportunity to interrogate the distribution of these patterns across very large numbers of cells.

3.27 MUC1 distribution patterns

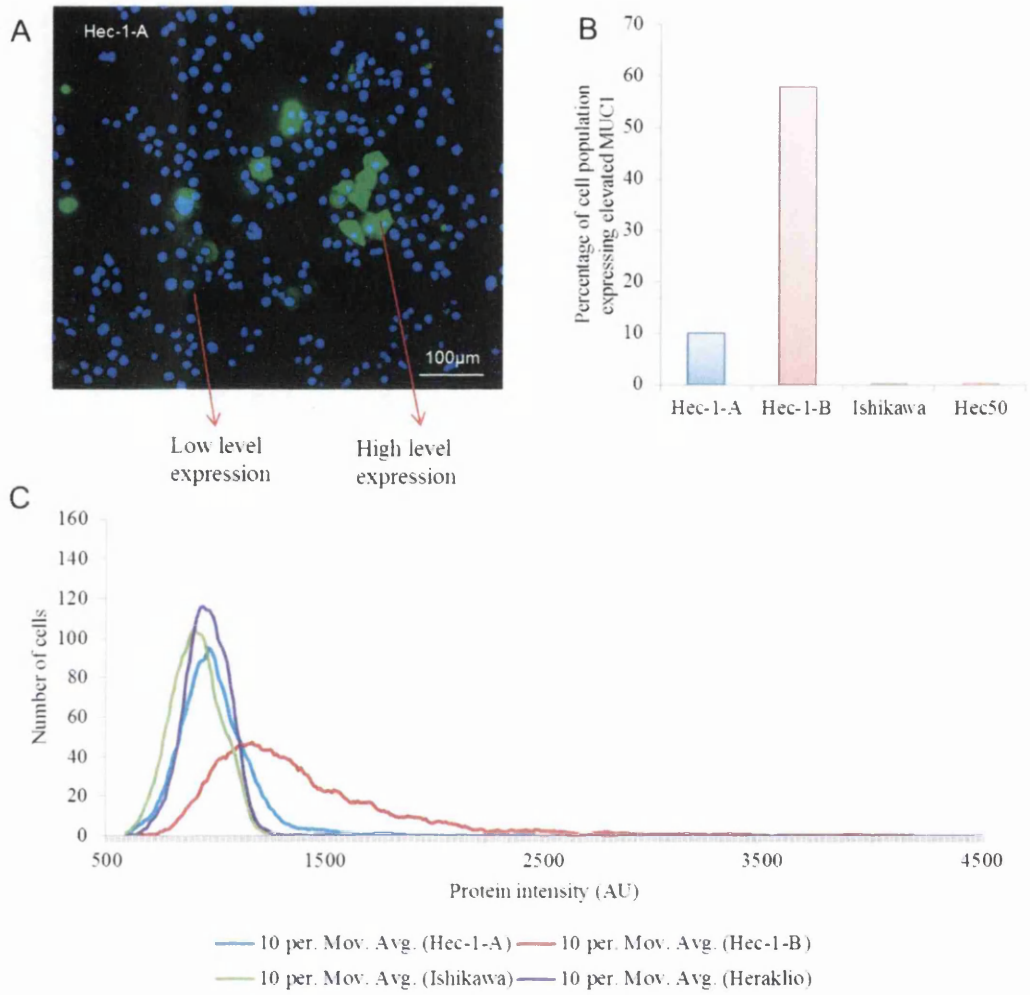

Figure 42: MUC1 protein distribution patterns in EEC cell lines. Hec-1-B cell populations display heterogeneous distributions of MUC1 protein. (A) Representative image of Hec-1-A cells showing the elevated MUC1 sub-population [MUC1 is stained green, nuclei are stained blue] (B) Bar graph shows the percentage of cells from the increased staining sub-population of each cell line. (C). Histogram shows spread of MUC1 staining intensity across model cell line populations

Cell monolayers were fixed and antibody stained for MUC1 protein. Nuclei were counterstained with DAPI. Images were acquired using automated high throughput bi-channel imaging using HCS. INCELL analyzer 2000 developer software identified approximately 3000-5000 (dependent on cell line) individual cells using a nuclear mask of the DAPI channel. Subsequent analysis in the Texas-red channel (MUC1) using a modified cytoplasmic mask assigned fluorescence value to each cell. The minimum cell number from four data sets (3062 individual cells) was used as a cap for analysis and allowed direct comparison of the cell lines. Cells were sorted into groups based on their fluorescent signal; groups consisted of a range between 500au and 4500au at intervals

of 10 allowing visualisation of the spread of data in histograms. The upper 10^{th} percentile of Hec-1-A cells was used as a benchmark to characterise high expressing cells and allowed the percentage of elevated MUC1 cells to be calculated for all the cell lines.

Figure 42A shows a representative image of Hec-1-A cells stained for MUC1 protein, and clearly demonstrates increased protein expression in a small cellular sub population. This patterning was present in Hec-1-A and Hec-1-B cell monolayers but less so in Ishikawa and Hec50.

Figure 42B shows high resolution histograms mapping the distribution of fluorescence intensity across the monolayer. The relatively narrow spread of values across the Ishikawa and Hec50 monolayers denotes a homogeneous expression profile. Hec-1-A has a somewhat flatter curve shifted to the right representing a higher proportion of high expressing cells. In sharp contrast, Hec-1-B has a very flat curve indicating a heterogeneous pattern of MUC1 protein expression across the cell population. Additionally, the extended tail reveals a residual population of cells occurring at very low frequency but exhibiting abundant MUC1 expression.

Figure 42C shows the percentage of cells expressing high levels of MUC1 protein in the cell line models. Across the Hec-1-A cell population, 10% of cells show increased MUC1 reactivity. The Hec-1-B population contained 57% of highly expressing cells. In, contrast less than 1% of Ishikawa and Hec50 cells expressed elevated MUC1. The significance of cells expressing elevated MUC1 on implantation is still unclear.

The data shown in Figure 41 and Figure 42 suggests that total MUC1 protein in Hec-1-A expression was relatively low and homogenous across the monolayer, with the exception of a small number of high expressing cells that represented 10% of the cell population. In contrast, Hec-1-B had higher total expression and a heterogeneous expression profile with a wide distribution of MUC1 intensities. These data aided understanding of the monolayer MUC1 distribution in the model cell lines, the functional implications of which are explored in chapter 5. HCS has the capability to identify subtle trends in expression that are not obvious using more traditional molecular biology techniques such as Western blot and QRTPCR that rely on pooled cell lysates for analysis.

3.28 Ovarian hormones influence MUC1 distribution patterns

3.281 E_2 and P_4 in isolation

Although MUC1 expression had been induced by P_4 and E_2 (Figure 34), the effect had been subtle and masked by variation in control samples. Despite this and to further exploit the HCS platform, protein analysis was conducted on a smaller data set of 3000-5000 cells. Cell monolayers were stained for MUC1 protein and counterstained with DAPI, images were post-processed, counted on a cell by cell basis, assigned a fluorescence value and sorted on fluorescence output.

Figure 43 shows the effect of ovarian hormones on distribution of MUC1 protein across monolayers. Histograms revealed very subtle increases in MUC1 protein after 48hrs of 100nM P_4 stimulation across endometrial monolayers in Ishikawa and Hec50 cells (Figure 43C+D) which are represented by shifts to the right on the curves. The Hec-1-B curve shifted further to the right suggesting a higher proportion of cells were expressing elevated MUC1 protein following treatment (Figure 43B). Hec-1-A showed almost no change as control (green) and P_4 treated (red) curves were almost superimposed.

The histograms show that 10nM E_2 reduced the expression of MUC1 protein in Hec-1-A. This effect was more noticeable in Ishikawa cells as denoted by the shift of the blue curve to the left. This result supported previous data (Figure 33C) that demonstrated a 3.2 fold reduction of MUC1 mRNA following stimulation with 10nM E_2 for 48hrs in Ishikawa cells. E_2 appeared to induce MUC1 expression in Hec-1-B, while in Hec50 there was no change as the two curves were superimposed. The application of HCS to the characterization of endometrial cell line models allowed the detection of subtle fluctuations in MUC1 distribution following hormone stimulation which were previously masked by variation at the mRNA level.

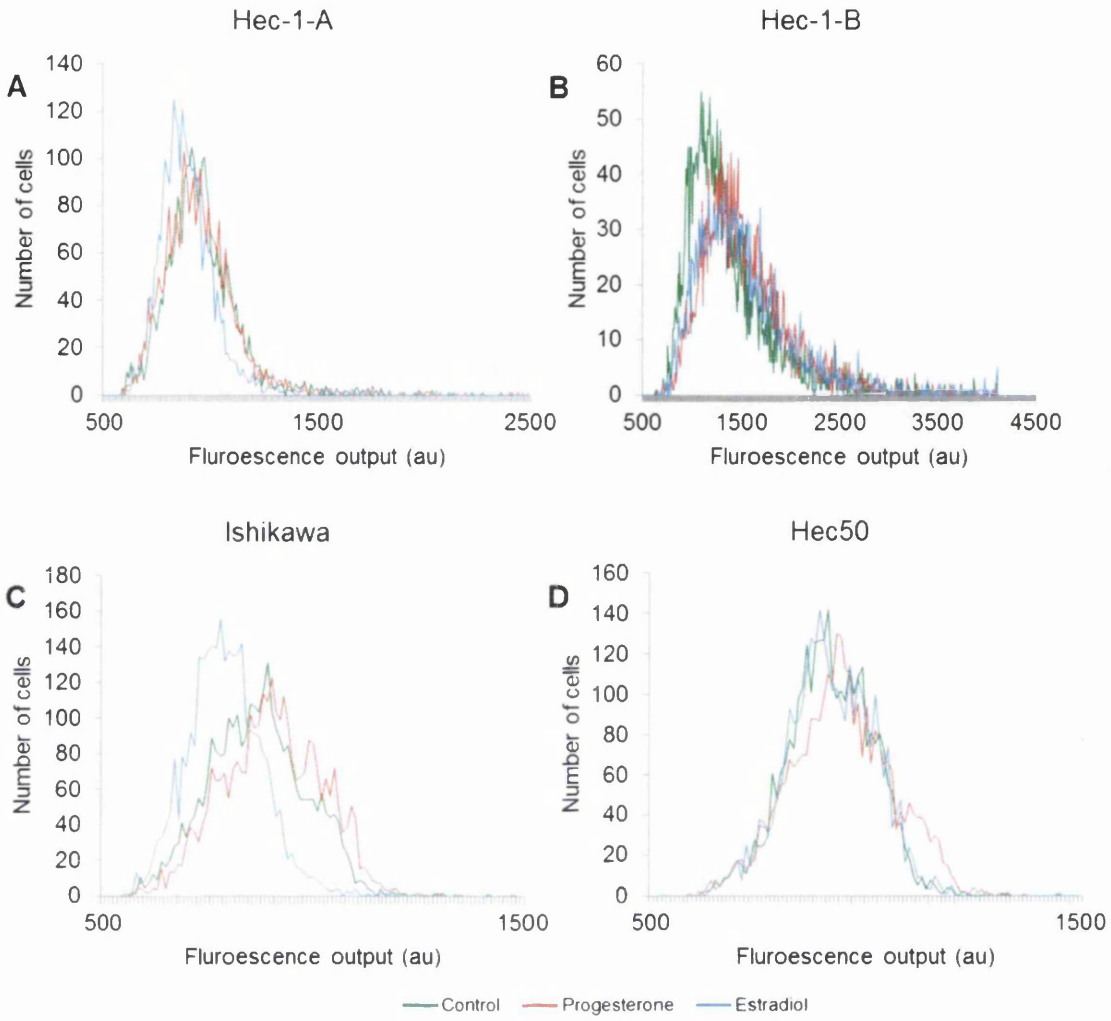

Figure 43: The effect of progesterone and estradiol on MUC1 protein distribution in EEC cell lines. (A-D) Histograms show MUC1 distribution across the population in Hec-1-A, Hec-1-B, Ishikawa and Hec50 cell monolayers following stimulation with 100nM P_4 and 10nM E_2 for 48hrs.

Cell monolayers were treated, fixed and antibody stained for MUC1 protein. Nuclei were counterstained with DAPI. Images were acquired using automated high throughput bi-channel imaging using HCS. INCELL analyzer 2000 developer software identified approximately 3000-5000 (dependent on cell line) individual cells using a nuclear mask of the DAPI channel. Subsequent analysis assigned fluorescence value to each cell. Cells were sorted into groups based on their fluorescent signal; groups consisted of a range between 500au and 4500au at intervals of 10 allowing visualisation of the spread of data in histograms. Individual cell data was grouped from 3 independent repeats.

3.282 E_2, P_4 and MPA in combination

Hec-1-A cell monolayers were primed with 10nM E_2 for 24hrs, and then treated with combinations of either 100nM P_4 or 100nM MPA without E_2 thus allowing the direct comparison of total mRNA, total protein and protein distribution analysis of cells

subject to hormone stimulation. The proportion of cells expressing high MUC1 protein was investigated to see if this changed following stimulation. Hec-1-A was a candidate for this focused investigation because previous data in this chapter (Figure 42) and published studies (Hey & Aplin 1996) have shown it to express heterogeneous patterns of MUC1 across adherent monolayers, referred to in the literature as the "mosaic" pattern (Hey & Aplin 1996).

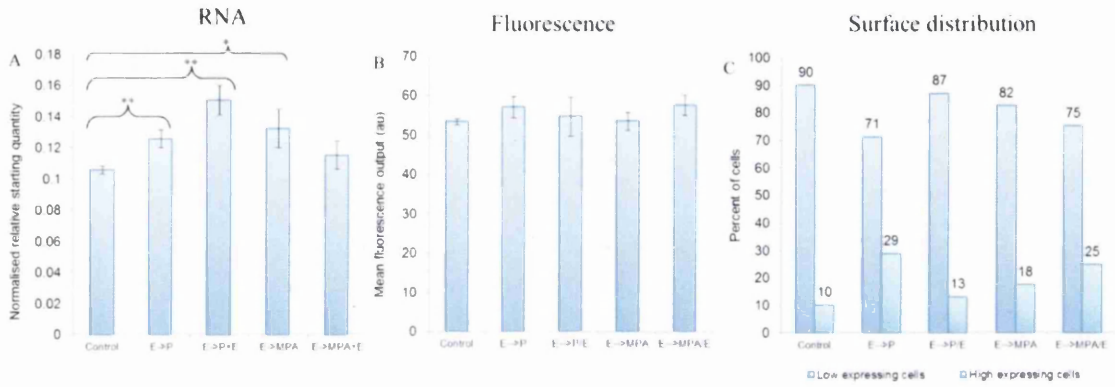

Figure 44: The effect of E_2 and P_4 on MUC1 mRNA expression, well fluorescence and cellular distribution in EEC cell lines. (A) MUC1 transcript levels, (B) MUC1 total well fluorescence output and (C) distribution of high and low expressing cells after 72hrs combined E_2 and P_4 stimulation in Hec-1-A cells.

Hec-1-A and Ishikawa cells were primed with 10nM E_2 for 24hrs then treated with 100nM P_4 or 100nM MPA for 48hrs (with and without E_2). Data shown are average from three independent experiments. (A) Values given are mean mRNA starting quantity normalised to RPL-19 ± STDEV from triplicates. Data was analysed using a two-tailed Student's T-test *p=<0.05, **p=<0.01 vs. control. (B) Values are total well fluorescence calculated from 3000 cells ± STDEV from triplicates (C) Individual cells were sorted into high and low. The 10^{th} percentile of the Hec-1-A control cell population used to determine a fluorescence value for high expressing cells.

Figure 44A shows MUC1 transcript was induced 1.18 fold after treatment with E_2 for 24hrs and then P_4 for 48hrs ($p \leq 0.01$) and 1.42 fold after treatment with E_2 for 24hrs with a combination of E_2 and P_4 for 48hrs ($p \leq 0.01$), showing that E_2 in combination with P_4 produced a heightened response. E_2 primed cells stimulated with MPA produced a significant 1.25 fold up-regulation in MUC1 ($p \leq 0.05$). The exception was E_2 primed cells followed by combined treatment of E_2 and MPA which showed no significant change in MUC1 mRNA expression. The tight grouping between replicates meant that trends were significant. Again responses to hormones were very subtle (1.18-1.42 fold) and not consistent with previous data shown in Figure 34. Despite the subtle change in

mRNA levels there were no measureable changes in total MUC1 protein expression following any of the hormone treatments (Figure 44B).

Subtle changes in percentage of cells expressing elevated MUC1 protein were observed following combined ovarian hormone stimulation (Figure 44C). The upper 10^{th} percentile of the control cells was used as the fluorescence threshold, and cells that exceeded this value were defined as high expressers. Monolayers were primed with E_2 for 24hrs, and subsequent stimulations of P_4, P_4+E_2, MPA, MPA+E_2 resulted in 29%, 13%, 18% and 25% high expressing cells out of the total cell population. All treatments increased the number of high expressers compare to control (10%) showing that the ovarian hormones can regulate the heterogeneity of the endometrial monolayer.

3.29 The effect of siRNA on MUC1 protein expression and distribution

Previous experiments (Figure 36 and Figure 37) had shown effective down-regulation of MUC1 gene expression following siRNA treatment. The effects of this modulation on MUC1 protein expression were also investigated at the protein level using HCS.

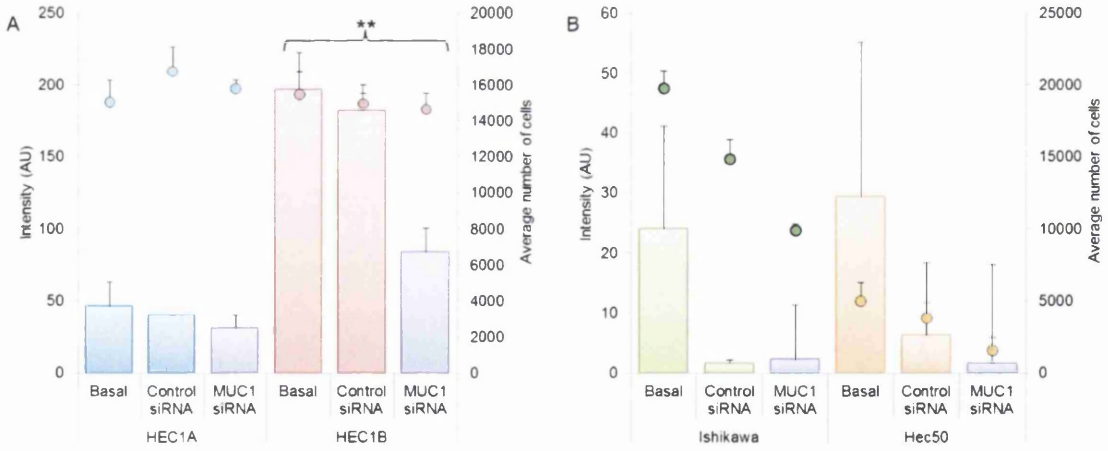

Figure 45: The effect of siRNA treatment on MUC1 protein expression in EEC cell lines.Bar graph shows cellular fluorescence output levels of MUC1 in (A) Hec-1-A (blue) + Hec-1-B (red) and (B) Ishikawa (green) + Hec50 (orange). Coloured dots represent numbers of attached cells at included in analysis.

Cells were treated with scrambled siRNA and MUC1 specific siRNA for 48hrs. They were then fixed, and antibody stained for MUC1 protein using Texas-red conjugated goat anti-Mouse secondary antibody. Cell nuclei were counter stained with DAPI. The INCELL analyzer 2000 platform imaged 30 fields at random in 2 channels. The INCELL analyzer developer software suite was used for subsequent image analysis. Bar graphs represent total well fluorescence output from all images. Each treatment had

a dedicated well negative for primary and secondary antibody and this well intensity value was deducted to account for background. Data shown is one representative repeat from two independent experiments. Values given are mean fluorescent output from adherent cell populations, normalised to background ± STDEV from triplicate wells.

Hec-1-A, Hec-1-B, Ishikawa and Hec50 cells were seeded on 96 well plates and three wells were subjected scrambled control siRNA (50nM for 48hrs), three wells treated with MUC1 siRNA (50nM for 48hrs) and three wells were left untreated.

Analysis revealed that MUC1 protein expression in Hec-1-B cells was reduced by 53.9% after 48hr MUC1 siRNA treatment compared to scrambled siRNA ($p \leq 0.001$) (Figure 45A). Hec-1-A cells showed a trend towards reduced MUC1 protein expression of 22.6%, but this result was not significant.

The data in Figure 45B demonstrates that the treatment with both control and MUC1 siRNA induced cell death in Ishikawa and Hec50 and their use was not continued for future experiments. This highlights the importance of cell viability assay during siRNA knockdown experiments. There was loss of cell viability in the scrambled siRNA control which suggests that the lipofectamine transfection reagent negatively affected cell viability in these two cell lines.

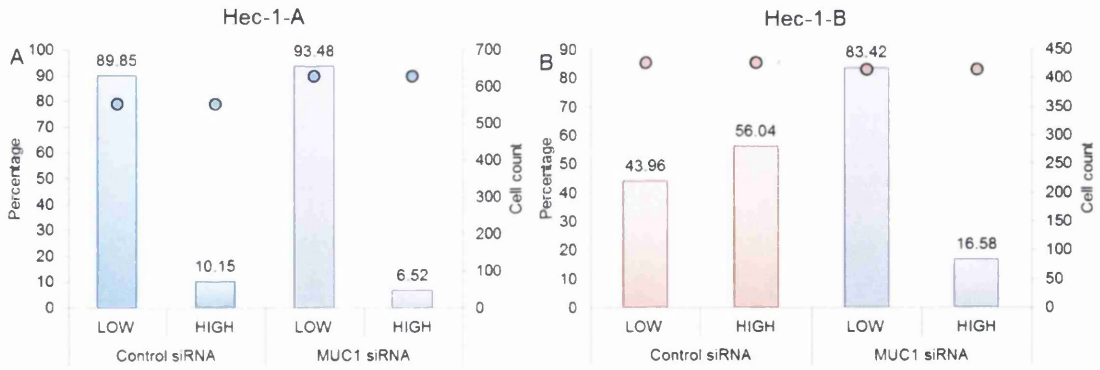

Figure 46: The effect of siRNA treatment on the MUC1 protein distribution in Hec-1-A and Hec-1-B cells. MUC1 siRNA reduces the number of high expressing cells in (A) Hec-1-A and (B) Hec-1-B cell models. Individual cells were sorted into high and low. The 10th percentile of the Hec-1-A control cell population used to determine a fluorescence value for high expressing cells.

Figure 46 shows the percent of cells expressing high MUC1 protein decreases from 10.15% to 6.52% after 48hrs MUC1 siRNA treatment. In the Hec-1-B cell line the

percentage of high expressing cells was reduced from 56.04% to 16.58% demonstrating that the siRNA reduced the percentage of high expressing cells.

3.3 Discussion

The expression of MUC1, MUC4 and MUC16 mRNA has been interrogated in the selected cell lines. Hec-1-B cells expressed relatively high levels of MUC1 mRNA, Hec-1-A expressed relatively high levels of MUC4 and Ishikawa expressed the highest levels of MUC16. The varying expression patterns of mucins in these three EEC cell lines provides an opportunity to study the role of mucins in implantation biology. The cell lines were screened for MUC4 and MUC16 because of the important roles they play in the endometrium (Gipson et al. 2008; Perez & Gipson 2008; Albrecht & Carraway 2011). However, MUC1 is of particular interest because clinical data has shown MUC1 to be up-regulated during the secretory phase (Song et al. 2012), able to present binding epitopes to the embryo (Margarit et al. 2009) and linked to infertility (Margarit et al. 2010; A. W. Horne et al. 2001).

The response of endometrial mucins to P_4 and E_2 in EEC cell lines was shown be inconsistent at the mRNA level. Healthy endometrial tissue has been shown to express a range of nuclear receptors such as estrogen receptor (ER) (Critchley 2002), progesterone receptor (PR) (Niklaus et al. 2007), androgen receptor (AR) (Slayden et al. 2001) and human chorionic gonadotrophin receptor (CG) (Zimmermann et al. 2012), that meditate the actions of their respective hormones, and elicit morphological changes across the endometrium during the menstrual cycle. P_4 serum concentration increases during the late secretory phase and promotes expression of molecules that facilitate embryo implantation. Indeed, expression of MUC1 in human endometrium is high during this period and experiments using the PR antagonist RU486 have resulted in MUC1 inhibition suggesting it is progesterone driven (Meng et al. 2009). The cell lines investigated were shown to express PR mRNA but treatment with P_4 had no effect and in combination with E_2 only slightly increased MUC1 expression in the Hec-1-A cell line. Progesterone signalling is mediated through two receptor isoforms, PR-A and PR-B (Wen et al. 1994) which are encoded by the same gene but have different promoters. PR-B is the stronger transcriptional activator in most cell types, and PR-A acts as a dominant negative repressor for PRB (Vegeto et al. 1993). It has been shown using transfected PR isoforms in Hec-1-A cells that PR-B stimulates MUC1 expression and

that PR-A acts as an antagonist for MUC1 expression (Brayman et al. 2006). Additionally, PR-B becomes the dominant receptor during the secretory phase (Arnett-Mansfield 2004) suggesting that it is likely to mediate the effect of progesterone during the receptive period. The ratio of PR-A:PR-B in endometrial cell lines is the subject of conflicting reports, mRNA data has shown that Hec-1-A cells express a high ratio of PR-A:PR-B (Harduf et al. 2009), whilst others have reported no PR-B protein expression in Hec-1-A or Hec-1-B and very low levels in Ishikawa (Neubauer et al. 2011). It is possible that the cell lines are expressing a high PR-A:PR-B ratio resulting in minimal activation of MUC1 transcription. Moreover, P_4 is able to suppress expression of PR, and the relatively high concentrations of P_4 (100nM) administered may have contributed to PR reduction.

When Hec-1-A cells were primed with E_2 and then treated with E_2 and P_4/MPA in combination there was a modest but significant increase in MUC1 expression at the mRNA level. Total protein showed no significant increase, but HCS analysis showed that the percentage of high MUC1 expressing cells increased with the combination treatments. E_2 signalling is mediated through two forms of estrogen receptor, ERα and ERβ which are encoded by two separate genes, ESR1 and ESR2. It has been established for some years that E_2 increases synthesis of PR while degradation remains constant (Nardulli et al. 1988) and whilst there are no ERE's in the promoter regions of PR-A or PR-B, ER is able to exert transcriptional changes through interaction with other DNA binding proteins such as SP1 (Petz & Nardulli 2000). Treatment with 10-20nM E_2 for 24hrs has been shown to increase PR mRNA (Lee & Gorski 1996), so it is plausible to suggest that administration of 10nM E_2 for 24hrs prior to 48hr incubation with P_4/MPA and E_2 up-regulated PR and increased the potency of the P_4 response in terms of increased MUC1 expression.

Experiments performed using a transfected MUC1 promoter to study regulation of the protein have used Hec-1-A (Wang et al. 2010; Brayman et al. 2007), Hec-1-B (Horne et al. 2006) to create null and constitutive models of MUC1 expression. In contrast we used Hec-1-B as a natural constitutive high expressing model for MUC1, and employed siRNA to down-regulate expression. This technique provided a valuable molecular tool with which to control mucin gene expression in endometrial cell lines. Monolayers of Hec-1-B cells are also ideal for the study of the role of mucins and specifically because

Hec-1-B does not express MUC4 or MUC16. Moreover, siRNA treatment reduced MUC1 mRNA levels by 96.1% and protein expression by 53.9%.

Using HCS to investigate pattern of adhesion proteins in endometrial cells showed that the heterogeneity of MUC1 expression across an endometrial monolayer can be modified with ovarian hormones. MUC1 is thought to be a regulator of implantation, and may exert some quality control over the potential embryos through mechanical trapping of the embryo and affinity for trophoblast localised molecules such as L-selectin. Hec-1-A and Hec-1-B cell lines in combination with post-transcriptional gene silencing represent a suitable model required to further interrogate the non-specific and specific roles played by MUC1 during embryo implantation

Chapter 4 Nano-mechanical mapping of a model endometrial cell surface

4.1 Introduction

The mechanical and molecular adhesion of the embryo to the uterine wall requires a plethora of adhesive markers that contribute to the endometrial glycocalyx. These molecules are regulated through the menstrual cycle by the actions of E_2 and P_4 (Young 2013). The apposition phase of implantation is likely to involve initial mechanical impedance when the embryo first encounters the membrane bound mucus layer and becomes trapped in a "mucin cloud" (Figure 47).

This membrane bound mucus layer typically consists the adhesive mucus layer (AML) located next to the cell surface and the apical luminal mucus layer (LML). These layers function as a barrier to non-specific nano-particles such as viruses, and protect apical membranes of endometrial epithelia from enzymatic and bacterial assault (DeSouza et al. 1999). The AML principally consists of large glycosylated mucins such as MUC1, MUC4 and MUC16 that are tethered to the cell membrane in a dynamic fashion. This system is dynamic because mucins are constantly secreted and when subjected to frictional forces large mucin proteins can detach from the apical surface and envelop an opposing body, a process mediated by the SEA and EGF domains. The LML is comprised of smaller mucins (Lai et al. 2009; Hattrup & Gendler 2008) such as MUC5A and MUC5B (Thornton et al. 2008) and is not thought to contribute significantly to the mucus layer because it is of much lower density (Gniewek & Kolinski 2012).

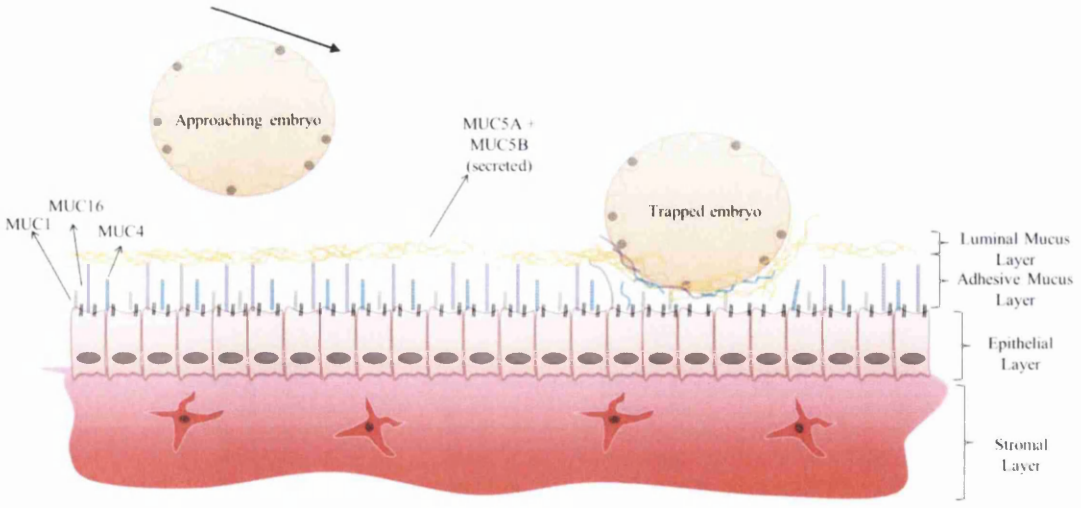

Figure 47: The composition of the epithelial mucus layers. The endometrial layer of the endometrium is protected by a membrane bound mucus layer. Comprised of two sub-layers; the adhesive mucus layer and the luminal mucus layer may act to mechanically

retard the embryo as it encounters the endometrial glycocalyx allowing specific adhesion to occur.

MUC1 is abundant in the AML protecting endometrial epithelia (Hattrup & Gendler 2008) but its precise adhesive contribution is not fully understood and elucidating the true function has been slow. Progress has been hampered by conflicting studies in the literature suggesting both adhesive (Geng et al. 2013; Costa et al. 2011) and anti-adhesive (Wesseling et al. 1995) roles for the protein. Fluorescence imaging of Hec-1-A monolayers co-cultured with mouse embryos show a halo of MUC1 reduction surrounding the embryo suggesting local clearance of MUC1 to be a requisite for implantation (Meseguer et al. 2001). Moreover, MUC1 does not correlate with pinopods, small mushroom-like projections positively associated with embryo adhesion (Horne et al. 2005). However, shorter structural MUC1 isoforms (resulting from a reduced number of tandem repeats in the extracellular domain) correlate positively with unexplained infertility (Horne et al. 2001) and decreased expression with increased implantation failure (Horne et al. 2005), which both suggest the expression of fully formed MUC1 protein is required for fertility. The carbohydrate moieties that decorate MUC1 are believed to be important in embryo recognition (Margarit et al. 2009) and this hypothesis is tested extensively in chapter 5.

In this chapter the mechanical properties of MUC1 endometrial were investigated using new quantitative AFM mode. Two avenues of nano-scale investigation are pursued; an exploratory study of fixed endometrial cell monolayers, and a complete investigation on their live cell counterparts under near physiological conditions.

Peak force quantitative nano-mechanical mapping (PFQNM) enables imaging at speeds comparable with AC mode but allows extraction of quantitative information (e.g. adhesion data) at very high resolution. PFQNM has been used to quantify forces on various living systems such as yeast (Alsteens et al. 2012), human epidermal (Heu et al. 2012) and neuronal (Berquand et al. 2012) cell lines. At the time of writing PFQNM has never been attempted on endometrial monolayers so a preliminary examination was undertaken on fixed Hec-1-A and Hec-1-B monolayers to optimise the technique.

Evidence suggests MUC1 is an important a regulator of implantation (Carson et al. 2006; Margarit et al. 2010). Nevertheless a paradox exists in which a protein described as anti-adhesive protein is required for successful implantation. My hypothesis is that

the apposition phase of implantation is dependent on two sequential interactions; the first is a non-specific trapping of the embryo in the AML, which retards it sufficiently to allow a second specific tethering to the uterine epithelium via specific molecular recognition events. The first part of this hypothesis is tested in this chapter and it is believed that high levels of MUC1 protein will increase adhesion across the monolayer. This notion is supported by insights into MUC1 structure and adhesive characteristics on non-endometrial epithelia in the literature (Kim & Lillehoj 2008; Albrecht & Carraway 2011). Moreover, the WOI is a defined period of high endometrial adhesion that coincides with a progesterone induced increase of MUC1 protein. The aim of this chapter is to assess the nano-mechanical properties of the endometrial cell surface and correlate these with MUC1 expression using the endometrial epithelial surface model developed in chapter 3.

4.2 Results

In order to understand the role of MUC1 and MUC16, cell monolayers were scanned using quantitative AFM. PFQNM scans consisted of large areas (up to 150μm^2) of monolayer encompassing multiple cells and allowed nano-mechanical quantification of the monolayer as a single entity. Fixing cells provides mechanical stability to the cells, which in turn enables them to withstand the perturbations of the scanning probe revealing ultra-fine structural cell surface detail (Francis et al. 2009). The fixed cell study revealed the cell surface topology and optimised examination of live cell nano-mechanical properties. Fixed endometrial epithelial cells are laid out in the form of 3 dimensional maps with accompanying bar graphs showing quantitative data extracted using bearing analysis.

4.21 High resolution quantitative mapping of the endometrial monolayer

Cell monolayers were fixed and imaged using PFQNM. These images contained a reduced number of cells compared to fluorescence microscopy techniques used in chapter 3 (Figure 48A) but benefited from increased resolution revealing details of the membrane ultra-structure from which nano-mechanical data could be obtained (Figure 48B+C).

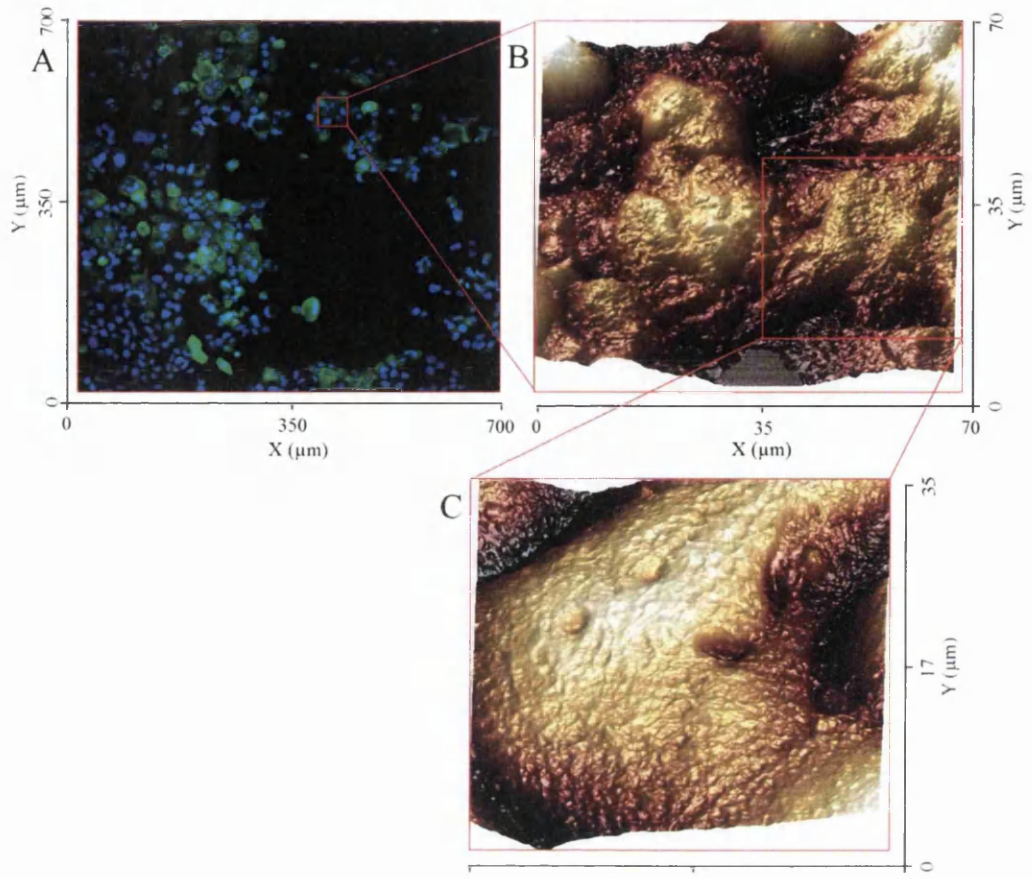

Figure 48: The transition from low magnification qualitative imaging to high magnification quantitative imaging using the atomic force microscope. Hec-1-A cells were grown until 90% confluence and fixed using paraformaldehyde. (A) Medium magnification immunofluorescence images of endometrial cells stained with anti-MUC1 mAb and counterstained with DAPI. (B) The AFM was used to image regions of the endometrial monolayer. (C) Higher magnification captured single cells.

4.22 Mapping the fixed cell monolayer

Studies from our group have identified variations in MUC1 expression between fertile (high) and infertile (low) pathology (Margarit et al. 2010). Previous studies from this group had correlated MUC1 expression with increased surface roughness and cell height in Hec-1-A and Ishikawa endometrial cell lines (Francis et al. 2009). This highlighted that MUC1 could influence nanoscale surface properties. In order to assess nano-scale differences between Hec-1-A and Hec-1-B, cells were grown in glass dishes until 90-100% confluent and fixed using paraformaldehyde. The fixed cells were quantitatively imaged using PFQNM in three separate areas across the monolayer. The cantilever deflection sensitivity was calculated buy ramping into hard surface (glass) in force spectroscopy mode, while the spring constant was calibrated using the thermal tune method, thus ensuring PFQNM was fully quantitative. Data was analysed using

Nanoscope analysis software using the "bearing analysis" function. Each region of cell monolayer was assessed for topography, adhesion, deformation and dissipation and stiffness. Nano-mechanical properties are visualised in 3-dimensional maps generated using Nanoscope analysis.

4.221 Topography and surface roughness

Hec-1-A and Hec-1-B were analysed for cell height and surface roughness using the AFM. Three regions of Hec-1-A were chosen at random across a monolayer and imaged using PFQNM. These consisted of area A1 ($40\mu m^2$), area A2 ($50\mu m^2$) and area A3 ($70\mu m^2$) having average heights of 3.8μm, 4.3μm and 5.1μm respectively. Combined average height of Hec-1-A monolayers was 4.4 +/- 0.65μm. Three areas of Hec-1-B were imaged: area B1 ($30\mu m^2$), area B2 ($30\mu m^2$) and area B3 ($50\mu m^2$) having average heights of 3.7μm, 4.3μm and 4.6μm respectively. Combined average height of Hec-1-B monolayers was 4.2+/-0.46μm.

Topographical maps of Hec-1-A and Hec-1-B and bar graphs reveal no significant differences in height between the two fixed cell monolayers (Figure 49). Roughness had been previously linked with MUC1 expression in these cell lines (Francis et al. 2009) and initial visual observations of topographical images suggested that Hec-1B cells had a rougher surface when compared to Hec-1A. In order to assess if MUC1 expression influenced the surface roughness of the endometrium thirty $3\mu m^2$ areas were measured for Ra from each cell line, ten areas were sampled from each area (A1-A3, B1-B3). Average roughness measurements from Hec-1-A and Hec-1-B had a mean Ra of 41.04nm and 45.68nm respectively (Figure 49D). Although Hec-1-B was slightly rougher than Hec-1-A the Kruskal-Wallis statistical test did not show this to be significant.

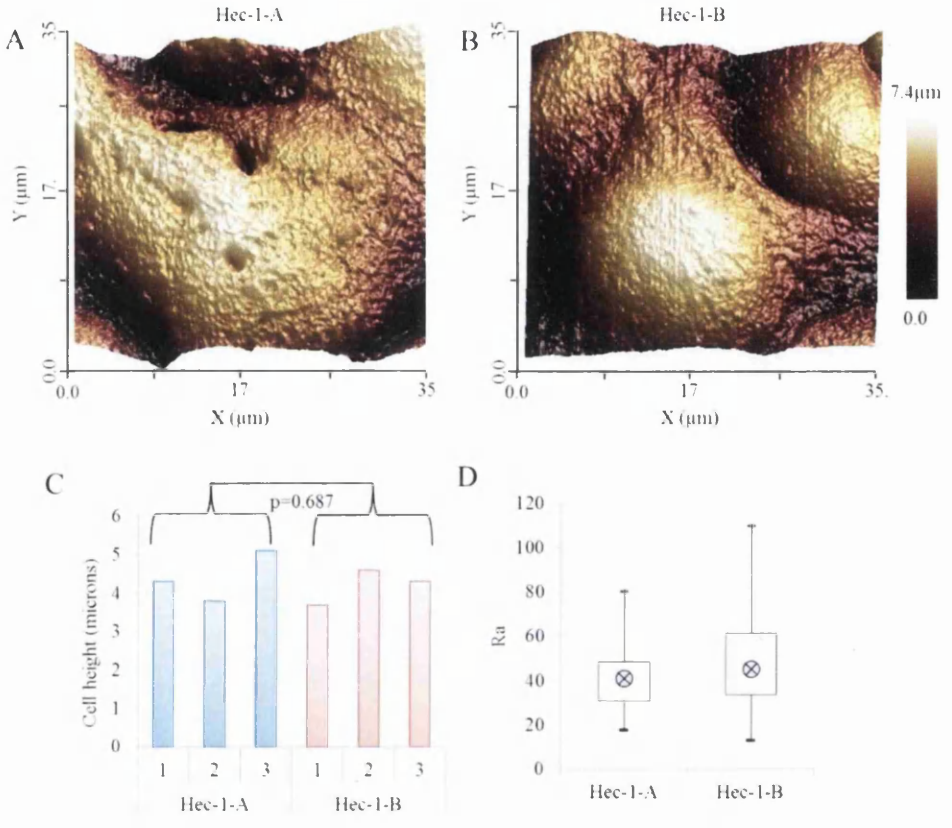

Figure 49: Topographical and surface roughness measurements of Hec-1-A and Hec-1B cells. Adherent Hec-1A and Hec-1B endometrial epithelial cells were grown to 80-100% confluence, fixed and imaged. Two representative topographical maps are shown. Each map shows~ 30 μm^2 the cell surface of (A) Hec-1-A and (B) Hec-1-B cell monolayers. Each map is generated from 262144 sample points (C) topographical data for three distant and distinct regions across the monolayer for both Hec-1-A and Hec-1-B Data was analysed using a two-tailed Student's t-test *p≤0.05, **p≤0.01, ***p≤0.001. (D) Surface roughness readings were taken at random from 30x 3μm^2 areas randomly selected from the whole cell surface of Hec-1-A and Hec-1-B cells. Ra readings (nm) are presented here summarized as boxplots (mean ⊗). The Kruskal-Wallis test was used to test for statistical significance at the 95% confidence level with a p value <0.05. Differences were not shown to be significant (P=0.145)

Height and surface roughness measurements show no significant differences between Hec-1-A and Hec-1-B. This suggests that MUC1 (strongly expressed by Hec-1-B) and MUC16 (expressed in Hec-1-A, not expressed in Hec-1-B) may contribute equally to the endometrial glycocalyx height.

4.222 Stiffness

When imaging soft surfaces such as cells the probe is able to indent far into the substrate. As this is past the tip apex, a spherical model for modulus is no longer suitable, so conical model (Sneddon) was used to calculate the elastic modulus of the

endometrial cell. By default, Peak Force QNM generates data in the elastic modulus channel using the DMT model for modulus (a spherical model suited to hard surfaces) and at the time of experiment did not allow for other models of elasticity. To account for this a high speed data capture (HSDC) file was generated for areas A1-A3 and B1-B3, totalling 6 HSDC files. Generating a HSDC file involved increasing the resolution from 128 samples/ line to 5000 samples/line, and then scanning a single high resolution line across the centre of the image (Figure 50).

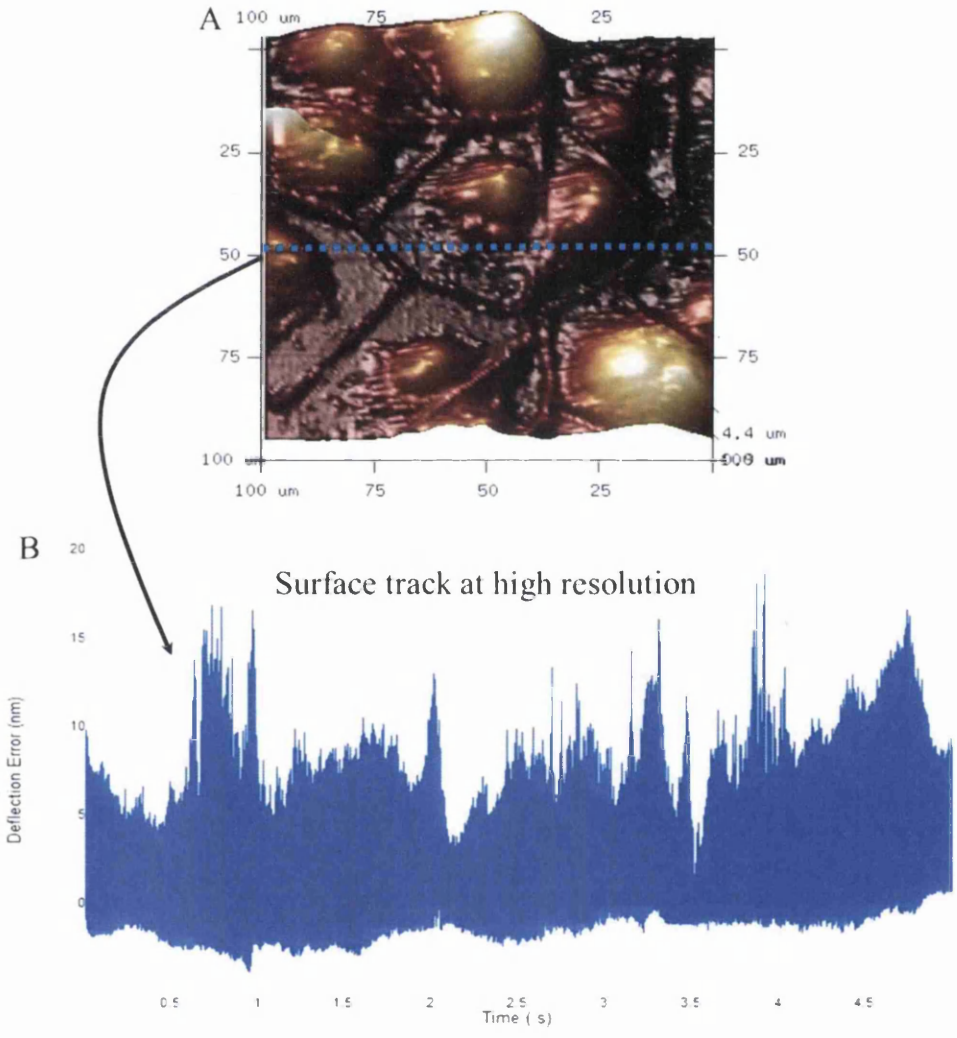

Figure 50: HSDC transect line across the monolayer. A HSDC file is generated for every monolayer image. (A) After imaging a very high resolution line is scanned across the body of the imaging frame. (B) High resolution scan profile showing track across cell monolayer against time. Force curves contained within this file can be exported for analysis using proprietary software.

Stiffness was calculated from HSDC file force curves, peripheral regions that did not traverse the cell were excluded from analysis. After excluding these force curves,

number of data points used to calculate stiffness was typically 4500-5000. Hec-1-A displayed an average stiffness of 53KPa, 74 KPa and 128 KPa for each HSDC (Figure 51C). Across all areas stiffness of Hec-1-A monolayers was 85 +/- 39KPa.

Hec-1-B areas displayed combined stiffness of 99KPa, 86KPa, and 123KPa respectively. Across all areas, stiffness of Hec-1-B monolayers was 103 +/- 18KPa. The stiffness profile of Hec-1B was higher than Hec-1A, although this trend was not shown to be significant (p=0.516), possibly due to the high degree of variation over the Hec-1-A areas. The stiffness of both cell lines displayed a high degree of inter-cellular variation. This ranged from 53 KPa to 128 KPa in Hec-1A and 99 KPa to 123 KPa in Hec-1B.

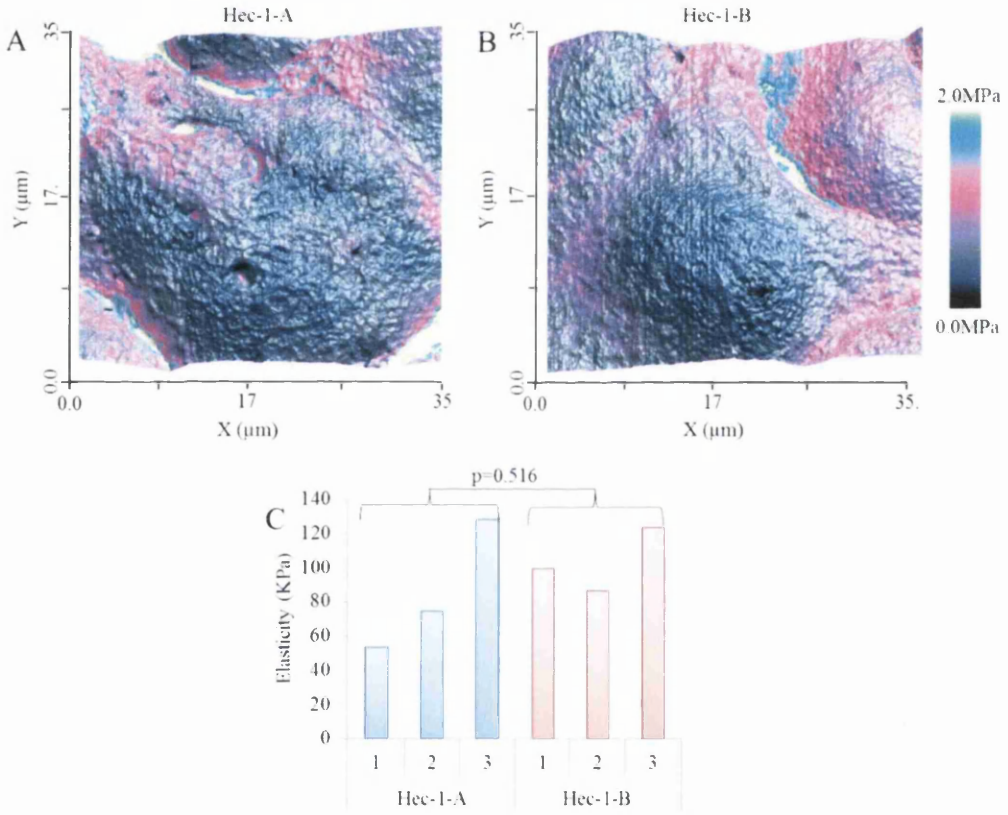

Figure 51: Stiffness measurements of Hec-1-A and Hec-1B cells. Hec-1A and Hec-1B cells were grown to 80-100% confluence, fixed and imaged. (A+B) Two representative topographical maps with elasticity overlay are shown (DMT). Each map shows 35 μm^2 the cell surface of (A) Hec-1-A and (B) Hec-1-B cell monolayers. Each map is generated from 262144 sample points. The HSDC feature was used to generate one very high resolution (5000 data point) scan line transecting the image for Hec-1A (A) and Hec-1B (B). (C) Force curves that occurred over the cell body were analysed. Stiffness data was generated from three HSDC scan lines from three different cells across the monolayer for both Hec-1-A and Hec-1-B.

4.223 Deformation

The AFM tip exerts a force on the sample surface which can range from 10^{-7} to 10^{-11} N, depending on imaging conditions. This force causes nano-indentation which is described as 'nN force causing nm indentation on nm^2 contact area' (Weisenhorn 1993), which induces sample deformation. Areas A1-A3 were assessed for surface deformation, having average deformation of 191nm, 156nm and 223nm respectively (Figure 52C). Across all areas, deformation of Hec-1-A monolayers was 190 +/- 34nm. Areas B1-B3 displayed average deformation of 145nm, 208nm and 182nm respectively (Figure 52C). Across all areas, deformation of Hec-1-B monolayers was 178 +/- 32nm. There were no significant differences between the two data sets (p=0.684). Membrane deformation is inversely proportional to membrane stiffness meaning a stiffer surface is less likely to deform under the applied force generated during tapping.

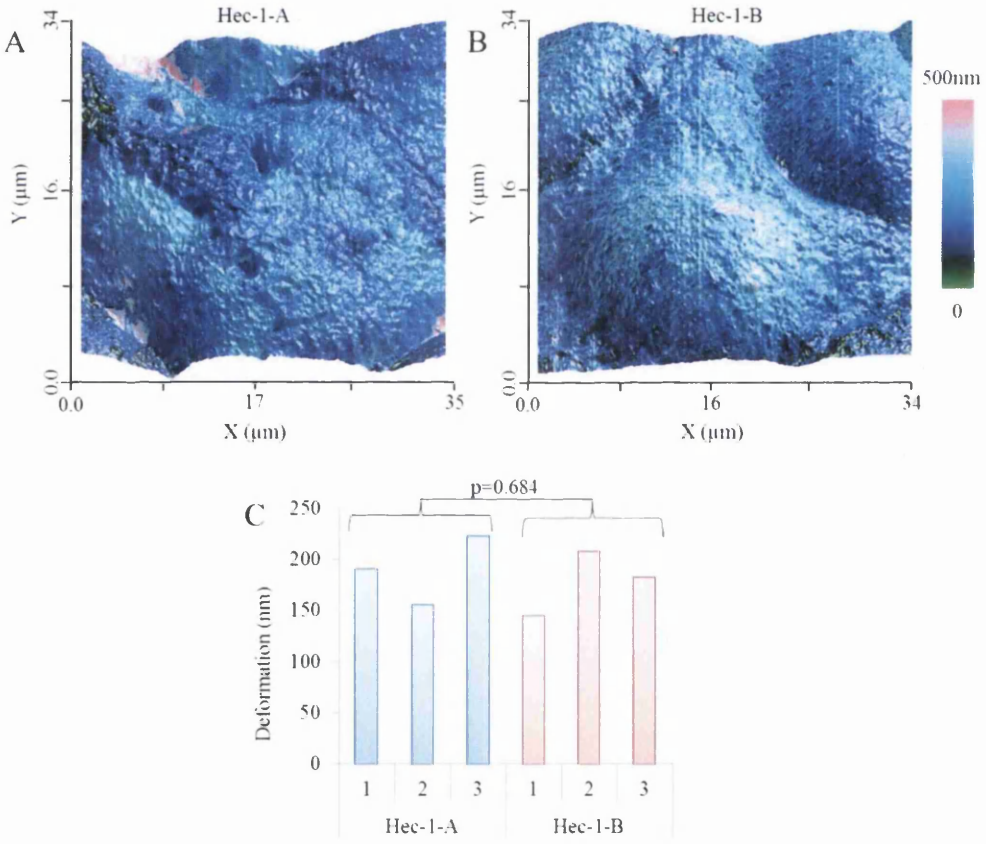

Figure 52: Deformation measurements of Hec-1-A and Hec-1B cells. Hec-1A and Hec-1B endometrial epithelial cells were grown to 80-100% confluence, fixed and imaged. (A+B) Examples of two representative topographical maps with deformation overlay encompassing approximately $30\mu m^2$ of Hec-1A and Hec-1B cell monolayers. Each map is generated from 262144 sample points. (C) Deformation data was generated for three distant regions across the monolayer for both Hec-1-A and Hec-1-B.

4.224 Dissipation

Changes in cell deformation can be related to the cytoskeletal changes (Müller et al. 2009), loss of microtubules or actin filaments and can lead to lower cell stiffness and higher deformation (Suresh 2007). AFM is often used to determine cell stiffness and relate this to altered cell physiology. However, the cell membrane is not a homogenous surface and during force spectroscopy experiments there exists a hysteresis between the approach and retraction curve indicating a dissipation of energy. It is possible to calculate the energy dissipated at the tip-sample junction by taking advantage of the observed steady-state motion of the cantilever during tapping, and calculating the energy inputs and outputs of the system. The phase of the oscillating cantilever can be directly related to the energy loss in the tip–sample junction, and a numerical value for the power being lost can be extracted (Cleveland et al. 1998). This has been recently shown using human skin fibroblast cells (Klymenko et al. 2009).

Hec-1-A areas (A1-A3) displayed average dissipation of 3.1 KeV, 2.5 KeV and 1.8 KeV (Figure 53C). Across all areas, energy dissipation of Hec-1-A monolayers was 2.7 +/- 0.65 KeV. Energy dissipation across the Hec-1-B areas (B1-B3) was shown to be 2.5 KeV, 4.2 KeV and 4.9 KeV respectively (Figure 53C). Across all areas, energy dissipation of Hec-1-B monolayers was 3.8 +/- 1.2nm. Average energy dissipation between the AFM tip and the surface of Hec-1A was 2.5 KeV while Hec-1B 3.9 KeV, however this trend was not shown to be a significant difference between the two data sets ($p=0.157$). Although there was no significant difference in energy dissipation between both cell types a strong trend existed between dissipation and cell height. Energy dissipation 3D maps show indicate a correlation with dissipation and cell boundaries, this could be related to topographical features or localised expression of adhesive molecules in this region.

4.225 Adhesion

MUC1 is an adhesion protein with relevance in implantation and is believed to contribute significantly to the AML. The adhesive characteristics of the endometrial glycocalyx may provide the mechanical environment required to trap the embryo and are likely to be heavily influenced by mucins

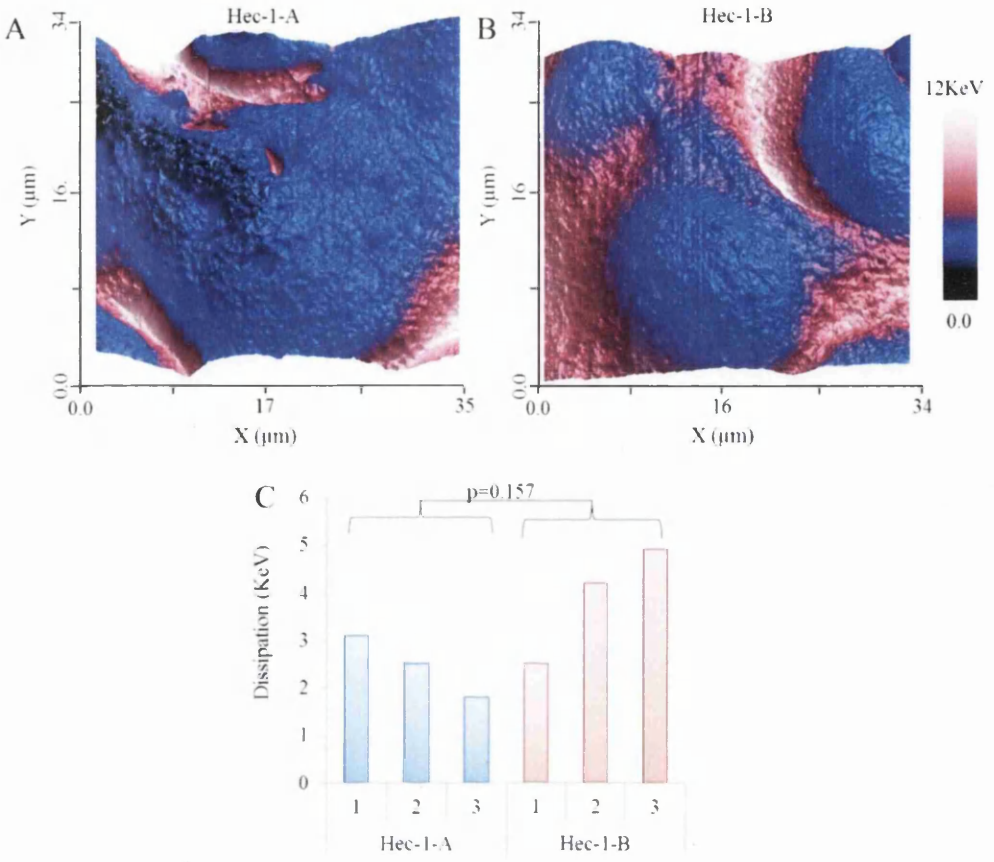

Figure 53: Energy dissipation measurements of Hec-1-A and Hec-1B cells. Hec-1A and Hec-1B were grown to 80-100% confluence, fixed and imaged (A+B) Two representative topographical maps with dissipation overlay encompassing approximately 30µm^2 of Hec-1A (A) and Hec-1B (B) cell monolayers. Each map is generated from 262144 sample points. (C) Deformation data was generated for three distant regions across the monolayer for Hec-1-A and Hec-1-B.

Hec-1-A and Hec-1-B cell lines were used as models for high and low MUC1 expression and positive and negative MUC16 expression. The three Hec-1-A areas (A1-A3) displayed adhesion of 181 pN, 142 pN and 98 pN respectively (Figure 54C). Across all areas, adhesion of Hec-1-A monolayers was 140 +/- 42 pN. Hec-1-B areas (B1-B3) showed average adhesion measurements of 207 pN, 215 pN and 243 pN respectively (Figure 54C). Across all areas, adhesion of Hec-1-B monolayers was 221 +/- 19 pN. The average adhesion for Hec-1B cell monolayers was 221pN while Hec-1A was 140pN which indicated a significant difference (p=0.036). In contrast to other nano-mechanical properties measured using PFQNM the differences in adhesion were marked. There was a high degree of variation across the Hec-1A monolayer, (98 to 181 pN). In contrast, Hec-1-B areas were similar, 207, 215 and 243 pN (Figure 54C). 3D topographical maps with adhesion overlay revealed that depressions surrounded by high

sides were more adhesive in both cell types. In the context of the monolayer this refers to the boundary between cells. (Figure 54A+B). There appears to be a spatial association between adhesion and energy dissipation across the monolayer. This could be due to a localised elevation of adhesive molecule expression at certain regions such as E-cadherin expression at intercellular junctions. The differences between the cell types could be related to expression differences of adhesion proteins on the apical membrane such as MUC1 protein.

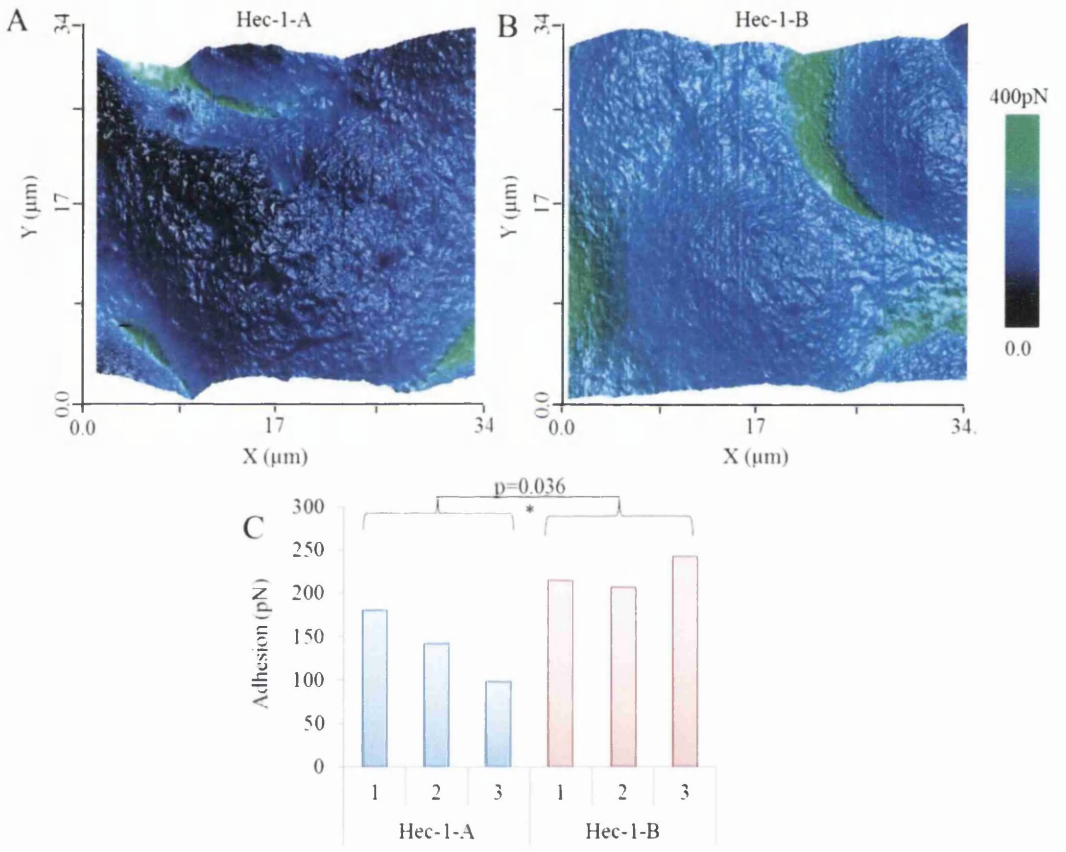

Figure 54: Adhesion measurements of Hec-1-A and Hec-1B cells. Hec-1A and Hec-1B endometrial epithelial cells were grown to 80-100% confluence, fixed and imaged. (A+B) Two representative topographical maps with adhesion overlay encompassing approximately 30µm^2 of Hec-1A (A) and Hec-1B (B) cell monolayers. Each map is generated from 262144 sample points. (C) Adhesion data was generated for three distant regions across the monolayer for both Hec-1-A and Hec-1-B.

The adhesion data implicates MUC1 as a dominant contributor to the adhesive characteristics of the cell glycocalyx because the Hec-1-B, a high MUC1 expresser is the most adhesive and does not express MUC4 or MUC16. However, Hec-1-A is not

without adhesion suggesting that MUC4 or MUC16 could be contributing as well as the residual MUC1 expressed on Hec-1-A cell monolayers.

4.226 Combined fixed cell properties

The nano-mechanical properties of fixed Hec-1-A and Hec-1-B cells revealed that topography, stiffness, dissipation and deformation were not significantly different between the two cell types (Figure 55). Adhesion, the notable exception, was significantly higher in Hec-1-B measuring around 220pN compared to 140pN of Hec-1-A ($p=0.036$). It is plausible to suggest that adhesion of the monolayer strongly influences endometrial receptivity during the implantation window. The data shows that adhesion is 1.57 fold higher in Hec-1-B cells relative to Hec-1-A which corresponds well with the elevated MUC1 protein levels in Hec-1-B relative to Hec-1-A (chapter 3:Figure 41).

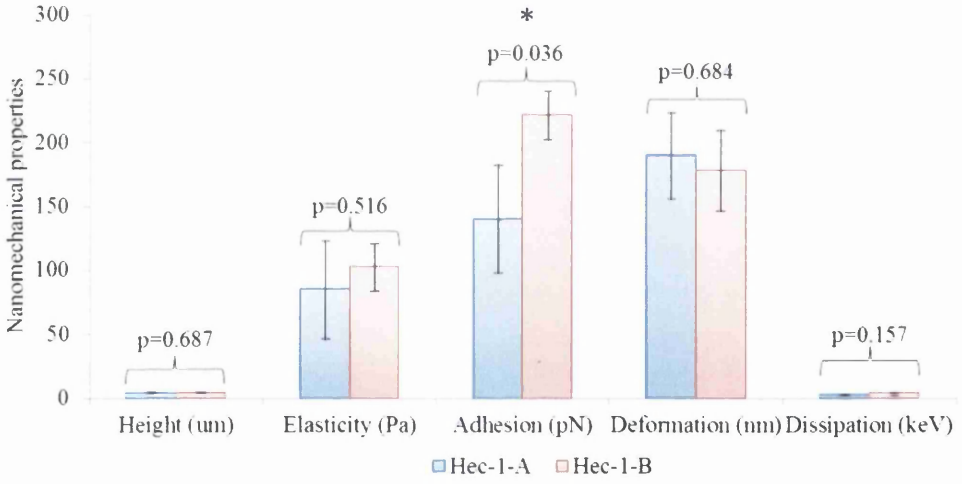

Figure 55: Combined nano-mechanical measurements of fixed Hec-1-A and Hec-1B cell monolayers. When compiled, the surface properties of the Hec-1 cell lines highlighted a divergence in the adhesive profile of the two cell lines. Data was analysed using a two-tailed Student's T-test *$p\leq0.05$, **$p\leq0.01$, ***$p\leq0.001$ vs. control.

The data obtained in this initial study of a small number of fixed cells revealed a significant difference in adhesion between Hec-1-A and Hec-1-B and demonstrated the utility of PFQNM. Experiments were therefore extended to live cell monolayers to enable a better insight into the adhesive function of MUC1.

4.23 Mapping the live cell monolayer

AFM imaging of living cells is challenging, and mammalian cells are sometimes very sensitive to the environment and physical contact. In order to avoid the deformation of cells by contact with an AFM tip during scanning, a non-contact mode of operation should be used. Nonetheless, the soft membrane means lateral resolution is reduced and the cells have to be maintained at physiological conditions for the duration of the experiment. Most AFM systems have the ability to image living cells in liquid, the living samples are covered in growth medium and the probe lowered into the liquid to scan the cell surface. The laser beam is still able to penetrate the liquid to detect changes in the probe position due to surface features. Horizontal resolution for living cells in aqueous medium is tens of nanometers compared to 1-5nm for imaging in air. Near-physiological conditions are achieved by maintaining the liquid growth medium at 37°C at carbon dioxide at 5% using specially design incubation chambers.

Initial images recorded with PFQNM illustrated that quantitative imaging of endometrial epithelial cells was possible. The Hec-1-B cell line was much more difficult to image than Hec-1-A and resulted in increased scanning artifacts. A combination of extreme cell heights, combined with steep relief features exceeded the capability of the tip to accurately map some areas of the monolayer surface (Figure 56).

Using the Hamamatsu ORCA camera it was not always possible to identify areas with topographical limitation prior to AFM mapping. This problem was circumvented by careful selection of scan areas across the monolayer; cells with high contrast or of round appearance were avoided. Due to imaging artifacts average scan size was reduced in Hec-1-B, Hec-1-A average scan size was 105 μm while Hec-1-B average scan size was 48 μm. Steep sided cells were bypassed using offset feature where appropriate. Lastly the peak force oscillating amplitude was increased to 1 μm from the standard 300 nm through manipulation to Nanoscope software. This final adaption improved scanning reliability significantly.

The experiments above using fixed cell monolayers suggested a correlation between MUC1 expression and adhesion. Application of the AFM to live cells allowed examination of the effect of altered MUC1 expression. Removal of any cross-linking artifacts due to fixation could reveal further insight into the biophysical state, and functionality of the cells. Endometrial epithelial cells were grown until 80-100%

confluent and imaged using PFQNM. Live Hec-1-A and Hec-1-B cell monolayers were quantitatively mapped for stiffness, deformation and adhesion at near physiological conditions.

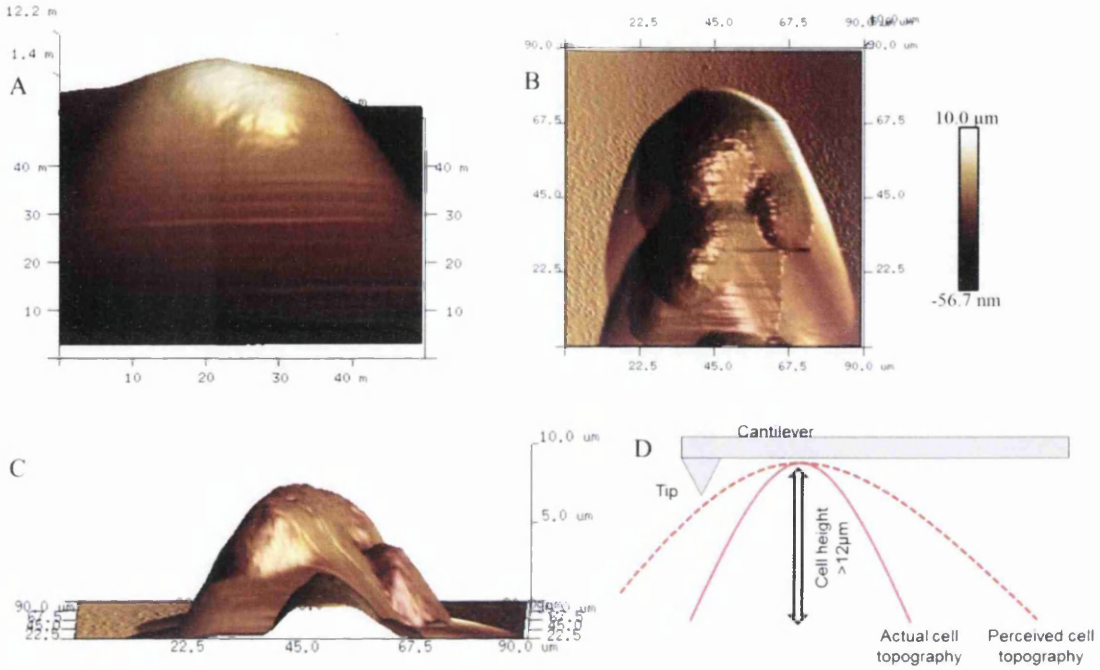

Figure 56: Overcoming scanning artifacts resulting from steep relief features. A proportion of Hec-1-B cells induced scanning artifacts due to their extreme height and steep relief features. (A) Height image of a Hec1-B cell measuring over 12 µm, the tip is unable to contact the cell periphery and results in a shadow. (B) Phase imaging shows a grouping of Hec-1-B cells induce "parachuting" and creates a false map of relief (the tip is scanning from top to bottom). (C) Substrate level view shows the steep relief of certain Hec-1-B cells. (D) The relationship between tip height and cell height is thought to be important here.

Excitingly, PFQNM-AFM was able to image live endometrial epithelial cell monolayers under physiological conditions at a range of scan areas and resolutions from 128 samples per line to 512 samples/ line (Figure 57).

Live Hec-1-A and Hec-1-B monolayers were imaged in nine separate areas that were chosen at random. Areas were scanned at 128 samples/line resolution in order to allow the maximum number of areas to be imaged and to reduce the chance of sample degradation.

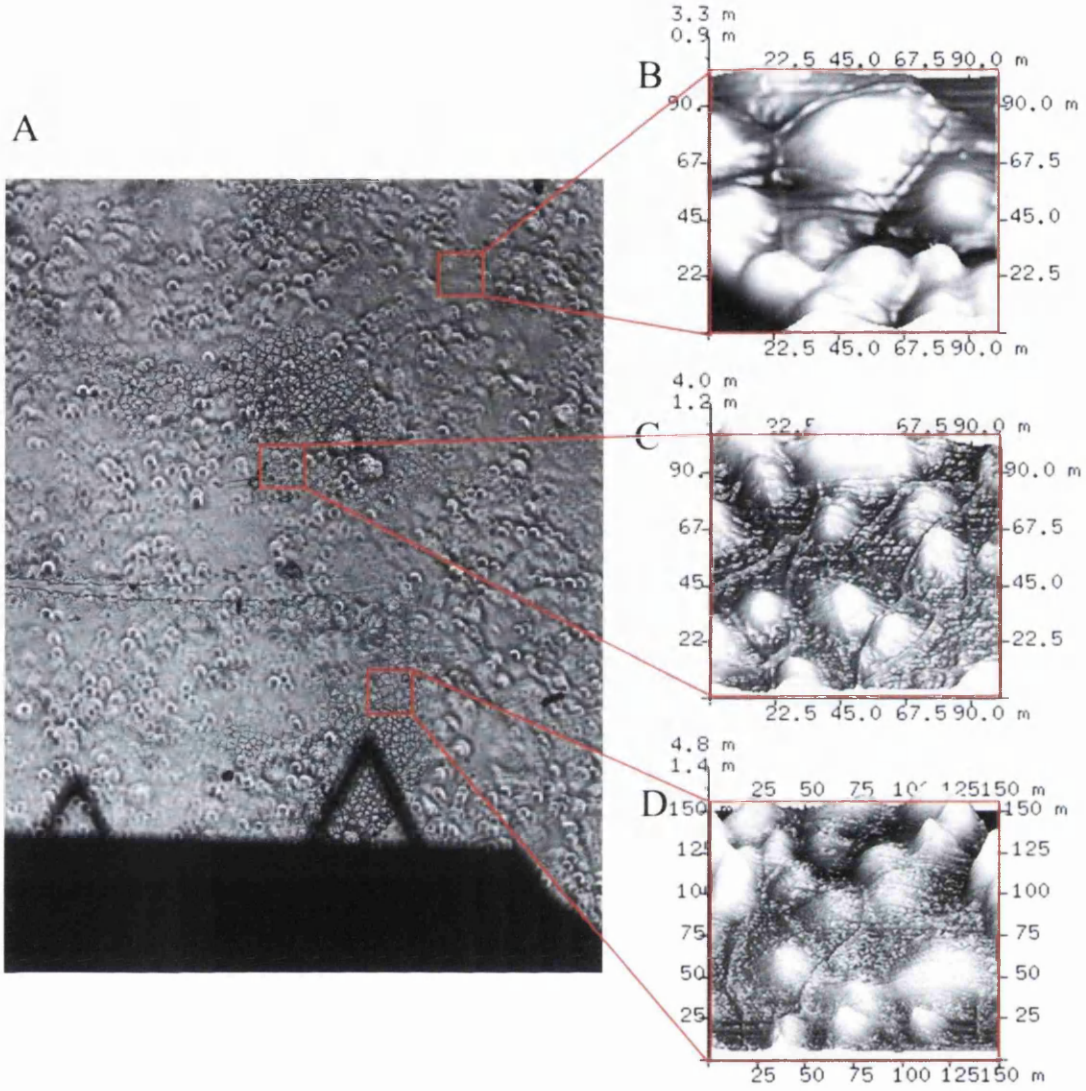

Figure 57: PFQNM is able to map endometrial cell monolayers. Hec-1 cell monolayers were grown until 80-100% confluence and imaged using Peak Force QNM. (A) Light microscope image showing monolayers of epithelial cells with the AFM cantilever above. The live monolayer was imaged at varying resolutions at randomly chosen locations. (A) 128, (B) 256 and (B) 512 samples/line. Scan sizes up to 150x150µm were possible but size depended on localised topographical features. Large scan sizes captured up to 20 adherent cells

Where possible a scan size of 100µm^2 was used, however in some cases topographical features limited the scan area. Three areas were scanned from each of the three biological repeats, resulting in nine total areas (3x3). Scans of Hec-1-A monolayer (Figure 58) consisted of scan areas A1 (100µm^2), A2 (100µm^2), A3 (100µm^2), A4 (100µm^2), A5 (100µm^2), A6 (100µm^2), A7 (100µm^2), A8 (65µm^2) and A9 (65µm^2).

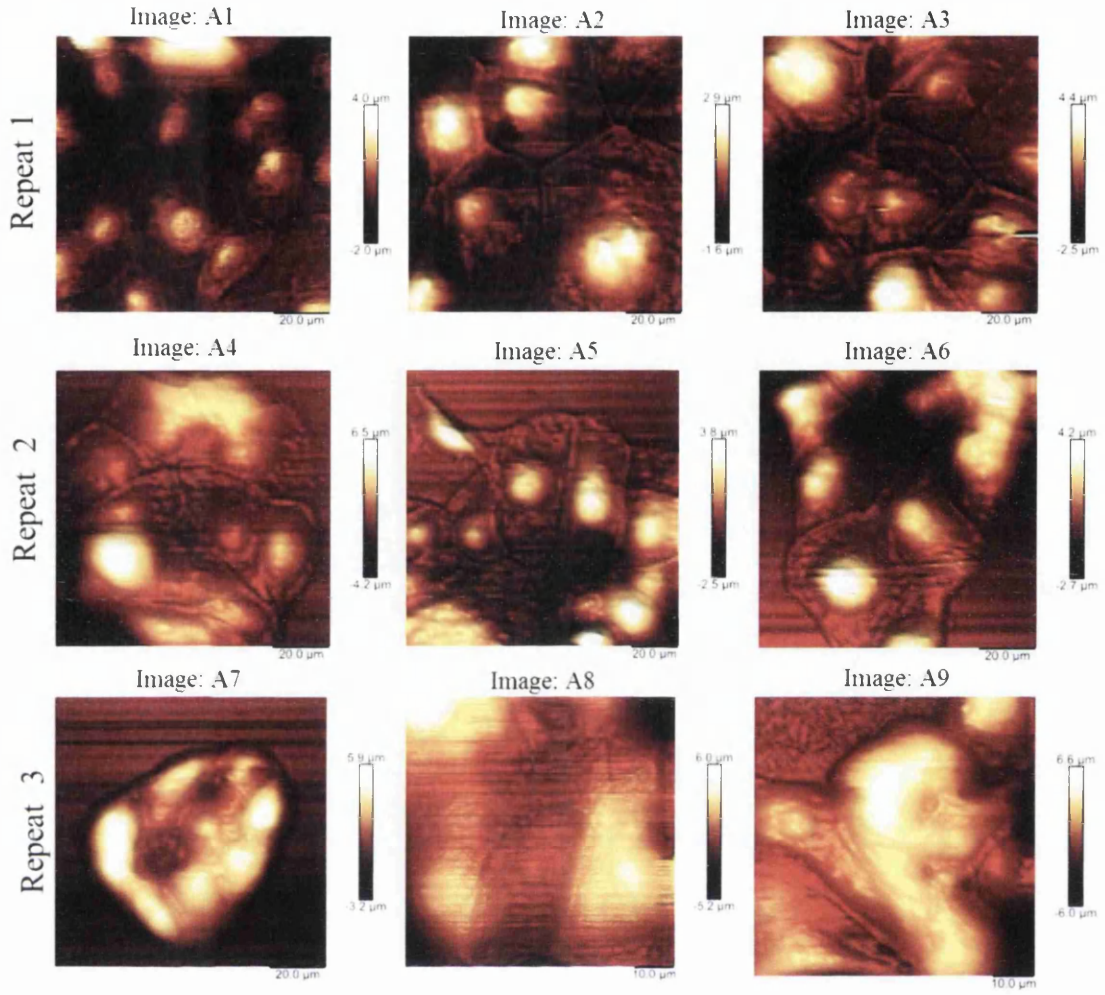

Figure 58: Panel of Hec-1-A monolayer images A1-A9. Hec-1-A cell monolayers were grown until 90-100% confluent and imaged live in media. (A1-A9) Bank of images used for extraction of nano-mechanical data.

Hec-1-B was also imaged resulting in areas B1 (50μm^2), B2 (50μm^2), B3 (50μm^2), B4 (50μm^2), B5 (20μm^2), B6 (50μm^2), B7 (50μm^2), B8 (100μm^2) and B9 (50μm^2) (Figure 59). Hec-1-B areas were smaller on average owing to the increased frequency of scanning artefacts as described earlier (Figure 56).

4.231 Stiffness

Hec-1-A and Hec-1-B had not shown differences in surface stiffness; however the process of fixation could be a contributory factor in the results. In order to maintain continuity with prior experiments on fixed monolayers, force curves were extracted from HSDC files that were generated for each of the nine areas scanned for Hec-1-A and Hec-1-B and stiffness analysed from approximately 5000 force curves. Hec-1-A

stiffness readings for repeats 1-3 were 79.6, 84.0 and 72.6KPa while Hec-1-B showed stiffness of 91.8, 78.8 and 69.8KPa (Figure 60).

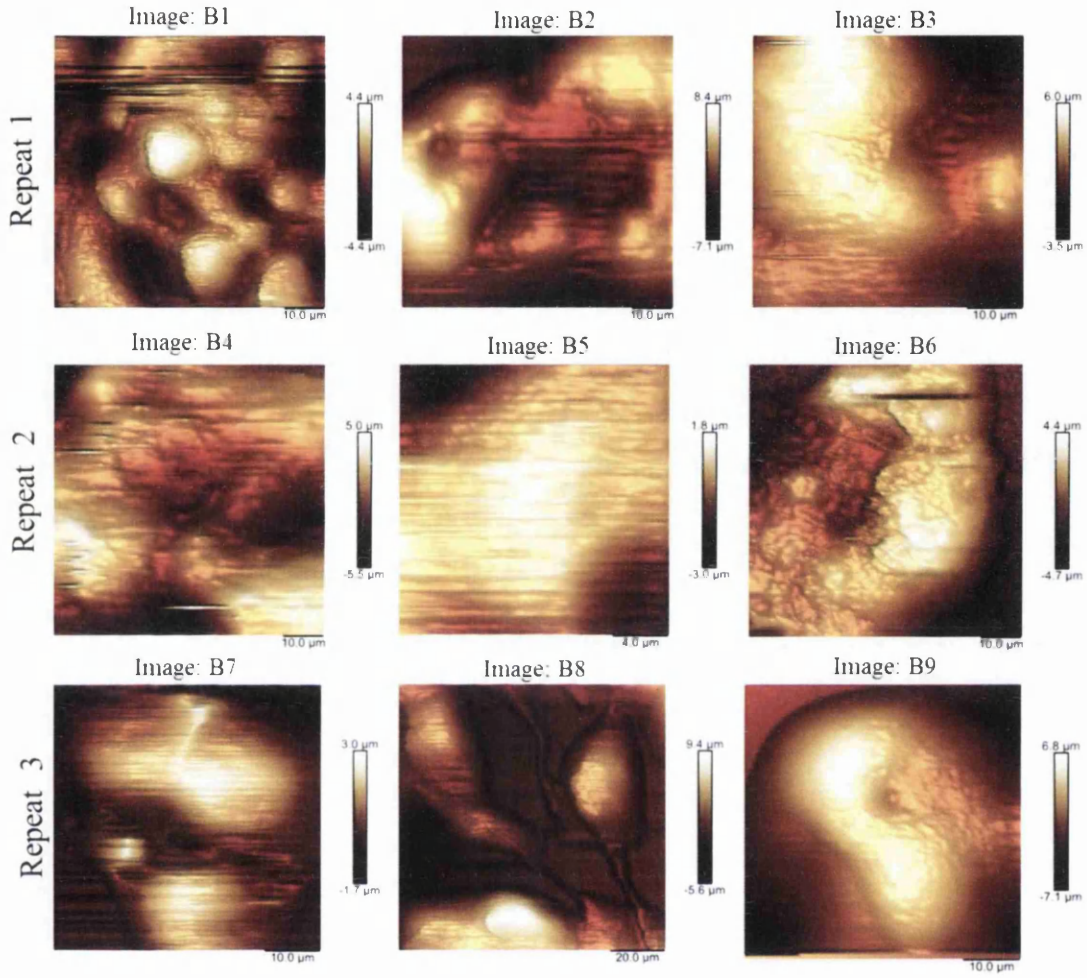

Figure 59: Panel of Hec-1-B monolayer images B1-B9.Hec-1-B cell monolayers were grown until 90-100% confluent and imaged live in media. (B1-B9) Bank of images used for extraction of nano-mechanical data.

Across all three repeats Hec-1-A areas displayed average stiffness 78.7 +/- 18.6 KPa. Hec-1-B areas produced average stiffness of 80 +/- 15KPa. The average stiffness of Hec-1-A and Hec-1-B membranes was very similar at 79 and 80 KPa respectively. Stiffness readings across the Hec-1-A areas were closely clustered ranging from 53.3 to 101.2 KPa while Hec-1-B areas were also clustered ranging from 64.2 to 107.8 KPa, and reflected fixed cell measurements. The cell stiffness, similar across both cell types, was similar to live cell stiffness measurements (13KPa-150KPa) reported by others (Weisenhorn 1993). As expected stiffness measurements on live cells were lower than previous experiments on the fixed cell monolayers, this is likely due to the cross-linking

effect of the paraformaldehyde fixative used. Similarly to the fixed cell approach the effect of the substrate was to increase stiffness in the cell periphery, while nuclear regions were softer. Stiffness is likely to be related to cell organelles and components of the cytoskeleton and not the expression of proteins such as MUC1 or MUC16 on the apical membrane.

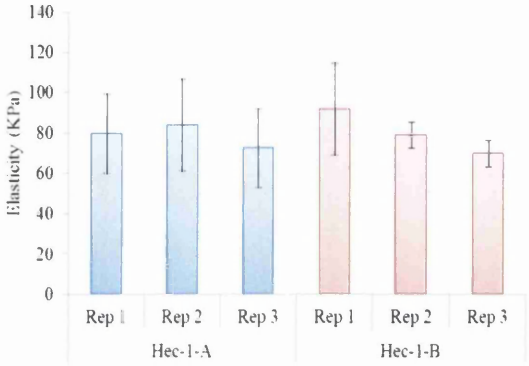

Figure 60: Stiffness measurements of Hec-1-A and Hec-1B cells. Adherent Hec-1-A and Hec-1-B endometrial epithelial cells were grown in glass dishes to 80-100% confluence and imaged at intermediate resolution using PFQNM-AFM. The High Speed Data Capture (HSDC) feature was used to generate one very high resolution (5000 data point) scan line transecting the image for Hec-1A (A) and Hec-1B (B). Force curves that occurred over the cell body were subjected to offline analysis using the sneddon variation. Stiffness data was generated from nine areas across the monolayer, three areas from each independent repeat. All three independent repeats are shown for both Hec-1-A (blue) and Hec-1-B (red). Error bars are ± STDEV from triplicate HSDC files. Data was analysed using a two-tailed Student's T-test *$p \leq 0.05$, **$p \leq 0.01$, ***$p \leq 0.001$ vs. control.

4.232 Deformation

Hec-1-A deformation for repeats 1-3 was 143.6, 151.8 and 169.3nm, similar to Hec-1-B which displayed deformation of 157.1, 154.5 and178.6nm for the three repeats (Figure 61). The average deformation of Hec-1-A areas (A1-A9) of cell monolayers was 155 +/- 27 nm while the average deformation of Hec-1-B monolayers measured 163 +/- 25 nm. This small difference was not shown to be significant ($p=0.498$). There was moderate variation across both Hec-1-A and Hec-1-B monolayers with readings from all areas ranging from 125 to 201 nm.

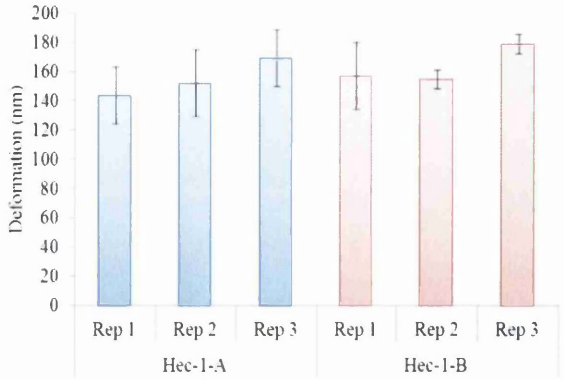

Figure 61: PFQNM deformation analysis of the endometrial cell line membranes. Hec-1 cell monolayers underwent quantitative mapping for nano-mechanical properties. PFQNM was used to image 9x 50-150μm^2 regions of the live cell monolayer from 3 biological repeats. Deformation data was generated from nine areas across the monolayer, three areas from each independent repeat. All three independent repeats are shown for both Hec-1-A (blue) and Hec-1-B (red). Error bars are ± STDEV from triplicate scans. Data was analysed using a two-tailed Student's T-test *p≤0.05, **p≤0.01, ***p≤0.001 vs. control.

4.233 Adhesion

Hec-1-A adhesion for repeats 1-3 was 136.7, 147.0 and 160.7pN, while Hec-1-B was much more adhesive showing 265.3, 277.7 and 271.3 for the three repeats (Figure 62). Across all Hec-1-A areas adhesion was 148 +/- 19 pN. In contrast, average adhesion across areas B1-B9 of the Hec-1-B monolayer was 271 +/- 35 pN which was shown to be a significant difference ($p=8.96x10^{-8}$). This represented a 1.83 fold difference. The difference in adhesion was more pronounced compared to fixed cells (1.57 fold) suggesting the fixative was dampening adhesion between the tip and the cell surface. There was some variation across the Hec-1-B monolayer with readings from all ranging from 205 to 318 pN while Hec-1-A areas were more closely clustered ranging from 117 to 172 pN. This reflects the increased heterogeneity of adhesion molecule expression in Hec-1-B shown in Chapter 3. Adhesion maps revealed that in Hec-1-A adhesion appeared to be unrelated to cell height, with similar adhesion in nuclear and cell periphery regions, while Hec-1-B did exhibit higher adhesion in nuclear regions. The adhesive characteristics of the endometrial monolayer are likely dependant on expression of adhesive proteins while deformation and elasticity are likely influenced by underlying substrate, such as the nucleus or the glass on the cell periphery.

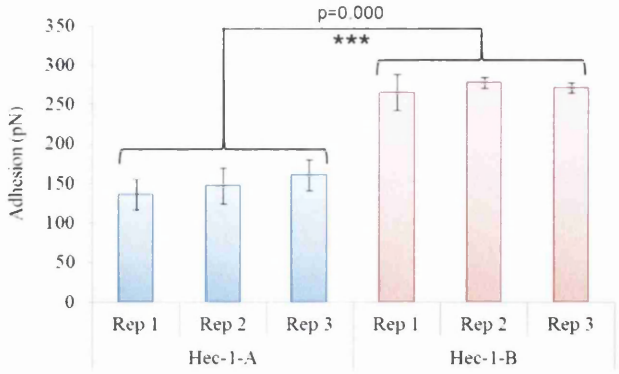

Figure 62: PFQNM adhesion analysis of the endometrial cells. PFQNM was used to image 9x 50-150μm^2 regions of the live cell monolayer from 3 biological repeats. Adhesion data was generated from nine areas across the monolayer, three areas from each independent repeat. All three independent repeats are shown for both Hec-1-A (blue) and Hec-1-B (red). Error bars are ± STDEV from triplicate scans. Data was analysed using a two-tailed Student's T-test *p≤0.05, **p≤0.01, ***p≤0.001 vs. control.

4.234 Combined live cell properties

When combined, the nano-mechanical properties of live Hec-1 cells revealed that stiffness and deformation were consistent between Hec-1-A and Hec-1-B monolayers (Figure 63). Adhesion, was significantly higher in Hec-1-B measuring 271 pN relative to 148 pN across Hec-1-A. These results are comparable to the data obtained from fixed cell monolayers, and show Hec-1-B exhibits a 1.8 fold increase in adhesion relative to Hec-1-A in a live cell system (Figure 63).

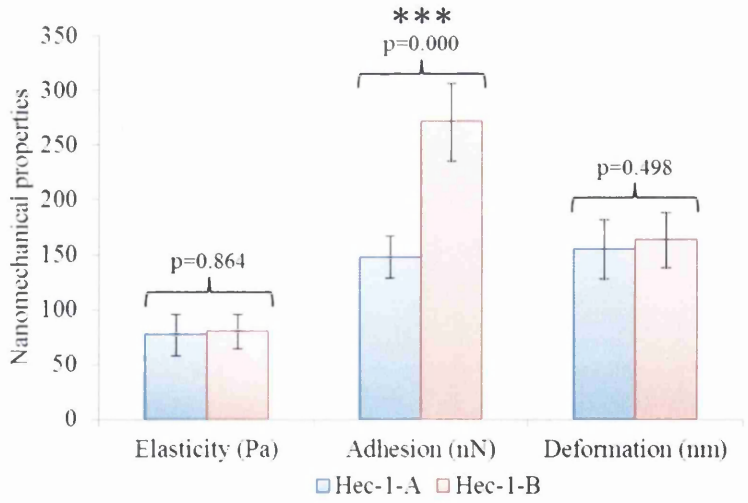

Figure 63: Combined nano-mechanical measurements of live Hec-1-A and Hec-1B cell monolayers. When compiled, the surface properties of the Hec-1 cell lines highlighted a divergence in the adhesive profile of the two cell lines while the monolayer stiffness and deformation remained consistent. Hec-1-A (blue) and Hec-1-B (red) are shown) All

three independent repeats are combined for both Hec-1-A (blue) and Hec-1-B (red). Error bars are ± STDEV from triplicate repeats. Data was analysed using a two-tailed Student's T-test *p≤0.05, **p≤0.01, ***p≤0.001 vs. control.

4.235 The effect of fixation

The nano-mechanical properties of the Hec-1-A and Hec-1-B cell monolayers followed the same trends whether within the fixed cell system or using the live cell approach. Fixation increased the membrane stiffness by 9% and 21% and increased the membrane deformation by 18% and 9% in Hec-1-A and Hec-1B respectively. In contrast adhesion decreased by -6% and -22% in Hec-1-A and Hec-1B respectively (Figure 64).

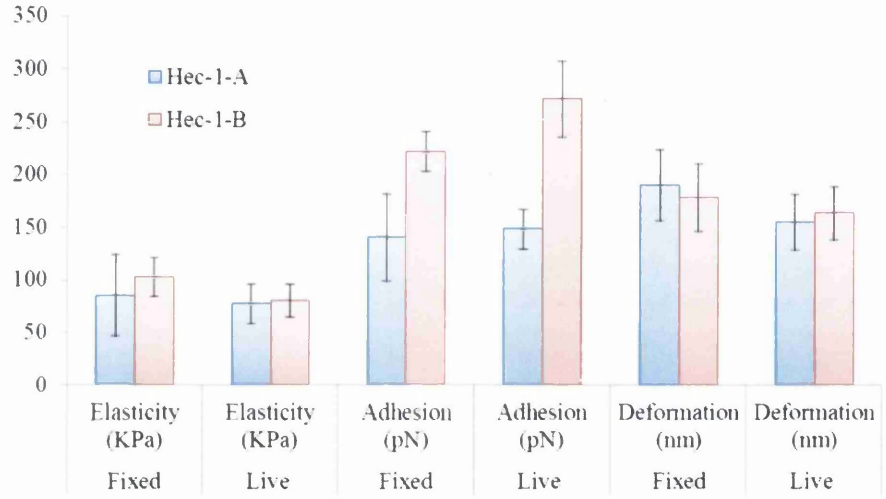

Figure 64: Stiffness, adhesion and deformation are all affected by fixation. Hec-1-A (blue) and Hec-1-B (red) cells exhibit similar trends in percentage change following addition of paraformaldehyde fixative.

This data suggests that far from being inferior fixed cell monolayers are good models for investigating nano-mechanical properties at the endometrial surfaces as they are representative of live cells. AFM imaging of live cells can be problematic but use of fixed cell monolayers provides an opportunity to study "real" nano-mechanical effects without the time constraints demanded by live cell imaging.

4.24 MUC1 and endometrial nano-mechanics

Hec-1-A and Hec-1-B have been used as a system for high and low expression of MUC1 protein, however this was an indirect assessment of MUC1 because expression of unknown adhesive mediators could be contributing towards the adhesive phenotype of Hec-1-B. In order to address this MUC1 gene expression was specifically targeted

using siRNA to determine whether any biophysical changes to the monolayer glycocalyx subsequently observed by AFM could be directly attributed to MUC1.

Knockdown of MUC1 resulted in a 96.1% reduction in gene expression and a 20% reduction in protein expression (detected by fluorescence) across the Hec-1-A monolayer. In Hec-1-B siRNA knockdown of MUC1 showed a greater effect with a 96.6% reduction in gene expression and corresponding 56% reduction in protein expression across the monolayer. This was likely due to the higher Hec-1-B basal expression levels. The Hec-1-B cell line was shown to express 4.5 fold greater MUC1 protein than Hec-1-A. However, following treatment with siRNA expression in Hec-1-B expression was shown to be similar to that of Hec-1-A basal levels. This provided a useful tool with which to compare the functional consequences of MUC1 on the surface properties of Hec-1-A and treated Hec-1-B.

The Hec-1-A and Hec-1-B monolayers treated with MUC1 siRNA were imaged using PFQNM. The experiment was repeated three times and each time three areas across the monolayer were imaged. Hec-1-A areas comprised; $A1^T$ ($100\mu m^2$), $A2^T$ ($120\mu m^2$), $A3^T$ ($100\mu m^2$), $A4^T$ ($100\mu m^2$), $A5^T$ ($100\mu m^2$), $A6^T$ ($100\mu m^2$), $A7^T$ ($100\mu m^2$), $A8^T$ ($100\mu m^2$) and $A9^T$ ($150\mu m^2$). Nine areas of Hec-1-B from three independent repeats were mapped resulting in; $B1^T$ ($50\mu m^2$), $B2^T$ ($50\mu m^2$), $B3^T$ ($50\mu m^2$), $B4^T$ ($50\mu m^2$), $B5^T$ ($50\mu m^2$), $B6^T$ ($50\mu m^2$), $B7^T$ ($50\mu m^2$), $B8^T$ ($50\mu m^2$) and $B9^T$ ($73\mu m^2$). Hec-1-B areas were generally smaller owing to the difficulties experienced when imaging these cells.

Figure 65 and Figure 66 show the regions of Hec-1-A and Hec-1-B cell monolayers captured using PFQNM. Data was extracted from these images using "bearing analysis", or HSDC methods in the case of membrane stiffness. Quantitative data showing membrane stiffness, deformation and adhesion from MUC1 siRNA treated Hec-1-A and Hec-1-B live cell monolayers was compared to control monolayers (Figure 67).

The range of stiffness readings from Hec-1-A cells was measured (Figure 67A), resulting in average stiffness of 78.7 +/- 18.6 KPa in control cells, and following MUC1 gene silencing 73.2 +/- 15.1KPa (Figure 68). Hec-1-A monolayers displayed a small 5% reduction in stiffness after treatment but this was not significant ($p=0.6507$). Hec-1-B cells displayed stiffness measurements of 80 +/- 15KPa KPa and, following MUC1 silencing, the average stiffness was found to be 76.9 +/- 17.6KPa (Figure 68). Hec-1-B

monolayers displayed a small 4% reduction in stiffness following MUC1 siRNA treatment but this was not significant (p=0.6849). The small, non-significant reduction in stiffness was likely a product of monolayer variation across areas rather than a biophysical consequence of MUC1 knockdown.

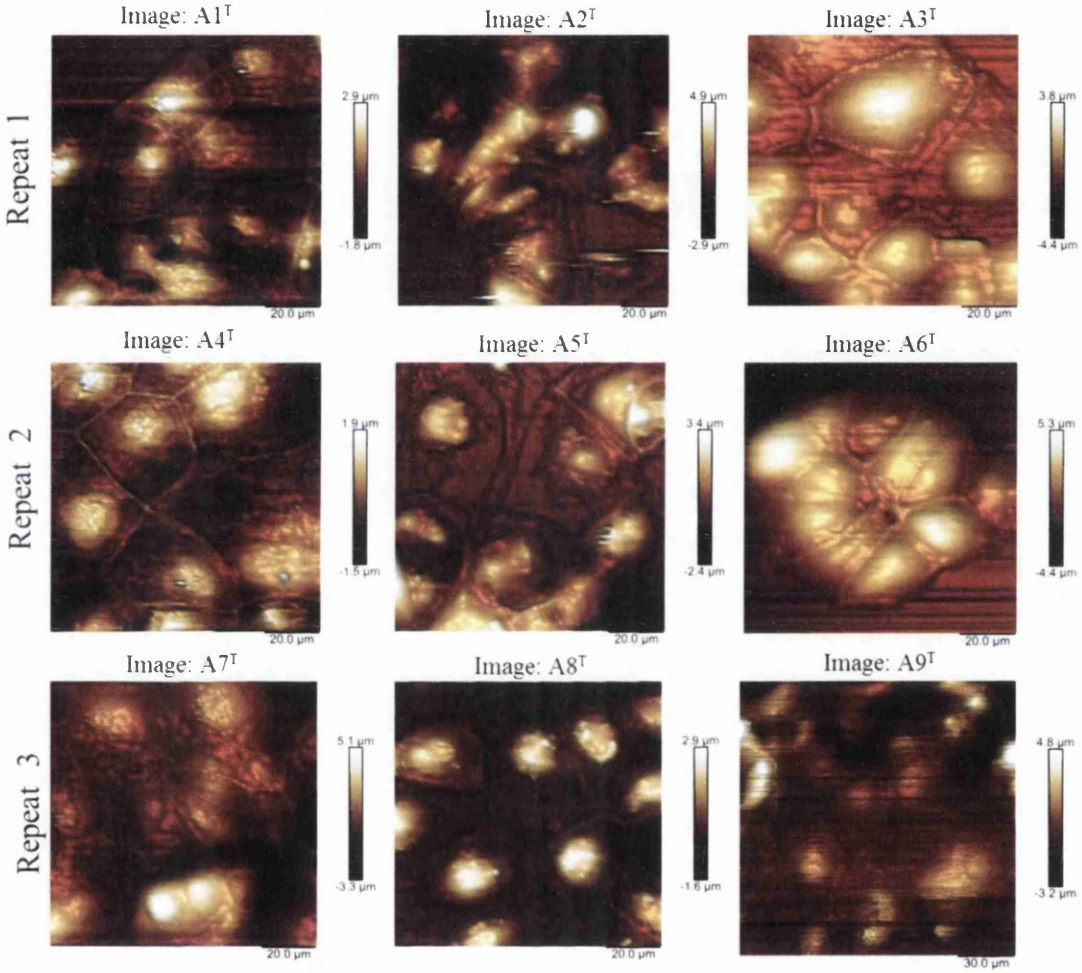

Figure 65: Panel of Hec-1-A monolayer images following treatment with MUC1 siRNA: $A1^T$-$A9^T$. Hec-1-A cell monolayers were grown until 60% confluent, treated with MUC1 siRNA for 48hrs and imaged live in media. ($A1^T$-$A9^T$) Bank of images used for extraction of nano-mechanical data.

Deformation readings across 18 areas of Hec-1-A monolayer are shown (Figure 67C) and average deformation was found to be 155 +/- 27 nm (Figure 68) and, following MUC1 gene silencing the average deformation measurement was calculated to be 175.0 +/- 28.9nm (Figure 68). While this represented a 13% increase inter-region variation resulted in no significant change (p=0.1449). Figure 67D shows the spread of deformation across the 18 Hec-1-B areas, and average deformation was calculated to be

163 +/- 25 nm (Figure 68). MUC1 gene silencing increased the average deformation measurement to 164.7 +/- 25.4nm. This resulted in no significant change in deformation as a result of MUC1 gene silencing (p=0.9145).

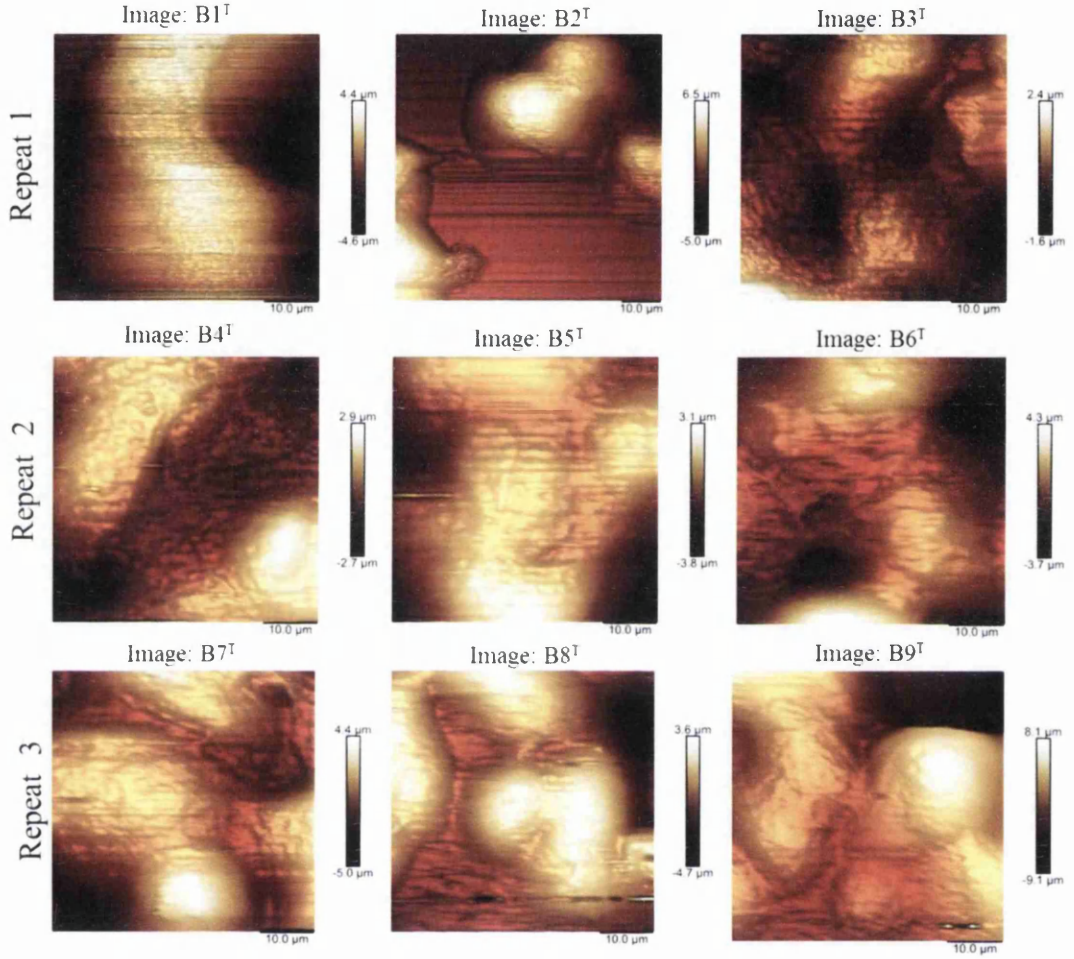

Figure 66: Panel of Hec-1-B monolayer images following treatment with MUC1 siRNA: $B1^T$-$B9^T$. Hec-1-B cell monolayers were grown until 60% confluent, treated with MUC1 siRNA for 48hrs and imaged live in media. ($B1^T$-$B9^T$) Bank of images used for extraction of nano-mechanical data.

Adhesion measurements were recorded from all nine untreated Hec-1-A areas (Figure 67E) and average adhesion was 148 +/- 19 pN (Figure 68). MUC1 knockdown reduced the average adhesion measurement to 116.9 +/- 23.9 pN (Figure 68). This represented a significant 21% reduction in adhesion (p=0.0071). Adhesion readings were taken from 18 Hec-1-B areas (Figure 67F) and average adhesion of control areas was 271 +/- 35 pN (Figure 68). MUC1 gene silencing reduced average adhesion measurement in all areas and the combined average was calculated to be 118 +/- 19.3pN (Figure 68). This represented a 56% reduction in adhesion and was highly significant (P= 0.0000).

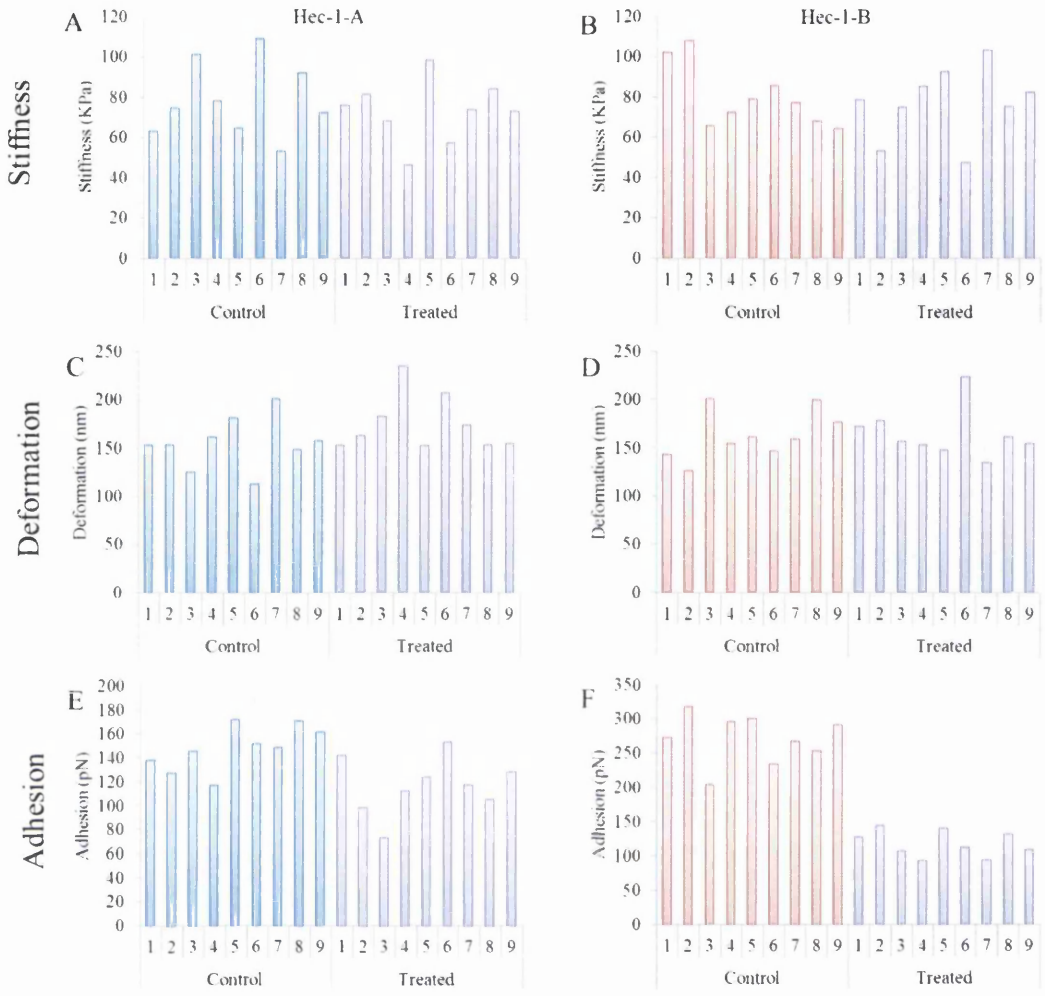

Figure 67: MUC1 gene silencing is able to affect surface nano-mechanical properties of EEC cell lines. Quantitative mapping of Hec-1-A (blue) and Hec-1-B (red) cell monolayers was undertaken to determine nano-mechanical properties following MUC1 siRNA treatment. Moreover, each region was subjected to HSDC for offline calculation of membrane stiffness using the sneddon variation. For each cell line nine areas were subjected to specific MUC1 siRNA treatment (purple bars) and nine areas with scrambled siRNA control (blue/red bars depending on cell line). Each treatment group comprised approximately nine areas from three biological repeats. Subsequent post processing made use of bearing analysis within Nanoscope software to compute adhesion and deformation. Stiffness was derived from HSDC files using RAINBOW software (Bruker-nano). Graphs show the stiffness (A+B), adhesion (C+D) and deformation (E+F) of Hec-1-A (blue bars) and Hec-1-B (red bars) respectively. Treatment refers to specific MUC1 siRNA and control is untreated cells.

MUC1 reduction from the monolayer resulted in no statistical change to deformation or membrane stiffness but a statistically significant decrease in adhesion in the two cell lines. Following treatment the Hec-1-B cells showed a greater reduction in adhesion when compared to Hec-1-A. This corresponded to a greater loss of MUC1 protein

across the Hec-1-B monolayer compared to Hec-1A, thus providing further support for a link between MUC1 protein and adhesion. This result shows for the first time the significant contribution MUC1 protein makes to the adhesive status of apical cell surfaces in two endometrial cell models.

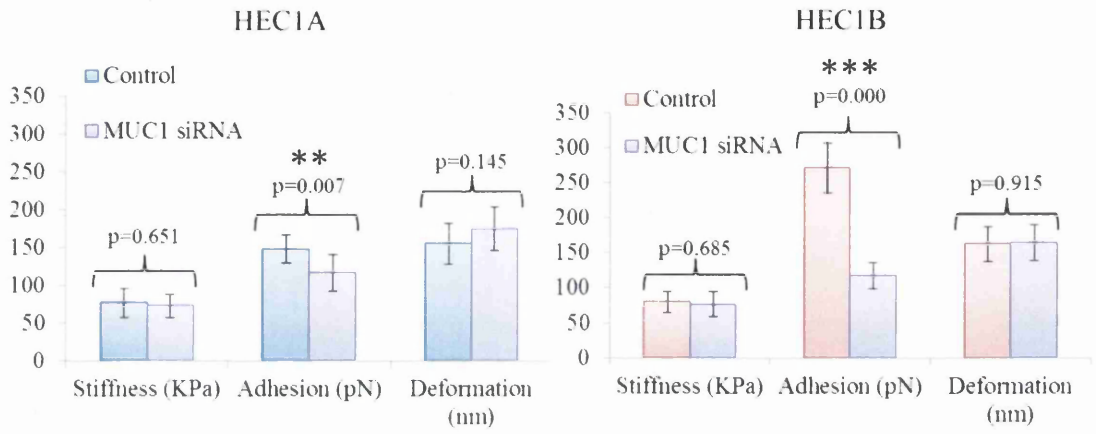

Figure 68: MUC1 gene silencing reduces adhesion in Hec-1-A and Hec-1-B cell monolayer. Hec-1 cells were treated with MUC1 specific siRNA and quantitatively mapped with PFQNM. Hec-1-A and Hec-1-B MUC1 siRNA treated monolayers (purple bars) were compared to scrambled siRNA control monolayers (blue and red bars respectively). Stiffness, adhesion and deformation mapped from nine regions of the monolayer and compiled here. ± STDEV from triplicate nine areas. Data was analysed using a two-tailed Student's T-test *$p \leq 0.05$, **$p \leq 0.01$, ***$p \leq 0.001$.

4.4 Discussion

In this chapter a thorough interrogation of the nano-mechanical status of two EEC cell lines was undertaken. Excitingly, it was revealed that MUC1 protein has a significant role regarding the functional adhesive status of the apical epithelium. The adhesive contribution was shown to be independent of two other biophysical properties; stiffness and deformation. The functional approach taken facilitated novel assessment of endometrial biomechanics and the role played by MUC1. The expression of MUC1 can be directly correlated with the biophysical state of these cell monolayers. The adhesive effect of MUC1 protein has been quantified, and a direct correlation between MUC1 and adhesion established.

Comparison of fixed and live monolayers provided a unique opportunity to assess the effect of fixation on endometrial epithelial cell bio-mechanics. Previous examination of endometrial cells within our group had made use of highly optimized glutaraldehyde

fixation procedures (Francis et al. 2010) to investigate correlations between MUC1 expression on the apical membrane and surface roughness (Francis et al. 2009).

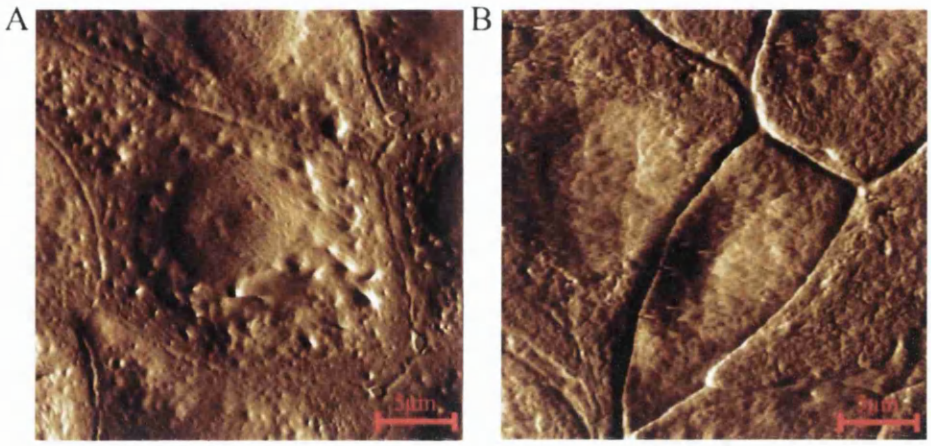

Figure 69: Hec-1-A endometrial epithelial cells phase imaged using PFT AFM. (A) Following fixation membrane appears stable and nano-scale structures are readily observed (B) When imaged live in media the membrane appears to undulate as a response to tip indentation (Resolution: 512 samples/line).

The direct comparison between live and fixed cell monolayers demonstrates that, as would be expected, artificial fixation alters the monolayer biophysical properties. However, despite this, the trends observed in the biophysical properties of these cells were unaffected using our fixation process. Following fixation, membrane stiffness increased by up to 21% and membrane deformation increased by up to 18%. Adhesion, central to our investigation, was reduced 21%. In the fixed cell system Hec-1-B was 1.57x more adhesive than Hec-1-A compared to 1.84x more at near physiological conditions. It is plausible that adhesion is dampened due to a loss of adhesion protein function as other components of the apical membrane (carbohydrates, lipids, nucleic acids) are thought to be trapped in a matrix of cross-linked proteins, thus also providing rationale for the increases in stiffness that was observed.

PFQNM was used to explore adhesion, deformation, energy dissipation and stiffness of EEC cell monolayers and to correlate any changes in these properties to epithelial mucins. Surface deformation results from tip sample interaction and has been shown to be related to energy dissipation (Zhang et al. 2013). The experiments in this chapter revealed that deformation did not differ significantly between Hec-1-A (190nm) and Hec-1-B (178nm) independent of MUC1 levels at the cell surface. This suggests that

surface protein expression does not influence the membrane deformation. It is likely that sub-membranous structures such as the cytoskeleton, actin filaments, organelles and microtubules could account for changes to membrane deformation caused by the tip, and this is reported in the literature (Berquand et al. 2010). Moreover, the images revealed a strong association between cell height and deformation and the nuclear regions of cells in the monolayer consistently show higher deformation compared to the cell periphery. This was expected as the underlying influence of the stiffer substrate does not permit high deformation while the nucleus is subject to increased deformation (Yokokawa et al. 2008).

Cell stiffness is often selected as the property with which to investigate mechanical function in pathologies such as cancer (Weder et al. 2013) and osteoarthritis (Khan et al. 2013) as cell stiffness directly impacts processes related to events such as cancer metastasis. In the endometrium monolayer stiffness may affect the interactions of the epithelial layer and the embryo. Stiffness was calculated using Sneddon model for elasticity which was selected because it accounts for the indentation of a tip featuring cone-shaped geometry, as opposed to hertz which considers a spherical model. Additionally, Sneddon considers short range forces acting within the contact area whereas hertz only considers long range surface forces acting outside the contact area. Membrane stiffness was very similar between live Hec-1-A (78.7KPa) and Hec-1-B (80.0KPa) and within the 13KPa-150KPa range reported by others (Weisenhorn 1993). There is a difference of MUC1 and MUC16 expression between Hec-1-A and Hec-1-B but this does not appear to affect the stiffness of the membrane. This property is more likely to dependent on alterations to sub-membranous structures such as the cytoskeleton and not apical expression of membrane proteins (Wang et al. 2013). Being closely related to deformation, stiffness was also shown to correlate with cell height. Again the influence of the underlying substrate is clearly shown. Nuclear regions appear soft, while the cell periphery and especially cell junctions are very stiff. This effect is due to the underlying substrate and a consequence of the *in vitro* approach taken here. It would be revealing to measure the stiffness of epithelial layer in co-culture with stromal cells. In the context of implantation and invasion the stiffness of the epithelial monolayer is likely to be affected by embryo derived signaling as it seeks to invade through the epithelia into the stroma, although as yet there are no studies in this area.

Evidence suggests that energy dissipation on cell surfacess is a primarily a result of frictional and viscous damping within the cell caused by cytoskeleton internal friction and actin de-polymerization (Smith et al. 2005). However, experiments here showed energy dissipation to be greater in Hec-1-B (3.8KeV) compared to Hec-1-A (2.7KeV). No differences in the deformation or stiffness of Hec-1-A and Hec-1-B were shown suggesting that the underlying cytoskeleton is not responsible for this trend, and the interaction of the tip with surface proteins could cause this mechanical dampening effect. In both cell types areas of high energy dissipation correlated with areas of high adhesion. Rupture of the adhesive bonds formed between the surface and the tip requires energy, which may explain why areas of high adhesion also exhibit high energy dissipation. Interestingly, energy dissipation was elevated at cell-cell junctions. When probing the cell boundary, the tip may be coming into contact with the lateral surface of the cell where other adhesive proteins are located, thus contributing towards increased energy dissipation. Additionally, it may be that area of contact with the cone-shaped tip increased due to surface relief in these regions. This may allow lateral forces to occur between the sides of the tip and the surface thus removing energy from the system, resulting in increased dissipation.

The MUC1 high expressing cell line, Hec-1-B had an average adhesion between the surface and the tip of 271pN compared to 148pN of the relatively low MUC1 expresser Hec-1-A. This represents an almost 2 fold difference in adhesion. Interestingly, this is a similar order of magnitude to the difference in MUC1 protein expression quantified across the same Hec-1-A and Hec-1-B monolayers. Protein expression across Hec-1-B and Hec-1-A monolayers was quantified by fluorescence as 196AU to 46AU respectively. The similarity in MUC1 expression and adhesion between Hec-1-A and Hec-1-B suggest there may be a close link between MUC1 expression and adhesion in the endometrial cell lines. When MUC1 siRNA was introduced to the Hec-1-A monolayer MUC1 protein expression was shown to decrease 22% and adhesion decreased by 21%. Following the same treatment in Hec-1-B cell monolayers MUC1 protein expression was shown to decrease 53% while adhesion decreased by 56%. The specificity afforded by siRNA dictates that only MUC1 mRNA was targeted, thus translation of MUC1 transcript is blocked while expression of other surface proteins is unaffected. These findings further support the suggestion that MUC1 ectodomain is a major component of adhesion in Hec-1-A and Hec-1-B endometrial epithelial cells.

There was a degree of intra-monolayer variation in the adhesion across individual areas imaged with the AFM and this again corresponds to fluorescence observation of heterogeneous MUC1 patterning. However, even considering normalization of the observed trends by intra-monolayer variation the differences in adhesion were still significant.

Whilst some reports have suggested that MUC1 has an anti-adhesive function the data presented here suggests, that in the context of indentation with an AFM tip, MUC1 is highly adhesive. Our data also demonstrates that endometrial mucins, and in particular MUC1, contribute significantly to an AML covering endometrial cells that could potentially trap the embryo allowing specific molecular recognition to occur. A suggested mechanism for this process is the L-selectin/sLe^x interaction which the following chapter explores in detail.

Chapter 5 Force spectroscopy analysis of MUC1 and L-selectin

5.1 Introduction

The focus of this chapter was to adapt AFM to investigate the distinct molecular interactions that are believed to occur during the initial stages of embryo implantation, the hypothesis being that an intimate biochemical and biophysical understanding, and quantification of such interactions can be significantly enhanced using single molecule force spectroscopy alongside well characterised endometrial epithelial live cell models. The specific adhesion which occurs between MUC1 and L-selectin is assessed at the nanoscale in this chapter.

Single molecule force spectroscopy (SMFS) has emerged as a technique able to quantify the interactions and mechanisms of molecular interactions contributing to the correct functioning of cellular systems (Hinterdorfer & Dufrêne 2006; Müller 2008). Some SMFS bio-applications characterize the interaction of proteins localised to artificial bio-molecular systems such as membrane rafts or purified proteins (Xu et al. 2013). Such *in vitro* experiments are limited in their scope because they characterise biomolecules that are removed from the cellular context. Deciphering how cells control bio-molecular interactions in such a highly complex and dynamic environment requires transferring SMFS to the living cell. During live cell experiments a ligand functionalised AFM tip is brought into contact with the cell surface allowing molecular bond formation. The tip is then retracted and as the tip separates from the cell membrane the bio-molecules first enter a stretched configuration and, if further mechanical stress is then applied, elongate (proteins may unfold during this stage) and then separate. If the tip is functionalised with a receptor and its ligand localised to the substrate, then ligand binding can be investigated (Müller 2009) (Figure 70A).

The sensitivity of the AFM allows quantification of nanonewton (10^{-9}N, nN) or even piconewton (10^{-12}N, pN) forces resulting from bio-molecular bond separation. These forces range from pN for example DNA binding proteins (Lee et al. 2012) to several nN as in the case of streptavidin-biotin bonds (Lee et al. 1994). In order to probe such bio-molecular interactions a cantilever with a spring constant 0.01N/m-0.1N/m must be used as this is sufficiently stiff to resist the inter-molecular and intra-molecular forces resulting from these bio-molecular interactions.

The cantilever and linker molecule pairing may be considered as an elastic element and thus obey Hooke's Law. Hooke's law states that force (F) needed to extend or compress

a spring by some distance (x) is proportional to that distance where (k) is a constant factor characteristic of the spring, its stiffness.

$$\text{Hooke's Law: } F = kx$$

The ligand-receptor bond can also be modelled as an elastic element which is generally stiffer than the AFM cantilever. This bound arrangement results in two elastic elements arranged in series. Hooke's law dictates that as the cantilever is withdrawn, distance x increases and thus force (F) also increases. Force may be considered as the change in potential energy (U) over a change in position (x).

$$\text{Force and potential energy: } F = \delta U/\delta x$$

When the potential energy in the system exceeds the local maximum the bond will break (Figure 70B).

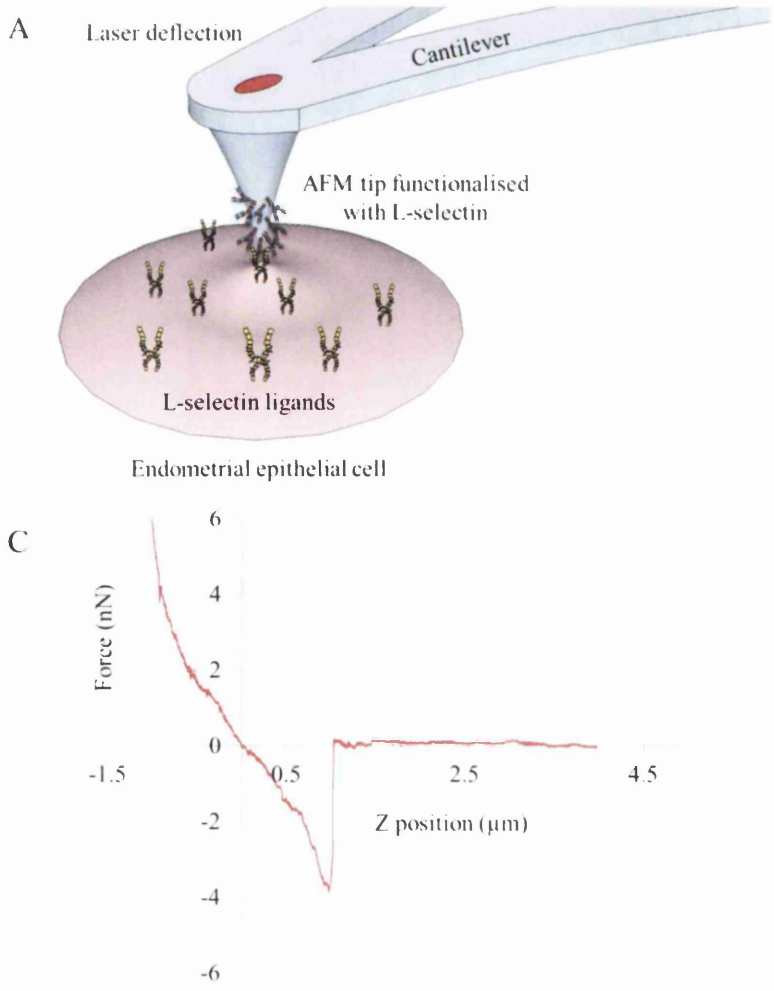

1.The AFM cantilever and linker molecule behave as an elastic element.

2. As the cantilever is withdrawn force F increases

3. Potential energy U increases

4. Potential energy U exceeds the local energy maximum and the bond breaks

Figure 70: The separation of Ligand Receptor pairs. Single molecule force spectroscopy of L-selectin and ligands on endometrial cells. (A) Graphical representation of an AFM tip functionalised with L-selectin protein. A laser dot reflected off the back of the cantilever records deflection. The tip is driven into the endometrial cell where it remains stationary for 100ms. If intermolecular bonding occurs between the tip and the surface then potential energy is required to separate molecular bonds when the tip is withdrawn. (B) Diagrammatical representation of the AFM cantilever and linker molecule which act as an elastic element obeying Hooke's law as force is applied to the system (C) This force is recorded as a change in laser deflection and is visualised as a curve of force against distance. The large change of deflection is the separation of an intermolecular bond.

The bond rupture event may be characterised by the distance that it occurs from the contact point, or by the force required for separation, and a field of research analysing retraction force curves and modelling bond ruptures has developed (Noy 2011). Specialised software packages to analyse rupture events on force curves such as PUNAIS, OpenFovea, and JPK data processing have been developed, with varying success. After consideration of the above software packages, JPK data processing was chosen to analyse force curves for bond rupture events. The "step-fitting" feature native to this platform detects and characterises bond rupture events as "steps". The software is able to distinguish between curves with one or more steps (Figure 71A) and curves that are negative for steps (Figure 71B). The algorithm highlights the step with a vertical line and records the position (μm) and step height (pN-nN) for every step detected on the force curve. After analysis has finished the data on all recorded steps can be exported for post-processing using spread-sheet software (Excel).

The force required for separation of ligand-receptor bonds pairs is dependent firstly on the method by which the ligand is attached onto the AFM tip, and secondly the velocity that the tip is withdrawn, referred to as bond loading (Evans 2001; Evans et al. 1995). This has been demonstrated in the case of the sLe^x-L-selectin bond using polyethylene glycol (PEG) linkers (Evans et al. 2001).

The approach taken here was to utilise a rigid linker strategy using glutaraldehyde (Li et al. 2011). Silicon nitride [Si_2N_3] probes are washed and silanization with (3-Aminopropyl)triethoxysilane [$H_2N(CH_2)_3Si(OC_2H_5)_3$] (Silberzan 1991) (Figure 72A).

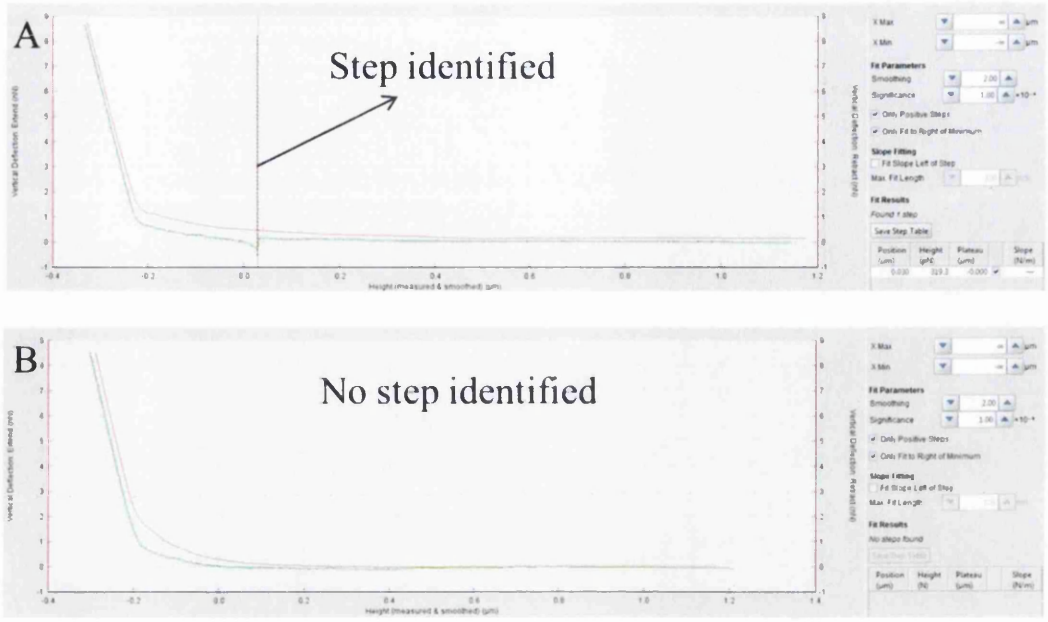

Figure 71: JPK data processing can identify steps on the retraction part of the force curve. User controlled parameters can set a maximum and minimum height within which the software will search for steps. The curves are smoothed before step analysis to reduce the noise. Significance is the factor which dictates how probable it is that the step is not due to background noise.

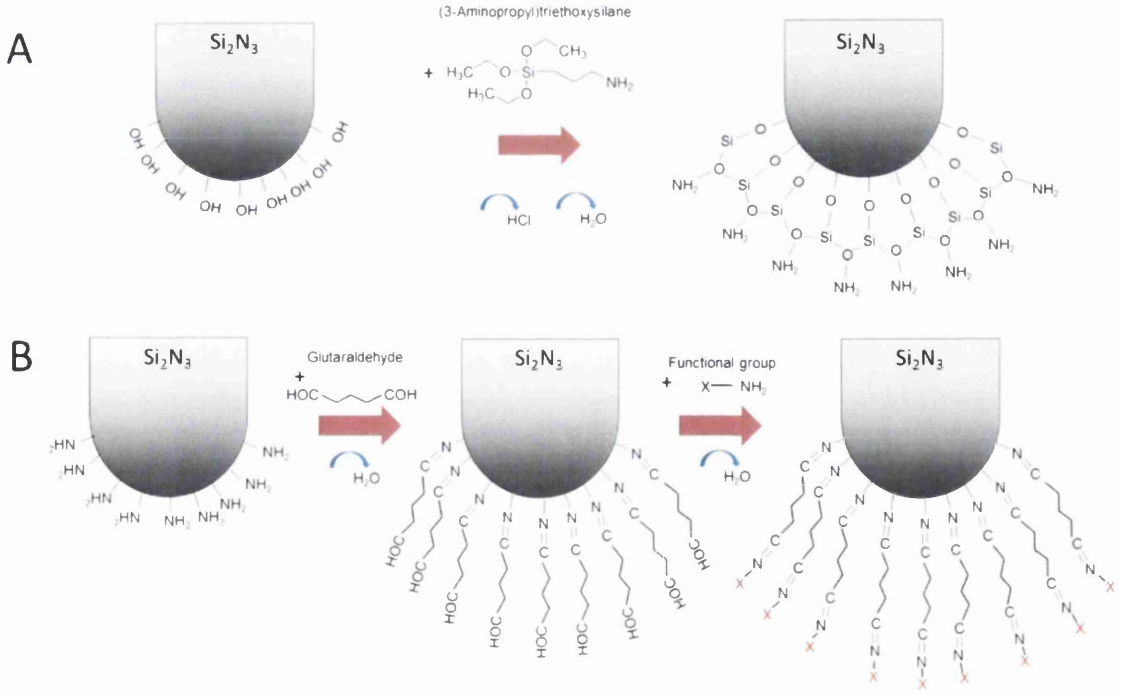

Figure 72: (A) Silanization reaction and (B) glutaraldehyde cross-linking and attachment of functional group to AFM tip.

The silanization approach offers the advantage that the probe can be functionalized directly without other prior surface preparation. This results in Si-O-Si covalent bonds between the tip and silane molecules, and hydrogen bonding interactions between the aliphatic chains of the silane molecules. The reactive NH_2 group is used for the next step of the functionalization. The probes are now treated with glutaraldehyde $[CH_2(CH_2CHO)_2]$ which reacts with the free NH_2 group and releases one molecule of water (Migneault et al. 2004) (Figure 72B).

The tips are then exposed to the desired ligand which binds to the remaining free end of the glutaraldehyde molecule releasing H_2O. This completes the cross linking reaction.

In this study DNP-10 tips were functionalised with monoclonal antibody and a recombinant peptide. The MUC1 VU4H5 antibody (Santa Cruz Biotechnology #sc-7313) is a mouse monoclonal raised against the naked peptide VNTR region located in the extracellular (ND) domain of MUC1.

In order to probe the surface for L-selectin ligands, tips were coated with recombinant L-selectin (Randox Life Sciences # RCP9253) consisting of a 294 amino acid fragment (aa39-332) corresponding to the mature and fully functional L-selectin extracellular domain. This extracellular region contains the lectin domain required for binding to sialyl lewis x (sLe^x) epitopes present on endometrial epithelium. AFM tips were coated in anti-MUC1 and L-selectin at 200µg/ml to ensure the tip density was comparative between to two functionalization molecules.

The molecular interactions at the embryo-maternal interface during the period of blastocyst adhesion are not yet fully understood continuing biochemical studies (Koot et al. 2012; Salilew-Wondim et al. 2012; Garrido-Gómez et al. 2013; Dharmaraj et al. 2013; Cheong et al. 2013). AFM probes were functionalised with recombinant L-selectin protein to allow probing of a cell monolayer for potential L-selectin ligands, such as sLe^x which has been shown to associate with MUC1 in Hec-1-A and Hec-1-B cells (Hey & Aplin 1996). The approach taken was to complement trophoblast spheroid attachment assays by assessing, at the molecular level, the involvement of embryo adhesion molecules, and characterising the number and strength of interactions with their representative ligands located on endometrial epithelial cell monolayers.

L-selectin and sLe^x interactions have parallels in other systems (Dominguez et al. 2005), and L-selectin and sLe^x antigen are up-regulated during the window of implantation. Additionally, it has been shown that disruption of the MUC1 and sLe^x correlates with PCOS and endometriosis (Margarit et al. 2010; Margarit et al. 2009). It is very likely that glycosylation is a requisite for MUC1 function at the endometrial surface in embryo recognition. Decoration of MUC1 with sLe^x is dependent on the VNTR region, and requires a host of glycosyltransferase enzymes (Tjew et al. 2005) that generate the sLe^x ligands that have been associated with MUC1 in these cell lines. These factors add additional regulatory control to the process through which MUC1 may present ligands to the embryo (Figure 73).

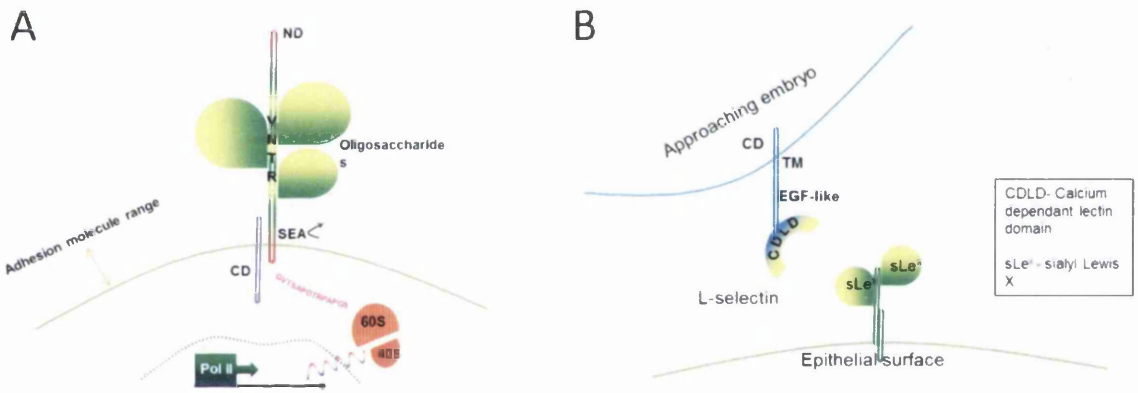

Figure 73: MUC1 may act as a scaffold for L-selectin ligands and present them to the approaching embryo. (A) MUC1 has a large extracellular domain (ND) that extends around 250-500nm into the lumen. The VNTR region of MUC1 consists of 20-125 repeats of the amino acid sequence GVTSAPDTRPAPGS. MUC1 also has an intracellular domain (CD) and sites for enzymatic cleavage (SEA). (B) MUC1 presents sLe^x epitopes to the calcium dependent lectin domain of L-selectin, the affinity between these regions may assist in tethering the embryo to the uterine surface.

The main objective of this chapter was to evaluate the distribution, localisation and force properties of the MUC1 protein and L-selectin ligands presenting on the endometrial epithelial cell surface. The secondary objective was to investigate whether L-selectin binding was related to MUC1 surface expression. AFM tips were functionalised with MUC1 antibody in order to investigate surface binding in Hec-1-A and Hec-1-B cells. MUC1 knock down allowed examination of the functional effect on L-selectin binding in the model cell lines thus testing the hypothesis that MUC1 presents ligands to the embryo.

5.2 Results

5.21 AFM operation

The JPK Nanowizard II AFM was operated in force spectroscopy mode and a 2x2μm region of the cell was probed. The cantilever was ramped 5mm from the cell surface, to ensure clearance between the tip and the cell glycocalyx upon retraction, and ensure any molecular binding between endometrial ligands and antibody (or L-selectin) on the tip occurred on the approach (Tsapikouni & Missirlis 2011). Resolution was initially 32x32 resulting in 1024 force curves per area but this was reduced to 16x16 resulting in 256 force curves per area. A retraction delay of 100ms (Sulchek et al. 2005) allowed the tip to rest on the surface and facilitating bond formation. In this chapter 'area' refers to a $2\mu m^2$ region of cell surface selected at random for force mapping.

5.22 Rupture analysis

Force volume files were analysed using the JPK Data Processing software package. This involved a semi-automated curve by curve analysis of each force volume file. Steps were detected and characterised using a pre-programmed algorithm. Force curves were subjected to visual quality control by an operator and excluded if they did not meet certain criteria of a flat baseline, low noise and a return to baseline (i.e complete separation of tip and sample) to prevent false positives resulting from electrical noise. The location and number of steps were visualised using 2D maps generated in JPK data processing. The spread of rupture forces (step size) was recorded and the distribution plotted in histogram format. The bond strength between L-selectin and any potential ligands on the endometrial surface is interesting in the context of embryo adhesion because a smaller number of high affinity bonds might be required for embryo adhesion to the uterine wall. These experiments sought to investigate the potential role of L-selectin and MUC1 in embryo adhesion.

5.23 Functional characterisation of MUC1 at the endometrial surface

MUC1 is up-regulated by progesterone in secretory phase endometrium but human *in vitro* models suggest localised MUC1 removal by embryo derived factors is a requisite for implantation (Meseguer et al. 2001). However, the interaction between endometrial MUC1 and the trophoblast expressed adhesion mediator L-selectin has yet to be determined.

5.231 Rupture event identification

Before functionally characterising MUC1 expression, the Hec-1-A and Hec-1-B cells were force mapped using DNP-10 tips functionalised with GAPDH antibody. As the cell surface is devoid of GAPDH this experiment served as a negative control for surface binding. Three areas across the monolayer were selected at random from both cell types (A-F). Out of a total of 768 force curves from 3 areas just 4 step featuring curves were detected representing a 0.65% of all curves. When probing Hec-1-B there were just 16 out of 786 curves with steps, representing a 2.6% positive ratio. These experiments characterised the null-binding model and established confidence that the functionalization strategy and "step-fitting" parameters would not induce false positives.

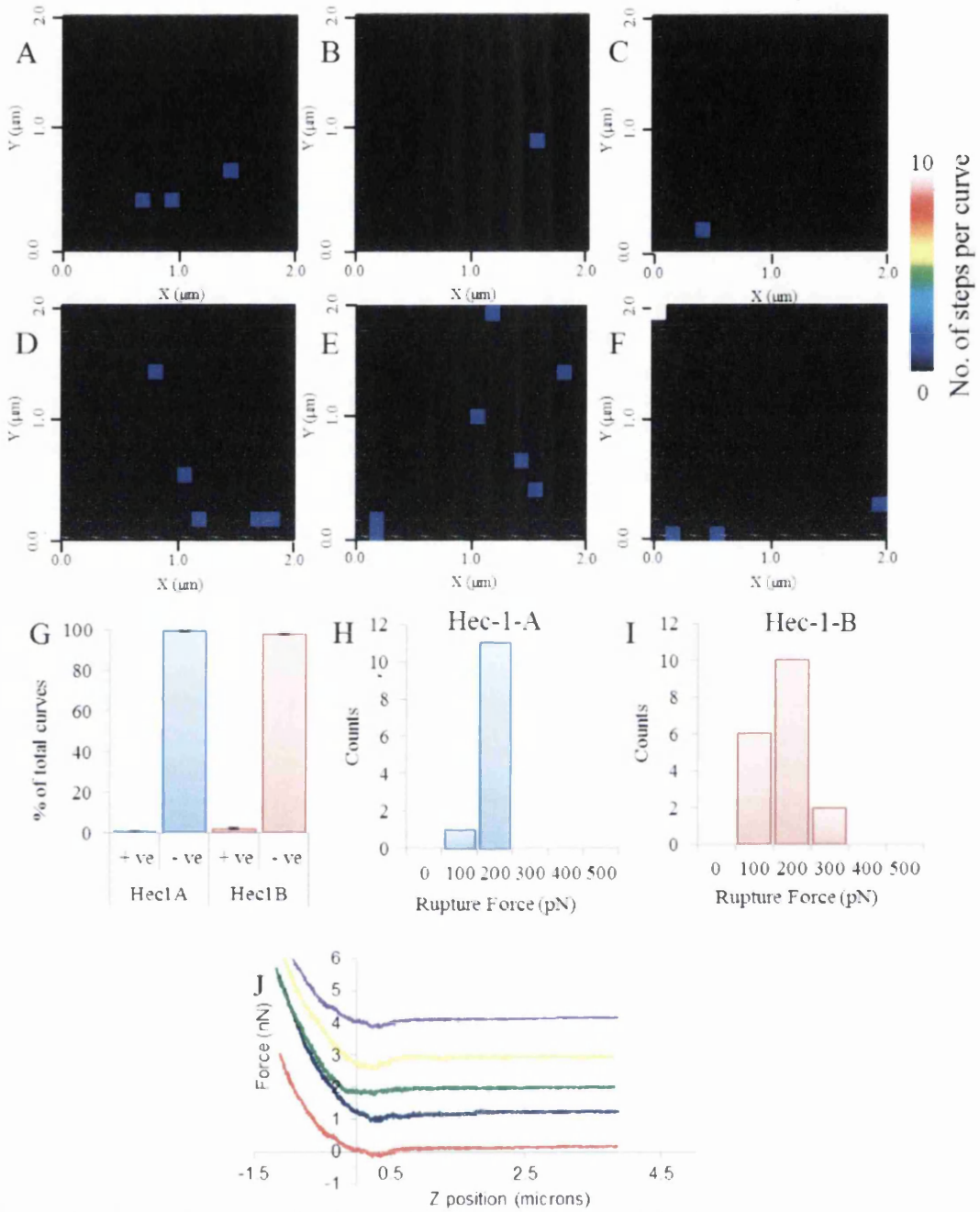

Figure 74: Detection, localization and rupture analysis of single GAPDH molecules on endometrial Hec-1-A and Hec-1-B cells using SMFS. (A-F) Maps showing number of steps on each force curve (2µm x 2µm) recorded with a GAPDH probe on living Hec-1-A (maps A-C) and Hec-1-B (maps D-F) cells. Steps (coloured pixels) were detected using JPK data processing software and colour scaled according to occurrence 1-10+. (G) Percentage of force curves considered positive [≥1 steps] or negative [<1 steps], data from all measured areas (n=3). (H-I) Distribution of step sizes measured on Hec-1-A and Hec-1-B respectively for all measured areas (n=3). (J) Example force curves with no steps. 3 areas (A-C,D-F) are shown from each experiment. Extracted data (G-I) from 3 areas (786 force curves).

5.232 MUC1 at the endometrial surface

Five areas of Hec-1-A and five areas of Hec-1-B were mapped resulting in 1280 force curves per cell line (5 x 256FC) (A-F). Hec-1-A was force mapped and 324/1280 force curves were positive for one or more steps, representing 25% of the total curves for this data set. Hec-1-B displayed increased MUC1 binding resulting in 538/1280 curves displaying steps (42% of total curves). This was consistent with data from chapter 3 showing MUC1 expression is higher in Hec-1-B than Hec-1-A. Hec-1-B is likely to present higher levels of MUC1 molecules at the surface explaining the increased binding.

The step size required for tip sample separation on Hec-1-A cell lines was between 100-200pN, whereas most steps occurring on Hec-1-B derived force curves were in the 200-300pN range (H+I).

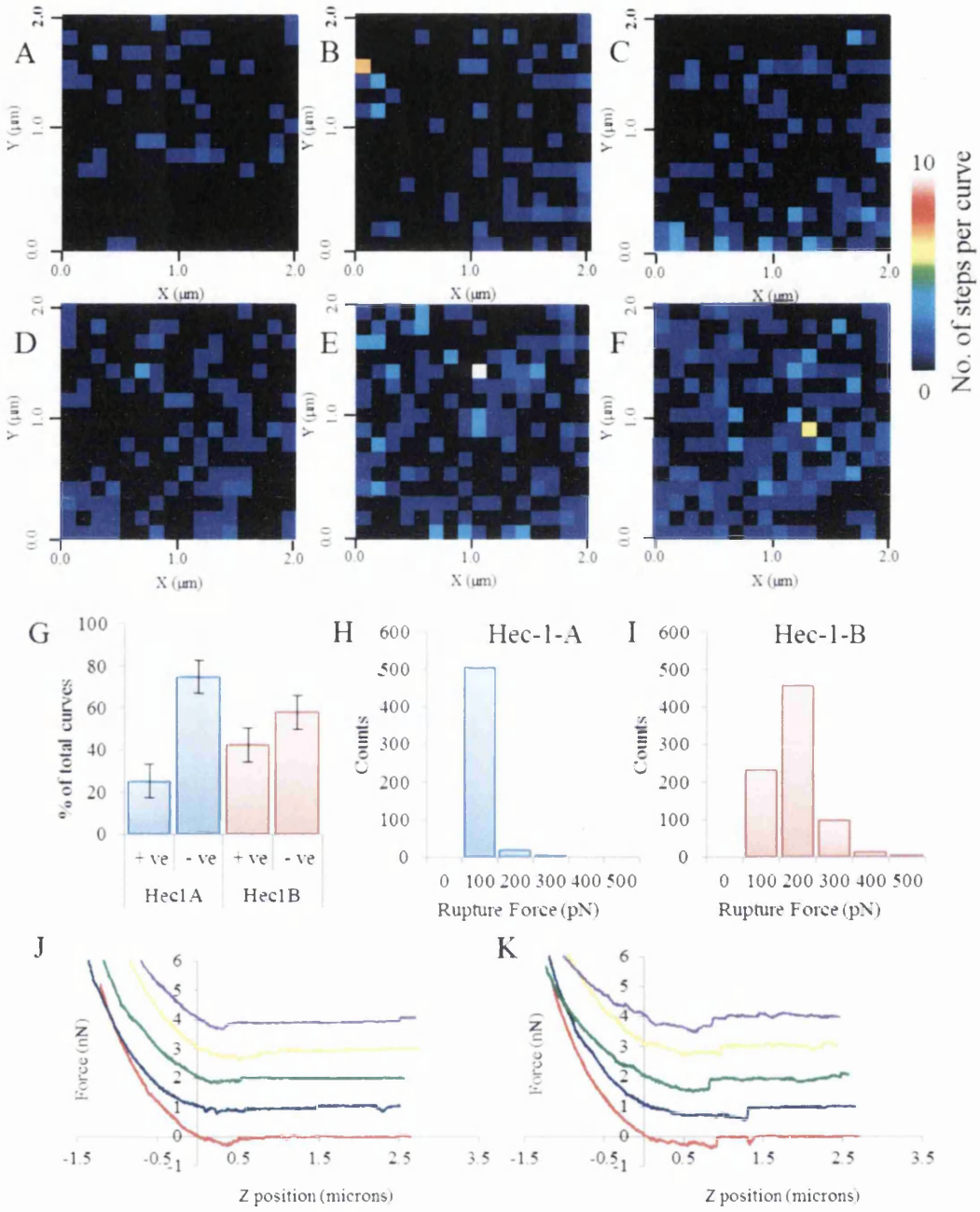

Figure 75: Detection, localization and rupture analysis of single MUC1-Antibody bonds on Hec-1-A and Hec-1-B cell monolayers using SMFS. (A-F) Maps showing number of steps on each force curve (2µm x 2µm) recorded with a MUC1 antibody probe on living Hec-1-A (maps A-C) and Hec-1-B (maps D-F) cells. Steps (coloured pixels) were detected using JPK data processing software and colour scaled according to occurrence (1-10+). (G) Percentage of force curves considered positive [≥1 event] or negative [<1 event], data from all measured areas n=10. (H-I) Distribution of step size measured on all Hec-1-A (n=5) and Hec-1-B (n=5) areas respectively. (J) Example force curves with no steps. (K) Example force curves with detectable steps. 3 representative areas (A-

C,D-F) are shown from each cell type. Extracted data (G-I) from 5 areas (1280 force curves). Blue and red bars represent Hec-1-A and Hec-1-B respectively

Taken together these results demonstrate that the AFM probe is able to quantify and spatially map the distribution of MUC1 protein across the endometrial cell monolayer. When probing the surface with anti-MUC1 the percentage of total force curves with steps was 25% and 42% in Hec-1-A and Hec-1-B respectively, compared to the 0.65% and 2.6% in the negative control.

In order to directly correlate any change in surface binding due to MUC1 surface expression, Hec-1-B cells were treated with siRNA treatments to knockdown MUC1. Force mapping was conducted on five $2\mu m^2$ areas from each treatment group using anti-MUC1 mAb tips, and step frequency was found to be decreased following reduction of MUC1 protein. The number of curves positive for one or more steps fell from 361/1280 to 81/1280, a change from 28% to 6% of the total curves (G). There was similarity between numbers of positive curves recorded on untreated basal Hec-1-B () (324/1280) and Hec-1-B treated with control siRNA () (361/1280) demonstrating there was no negative effect on surface binding as a result of the lipofectamine transfection vehicle or control siRNA and therefore that the observed measurements could be attributed to the loss of MUC1. In the control samples step size was mainly between 200-300pN, while a small number of steps were shown to be between 200-600pN in size (H). Large bond rupture forces may result from the breaking of multiple MUC1-antibody bonds, given that multiple binding is less likely the occurrence of such events would be infrequent. The data clearly shows a decrease in steps occurring at higher forces; 200-300pN (305 steps) 300-400pN (61 steps) 400-500pN (13 steps) and 500-600pN (4 steps). With each 100pN increment, the number of detected steps decreased. Reduction of MUC1 expression resulted in a loss of surface associations greater than 200pN in strength, but binding did remain in the 100-200pN range (I).

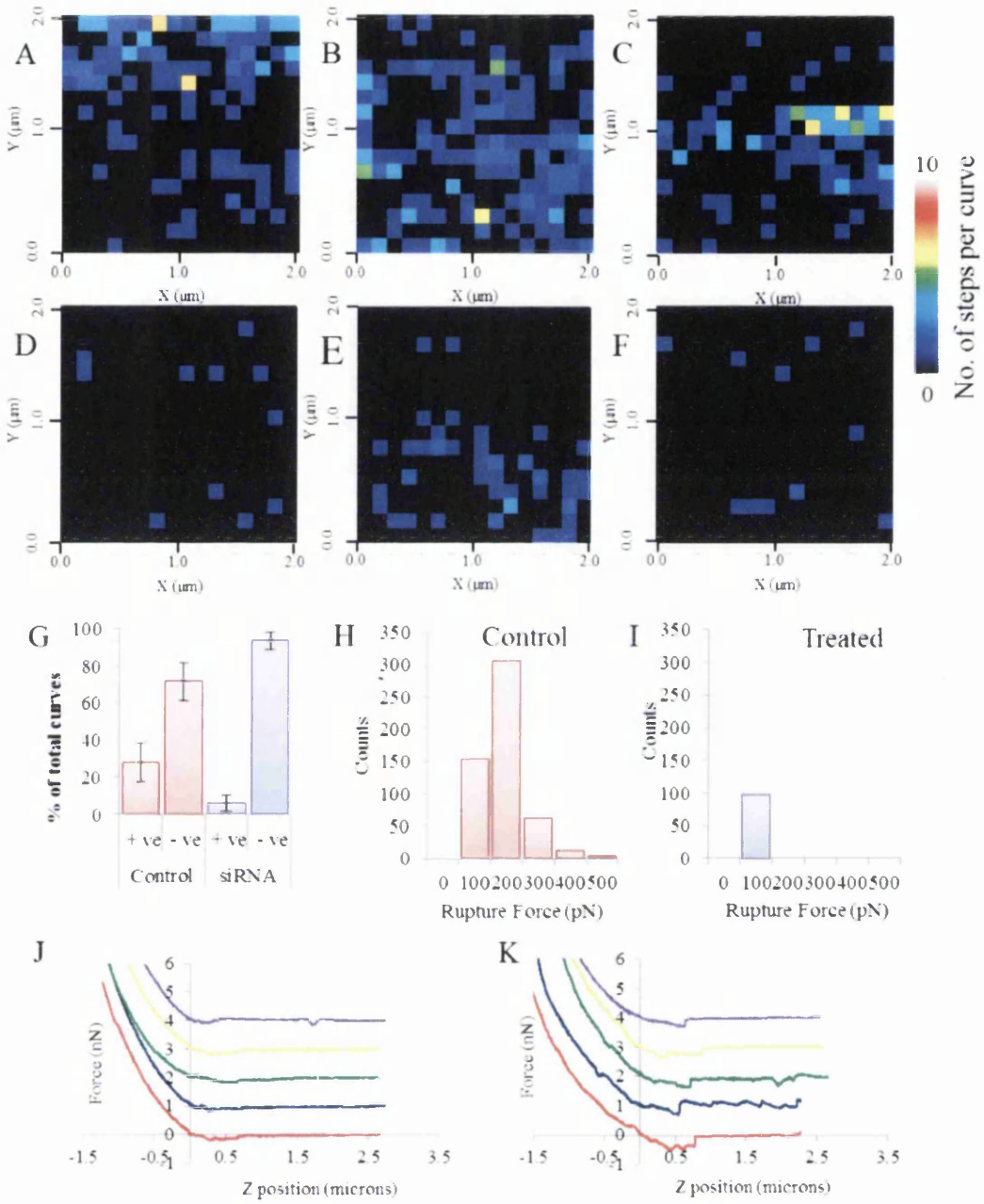

Figure 76: Detection, localization and rupture analysis of single MUC1 molecules on endometrial Hec-1-B cells following siRNA treatment using SMFS. Force Imaging living Hec-1-B cells using single-molecule AFM. (A-F) Maps showing number of steps on each force curve (2µm x 2µm) recorded with a MUC1 antibody probe. (A-C) Scrambled siRNA treatment. (D-F) Specific MUC1 siRNA treatment. Steps (bright pixels) were detected using JPK data processing software are colour scaled according to occurrence. (G) Percentage of force curves considered positive [≥1 step] or negative [<1 step], data from all measured areas n=10. (H-I) Distribution of step size measured on scrambled siRNA and MUC1 siRNA respectively. 3 representative areas (A-C,D-F) are shown from each treatment. Extracted data (G-I) from 5 areas (1280 force curves)

5.24 Functional characterisation of L-selectin ligands at the endometrial surface

Steps were fitted to retraction curves using the JPK "step fitting" program. Within the parameters of the software the significance value of $1x10^{-4}$ dictates that that there is less than 1/1000 chance the identified steps are the results of noise. As the bond strength of the L-selectin binding that may characterises the initial tethering between the embryo and the uterine epithelium is not known, it cannot be used to identify the bond here, rather these experiments rely on the step fitting algorithm to clearly differentiate steps from background noise to a high degree of probability. If the probe is calibrated by ramping into a hard surface and calculating D_{sens} then the size of the steps is fully quantitative and may identify a characteristic L-selectin binding event. Here we use SMFS to quantify the interaction between L-selectin and the endometrial epithelium and investigate the effect on this interaction following loss of MUC1. Nine $2\mu m^2$ areas of Hec-1-A monolayer were selected at random for force mapping, three areas from each of the three biological repeats (Figure 77A-I). Out of 2304 force curves only 219 were positive for step(s), representing a 9% of the total curves (Figure 77J). Step size was in the 300-400pN range, although significant numbers of steps did occur between 100-600pN (Figure 77K). Percentages of curves positive for step(s) and step size were plotted for each area in order to examine variation between areas (Figure 77L-M). Average step size across areas 1-9 were between 97-301pN (Figure 77L). With the exception of area 1 (which had only 1 bond rupture) the average step size across all remaining areas was between 200pN and 301pN (Figure 77L).

The rupture force required for separation of L-selectin and its ligands on the endometrial surface of Hec-1-A did not show great variation between cells and suggests a characteristic interaction (Figure 77). These data suggest that the representative bond strength between L-selectin and a ligand expressed on Hec-1-A is between 200-300pN.

The number of steps in 2 areas (Figure 77H+I), was elevated relative to the other 7 areas (Figure 77A-G). Analysis of area H resulted in 25% curves with steps and area I, 17% of curves with steps, these figures represented 4.87 fold and 2.86 fold increases in step frequency compared to the remaining 7 areas which averaged 6%. This suggests that certain cells across the Hec-1-A monolayer have increased affinity for L-selectin, possibly through expression of L-selectin ligands leading to the notion of an endometrial monolayer with regions of high L-selectin affinity. This corresponds to the observation that MUC1 is expressed in a heterogeneous pattern of across the

endometrial monolayer (Chapter 3), and with the HCS data that showed approximately 7.5% of Hec-1-A cells expressed high MUC1 protein relative to the rest of the monolayer. As MUC1 is able to host sLe^x moieties required for L-selectin binding it is plausible to suggest that increased MUC1 in certain cells accounts for the increased frequency of L-selectin binding. These experiments show for the first time a functional difference between areas of the live endometrial monolayer in terms of frequency of L-selectin binding, which could be related to MUC1 expression patterning on this tissue.

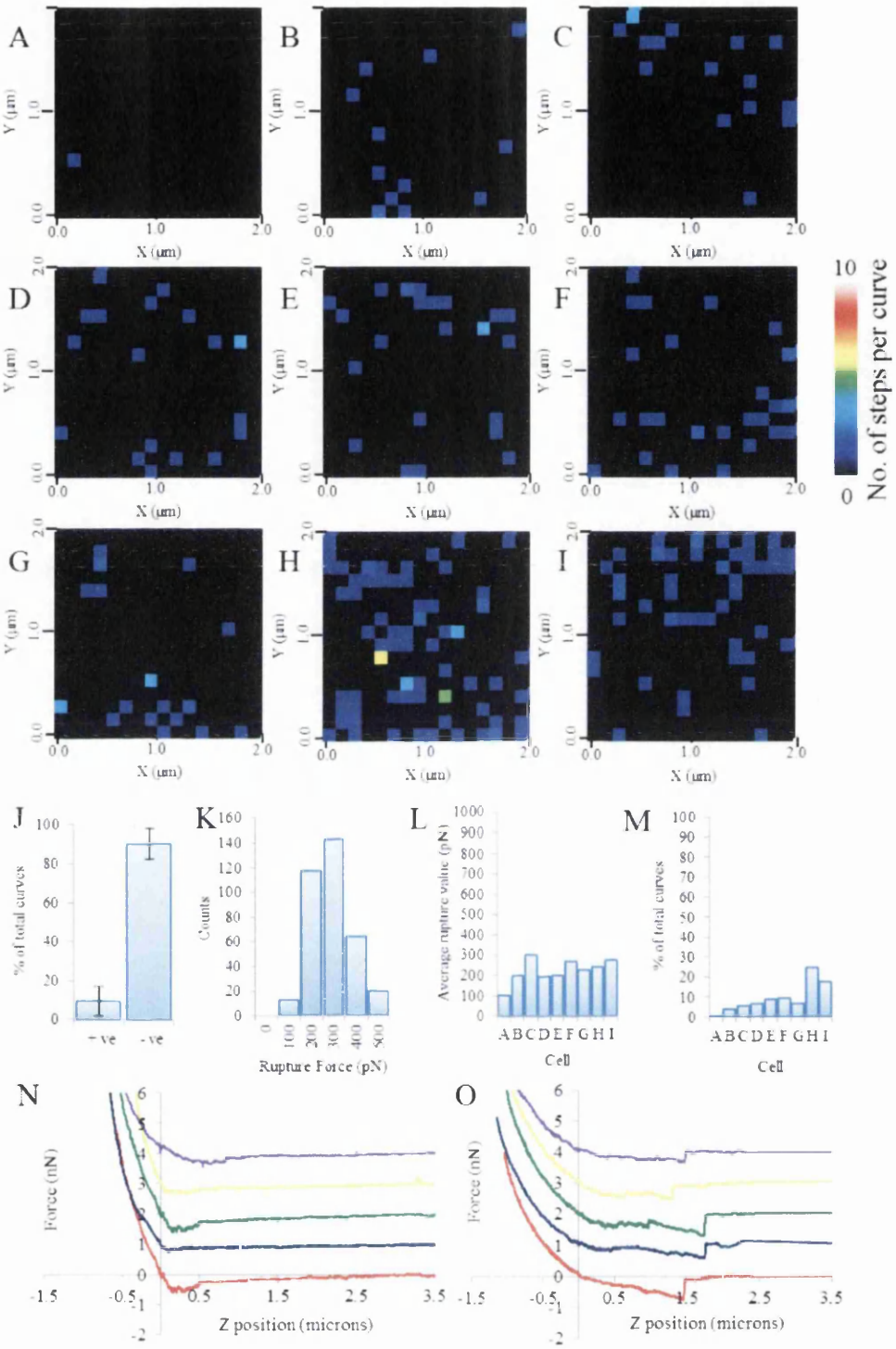

Figure 77: Detection, localization and rupture analysis of L-selectin ligands on endometrial Hec-1-A cells using SMFS. (A-I) Maps showing number of steps on each force curve (2µm x 2µm) of Hec-1-A cell surface recorded with a L-selectin functionalised probe. Steps (coloured pixels) were detected using JPK data processing

software are colour scaled according to occurrence (0-10+). (J) Percentage of force curves considered positive [≥1 step] or negative [<1 step], data from all measured areas (n=9). (K) Distribution of step size, compiled data from all measured areas (n=9). (L) Average step size from steps on areas 1-9. (M) Percentage of total curves featuring 1 or more steps on areas 1-9. (N) Example of no step force curves. (O) Examples of force curves showing a step. Extracted data (J-M) from nine areas (2304 force curves). Blue bars indicate Hec-1-A cell line.

The Hec-1-B cell line is a high expressing model for MUC1 protein. In order to investigate whether elevated MUC1 expression in Hec-1-B resulted in increased or decreased L-selectin binding efficiency, it was also probed with L-selectin functionalised tips. Step fitting analysis detected steps on 239/2304 force curves, representing 10% of the total (Figure 79: Detection, localization and rupture analysis of L-selectin ligands on endometrial Hec-1-A cells treated with MUC1 siRNA using SMFS. (A-F) Maps showing number of steps on each force curve (2μm x 2μm) of Hec-1-A cell surface recorded with a L-selectin functionalised probe. Steps (coloured pixels) were detected using JPK data processing software are colour scaled according to occurrence (0-10+). (G) Percentage of force curves considered positive [≥1 step] or negative [<1 step], data from all measured areas (n=9). Purple bars indicated MUC1 siRNA treatment.

J). Step sizes were mainly in the 300-400pN range, although steps did occur across the whole 100-600pN spectrum (Figure 79: Detection, localization and rupture analysis of L-selectin ligands on endometrial Hec-1-A cells treated with MUC1 siRNA using SMFS. (A-F) Maps showing number of steps on each force curve (2μm x 2μm) of Hec-1-A cell surface recorded with a L-selectin functionalised probe. Steps (coloured pixels) were detected using JPK data processing software are colour scaled according to occurrence (0-10+). (G) Percentage of force curves considered positive [≥1 step] or negative [<1 step], data from all measured areas (n=9). Purple bars indicated MUC1 siRNA treatment.

K). When compared, the number of force curves displaying L-selectin surface binding on Hec-1-A (219/2304, 9% of total) and Hec-1-B (239/2304, 10% of total) monolayers are both similar. This suggests that affinity for L-selectin is not totally dependent on absolute MUC1 expression levels (as Hec-1-B is a much higher expresser), it may be that variations in MUC1 structure such as the VNTR length or glycosylation status could influence L-selectin binding. Additionally, step size analysis showed a very

similar distribution of L-selectin rupture forces between both cell types (Figure 77K and Figure 79: Detection, localization and rupture analysis of L-selectin ligands on endometrial Hec-1-A cells treated with MUC1 siRNA using SMFS. (A-F) Maps showing number of steps on each force curve (2μm x 2μm) of Hec-1-A cell surface recorded with a L-selectin functionalised probe. Steps (coloured pixels) were detected using JPK data processing software are colour scaled according to occurrence (0-10+). (G) Percentage of force curves considered positive [≥1 step] or negative [<1 step], data from all measured areas (n=9). Purple bars indicated MUC1 siRNA treatment.

K) with the most commonly occurring step size being 300-400pN. This result further supported the idea that total MUC1 expression does not regulate the binding of L-selectin to the uterine epithelium. Whilst there were fewer steps detected when probing with L-selectin relative to MUC1 mAb, there were more than detected with the GAPDH mAb negative control (), which suggests a ligand for L-selectin was present at the surface of Hec-1-A and Hec-1-B.

Hec-1-B cells were then analysed across nine areas to assess for variation across the monolayer. Two areas (Figure 79: Detection, localization and rupture analysis of L-selectin ligands on endometrial Hec-1-A cells treated with MUC1 siRNA using SMFS. (A-F) Maps showing number of steps on each force curve (2μm x 2μm) of Hec-1-A cell surface recorded with a L-selectin functionalised probe. Steps (coloured pixels) were detected using JPK data processing software are colour scaled according to occurrence (0-10+). (G) Percentage of force curves considered positive [≥1 step] or negative [<1 step], data from all measured areas (n=9). Purple bars indicated MUC1 siRNA treatment.

H+I) displayed elevated average step size when compared to the other 7 areas (Figure 79: Detection, localization and rupture analysis of L-selectin ligands on endometrial Hec-1-A cells treated with MUC1 siRNA using SMFS. (A-F) Maps showing number of steps on each force curve (2μm x 2μm) of Hec-1-A cell surface recorded with a L-selectin functionalised probe. Steps (coloured pixels) were detected using JPK data processing software are colour scaled according to occurrence (0-10+). (G) Percentage of force curves considered positive [≥1 step] or negative [<1 step], data from all measured areas (n=9). Purple bars indicated MUC1 siRNA treatment.

L). The combined average step size from L-selectin-ligand separation occurring over the first 7 areas was 154pN, while area H averaged 410pN, a 2.65 fold increase when compared to the first 7 areas. The second anomalous area, I, displayed average step size of 873pN, a 5.63 fold increase compared to the first 7 areas. These areas with large step sizes also displayed increased numbers of steps occurring across the $2\mu m^2$ region. When combined, the first 7 areas had low numbers of curves featuring steps (5% of the total) while areas H+I showed increased frequency of these curves (15% and 39% of all curves from these areas) representing a 2.82 fold and 7.01 fold increases in numbers of

curves with one or more steps respectively.

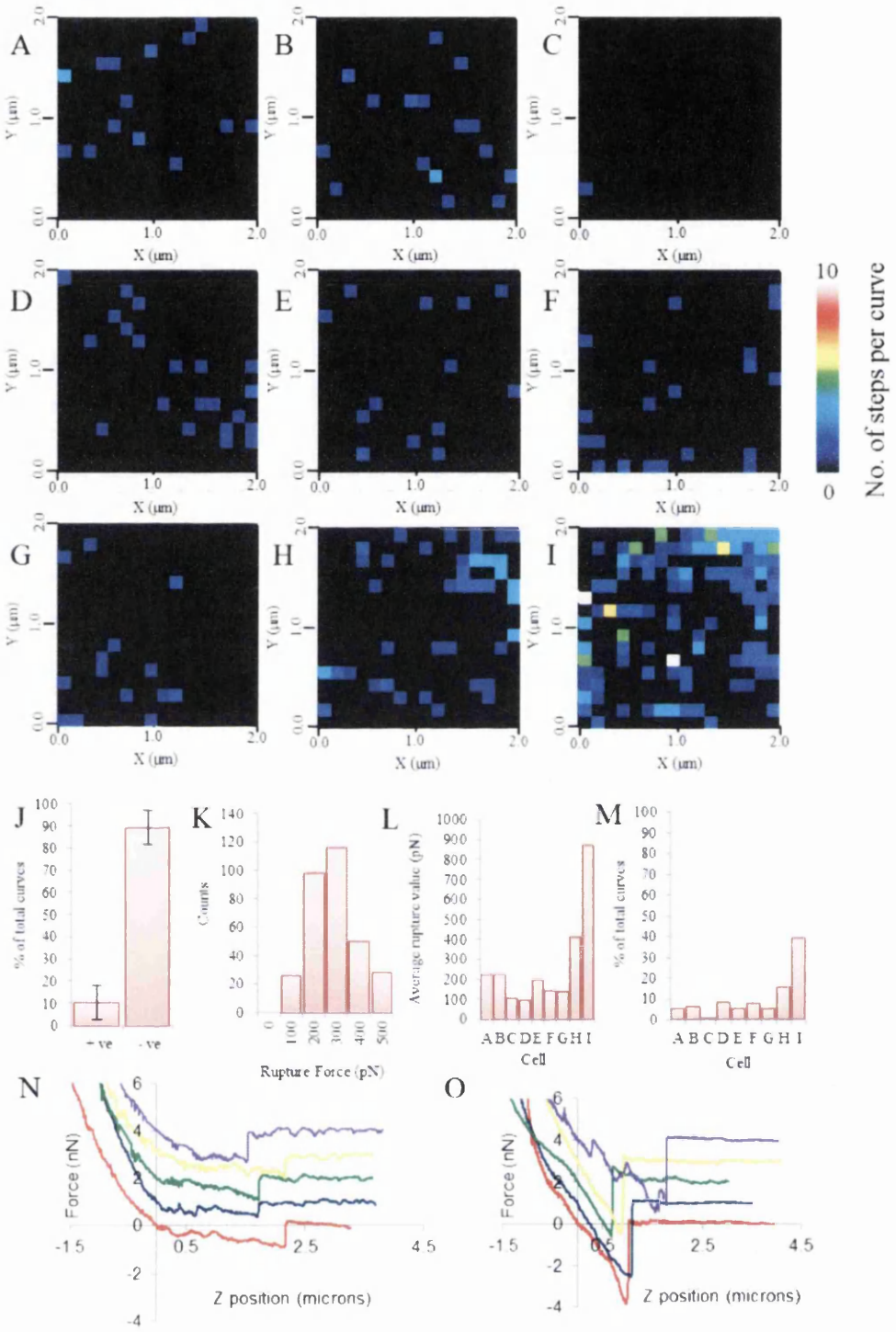

Figure 78: Detection, localization and rupture analysis of L-selectin ligands on endometrial Hec-1-B cells using SMFS. (A-I) Maps showing number of steps on each force curve (2µm x 2µm) of Hec-1-B cell surface recorded with a L-selectin functionalised probe. Steps (coloured pixels) were detected using JPK data processing software are colour scaled according to occurrence (0-10+). (J) Percentage of force curves considered positive [≥1 step] or negative [<1 step], data from all measured areas

(n=9). (K) Distribution of step sizes, compiled data from all measured areas (n=9). (L) Average step size from events on areas 1-9. (M) Percentage of total curves featuring 1 or more steps on areas 1-9. (N) Examples of force curves featuring steps from area (H). (O) Subset of force curves from area (I). Extracted data (J-M) from nine areas (2304 force curves). Red bars indicate Hec-1-B cell line.

Certain Hec-1-B cells had an increased number of surface binding events (steps) and the force require for bond separation of these bonds (step size) was elevated in these cells (Figure 79: Detection, localization and rupture analysis of L-selectin ligands on endometrial Hec-1-A cells treated with MUC1 siRNA using SMFS. (A-F) Maps showing number of steps on each force curve (2μm x 2μm) of Hec-1-A cell surface recorded with a L-selectin functionalised probe. Steps (coloured pixels) were detected using JPK data processing software are colour scaled according to occurrence (0-10+). (G) Percentage of force curves considered positive [≥1 step] or negative [<1 step], data from all measured areas (n=9). Purple bars indicated MUC1 siRNA treatment.

L+M). In contrast the variation of steps across Hec-1-A cell monolayers was limited to number only and the force required to break these bonds was more consistent across each area (Figure 77L+M).

These results document a second example of inter-monolayer heterogeneity of L-selectin binding to the cell surface in an endometrial *in vitro* model. Some regions of monolayer displayed high-strength bonds requiring large rupture forces for separation (Figure 79: Detection, localization and rupture analysis of L-selectin ligands on endometrial Hec-1-A cells treated with MUC1 siRNA using SMFS. (A-F) Maps showing number of steps on each force curve (2μm x 2μm) of Hec-1-A cell surface recorded with a L-selectin functionalised probe. Steps (coloured pixels) were detected using JPK data processing software are colour scaled according to occurrence (0-10+). (G) Percentage of force curves considered positive [≥1 step] or negative [<1 step], data from all measured areas (n=9). Purple bars indicated MUC1 siRNA treatment.
N+O), which were up to 4nN in extreme cases (Figure 79: Detection, localization and rupture analysis of L-selectin ligands on endometrial Hec-1-A cells treated with MUC1 siRNA using SMFS. (A-F) Maps showing number of steps on each force curve (2μm x 2μm) of Hec-1-A cell surface recorded with a L-selectin functionalised probe. Steps (coloured pixels) were detected using JPK data processing software are colour scaled according to occurrence (0-10+). (G) Percentage of force curves considered positive [≥1

step] or negative [<1 step], data from all measured areas (n=9). Purple bars indicated MUC1 siRNA treatment.

O). Within the context of the endometrial cell line model, the cells that exhibit increased frequency of high-strength interactions could have significantly increased affinity for L-selectin (and therefore the embryo). It is possible that these cells express significantly increased MUC1 but that MUC1 must be appropriately decorated with the correct carbohydrate moieties to allow L-selectin to bind.

Force curves from this data set suggest the extracellular domain of L-selectin is able to bind to the surface of endometrial epithelial cells. However the variation in step frequency between Hec-1-A and Hec-1-B suggested that L-selectin recognition was not entirely dependent on levels of MUC1 expressed by cells. Hec-1-A and Hec-1-B cells were treated with MUC1 siRNA to reduce apical expression of the protein and the effect on L-selectin binding is further investigated.

Following MUC1 siRNA treatment six areas across the Hec-1-A monolayer (total curves: 3072) and eight areas across the Hec-1-B monolayer (total curves: 2816) were selected at random for force mapping with L-selectin functionalised tips (and). The curves were analysed using the "step-fitting" algorithm and steps were detected in only 2% of total force curves following MUC1 knockdown, compared to 9% in untreated Hec-1-A areas. In Hec-1-B, steps were identified in 14% of the total curves, a slight increase when compared to 10% in the control. However, this increase may be the result of area (B) which displayed uncharacteristically high binding and could have affected the average (B), and could be a consequence of the heterogeneous monolayer. If area B is excluded from the analysis then the number of L-selectin curves is reduced to 3.5%.

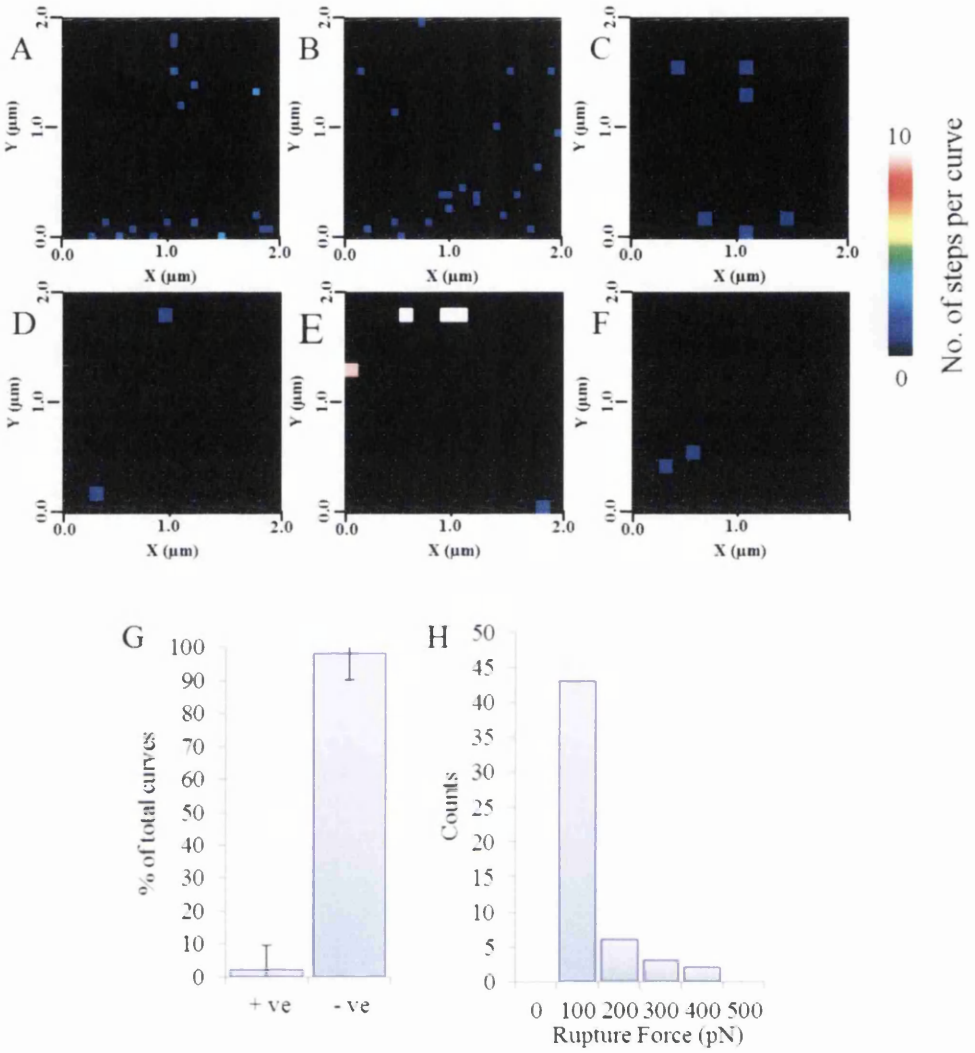

Figure 79: Detection, localization and rupture analysis of L-selectin ligands on endometrial Hec-1-A cells treated with MUC1 siRNA using SMFS. (A-F) Maps showing number of steps on each force curve (2µm x 2µm) of Hec-1-A cell surface recorded with a L-selectin functionalised probe. Steps (coloured pixels) were detected using JPK data processing software are colour scaled according to occurrence (0-10+). (G) Percentage of force curves considered positive [≥1 step] or negative [<1 step], data from all measured areas (n=9). Purple bars indicated MUC1 siRNA treatment.

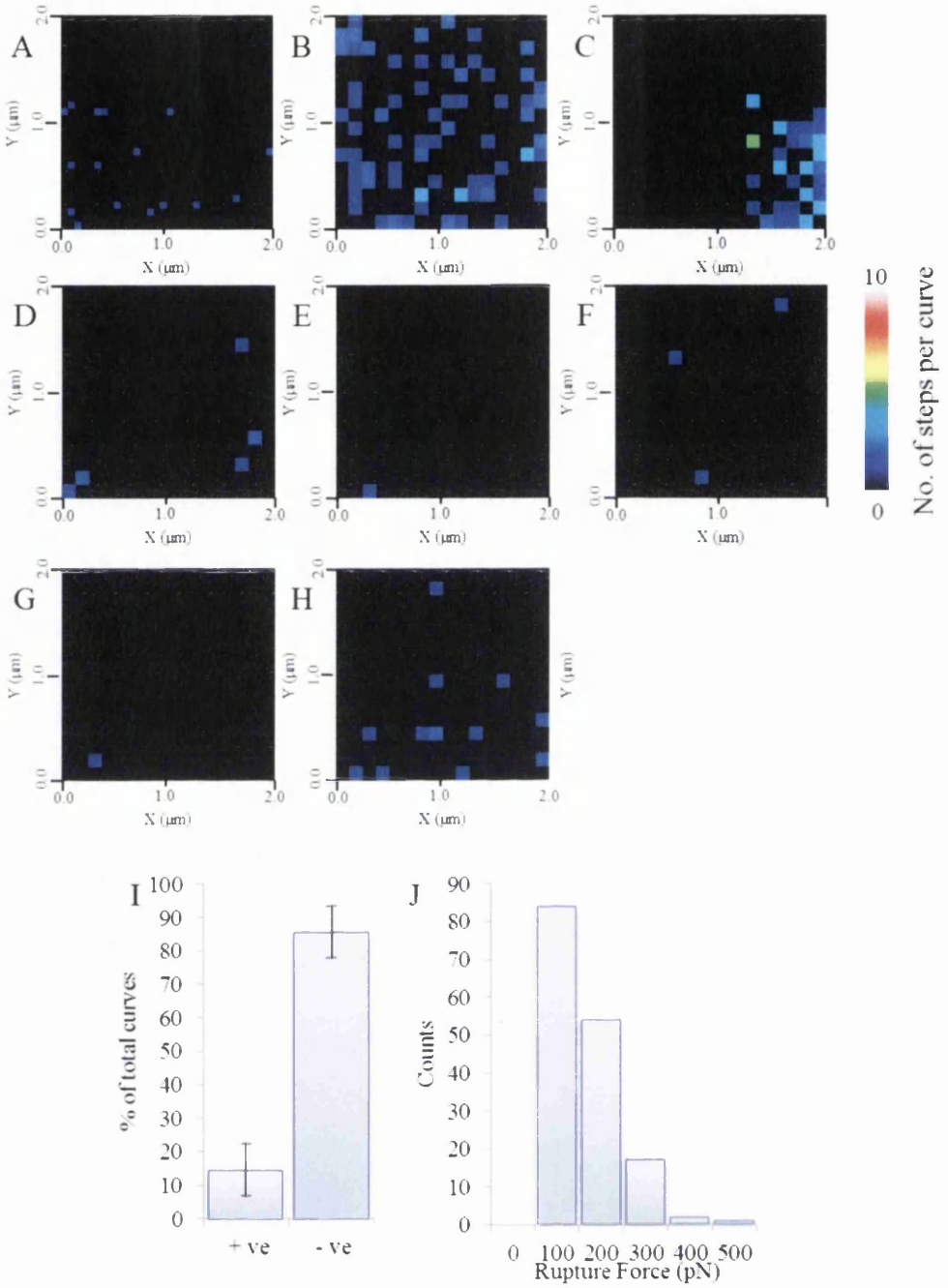

Figure 80: Detection, localization and rupture analysis of L-selectin ligands on endometrial Hec-1-B cells treated with MUC1 siRNA using SMFS. (A-F) Maps showing number of steps on each force curve (2µm x 2µm) of Hec-1-B cell surface recorded with an L-selectin functionalised probe. Steps (coloured pixels) were detected using JPK data processing software are colour scaled according to occurrence (0-10+). (G) Percentage of force curves considered positive [≥1 step] or negative [<1 step], data from all measured areas (n=9). Purple bars indicated MUC1 siRNA treatment.

The average step size for Hec-1-A and Hec-1-B monolayers was reduced following MUC1 knockdown (H and J), with most steps measuring 100-200pN, whereas step size

was typically 300-400pN on untreated monolayers (Figure 77K and Figure 79: Detection, localization and rupture analysis of L-selectin ligands on endometrial Hec-1-A cells treated with MUC1 siRNA using SMFS. (A-F) Maps showing number of steps on each force curve (2μm x 2μm) of Hec-1-A cell surface recorded with a L-selectin functionalised probe. Steps (coloured pixels) were detected using JPK data processing software are colour scaled according to occurrence (0-10+). (G) Percentage of force curves considered positive [≥1 step] or negative [<1 step], data from all measured areas (n=9). Purple bars indicated MUC1 siRNA treatment.

K). The reduction of MUC1 expression at the cell surface resulted in a corresponding reduction of L-selectin average rupture force (step size) and in a reduction of the number of ruptures (steps) detected in Hec-1-A and Hec-1-B cells. As L-selectin binding is mediated through sLe^x epitopes and MUC1 reduction decreases this binding in terms of strength and frequency it is plausible to suggest that these epitopes are hosted by MUC1, and it is the MUC1:L-selectin interaction that is being detected. However, it is likely that variation in glycosylation for example through alterations in glycosyl-transferase enzyme expression, further regulates this adhesive interaction.

5.25 Sialyl Lewis x distribution patterns

MUC1 knockdown using siRNA reduces the binding of L-selectin to the surface of Hec-1-A and Hec-1-B cells. While this does suggest that MUC1 is able to mediate L-selectin binding, the surface recognition events occurring between AFM tips and cell surface were more frequent when tips were functionalised with a MUC1 antibody (raised against the naked VNTR peptide) than when compared to L-selectin (which requires glycosylated epitopes for recognition). This suggests that not all MUC1 present at the apical cell surface is presenting the epitopes required for L-selectin recognition. The carbohydrate decoration of MUC1 is important to the functionality of the molecule, and the initial glycosylation step involves synthesis of GalNAc through α-O-glycosidic linkage to Serine/Threonine residues in the MUC1 VNTR naked peptide. This process is dependent on the glycosyltransferase enzyme GlcNAc6ST-2 (Okayama et al. 2011). The presence of sLe^x on Hec-1-A and Hec-1-B monolayers was investigated using two approaches; immunofluorescence against the carbohydrate epitope sLe^x (recognised by MECA-79 mAb) and mRNA quantification of a GlcNA2-6ST. Protein expression of sulphated sLe^x was quantified using the INCELL analyzer HCS system and mRNA expression of GlcNA2-6ST was assessed using qRTPCR.

Analysis of immunofluorescence images of Hec-1-A and Hec-1-B monolayers (Figure 82A and B) stained for sulphated sLe^x and counterstained with DAPI showed that, 6% of Hec-1-A and 15% of Hec-1-B cells were positive for sLe^x (Figure 82C). GlcNA2-6ST mRNA was found to be expressed at low levels in both cell types (Figure 82D). As GlcNA2-6ST is required for generation of L-selectin ligands, low expression could result in limited L-selectin binding as the MUC1 presenting at the apical surface may not be functionally receptive to L-selectin. Moreover, the images reveal certain cells across the monolayers that express very high sLe^x relative to the main population.

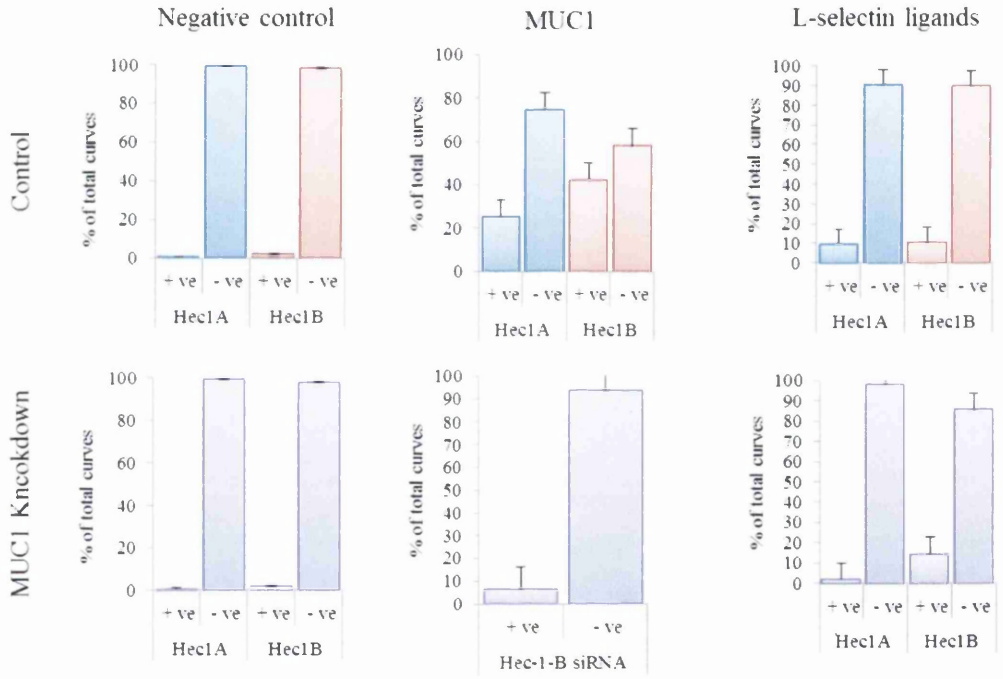

Figure 81: Combined effect on percentage of force curves that showed molecular bond ruptures

Heterogeneous expression of the L-selectin ligand seen in these cell lines is consistent with recent *in vivo* data (Nejatbakhsh et al. 2012) and could explain the frequent and strong force required to separate the L-selectin-ligand interactions observed on a small number of cells across the Hec-1-B monolayer (Figure 79: Detection, localization and rupture analysis of L-selectin ligands on endometrial Hec-1-A cells treated with MUC1 siRNA using SMFS. (A-F) Maps showing number of steps on each force curve (2µm x 2µm) of Hec-1-A cell surface recorded with a L-selectin functionalised probe. Steps (coloured pixels) were detected using JPK data processing software are colour scaled according to occurrence (0-10+). (G) Percentage of force curves considered positive [≥1

step] or negative [<1 step], data from all measured areas (n=9). Purple bars indicated MUC1 siRNA treatment.

O). The majority of cells across the endometrial monolayer of Hec-1-A and Hec-1-B cell lines are not decorated (to the same extent) with the epitope recognised by L-selectin and therefore would not present an adhesive surface to the embryo through this mechanism (Figure 82). Hec-1-A and Hec-1-B cell lines are described as poorly adhesive in implantation assays using JAR cells (human trophoblast) or mouse blastocysts (Harduf et al. 2009; Martín et al. 2000; Domínguez et al. 2010) when compared to other endometrial cell lines such as RL95. The low frequency expression of L-selectin ligands in these cells may contribute to this poor adhesiveness.

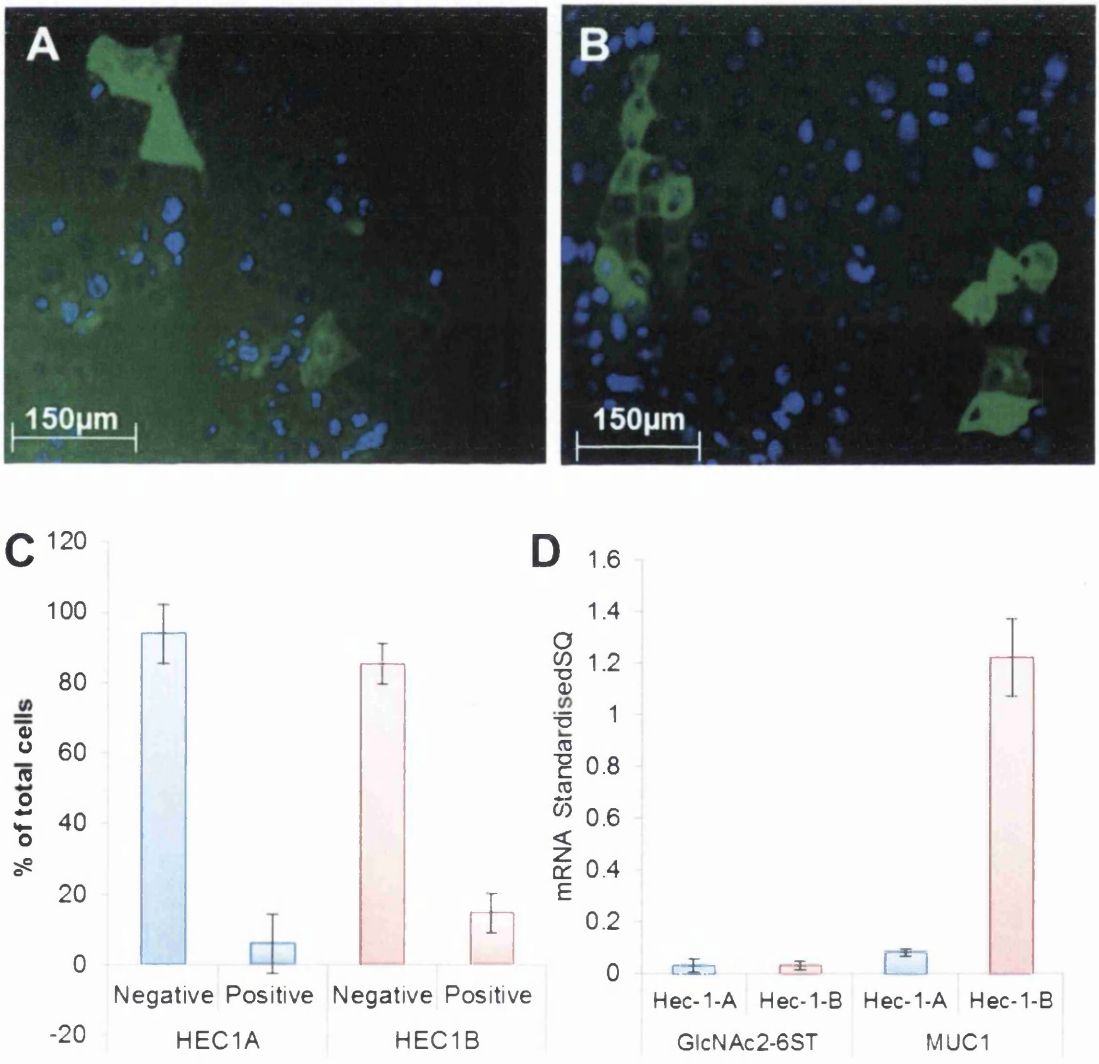

Figure 82: The level of glycosylation in Hec-1-A and Hec-1-B cell monolayers. (A+B) Hec-1-A and Hec-1-B cells were grown until 80% confluence and fixed and stained for MECA-79. (C) The INCELL analyzer 2000 protein analysis platform was used to determine the number of cells that were positive for MECA-79 expression. (D) mRNA expression of GlcNA2-6ST glycosyltransferase and MUC1.

5.3 Discussion

In this chapter, specific interactions between AFM tips functionalised with MUC1 mAb or L-selectin and the endometrial epithelium were investigated using direct and quantifiable approaches. For the first time in isolation, L-selectin protein has been shown to bind to the surface of endometrial epithelial cells. The strength (step size) and frequency (step count) of L-selectin binding can vary between cells across a population, and increased L-selectin affinity in a small number of cells correlates with increased expression of the L-selectin ligand sLe^x in a small cellular sub population. Down regulating the expression of MUC1 protein reduced the number of L-selectin binding events, suggesting that MUC1 hosts L-selectin ligands under the conditions tested.

The approach taken here was to functionalise the AFM tip using a rigid linker system and specialised software to detect 'steps' in the retraction force curves resulting from force induced bond ruptures. This allowed for the characterisation of the L-selectin interaction on live endometrial monolayers. As previously mentioned the bond rupture force can be affected by the rate of bond loading and functionalisation strategy. Alexandre Noy describes '*A force-induced bond rupture in the atomic force microscope is simply a thermally driven transition from the bound state into an unbound state over a potential energy surface that is constantly modified by the time- dependent potential of the loading spring'* (Noy 2011). However, the potential energy requirement for bond separation may be modified by the linker strategy used. Rigid linker systems preserve the Hookean spring model during bond separation whereas more flexible tethers (such as PEG) make the probe behave in a semi-harmonic fashion (Noy 2011). The implication of flexible linker molecules is that once an unbound state is reached the entropic elasticity of the tether pulls the molecules apart and prevents bond reformation. This means the first passage dissociation is characteristic of the bond rupture because the bond never returns to the equilibrium state (before energy maxima is reached). However, when a rigid linker is used the bond has a chance to reform and return to a state of equilibrium or existing in a near equilibrium state thus requiring a secondary dissociation event. In this situation the bond dissociation is determined by the rate of

bond loading, and so if the cantilever is withdrawn quickly the transition from the bound to unbound state will mimic the first passage dissociation that occurs with flexible tethers. However, if the cantilever is withdrawn slowly the system will be permitted to sample both bound and unbound states and exist at near equilibrium.

This first passage analysis of SMFS measurements is known as dynamic force spectroscopy where the rupture strengths for weak biochemical bonds are not constants but instead depend on the rate of force application and duration of (Evans & Ritchie 1997; Merkel et al. 1999; Evans 1998). The loading rate acting on the bond is not equivalent to the loading force applied by cantilever, due to the fact that the molecule being probed is akin to a non-linear spring and conforms to a freely jointed chain (FJC) model of elastic extension rather than the hookean spring. Analysing bond dissociation is a major challenge in AFM because the strength of bond rupture can easily be affected by experimental conditions. This highlights importance of maintaining a constant loading force, and thus it is important to keep the AFM cantilever and functionalization strategy consistent during dynamic SMFS experiments.

The direct functionalization of Si_2N_3 tips used in this chapter ensures is there is no loss of tip accuracy. In contrast, when tips are coated with successive metal layers such as gold (Takano et al. 1999), tungsten (Albrecht et al. 1990) or chromium (Oesterschulze et al. 1997) to improve surface properties prior to functionalization, the metallic layer(s) may add some 40-100nm to surface thickness (Barattin & Voyer 2008) and can negatively affect tip geometry. The direct silanization of Si_2N_3 results in the grafting of aliphatic chains onto the silica surface, via trichlorosilane groups, to form organosilane layers. Using 3-aminopropyl triethoxysilane (APTES) as the silanization reagent results in a monolayer with a terminal amino group (Riener et al. 2003), a distinct advantage when tethering proteins such as antigen (Ros et al. 1998) or antibody (Li et al. 2005). The terminal amino group can be reacted with glutaraldehyde creating an imine bond and resulting in a free aldehyde group to accept the protein of interest through an addition imine bond (Vinckier et al. 1995). This approach has been applied and reproduced in other biological systems such as probing synaptic vesicle fusion proteins (Yersin et al. 2003), glutamate receptor (Steiner et al. 2005) and glycosylphosphatidylinositol (GPI) membrane proteins (Roduit et al. 2008). The functionalization of silicon-based tips by the formation of organosilane layers is

therefore a convenient way to change the surface chemistry of a tip and a valuable complement to the metallization strategy.

5.31 MUC1 surface presentation

The Hec-1-A and Hec-1-B cell lines were used as high and low models of MUC1 expression but surface affinity for L-selectin was consistent across both cell monolayers. This suggested one of two possibilities; either MUC1 did not host sLe^x in Hec-1-A and Hec-1-B or not all MUC1 was not decorated with sLe^x in these cell lines. MUC1 gene knockdown reduced L-selectin binding demonstrating that MUC1 does host sLe^x. Moreover, HCS revealed that a small sub-population of cells strongly expressed the MECA-79 epitope corresponding to sLe^x. It is possible that these cells are targeted in the small subset of curves which show high L-selectin binding and therefore have an increased adhesiveness to L-selectin due to this increased glycosylation status.

SMFS was used to characterise the interaction between MUC1 and a mAb recognising MUC1 VNTR naked peptide across the live cell surface of the Hec-1-A and Hec-1-B EEC cell lines. The surface interactions observed between tips functionalised with MUC1 mAb and the cell surface were higher in Hec-1-B than Hec-1-A which supported data showing Hec-1-B to be a relative high expresser of MUC1. Moreover, down-regulation of MUC1 reduced surface binding clearly demonstrating that the AFM can be used to detect specific changes in surface expression of MUC1 protein. Rupture forces differed between the two cell lines, across Hec-1-A monolayers most ruptures occurred between 100-200pN. In contrast, Hec-1-B showed a clustering of rupture forces in the 200-300pN range.

Interactions between MUC1 and antibody have been previously studied, Sulchek and colleagues quantified the force required for MUC1-antibody bond separation and showed this to be directly proportional to the number of bonds (Sulchek et al. 2006) (Figure 83). The rupture force for a single bond between a single-chain variable fragment (scFv) fusion MUC1 antibody and a MUC1 peptide immobilised on a gold substrate was shown to be approximately 150pN (Sulchek et al. 2006). Each additional MUC1-scFv bond was shown to increase the required rupture force by ~150pN (Figure 83). In the present study the most frequent rupture force measured on Hec-1-A was between 100-200pN, which equates to a single MUC1-mAb interaction. Whilst Hec-1-B ruptures generally occurred in the 200-300pN range, suggesting the possibility that

this rupture resulted from multiple bond separations possibly due to the increased density of MUC1 on the Hec-1-B cell surface.

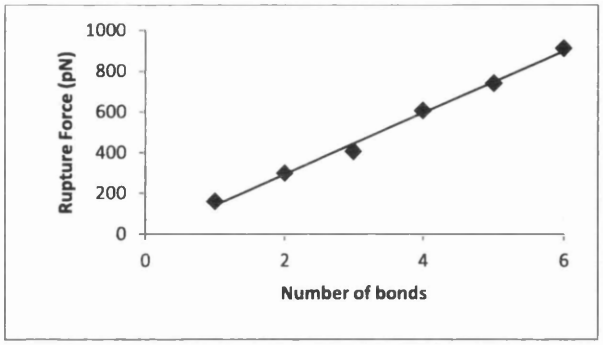

Figure 83: The measured rupture forces as a function of the number of MUC1-Antibody fragment bonds between the AFM tip and sample Graph adapted from (Sulchek et al. 2006)

In the context of implantation biology, the use of live cells to investigate MUC1 biology has many advantages including the carbohydrate decoration that is a requisite for L-selectin recognition and potential embryo implantation.

5.32 MUC1 and L-selectin ligand

AFM tips functionalised with recombinant L-selectin used to probe Hec-1-A and Hec-1-B allowed the detection of L-selectin binding events on 10% of all curves taken from both Hec-1-A and Hec-1-B cells and there was no difference in step frequency between the two cell lines. Hec-1-B expresses MUC1 at a much higher level than Hec-1-A, however this did not result in increased L-selectin binding through sLe^x. The bulk of MUC1 glycosylation consists of O-linked glycans with minimal presence of N-linked glycans on the VNTR protein core. The decoration of serine and threonine residues present in the VNTR that are targets of O-linked glycosylation and each VNTR motif is able to host five glycans (Figure 13) (Albrecht & Carraway 2011). It is unclear whether the primary amino acid sequence of MUC1 or the expression of fucosyltransferases determines sLe^x the content of the protein (López-Ferrer et al. 2000).

The VNTR region of MUC1 can vary from 20-125 repeats of the sequence $^{'N-}$ GSTAPPAHGVTSAPDTRPAP$^{-C'}$, influencing the length (and thus glycosylation) of the α sub-unit (extracellular ND domain) of the protein. The VUH45 antibody used in these experiments is raised against the VNTR naked peptide so variation in VNTR length between Hec-1-A and Hec-1-B could result in multiple binding to a single MUC1 molecule, thus increasing the rupture force required for bond separation.

The cell Hec-1-A and Hec-1-B cell lines are derived from endometrial adenocarcinoma and express under-glycosylated MUC1. This could be a consequence of the structural isoform (VNTR region), and also the pattern of glycosyltransferases expressed in these cells. Analysis of Hec-1-A and Hec-1-B for carbohydrate epitope sLe^x using MECA-79 mAb in a HCS for every cell across a population (10,000+ cells) revealed a small subset of cells that expressed the moiety. This was approximately 6% of Hec-1-A cells and 15% of Hec-1-B cells. The majority of both Hec-1-A and Hec-1-B cells exhibited very low expression (close to background).

These results support qualitative observations of functional patterning in primary tissue (Horne et al. 2002). Electron microscopy has provided compelling visual evidence for variation of MUC1 sialylation across epithelial monolayers of primary explants of healthy secretory phase endometrium (Campbell et al. 2000). Expression of the glycosyltransferase enzyme GlcNAc2-6ST has been shown to be low in both cell lines which support the protein data showing limited sLe^x expression as GlcNAc2-6ST is required for sLe^x generation.

5.33 Selectin ligands

Several AFM studies have reported P-selectin-sLe^x bonds. Rupture forces have been shown to range between 50pN (Askarova et al. 2013), 250pN (Zhang, Chen, et al. 2004) and 312pN on live capillary endothelial cells (Tsapikouni & Missirlis 2011), but vary depending on the functionalization strategy employed (Tsapikouni & Missirlis 2011). These forces are a similar order of magnitude to the forces required for L-selectin-sLe^x bond separation observed on live endometrial epithelial cell surfacess in this chapter; typically between 100-400pN. However, the very high, nano-newton scale L-selectin bond separation forces observed here on a small sub-population of cells appears to be an endometrial specific phenomena. Previous studies mounting a single (trophoblast derived) JAR cell onto an AFM cantilever, and bringing it into contact with monolayers of Hec-1-A cells for durations ranging from ms - 40mins have been attempted. A 1 minute interaction time between the JAR cell and the Hec-1-A cell layer resulted in significant adhesion (7.1 +/- 2 nN) while after 40mins adhesion increased further (16.0 +/- 4 nN) (Thie et al. 1998). This suggests that the time required for stable adhesion to occur between the embryo and the maternal surface meaning the initial embryo capture (possibly through selectins) is important.

Previous functional adhesion studies focusing on attachment rates of embryos or trophoblast derived cell lines (Lalitkumar et al. 2007; Mardon et al. 2007; Teklenburg & Macklon 2009b; Wang et al. 2012b) to endometrial monolayer or co-culture models and show the effect of certain implantation molecules and the effect of hormones on implantation success. Here we show that MUC1 can serve as a scaffold for the glycosylated epitope sLe^x and have characterised the binding between L-selectin and the endometrial epithelial cell surfacee showing it to be highly variable. While experiments detected both MUC1 expression and limited expression sLe^x on both cell types a co-localisation antibody study is necessary to demonstrate that the observed correlation represents functional activity on specific cells

.

Chapter 6 Thesis summary and conclusions

6.01 Summary of results

In this thesis the INCELL cell analyzer has been used for HCS to quantify the distribution of MUC1 protein across endometrial epithelial monolayers and revealed that ovarian hormones E_2 and P_4 can exert their influence in the endometrium by affecting the patterning of adhesion proteins such as MUC1. Additionally, for the first time integrated high resolution FD curve based AFM and live endometrial monolayers showing that the high MUC1 expressing cell line Hec-1-B was almost 2 fold more adhesive than Hec-1-A, and that this highly adhesive state was reduced following MUC1 gene silencing signifying that MUC1 contributes significantly to the non-specific mechanical adhesion in the endometrium. Finally single molecule force spectroscopy revealed insights into the surface distribution of MUC1 at molecular resolution on live cells which was again specifically targeted using gene silencing. Single molecule force spectroscopy showed that the Hec-1-A and Hec-1-B present ligands for L-selectin, while immunofluorescence imaging confirmed the presence of the endometrial L-selectin ligand, sLe^x on these cell surfaces. MUC1 gene silencing reduced L-selectin binding suggesting that it can act as a scaffold for sLe^x L-selectin ligands in the endometrium making the MUC1/L-selectin adhesion mechanism an important contributor to endometrial receptivity.

6.02 Adhesion molecule patterning

MUC1 is expressed in heterogeneous patterns across endometrial epithelial cell monolayers. The literature describes "small numbers of cells with increased MUC1 reactivity" (Quenby et al. 2007) and this heterogeneous patterning of MUC1 has been referred to as "characteristic MUC1 staining" (Singh et al. 2010). INCELL analyzer based HCS has for the first time quantified the proportion of cells in the population expressing high levels of an endometrial adhesion protein. Characteristic MUC1 staining patterns have been observed in Ishikawa cells (Singh et al. 2010) and secretory phase biopsies, and may relate to local sites of implantation. Primary tissue samples clearly illustrate differential expression patterns of MUC1 (Horne et al. 2005) (Figure 84) and demonstrate that the endometrial cell lines used for this project are good models for MUC1 presentation. The importance of MUC1 patterning is further highlighted by a correlation between increased numbers of high expressing cells and the infertile phenotype (Horne et al. 2005). The application of HCS to this *in vitro* cell line model

permits quantitative analysis of the heterogeneous patterning of MUC1 and can be applied to other adhesion proteins (Figure 84).

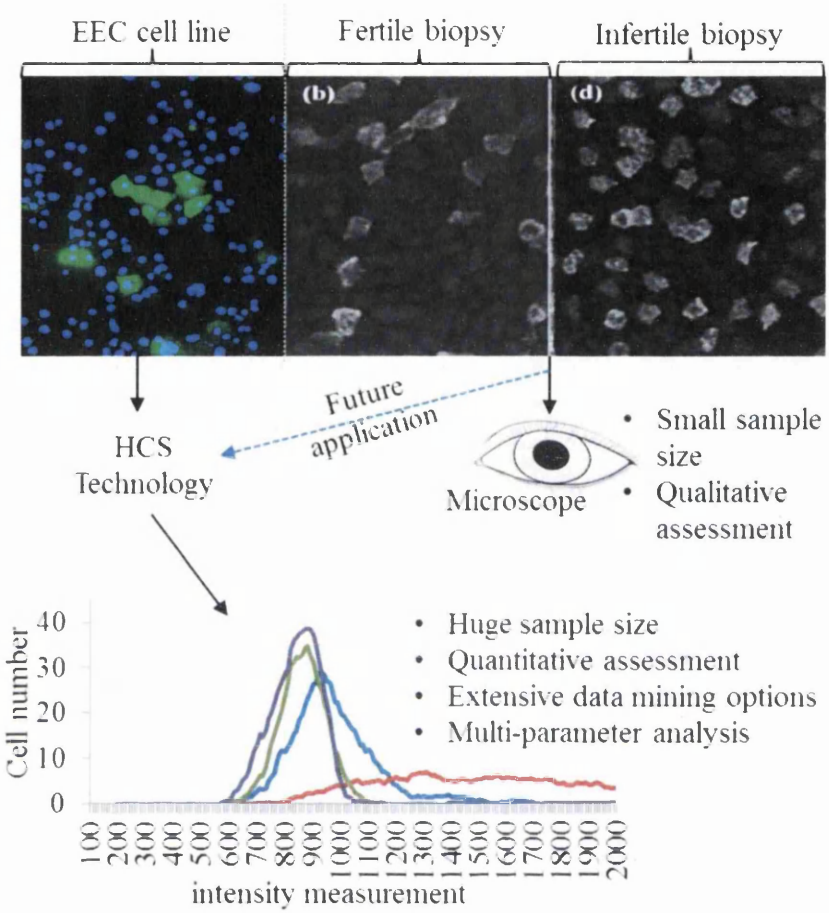

Figure 84: Integrating HCS with endometrial biopsies. Images show the comparison of MUC1 staining between EEC cell lines imaged and analysed using HCS and endometrial biopsies imaged using confocal microscopy (Horne et al. 2005). The histogram shows a comparison between MUC1 expression patterns in 4 EEC cell lines.

Despite a variety of emerging approaches such as genomics (Garrido-Gómez et al. 2013), secretomics (Cheong et al. 2013), and lipidomics (Vilella et al. 2013) there are no reliable endometrial markers of receptivity (Edgell et al. 2013). The application of HCS is complementary to these approaches, and could be used to screen endometrial biopsy tissue for patterns of biomarker expression and possibly, for example provide some insight into the suitability of individuals for IVF. Whilst obtaining uterine fluid required for secretomics, proteomics and lipidomics approaches is less invasive than endometrial biopsy required for HCS, uterine fluid contains abundant serum proteins (Hannan et al. 2009) which may mask low abundance secreted proteins in uterine fluid.

In contrast, HCS provides a direct quantifiable analysis adhesion molecule patterning of the epithelial cell layer that presents to the embryo.

HCS was able quantify very subtle changes in MUC1 distribution patterns resulting from ovarian hormone stimulation. In contrast to the subtle effects of hormones, specific gene silencing reduced MUC1 protein levels by 56% while the proportion of high expressing cells decreased 72%, demonstrating that the gene silencing using RNAi was more pronounced in the high expressing cells because of the higher basal transcript levels. Such detailed analysis highlights the power of HCS and informs and strengthens the biophysical observations in by providing rationale for the reduction in L-selectin binding affinity following MUC1 gene silencing.

6.03 MUC1 is adhesive

Several studies have suggested a role for MUC1 in human implantation, yet it has been implicated in both adhesive and anti-adhesive roles, and its expression is retained throughout the late secretory phase (Meseguer et al. 2001). If MUC1 is correctly categorised as an anti-adhesion molecule this presents a somewhat confusing paradox. The intrinsic heterogeneity of expression demonstrated by the molecule in the endometrium may define a receptive site for implantation or act as a quality control for embryos by blocking adhesion for defective embryos that lack paracrine signalling. Quantitative mapping of live Hec-1-A and Hec-1-B endometrial monolayers suggested MUC1 to be an adhesive component of the endometrial glycocalyx. MUC1 specific gene silencing clearly reduced the ability of the AFM tip to adhere to the cell surface and further supported this notion. Previous publications from our group reported increases in fixed cell surface roughness following hormone treatments and correlated roughness with MUC1 expression (Francis et al. 2009). The approach taken here was complementary to the surface roughness data but returns a wide range of nano-mechanical properties at high resolution, and takes into consideration live cells in a monolayer configuration. Gene silencing targeted MUC1, therefore the observed changes to the adhesion between the tip and cell surface can be directly attributed to loss of MUC1. Moreover, the reduction in adhesion following gene silencing proved to be significant despite the observed heterogeneity of the monolayer, directly linking MUC1 with adhesion and independent of other nano-mechanical properties. MUC1 has been described in the literature as an anti-adhesive molecule (Makiguchi et al. 1996), that is anti-adhesive to the embryo (Meseguer et al. 1998). Whilst MUC1 may regulate

embryo adhesion by masking the effect of other adhesion molecules, and the embryo has been shown to locally clear MUC1 after initial implantation (Meseguer et al. 2001), our observations suggest it likely that MUC1 is directly adhesive. Furthermore, the adhesive characteristics presented here, and the characteristic spontaneous shedding and cleavage of mucin proteins (Thathiah et al. 2003) provide a modus operandi for mechanical retardation of the embryo during the apposition stage of implantation. Once ensnared in a mucin cloud 'juxtacrine' signalling between the embryo and epithelium may reveal further adhesive contacts through targeted MUC1 clearance.

Peak force mode imaging of live cells is not routine (Pittenger et al. 2013) and there is only one other study of live mammalian cells using PFQNM mode (Heu et al. 2012), therefore a preliminary study was conducted using endometrial monolayers following fixation. When compared to subsequent live cell monolayers, fixed cells are shown to be representative of the live cell model. When combined with the distribution patterns these results suggest an endometrium with a distinctly heterogeneous adhesion profile which could result in regions of elevated and impaired receptivity.

It appears that MUC1 contributes significantly to the AML in these cell lines. As MUC1 is an adhesive component of the AML it is potentially able to to retard the embryo to allow for initial apposition against the endometrial epithelium, allowing specific interactions to occur.

6.04 MUC1 presents ligands for L-selectin

MUC1 has been shown to co-localised with the L-selectin ligand sLe^x (Hey & Aplin 1996) in endometrial epithelial cells. Carson showed that MUC1 functions as a scaffold for selectin ligands through the secretory phase of the menstrual cycle (Carson et al. 2000). Moreover, the HECA-452 and MECA-79 epitope selectin ligands have been shown to increase from proliferative to the secretory phase in fertile individuals (Lai et al. 2005; Horne et al. 2002). More recent studies from our group demonstrated not only an association of L-selectin ligand with menstrual cycle phase but also with fertility status (Margarit et al. 2009). Supported by the weight of clinical data surrounding L-selectin ligands, a further step has been taken here to interrogate the functional mechanism by which L-selectin ligand can mediate embryo attachment. SMFS AFM was used to detect the presence of MUC1 on the surface of two endometrial cells lines at molecular resolution. Again, gene silencing reduced specific surface interactions

detected with MUC1 mAb and provided a model with which to test the hypothesis that MUC1 hosts ligands for L-selectin. MUC1 gene silencing reduced L-selectin binding demonstrating for the first time that the affinity of L-selectin for the surface of endometrial cells was influenced by MUC1. While L-selectin binding was detected, surface binding was less than that of the MUC1 antibody suggesting that not all MUC1 expressed in these cells is functionally receptive to L-selectin. The application of SMFS is a unique approach in the endometrium and has been able to quantify the strength and frequency of L-selectin binding at nano-meter resolution, and complements adhesion assays using trophoblast spheroids (Harduf et al. 2009; Wang et al. 2012; Xiong et al. 2012; Tinel et al. 2000). The disparity of L-selectin binding affinity to cells across the monolayers is highlighted by a small proportion of Hec-1-B (and to a lesser extent Hec-1-A) cells that displayed altered L-selectin binding characteristics. These included increased binding frequency and greatly increased bond strength, suggesting that areas of the monolayer vary with respect to embryo affinity. Moreover, there is a strong correlation between the heterogeneous expression patterns of L-selectin ligands sLe^x in Hec-1-A and Hec-1-B cells and the heterogeneity in L-selectin binding across monolayers of these cells. MUC1 gene silencing treatment disproportionately reduced the size of the sub-population of high expressing cells, and resulted in the loss of strong L-selectin binding in Hec-1-B suggesting that the MUC1 high expressing cells associate with L-selectin binding. Moreover, ovarian hormones can subtly alter the proportions of high expressing cells, which was most notable in E_2 treated Ishikawa cells where numbers of MUC1 high expressing cells were reduced. The effect of ovarian hormones on cells expressing elevated adhesion molecules provides rationale for the impaired receptivity in hyperstimulated endometria because the sub-population of high expressing cells affected by hormones (excess E_2) could be important in embryo implantation.

In order to fully delineate the role of MUC1 and sLe^x with respect to L-selectin binding at the endometrial surface, a direct correlation needs to be made between sLe^x expression and L-selectin binding affinity. This objective could be met with a combination of fluorescence staining and targeted single molecule force spectroscopy, using an integrated AFM-confocal microscope. Studies of this nature are starting to emerge, for example lymphoma cells populations were stained for CD20 (cancer marker) and +ve cells were force mapped with a tip functionalised with rituximab, an

anti-CD20 monoclonal antibody targeted drug (Li et al. 2013), the resulting force curves were used to estimate the drug binding affinity to cancer cells. A similar strategy employed in the endometrial setting could compare a cohort of cells from each sub-population (high and low) for binding of embryo adhesion markers such as L-selectin. Once functional adhesion markers have been identified, HCS can be used to assess their expression and distribution in infertile pathologies.

A recurring theme throughout this thesis is the heterogeneity of the adhesion molecule expression in the endometrium, this has been shown independently using molecular biology and biophysical analysis. During the final stage of IVF a fertilised embryo is inserted into the endometrium in fluid using a slender catheter device, the fluid and embryo are expelled and any implantation site is random. A greater understanding of the molecular patterning that defines the adhesive characterises of the endometrium may help improve the current low success rates associated with IVF by identifying adhesion molecule patterns associated with infertility or regions within the endometrium that are more likely to be receptive to the embryo.

6.05 Final conclusions

Infertile pathologies such as ovulatory PCOS and unexplained infertility have been linked with high MUC1 expression and altered MUC1 patterning across the endometrial epithelium. The heterogeneous expression of MUC1 is likely to result in variation of receptivity across the endometrium.

AFM is a very valuable tool in determining the functional availability of MUC1 at the endometrial epithelial cell surface and has shown that levels of L-selectin binding are independent of total MUC1 expression and more likely to be dependent on glycosylation of MUC1. Sialyl lewis x is down regulated in PCOS, unexplained infertility and endometriosis. A small sub-population of endometrial cells expressed sialyl lewis x moieties and this corresponds with areas of elevated L-selectin affinity highlighting the importance of this mechanism in embryo implantation.

Bibliography

Ahmad SF, Chtcheglova LA, Mayer B, Kuznetsov SA, Hinterdorfer P. 2011. Nanosensing of Fcγ receptors on macrophages. *Analytical and bioanalytical chemistry*, 399(7), pp.2359–67.

Akoum A, Metz CN, Morin M. 2005. Marked increase in macrophage migration inhibitory factor synthesis and secretion in human endometrial cells in response to human chorionic gonadotropin hormone. *The Journal of clinical endocrinology and metabolism*, 90(5), pp.2904–10.

Albitar L, Pickett G, Morgan M, Davies S, Leslie KK. 2007. Models representing type I and type II human endometrial cancers: Ishikawa H and Hec50co cells. *Gynecologic oncology*, 106(1), pp.52–64.

Albrecht H, Carraway KL. 2011. MUC1 and MUC4: switching the emphasis from large to small. *Cancer biotherapy & radiopharmaceuticals*, 26(3), pp.261–71.

Albrecht TR, Akamine S, Carver TE, Quate CF. 1990. Microfabrication of cantilever styli for the atomic force microscope. *Journal of Vacuum Science & Technology A: Vacuum, Surfaces, and Films*, 8(4), pp.3386–3396.

Sharma A, Kumar P. 2012. Understanding implantation window, a crucial phenomenon. *J Hum Reprod Sci.*, Jan-Apr; 5, pp.2–6.

Alon R, Fuhlbrigge RC, Finger EB, Springer TA. 1996. Interactions through L-selectin between Leukocytes and Adherent Leukocytes Nucleate Rolling Adhesions on Selectins and VCAM-1 in Shear Flow. , 135(3).

Alon R, Feigelson S. 2002. From rolling to arrest on blood vessels: leukocyte tap dancing on endothelial integrin ligands and chemokines at sub-second contacts. *Seminars in immunology*, 14(2), pp.93–104.

Alsteens D, Dupres V, Yunus S, Latgé JP, Heinisch JJ, Dufrêne YF. 2012. High-resolution imaging of chemical and biological sites on living cells using peak force tapping atomic force microscopy. *Langmuir : the ACS journal of surfaces and colloids*, 28(49), pp.16738–44.

Aplin JD. 2006. Embryo implantation: the molecular mechanism remains elusive. *Reproductive BioMedicine Online*, 13(6), pp.833–839.

Aplin JD. 2000. The cell biological basis of human implantation. *Baillière's best practice & research. Clinical obstetrics & gynaecology*, 14(5), pp.757–64.

Aplin JD, Seif MW, Graham RA, Hey NA, Behzad F, Campbell S. 1994. The endometrial cell surface and implantation. Expression of the polymorphic mucin MUC-1 and adhesion molecules during the endometrial cycle. *Annals of the New York Academy of Sciences*, 734, pp.103–21.

Apparao KB, Murray MJ, Fritz MA, Meyer WR, Chambers AF, Truong PR, Lessey BA. 2001. Osteopontin and its receptor alphavbeta(3) integrin are coexpressed in

the human endometrium during the menstrual cycle but regulated differentially. *The Journal of clinical endocrinology and metabolism*, 86(10), pp.4991–5000.

Argaman M, Golan R, Thomson NH, Hansma HG. 1997. Phase imaging of moving DNA molecules and DNA molecules replicated in the atomic force microscope. *Nucleic acids research*, 25(21), pp.4379–84.

Armant DR. 2005. Blastocysts don't go it alone. Extrinsic signals fine-tune the intrinsic developmental program of trophoblast cells. *Developmental biology*, 280(2), pp.260–80.

Arnal JF, Fontaine C, Billon-Galés A, Favre J, Laurell H, Lenfant F, Gourdy P. 2010. Estrogen receptors and endothelium. *Arteriosclerosis, thrombosis, and vascular biology*, 30(8), pp.1506–12.

Arnett-Mansfield RL, DeFazio A, Mote PA, Clarke CL. 2004. Subnuclear Distribution of Progesterone Receptors A and B in Normal and Malignant Endometrium. *Journal of Clinical Endocrinology & Metabolism*, 89(3), pp.1429–1442.

Arnold JT, Kaufman DG, Seppälä M, Lessey BA. 2001. Endometrial stromal cells regulate epithelial cell growth in vitro: a new co-culture model. *Human reproduction (Oxford, England)*, 16(5), pp.836–45.

Askarova S, Sun Z, Sun GY, Meininger GA, Lee JC. 2013. Amyloid-β peptide on sialyl-Lewis(X)-selectin-mediated membrane tether mechanics at the cerebral endothelial cell surface. *PloS one*, 8(4), p.e60972.

Ayaz A, Alwan Y, Farooq MU. 2013. Efficacy of combined metformin-clomiphene citrate in comparison with clomiphene citrate alone in infertile women with polycystic ovarian syndrome (PCOS). *Journal of medicine and life*, 6(2), pp.199–201.

Babcock K, Prater C. 1995. Phase Imaging: Beyond Topography. *(Santa Barbara, CA: Digital Instruments)*, Bruker Nano.

Baerwald AR, Adams GP, Pierson RA. 2012. Ovarian antral folliculogenesis during the human menstrual cycle: a review. *Human reproduction update*, 18(1), pp.73–91.

Barattin R, Voyer N. 2008. Chemical modifications of AFM tips for the study of molecular recognition events. *Chemical communications (Cambridge, England)*, (13), pp.1513–32.

Barth AI, Näthke IS, Nelson WJ. 1997. Cadherins, catenins and APC protein: interplay between cytoskeletal complexes and signaling pathways. *Current opinion in cell biology*, 9(5), pp.683–90.

Barthel SR, Gavino JD, Descheny L, Dimitroff CJ. 2007. Targeting selectins and selectin ligands in inflammation and cancer. *Expert opinion on theraputic targets*, 11(11), pp.1473–1491.

Baumgartner W, Hinterdorfer P, Ness W, Raab A, Vestweber D, Schindler H, Drenckhahn D. 2000. Cadherin interaction probed by atomic force microscopy. *Proceedings of the National Academy of Sciences of the United States of America*, 97(8), pp.4005–10.

Béliard A, Donnez J, Nisolle M, Foidart JM. 1997. Localization of laminin, fibronectin, E-cadherin, and integrins in endometrium and endometriosis. *Fertility and sterility*, 67(2), pp.266–72.

Belikov S, Erina N, Huang L, Su C, Prater C, Magonov S, Ginzburg V, McIntyre B, Lakrout H, Meyers G. 2009. Parametrization of atomic force microscopy tip shape models for quantitative nanomechanical measurements. Journal of Vacuum Science and Technology: Microelectronics and Nanometer Structures, 27(2) pp. 984–992.

Bentin-Ley U, Horn T, Sjögren A, Sorensen S, Falck Larsen J, Hamberger L. 2000. Ultrastructure of human blastocyst-endometrial interactions *in vitro*. *Journal of reproduction and fertility*, 120(2), pp.337–50.

Bentin-Ley U, Lopata A. 2000. In vitro models of human blastocyst implantation. *Baillière's best practice & research. Clinical obstetrics & gynaecology*, 14(5), pp.765–74.

Bergh PA, Navot D. 1992. The impact of embryonic development and endometrial maturity on the timing of implantation. *Fertility and Sterility*, 58(3), pp.537–42.

Berndt S, Blacher S, Perrier D, Hauterive S, Thiry M, Tsampalas M, Cruz A, Péqueux C, Lorquet S, Munaut C, Noël A, Foidart JM. 2009. Chorionic gonadotropin stimulation of angiogenesis and pericyte recruitment. *The Journal of clinical endocrinology and metabolism*, 94(11), pp.4567–74.

Berquand A, Holloschia A, Trendelenburga M, Kioschisa P. 2010. Analysis of Cytoskeleton-Destabilizing Agents by Optimized Optical Navigation and AFM Force Measurements. *Microscopy Today*, 18(02), p.34.

Berquand A. 2011. Quantitative Imaging of Living Biological Samples by PeakForce QNM Atomic Force Microscopy. Bruker nano, Application Note # 135, pp.1–10.

Berquand A, Kuhn HM, Holloschi A, Mollenhauer J, Kioschisa P. 2013. Expression of Tumor Suppressors PTEN and TP53 in Isogenic Glioblastoma U-251MG Cells Affects Cellular Mechanical Properties – An AFM-based Quantitative Investigation. *Unpublished.*

Bhagwat SR, Chandrashekar DS, Kakar R, Davuluri S, Bajpai AK, Nayak S, Bhutada S, Acharya K, Sachdeva G. 2013. Endometrial receptivity: a revisit to functional genomics studies on human endometrium and creation of HGEx-ERdb. *PloS one*, 8(3), e58419.

Bhiladvala RB, Wang ZJ. 2004. Effect of fluids on the Q factor and resonance frequency of oscillating micrometer and nanometer scale beams. *Physical Review. E, Statistics, Nonlinear and Soft Matter Physyics*, 69(3), p.036307.

Bianchi E, Molteni R, Pardi R, Dubini G. Microfluidics for in vitro biomimetic shear stress-dependent leukocyte adhesion assays. *Journal of biomechanics*, 46(2), pp.276–83.

Binnig G, Quate CF. 1986. Atomic Force Microscope. *Physical Review Letters*, 56(9), pp.930-933

Blair IA. 2010. Analysis of estrogens in serum and plasma from postmenopausal women: past present, and future. *Steroids*, 75(4-5), pp.297–306.

Boehme K, Simon S, Mueller SO. 2009. Gene expression profiling in Ishikawa cells: a fingerprint for estrogen active compounds. *Toxicology and applied pharmacology*, 236(1), pp.85–96.

Bowen JA, Bazer FW, Burghardt RC. 1996. Spatial and temporal analyses of integrin and Muc-1 expression in porcine uterine epithelium and trophectoderm in vivo. *Biology of reproduction*, 55(5), pp.1098–106.

Bramwell ME, Wiseman G, Shotton DM. 1986. Electron-microscopic studies of the CA antigen, epitectin. *Journal of cell science*, 86(2), pp.249–61.

Brayman M, Thathiah A, Carson DD. 2004. MUC1: a multifunctional cell surface component of reproductive tissue epithelia. *Reproductive biology and endocrinology* , 2(4), pp.1-9

Brayman MJ, Dharmaraj N, Lagow E, Carson DD. 2007. MUC1 expression is repressed by protein inhibitor of activated signal transducer and activator of transcription-y. *Molecular endocrinology*, 21(11), pp.2725–37.

Brayman MJ, Julian J, Mulac-Jericevic B, Conneely OM, Edwards DP, Carson DD. 2006. Progesterone receptor isoforms A and B differentially regulate MUC1 expression in uterine epithelial cells. *Molecular endocrinology*, 20(10), pp.2278–91.

Bricou A, Batt RE, Chapron C. 2008. Peritoneal fluid flow influences anatomical distribution of endometriotic lesions: why Sampson seems to be right. *European journal of obstetrics, gynecology, and reproductive biology*, 138(2), pp.127–34.

Brockhausen I. 2006. Mucin-type O-glycans in human colon and breast cancer: glycodynamics and functions. *EMBO reports*, 7(6), pp.599–604.

Buck VU, Windoffer R, Leube RE, Classen-Linke I. 2012. Redistribution of adhering junctions in human endometrial epithelial cells during the implantation window of the menstrual cycle. *Histochemistry and cell biology*, 137(6), pp.777–90.

Caligioni CS. 2009. Assessing reproductive status/stages in mice. *Current protocols in neuroscience*, Appendix 4, pp.4I.

Cameo P, Srisuparp S, Strakova Z, Fazleabas AT. 2004. Chorionic gonadotropin and uterine dialogue in the primate. *Reproductive biology and endocrinology : RB&E*, 5(2), pp.50.

Campbell S, Larsen J, Seif MW, Allen TD, Knox F, Jones CJ, Aplin JD. 2000. Mosaic characteristics of human endometrial epithelium *in vitro*: analysis of secretory markers and cell surface ultrastructure. *Molecular human reproduction*, 6(1), pp.41–9.

Cao TC, Thirkill TL, Wells M, Barakat AI, Douglas GC. 2008. Trophoblasts and shear stress induce an asymmetric distribution of icam-1 in uterine endothelial cells. *American journal of reproductive immunology*, 59(2), pp.167–81.

Carson DD, Bagchi I, Dey SK, Enders AC, Fazleabas AT, Lessey BA, Yoshinaga K. 2000. Embryo implantation. *Developmental biology*, 223(2), pp.217–37.

Carson DD, Julian J, Lessey BA, Prakobphol A, Fisher SJ. 2006. MUC1 is a scaffold for selectin ligands in the human uterus. *Frontiers in bioscience : a journal and virtual library*, 1(11), pp.2903–8.

Casper RF. 2007. Aromatase inhibitors in ovarian stimulation. *The Journal of steroid biochemistry and molecular biology*, 106(1-5), pp.71–5.

Cervero A, Domínguez F, Horcajadas JA, Quiñonero A, Pellicer A, Simón C. 2007. Embryonic adhesion is not affected by endometrial leptin receptor gene silencing. *Fertility and sterility*, 88(4), pp.1086–92.

Chae SJ, Lee GH, Choi YM, Hong MA, Kim JM, Lee KS, Ku SY, Moon SY. 2010. Intercellular Adhesion Molecule-1 and Interleukin-6 Gene Polymorphisms in Patients with Advanced-Stage Endometriosis. *Gynecologic and Obstetric Investigation*, 70(1), pp.34–39.

Chafidz A, Ali I, Elleithy R, Al-Zahrani S. 2012. Atomic Force Microscopy, thermal, viscoelastic and mechanical properties of HDPE/CaCO3 nanocomposites. *Journal of Polymer Research*, 19(4), pp.9860.

Chai J, Lee KF, Ng EH, Yeung WS, Ho PC. 2011. Ovarian stimulation modulates steroid receptor expression and spheroid attachment in peri-implantation endometria: studies on natural and stimulated cycles. *Fertility and sterility*, 96(3), pp.764–8.

Chappuis-Flament S, Wong E, Hicks LD, Kay CM, Gumbiner BM. 2001. Multiple cadherin extracellular repeats mediate homophilic binding and adhesion. *The Journal of Cell Biology*, 154(1), pp.231–243.

Cheong Y, Boomsma C, Heijnen C, Macklon N. 2013. Uterine secretomics: a window on the maternal-embryo interface. *Fertility and sterility*, 99(4), pp.1093–9.

Choudhury A, Moniaux N, Ringel J, King J, Moore E, Aubert JP, Batra SK. 2001. Alternate splicing at the 3'-end of the human pancreatic tumor-associated mucin MUC4 cDNA. *Teratogenesis, carcinogenesis, and mutagenesis*, 21(1), pp.83–96.

Christensen A, Bentley GE, Cabrera R, Ortega HH, Perfito N, Wu TJ, Micevych P. 2012. Hormonal regulation of female reproduction. *Hormone and metabolic research,* 44(8), pp.587–91.

Cleveland JP, Anczykowski B, Schmid AE, Elings, VB. 1998. Energy dissipation in tapping-mode atomic force microscopy. *Applied Physics Letters*, 72(20), p.2613.

Cork BA, Tuckerman EM, Li TC, Laird SM. 2002. Expression of interleukin (IL)-11 receptor by the human endometrium in vivo and effects of IL-11, IL-6 and LIF on the production of MMP and cytokines by human endometrial cells *in vitro*. *Molecular human reproduction*, 8(9), pp.841–8.

Costa NR, Paulo P, Caffrey T, Hollingsworth MA, Santos-Silva F. 2011. Impact of MUC1 mucin downregulation in the phenotypic characteristics of MKN45 gastric carcinoma cell line. *PloS one*, 6(11), e.26970.

Coughlan C, Sinagra M, Ledger W, Li TC, Laird S. 2013. Endometrial integrin expression in women with recurrent implantation failure after IVF and its relationship to pregnancy outcome. *Fertility and Sterility*, 100(3), pp.825-30

Coutifaris C, Kao LC, Sehdev HM, Chin U, Babalola GO, Blaschuk OW, Strauss JF. 1991. E-cadherin expression during the differentiation of human trophoblasts. *Development*, 113(3), pp.767–77.

Critchley HO, Henderson TA, Kelly RW, Scobie GS, Evans LR, Groome NP, Saunders PT. 2002. Wild-Type Estrogen Receptor (ERbeta1) and the Splice Variant (ERbetacx/beta2) Are Both Expressed within the Human Endometrium throughout the Normal Menstrual Cycle. *Journal of Clinical Endocrinology & Metabolism*, 87(11), pp.5265–5273.

Croxtall JD, Elder MG, White JO. 1990. Hormonal control of proliferation in the Ishikawa endometrial adenocarcinoma cell line. *Journal of steroid biochemistry*, 35(6), pp.665–9.

Davies S, Dai D, Feldman I, Pickett G, Leslie KK. 2004. Identification of a novel mechanism of NF-kappaB inactivation by progesterone through progesterone receptors in Hec50co poorly differentiated endometrial cancer cells: induction of A20 and ABIN-2. *Gynecologic oncology*, 94(2), pp.463–70.

Dawood MY, Lau M, Khan-Dawood FS. 1998. E-cadherin and its messenger ribonucleic acid in periimplantation phase human endometrium in normal and clomiphene-treated cycles. *American journal of obstetrics and gynecology*, 178(5), pp.996–1001.

Defrère S, Van Langendonckt A, Moulin P, Befahy P, Gonzalez D, Martinez-Madrid B, Dolmans MM, Donnez J. 2005. Human endometrial epithelial cells (EEC)

constitutively express more intercellular adhesion molecule (ICAM)-1 than endometrial stromal cells (ESC) in culture. *American journal of reproductive immunology*, 54(1), pp.5–12.

Degand P, Moniaux N, Maury J, Petitprez D, Nollet S, Laine A, Porchet N, Aubert JP. 1998. Human mucin gene MUC4: organization of its 5'-region and polymorphismof its central tandem repeat array. The *Biochemistry Journal*, 15(332), pp.739–748.

DeLoia JA, Krasnow JS, Brekosky J, Babaknia A, Julian J, Carson DD. 1998. Regional specialization of the cell membrane-associated, polymorphic mucin (MUC1) in human uterine epithelia. *Human reproduction*, 13(10), pp.2902–9.

Derjaguin BV, Muller VM, Toporov YP. 1975. Effect of contact deformations on the adhesion of particles. *Journal of Colloid and Interface Science*, 53(2), pp.314–326.

Derrien M, van Passel MW, van de Bovenkamp JH, Schipper RG, de Vos WM, Dekker J. 2010. Mucin-bacterial interactions in the human oral cavity and digestive tract. *Gut microbes*, 1(4), pp.254–268.

DeSouza MM, Surveyor GA, Price RE, Julian J, Kardon R, Zhou X, Gendler S, Hilkens J, Carson DD. 1999. MUC1/episialin: a critical barrier in the female reproductive tract. *Journal of reproductive immunology*, 45(2), pp.127–58.

DeSouza MM, Mani SK, Julian J, Carson DD. 1998. Reduction of mucin-1 expression during the receptive phase in the rat uterus. *Biology of reproduction*, 58(6), pp.1503–7.

Dey SK, Lim H, Das SK, Reese J, Paria BC, Daikoku T, Wang H. 2004. Molecular cues to implantation. *Endocrine reviews*, 25(3), pp.341–73.

Dey S.K. 2006. Visualizing early embryo implantation sites by dye injection. *CSH protocols*, 2006(2).

Dharmaraj N, Engel BJ, Carson DD. 2013. Activated EGFR stimulates MUC1 expression in human uterine and pancreatic cancer cell lines. *Journal of cellular biochemistry*, 114(10) pp.2314-22.

Dharmaraj N, Gendler SJ, Carson DD. 2009. Expression of human MUC1 during early pregnancy in the human MUC1 transgenic mouse model. *Biology of reproduction*, 81(6), pp.1182–8.

Dharmaraj N, Wang P, Carson DD. 2010. Cytokine and progesterone receptor interplay in the regulation of MUC1 gene expression. *Molecular endocrinology*, 24(12), pp.2253–66.

Diedrich K, Fauser BC, Devroey P, Griesinger G. 2007. The role of the endometrium and embryo in human implantation. *Human reproduction update*, 13(4), pp.365–77.

Dominguez F, Yáñez-Mó M, Sanchez-Madrid F, Simón C. 2005. Embryonic implantation and leukocyte transendothelial migration: different processes with similar players? *Federation of American Societies for Experimental Biology*, 19(9), pp.1056–60.

Domínguez F, Simón C, Quiñonero A, Ramírez MÁ, González-Muñoz E, Burghardt H, Cervero A, Martínez S, Pellicer A, Palacín M, Sánchez-Madrid F, Yáñez-Mó M. 2010. Human endometrial CD98 is essential for blastocyst adhesion. *PloS one*, 5(10), e13380.

Dufrêne YF, Martínez-Martín D, Medalsy I, Alsteens D, Müller DJ. 2013. Multiparametric imaging of biological systems by force-distance curve-based AFM. *Nature Methods*, 10(9), pp.847–854.

Dunér G, Iruthayaraj J, Daasbjerg K, Pedersen SU, Thormann E, Dėdinaitė A. 2012. Attractive double-layer forces and charge regulation upon interaction between electrografted amine layers and silica. *Journal of Colloid and Interface Science*, 385(1), pp.225–234.

Edgell TA, Rombauts LJ, Salamonsen LA. 2013. Assessing receptivity in the endometrium: the need for a rapid, non-invasive test. *Reproductive biomedicine online*, 27(5), pp.486-96.

Edwards RG. 1988. Human uterine endocrinology and the implantation window. *Annals of the New York Academy of Sciences*, 541, pp.445–54.

Enders AC. 2000. Trophoblast-uterine interactions in the first days of implantation: models for the study of implantation events in the human. *Seminars in reproductive medicine*, 18(3), pp.255–63.

Enders AC, Hendrickx AG, Schlafke S. 1983. Implantation in the rhesus monkey: initial penetration of endometrium. *The American journal of anatomy*, 167(3), pp.275–98.

Enders AC, Schlafke S. 1969. Cytological aspects of trophoblast-uterine interaction in early implantation. *The American journal of anatomy*, 125(1), pp.1–29.

Enders AC, Lantz KC, Schlafke S. 1989. Differentiation of trophoblast of the baboon blastocyst. *The Anatomical Record*, 225(4), pp.329–340.

Enders AC, Lopata A. 1999. Implantation in the Marmoset Monkey : Expansion of the Early implantation site. *The Anatomical Record*, 256(3), pp.279–299.

Evans E, Leung A, Hammer D, Simon S. 2001. Chemically distinct transition states govern rapid dissociation of single L-selectin bonds under force. *Proceedings of the National Academy of Sciences of the United States of America*, 98(7), pp.3784–9.

Evans E. 1998. Energy landscapes of biomolecular adhesion and receptor anchoring at interfaces explored with dynamic force spectroscopy. *Faraday discussions*, (111), pp.1–16.

Evans E. 2001. Probing the relationship between force and lifetime in single intramolecular bonds. *Annual Review of Biophysics and Biomolecular Structure*, 30, pp.105–128.

Evans EA, Calderwood DA. 2007. Forces and bond dynamics in cell adhesion. *Science*, 316(5828), pp.1148–53.

Evans E, Ritchie K. 1997. Dynamic strength of molecular adhesion bonds. *Biophysical journal*, 72(4), pp.1541–55.

Evans E, Ritchie K, Merkel R. 1995. Sensitive force technique to probe molecular adhesion and structural linkages at biological interfaces. *Biophysical journal*, 68(6), pp.2580–7.

Evers JL. 2002. Female subfertility. *Lancet*, 360(9327), pp.151–9.

Evron A, Goldman S, Shalev E. 2011. Effect of primary human endometrial stromal cells on epithelial cell receptivity and protein expression is dependent on menstrual cycle stage. *Human reproduction*, 26(1), pp.176–90.

Eytan O, Jaffa AJ, Har-Toov J, Dalach E, Elad D. 1999. Dynamics of the Intrauterine Fluid–Wall Interface. *Annals of Biomedical Engineering*, 27(3), pp.372–379.

Falconer H. 2013. Pregnancy outcomes in women with endometriosis. *Seminars in reproductive medicine*, 31(2), pp.178–82.

Fazleabas AT, Donnelly KM, Srinivasan S, Fortman JD, Miller JB. 1999. Modulation of the baboon (Papio anubis) uterine endometrium by chorionic gonadotrophin during the period of uterine receptivity. *Proceedings of the National Academy of Sciences of the United States of America*, 96(5), pp.2543–8.

Ferrell AD, Malayer JR, Carraway KL, Geisert RD. 2003. Sialomucin complex (Muc4) expression in porcine endometrium during the oestrous cycle and early pregnancy. *Reproduction in domestic animals*, 38(1), pp.63–5.

Foulk RA, Zdravkovic T, Genbacev O, Prakobphol A. 2007. Expression of L-selectin ligand MECA-79 as a predictive marker of human uterine receptivity. *Journal of assisted reproduction and genetics*, 24(7), pp.316–21.

Foxall C, Watson SR, Dowbenko D, Fennie C, Lasky LA, Kiso M, Hasegawa A, Asa D, Brandley BK. 1992. The three members of the selectin receptor family recognize a common carbohydrate epitope, the sialyl Lewis(x) oligosaccharide. *The Journal of cell biology*, 117(4), pp.895–902.

Francis LW, Gonzalez D, Ryder T, Baer K, Rees M, White JO, Conlan RS, Wright CJ. 2010. Optimized sample preparation for high-resolution AFM characterization of fixed human cells. *Journal of Microscopy*, 240(2), pp.111–121.

Francis LW, Lewis PD, Gonzalez D, Ryder TA, Webb G, Joels LA, White JO, Wright CJ, Conlan RS. 2009. Progesterone induces nano-scale molecular modifications on endometrial epithelial cell surfaces. *Biology of the cell*, 101(8), pp.481–93.

Frederix PL, Bosshart PD, Engel A. 2009. Atomic force microscopy of biological membranes. *Biophysical journal*, 96(2), pp.329–38.

Fujimoto J, Ichigo S, Hori M, Tamaya T. 1996. Alteration of E-cadherin, alpha- and beta-catenin mRNA expression in human uterine endometrium during the menstrual cycle. *Gynecological endocrinology*, 10(3), pp.187–91.

Surveyor GA, Gendler SJ, Pemberton L, Das SK, Chakraborty I, Julian J, Pimental RA, Wegner CC, Dey SK, Carson DD. 1995. Expression and steroid hormonal control of Muc-1 in the mouse uterus. *Endocrinology*, 136(8), pp.3639–3647.

Galustian C, Childs RA, Stoll M, Ishida H, Kiso M, Feizi T. 2002. Synergistic interactions of the two classes of ligand, sialyl-Lewis(a/x) fuco-oligosaccharides and short sulpho-motifs, with the P- and L-selectins: implications for therapeutic inhibitor designs. *Immunology*, 105(3), pp.350–9.

García R, San Paulo A. 2000. Amplitude curves and operating regimes in dynamic atomic force microscopy. *Ultramicroscopy*, 82(1-4), pp.79–83.

García R, San Paulo A. 1999. Attractive and repulsive tip-sample interaction regimes in tapping-mode atomic force microscopy. *Physical Review X*, 60(7), pp.4961–4967.

Garrido-Gómez T, Ruiz-Alonso M, Blesa D, Diaz-Gimeno P, Vilella F, Simón C. 2013. Profiling the gene signature of endometrial receptivity: clinical results. *Fertility and sterility*, 99(4), pp.1078–85.

Gellersen B, Brosens IA, Brosens JJ. 2007. Decidualization of the human endometrium: mechanisms, functions, and clinical perspectives. *Seminars in reproductive medicine*, 25(6), pp.445–53.

Genbacev OD, Prakobphol A, Foulk RA, Krtolica AR, Ilic D, Singer MS, Yang ZQ, Kiessling LL, Rosen SD, Fisher SJ. 2003. Trophoblast L-selectin-mediated adhesion at the maternal-fetal interface. *Science*, 299(5605), pp.405–8.

Gendler SJ. 2001. MUC1, the renaissance molecule. *Journal of mammary gland biology and neoplasia*, 6(3), pp.339–53.

Geng Y, Takatani T, Yeh K, Hsu JW, King MR. 2013. Targeting underglycosylated MUC1 for the selective capture of highly metastatic breast cancer cells under flow. *Cellular and Molecular Bioengineering*, 6(2), pp.148-59

Germain P, Staels B, Dacquet C, Spedding M, Laudet V. 2006. Overview of Nomenclature of Nuclear Receptors. *Pharmacological Reviews*, 58(4), pp.685–704.

Giessibl F. 1997. Forces and frequency shifts in atomic-resolution dynamic-force microscopy. *Physical Review B*, 56(24), pp.16010–16015.

Giessibl FJ. 2005. AFM's path to atomic resolution. *Materials Today*, 8(5), pp.32–41.

Gipson IK, Blalock T, Tisdale A, Spurr-Michaud S, Allcorn S, Stavreus-Evers A, Gemzell K. 2008. MUC16 is lost from the uterodome (pinopode) surface of the receptive human endometrium: in vitro evidence that MUC16 is a barrier to trophoblast adherence. *Biology of reproduction*, 78(1), pp.134–42.

Gipson IK, Ho SB, Spurr-Michaud SJ, Tisdale AS, Zhan Q, Torlakovic E, Pudney J, Anderson DJ, Toribara NW, Hill JA. 1997. Mucin genes expressed by human female reproductive tract epithelia. *Biology of reproduction*, 56(4), pp.999–1011.

Gniewek P, Kolinski A. 2012. Coarse-grained modeling of mucus barrier properties. *Biophysical journal*, 102(2), pp.195–200.

Gotsmann B, Seidel C, Anczykowski B, and Fuchs H. 1999. Conservative and dissipative tip-sample interaction forces probed with dynamic AFM. *Physical Review B*, 60(15), pp.11051–11061.

Graham RA, Seif MW, Aplin JD, Li TC, Cooke ID, Rogers AW, Dockery P. 1990. An endometrial factor in unexplained infertility. *BMJ*, 300(6737), pp.1428–31.

Gray CA, Burghardt RC, Johnson GA, Bazer FW, Spencer TE. 2002. Evidence that absence of endometrial gland secretions in uterine gland knockout ewes compromises conceptus survival and elongation. *Reproduction*, 124(2), pp.289–300.

Gray CA, Bartol FF, Tarleton BJ, Wiley AA, Johnson GA, Bazer FW, Spencer TE. 2001. Developmental Biology of Uterine Glands. *Biology of reproduction*, 65(5), pp.1311–1323.

Gross L, Mohn F, Moll N, Liljeroth P, Meyer G. 2009. The chemical structure of a molecule resolved by atomic force microscopy. *Science*, 325(5944), pp.1110–4.

Grzmil P, Altmann ME, Adham IM, Engel U, Jarry H, Schweyer S, Wolf S, Mänz J, Engel W. 2013. Embryo implantation failure and other reproductive defects in Ube2q1-deficient female mice. *Reproduction*, 145(1), pp.45–56.

Gum JR. 1995. Human mucin glycoproteins: varied structures predict diverse properties and specific functions. *Biochemical Society transactions*, 23(4), pp.795–9.

Gumbiner BM. 1996. Cell adhesion: the molecular basis of tissue architecture and morphogenesis. *Cell*, 84(3), pp.345–57.

Handschuh K, Guibourdenche J, Tsatsaris V, Guesnon M, Laurendeau I, Evain-Brion D, Fournier T. 2007. Human chorionic gonadotropin produced by the invasive trophoblast but not the villous trophoblast promotes cell invasion and is down-

regulated by peroxisome proliferator-activated receptor-gamma. *Endocrinology*, 148(10), pp.5011–9.

Hanisch FG, Kinlough CL, Staubach S, Hughey RP. 2012. MUC1 membrane trafficking: protocols for assessing biosynthetic delivery, endocytosis, recycling, and release through exosomes. *Methods in molecular biology*, 842, pp.123–40.

Hannan NJ, Stoikos CJ, Stephens AN, Salamonsen LA. 2009. Depletion of high-abundance serum proteins from human uterine lavages enhances detection of lower-abundance proteins. *Journal of proteome research*, 8(2), pp.1099–103.

Hannan NJ, Paiva P, Dimitriadis E, Salamonsen LA. 2010. Models for study of human embryo implantation: choice of cell lines? *Biology of reproduction*, 82(2), pp.235–45.

Hannan NJ, Jones RL, White CA, Salamonsen LA. 2006. The chemokines, CX3CL1, CCL14, and CCL4, promote human trophoblast migration at the feto-maternal interface. *Biology of reproduction*, 74(5), pp.896–904.

Harduf H, Goldman S, Shalev E. 2009. Progesterone receptor A and c-Met mediates spheroids-endometrium attachment. *Reproductive biology and endocrinology : RB&E*, 16(7), pp1-14.

Harris LK, Jones CJ, Aplin JD. 2009. Adhesion molecules in human trophoblast - a review. II. extravillous trophoblast. *Placenta*, 30(4), pp.299–304.

Hattrup CL, Gendler SJ. 2008. Structure and function of the cell surface (tethered) mucins. *Annual review of physiology*, 70, pp.431–57.

Hawkins LK, Correia KF, Srouji SS, Hornstein MD, Missmer SA. 2013. Uterine length and fertility outcomes: a cohort study in the IVF population. *Human reproduction*, 28(11), pp.3000-6.

Hazel JL, Tsukruk VV. 1999. Spring constants of composite ceramic/gold cantilevers for scanning probe microscopy. *Thin Solid Films*, 339(1-2), pp.249–257.

Hecht E, Usmani SM, Albrecht S, Wittekindt OH, Dietl P, Mizaikoff B, Kranz C. 2011. Atomic force microscopy of microvillous cell surface dynamics at fixed and living alveolar type II cells. *Analytical and bioanalytical chemistry*, 399(7), pp.2369–78.

Heinz WF, Hoh JH. 1999. Spatially resolved force spectroscopy of biological surfaces using the atomic force microscope. *Trends in biotechnology*, 17(4), pp.143–50.

Hemmerich S, Rosen, SD. 2000. Carbohydrate sulfotransferases in lymphocyte homing. *Glycobiology*, 10(9), pp.849–56.

Heneweer C, Schmidt M, Denker HW, Thie M. 2005. Molecular mechanisms in uterine epithelium during trophoblast binding: the role of small GTPase RhoA in human uterine Ishikawa cells. *Journal of experimental & clinical assisted reproduction*, 2(1), pp.4

Heu C, Berquand A, Elie-Caille C, Nicod L. 2012. Glyphosate-induced stiffening of HaCaT keratinocytes, a Peak Force Tapping study on living cells. *Journal of structural biology*, 178(1), pp.1–7.

Hey NA, Graham RA, Seif MW, Aplin JD. 1994. The polymorphic epithelial mucin MUC1 in human endometrium is regulated with maximal expression in the implantation phase. *The Journal of clinical endocrinology and metabolism*, 78(2), pp.337–42.

Hey NA, Aplin JD. 1996. Sialyl-Lewis x and Sialyl-Lewis a are associated with MUC1 in human endometrium. *Glycoconjugate journal*, 13(5), pp.769–79.

Hey NA, Li TC, Devine PL, Graham RA, Saravelos H, Aplin JD. 1995. MUC1 in secretory phase endometrium: expression in precisely dated biopsies and flushings from normal and recurrent miscarriage patients. *Human reproduction*, 10(10), pp.2655–2662.

Hild-Petito S, Fazleabas AT, Julian J, Carson DD. 1996. Mucin (Muc-1) Expression Is Differentially Regulated in Uterine Luminal and Glandular Epithelia of the Baboon (Papio anubis)'. *Biology of reproduction* , 54(5), pp.939–947.

Hilkens J, Ligtenberg MJ, Vos HL, Litvinov SV. 1992. Cell membrane-associated mucins and their adhesion-modulating property. *Trends in biochemical sciences*, 17(9), pp.359–63.

Hinterdorfer P, Dufrêne YF. 2006. Detection and localization of single molecular recognition events using atomic force microscopy. *Nature methods*, 3(5), pp.347–55.

Hiraoka N, Petryniak B, Nakayama J, Tsuboi S, Suzuki M, Yeh JC, Izawa D, Tanaka T, Miyasaka M, Lowe JB, Fukuda M. 1999. A novel, high endothelial venule-specific sulfotransferase expresses 6-sulfo sialyl Lewis(x), an L-selectin ligand displayed by CD34. *Immunity*, 11(1), pp.79–89.

Ho H, Singh H, Aljofan M, Nie G. 2012. A high-throughput in vitro model of human embryo attachment. *Fertility and sterility*, 97(4), pp.974–8.

Hoffman LH, Olson GE, Carson DD, Chilton BS. 1998. Progesterone and implanting blastocysts regulate Muc1 expression in rabbit uterine epithelium. *Endocrinology*, 139(1), pp.266–71.

Hohn HP, Linke M, Denker HW. 2000. Adhesion of trophoblast to uterine epithelium as related to the state of trophoblast differentiation: in vitro studies using cell lines. *Molecular reproduction and development*, 57(2), pp.135–45.

Holmberg JC, Haddad S, Wünsche V, Yang Y, Aldo PB, Gnainsky Y, Granot I, Dekel N, Mor G. 2012. An in vitro model for the study of human implantation. *American journal of reproductive immunology*, 67(2), pp.169–78.

Hölscher H, Schwarz UD. 2007. Theory of amplitude modulation atomic force microscopy with and without Q-Control. *International Journal of Non-Linear Mechanics*, 42(4), pp.608–625.

Horne AW, White JO, Margara RA, Williams R, Winston RM, Lalani E. 2001. MUC 1: a genetic susceptibility to infertility? *Lancet*, 28(357), pp.1336–7.

Horne AW, Lalani EN, Margara RA, White JO. 2006. The effects of sex steroid hormones and interleukin-1-beta on MUC1 expression in endometrial epithelial cell lines. *Reproduction*, 131(4), pp.733–42.

Horne AW, Lalani EN, Margara RA, Ryder TA, Mobberley MA, White JO. 2005. The expression pattern of MUC1 glycoforms and other biomarkers of endometrial receptivity in fertile and infertile women. *Molecular reproduction and development*, 72(2), pp.216–29.

Horne AW, White JO, Lalani el-N, Mobberley MA, Margara RA, Trew GH, Ryder TA. 2002. Analysis of epitopes on endometrial epithelium by scanning immunoelectron microscopy. *Biochemical and biophysical research communications*, 292(1), pp.102–8.

Howard AJ, Rye RR, Houston JE. 1996. Nanomechanical basis for imaging soft materials with tapping mode atomic force microscopy. *Journal of Applied Physics*, 79(4), pp.1885–1890.

Hubbard AK, Rothlein R. 2000. Intercellular adhesion molecule-1 (ICAM-1) expression and cell signaling cascades. *Free Radical Biology and Medicine*, 28(9), pp.1379–1386.

Hugel T, Seitz M. 2001. The Study of Molecular Interactions by AFM Force Spectroscopy. *Macromolecular Rapid Communications*, 22(13), pp.989–1016.

Huhtinen K, Desai R, Ståhle M, Salminen A, Handelsman DJ, Perheentupa A, Poutanen M. 2012. Endometrial and endometriotic concentrations of estrone and estradiol are determined by local metabolism rather than circulating levels. *The Journal of clinical endocrinology and metabolism*, 97(11), pp.4228–35.

Idris N, Carraway KL. 2000. Regulation of sialomucin complex/Muc4 expression in rat uterine luminal epithelial cells by transforming growth factor-beta: implications for blastocyst implantation. *Journal of cellular physiology*, 185(2), pp.310–6.

James JL, Cartwright JE, Whitley GS, Greenhill DR, Hoppe A. 2012. The regulation of trophoblast migration across endothelial cells by low shear stress: consequences for vascular remodelling in pregnancy. *Cardiovascular research*, 93(1), pp.152–61.

James JL, Whitley GS, Cartwright JE. 2011. Shear stress and spiral artery remodelling: the effects of low shear stress on trophoblast-induced endothelial cell apoptosis. *Cardiovascular research*, 90(1), pp.130–9.

Jebali J, Jeanneau C, Bazaa A, Mathieu S, El Ayeb M, Luis J, El Battari A, Marrakchi N. 2011. Selectins as adhesion molecules and potential therapeutic target. *Archives de l'Institut Pasteur de Tunis*, 88(1-4), pp.3–18.

Jha RK, Titus S, Saxena D, Kumar PG, Laloraya M. 2006. Profiling of E-cadherin, beta-catenin and Ca(2+) in embryo-uterine interactions at implantation. *FEBS letters*, 580(24), pp.5653–60.

John NJ, Linke M, Denker HW. 1993. Quantitation of human choriocarcinoma spheroid attachment to uterine epithelial cell monolayers. *In vitro cellular & developmental biology* 29A(6), pp.461–8.

JPK instruments, 2012. QI™ mode - Quantitative Imaging with the NanoWizard ® 3 AFM, pp.1–7.

Julian J, Enders AC, Fazleabas AT, Carson DD. 2005. Compartmental distinctions in uterine Muc-1 expression during early pregnancy in cynomolgous macaque (Macaca fascicularis) and baboon (Papio anubis). *Human reproduction*, 20(6), pp.1493–503.

Kamruzzahan AS, Kienberger F, Stroh CM, Berg J, Huss R, Ebner A, Zhu R, Rankl C, Gruber HJ, Hinterdorfer P. 2004. Imaging morphological details and pathological differences of red blood cells using tapping-mode AFM. *Biological chemistry*, 385(10), pp.955–60.

Kaneko Y, Day ML, Murphy CR. 2011. Integrin β3 in rat blastocysts and epithelial cells is essential for implantation in vitro: studies with Ishikawa cells and small interfering RNA transfection. *Human reproduction*, 26(7), pp.1665–74.

Kaneko Y, Murphy CR, Day ML. 2013. Extracellular matrix proteins secreted from both the endometrium and the embryo are required for attachment: a study using a co-culture model of rat blastocysts and Ishikawa cells. *Journal of morphology*, 274(1), pp.63–72.

Kansas GS. 1996. Selectins and their ligands: current concepts and controversies. *Blood*, 88(9), pp.3259–87.

Kaplova E, Tomankova K, Kolarova H, Krejci P. 2012. Study of developmental enamel defects of permanent teeth by atomic force microscopy. *Current Microscopy Contributions to Advances in Science and Technology*, pp.555–560.

Karlen Y, McNair A, Perseguers S, Mazza C, Mermod N. 2007. Statistical significance of quantitative PCR. *BMC bioinformatics*, 20(8), pp.131.

Kassan S, Mechanick JI, Gurpide E. 1989. Altered estrogen receptor system in estrogen-unresponsive human endometrial adenocarcinoma cells. *Journal of steroid biochemistry*, 33(3), pp.327–33.

Kastner P, Krust A, Turcotte B, Stropp U, Tora L, Gronemeyer H, Chambon P. 1990. Two distinct estrogen-regulated promoters generate transcripts encoding the two

functionally different human progesterone receptor forms A and B. *EMBO Journal*, 9(5), pp.1603–1614.

Kato K, Takegawa Y, Ralston KS, Gilchrist CA, Hamano S, Petri WA Jr, Shinohara Y. 2013. Sialic acid-dependent attachment of mucins from three mouse strains to Entamoeba histolytica. *Biochemical and biophysical research communications*, 436(2), pp.252–8.

Khan IM, Francis LW, Theobald PS, Perni S, Young RD, Prokopovich P, Conlan RS, Archer CW. 2013. In vitro growth factor-induced bio engineering of mature articular cartilage. *Biomaterials*, 34(5), pp.1478–87.

Kim JJ, Kurita T, Bulun SE. 2013. Progesterone action in endometrial cancer, endometriosis, uterine fibroids, and breast cancer. *Endocrine reviews*, 34(1), pp.130–62.

Kim KC, Lillehoj EP. 2008. MUC1 mucin: a peacemaker in the lung. *American journal of respiratory cell and molecular biology*, 39(6), pp.644–7.

Kim YJ, Borsig L, Han HL, Varki NM, Varki A. 1999. Distinct selectin ligands on colon carcinoma mucins can mediate pathological interactions among platelets, leukocytes, and endothelium. *The American journal of pathology*, 155(2), pp.461–72.

King AE, Critchley HO. 2010. Oestrogen and progesterone regulation of inflammatory processes in the human endometrium. *The Journal of steroid biochemistry and molecular biology*, 120(2-3), pp.116–26.

Kinlough CL, Poland PA, Gendler SJ, Mattila PE, Mo D, Weisz OA, Hughey RP. 2011. Core-glycosylated mucin-like repeats from MUC1 are an apical targeting signal. *The Journal of biological chemistry*, 286(45), pp.39072–81.

Kinoshita K, Leung A, Simon S, Evans E. 2010. Long-lived, high-strength states of ICAM-1 bonds to β2 integrin, II: lifetimes of LFA-1 bonds under force in leukocyte signaling. *Biophysical journal*, 98(8), pp.1467–75.

Kirmizis D, Logothetidis S. 2010. Atomic force microscopy probing in the measurement of cell mechanics. *International journal of nanomedicine*, 7(5), pp.137–45.

Klaassens AH, van Wijk FH, Hanifi-Moghaddam P, Sijmons B, Ewing PC, Ten Kate-Booij MJ, Kooi GS, Kloosterboer HJ, Blok LJ, Burger CW. 2006. Histological and immunohistochemical evaluation of postmenopausal endometrium after 3 weeks of treatment with tibolone, estrogen only, or estrogen plus progestagen. *Fertility and Sterility*, 86(2), pp.352–361.

Klymenko O, Wiltowska-Zuber J, Lekka M, Kwiatek WM. 2009. Energy Dissipation in the AFM Elasticity Measurements. *Acta Physica Polonia A*, 115(2), pp.548–551.

Koot YE, Teklenburg G, Salker MS, Brosens JJ, Macklon NS. 2012. Molecular aspects of implantation failure. *Biochimica et biophysica acta*, 1822(12), pp.1943–50.

Kosaka K, Fujiwara H, Tatsumi K, Yoshioka S, Higuchi T, Sato Y, Nakayama T, Fujii S. 2003. Human peripheral blood mononuclear cells enhance cell-cell interaction between human endometrial epithelial cells and BeWo-cell spheroids. *Human Reproduction*, 18(1), pp.19–25.

Koscinski I, Viville S, Porchet N, Bernigaud A, Escande F, Defossez A, Buisine MP. 2006. MUC4 gene polymorphism and expression in women with implantation failure. *Human reproduction*, 21(9), pp.2238–45.

Królik M, Milnerowicz H. 2012. The effect of using estrogens in the light of scientific research. *Advances in clinical and experimental medicine*, 21(4), pp.535–43.

Krysiak R, Okopień B, Gdula-Dymek A, Herman ZS. 2006. Update on the management of polycystic ovary syndrome. *Pharmacological reports*, 58(5), pp.614–25.

Kühner F, Costa LT, Bisch PM, Thalhammer S, Heckl WM, Gaub HE. 2004. LexA-DNA bond strength by single molecule force spectroscopy. *Biophysical journal*, 87(4), pp.2683–90.

Kumar NS, Richer J, Owen G, Litman E, Horwitz KB, Leslie KK. 1998. Selective Down-Regulation of Progesterone Receptor Isoform B in Poorly Differentiated Human Endometrial Cancer Cells : Implications for Unopposed Estrogen Action. *Cancer Research*, 58(9), pp.1860–1865.

Kumar S, Zhu LJ, Polihronis M, Cameron ST, Baird DT, Schatz F, Dua A, Ying YK, Bagchi MK, Bagchi IC. 1998. Progesterone induces calcitonin gene expression in human endometrium within the putative window of implantation. *The Journal of clinical endocrinology and metabolism*, 83(12), pp.4443–50.

Kuramoto H. 1972. Studies of the growth and cytogenetic properties of human endometrial adenocarcinoma in culture and its development into an established line. *Acta obstetrica et gynaecologica Japonica*, 19(1), pp.47–58.

Kuramoto H, Tamura S, Notake Y. 1972. Establishment of a cell line of human endometrial adenocarcinoma in vitro. *American journal of obstetrics and gynecology*, 114(8), pp.1012–9.

Kuznetsova TG, Starodubtseva MN, Yegorenkov NI, Chizhik SA, Zhdanov RI. 2007. Atomic force microscopy probing of cell elasticity. *Micron*, 38(8), pp.824–33.

Lagow E, DeSouza MM, Carson DD. 1999. Mammalian reproductive tract mucins. *Human reproduction update*, 5(4), pp.280–92.

Lai SK, Wang YY, Wirtz D, Hanes J. 2009. Micro- and macrorheology of mucus. *Advanced drug delivery reviews*, 61(2), pp.86–100.

Lai TH, Shih IM, Vlahos N, Ho CL, Wallach E, Zhao Y. 2005. Differential expression of L-selectin ligand in the endometrium during the menstrual cycle. *Fertility and sterility*, 83, pp.1297–302.

Lai TH, Zhao Y, Shih IeM, Ho CL, Bankowski B, Vlahos N. 2006. Expression of L-selectin ligands in human endometrium during the implantation window after controlled ovarian stimulation for oocyte donation. *Fertility and sterility*, 85(3), pp.761–3.

Lalitkumar PG, Lalitkumar S, Meng CX, Stavreus-Evers A, Hambiliki F, Bentin-Ley U, Gemzell-Danielsson K. 2007. Mifepristone, but not levonorgestrel, inhibits human blastocyst attachment to an *in vitro* endometrial three-dimensional cell culture model. *Human reproduction*, 22(11), pp.3031–7.

Lamont JT. 1992. Mucus: the front line of intestinal mucosal defense. *Annals of the New York Academy of Sciences*, 664, pp.190–201.

Lasky, LA. 1995. Selectin-carbohydrate interactions and the initiation of the inflammatory response. *Annual review of biochemistry*, 64, pp.113–39.

Lasky LA, Singer MS, Yednock TA, Dowbenko D, Fennie C, Rodriguez H, Nguyen T, Stachel S, Rosen SD. 1989. Cloning of a lymphocyte homing receptor reveals a lectin domain. *Cell*, 56(6), pp.1045–1055.

Lee GU, Kidwell DA, Colton RJ. 1994. Sensing Discrete Streptavidin-Biotin Interactions with Atomic Force Microscopy. *Langmuir*, 10(2), pp.354–357.

Lee JY, Wang F, Fazio T, Wind S, Greene EC. 2012. Measuring intermolecular rupture forces with a combined TIRF-optical trap microscope and DNA curtains. *Biochemical and biophysical research communications*, 426(4), pp.565–70.

Lee KY, DeMayo FJ. 2004. Animal models of implantation. *Reproduction*, 128(6), pp.679–95.

Lee YJ, Gorski J. 1996. Estrogen-induced transcription of the progesterone receptor gene does not parallel estrogen receptor occupancy. *Proceedings of the National Academy of Sciences of the United States of America*, 93(26), pp.15180–4.

Legleiter J, Park M, Cusick B, Kowalewski T. 2006. Scanning probe acceleration microscopy (SPAM) in fluids: mapping mechanical properties of surfaces at the nanoscale. *Proceedings of the National Academy of Sciences of the United States of America*, 103(13), pp.4813–8.

Lessey BA. 1998. Endometrial integrins and the establishment of uterine receptivity. *Human reproduction*, 13, pp.247–61.

Lessey BA, Castelbaum AJ, Buck CA, Lei Y, Yowell CW, Sun J. 1994. Further characterization of endometrial integrins during the menstrual cycle and in pregnancy. *Fertility and Sterility*, 62(3), pp.497–506.

Lessey BA, Damjanovich L, Coutifaris C, Castelbaum A, Albelda SM, Buck CA. 1992. Integrin adhesion molecules in the human endometrium. Correlation with the normal and abnormal menstrual cycle. *The Journal of clinical investigation*, 90(1), pp.188–95.

Lessey BA, Castelbaum AJ, Wolf L, Greene W, Paulson M, Meyer WR, Fritz MA. 2000. Use of integrins to date the endometrium. *Fertility and Sterility*, 73(4), pp.779–87.

Ley K. 2003. The role of selectins in inflammation and disease. *Trends in Molecular Medicine*, 9(6), pp.263–268.

Li G, Xi N, Wang DH. 2005. In situ sensing and manipulation of molecules in biological samples using a nanorobotic system. *Nanomedicine*, 1(1), pp.31–40.

Li HY, Chang SP, Yuan CC, Chao HT, Ng HT, Sung YJ. 2002. Establishment of an efficient method to quantify embryo attachment to endometrial epithelial cell monolayers. *In vitro cellular & developmental biology*, 38(9), pp.505–11.

Li M, Liu L, Xi N, Wang Y, Dong Z, Xiao X, Zhang W. 2013. Atomic force microscopy imaging of live mammalian cells. *Science China. Life sciences*, 56(9), pp.811–7.

Li M, Xiao X, Liu L, Xi N, Wang Y, Dong Z, Zhang W. 2013. Atomic force microscopy study of the antigen-antibody binding force on patient cancer cells based on ROR1 fluorescence recognition. *Journal of molecular recognition*, 26(9), pp.432–8.

Li M, Liu L, Xi N, Wang Y, Dong Z, Li G, Xiao X, Zhang W. 2011. Detecting CD20-Rituximab interaction forces using AFM single-molecule force spectroscopy. *Chinese Science Bulletin*, 56(35), pp.3829–3835.

Li M, Liu L, Xi N, Wang Y, Xiao X, Zhang W. 2013. Imaging and measuring the biophysical properties of Fc gamma receptors on single macrophages using atomic force microscopy. *Biochemical and biophysical research communications*, 438(4), pp.709–14.

Li Q, Wang J, Armant DR, Bagchi MK, Bagchi IC. 2002. Calcitonin down-regulates E-cadherin expression in rodent uterine epithelium during implantation. *The Journal of biological chemistry*, 277(48), pp.46447–55.

Lin WH, Zhao YP. 2005. Nonlinear behavior for nanoscale electrostatic actuators with Casimir force. *Chaos, Solitons & Fractals*, 23(5), pp.1777–1785.

Liu H, Fu S, Zhu J, Li H, Zhan H. 2009. Visualization of enzymatic hydrolysis of cellulose using AFM phase imaging. *Enzyme and Microbial Technology*, 45(4), pp.274–281.

Liu N, Zhou C, Chen Y, Zhao J. 2013. The involvement of osteopontin and β3 integrin in implantation and endometrial receptivity in an early mouse pregnancy model.

European journal of obstetrics, gynecology, and reproductive biology, 170(1), pp.171–6.

Liu S, Zhang Y, Liu Y, Qin H, Wang X, Yan Q. 2008. FUT7 antisense sequence inhibits the expression of FUT7 / sLeX and adhesion between embryonic and uterine cells. *IUBMB Life*, 60(7), pp.461–466.

Liu S, Yang X, Liu Y, Wang X, Yan Q. 2011. sLeX/L-selectin mediates adhesion *in vitro* implantation model. *Molecular and cellular biochemistry*, 350(1-2), pp.185–92.

Liu, W. et al., 2010. Effect of integrin beta1 on adhesion and migration of human trophoblast cells. *Journal of biomedical engineering*, 27(1), pp.67–70, 108.

Lombardo M, Lombardo G, Carbone G, De Santo MP, Barberi R, Serrao S. 2012. Biomechanics of the anterior human corneal tissue investigated with atomic force microscopy. *Investigative ophthalmology & visual science*, 53(2), pp.1050–7.

Lonard DM, Lanz RB, O'Malley BW. 2007. Nuclear receptor coregulators and human disease. *Endocrine reviews*, 28(5), pp.575–87.

Lonard DM, O'Malley BW. 2006. The expanding cosmos of nuclear receptor coactivators. *Cell*, 125(3), pp.411–4.

López-Ferrer A, de Bolós C, Barranco C, Garrido M, Isern J, Carlstedt I, Reis CA, Torrado J, Real FX. 2000. Role of fucosyltransferases in the association between apomucin and Lewis antigen expression in normal and malignant gastric epithelium. *Gut*, 47(3), pp.349–56.

Makiguchi Y, Hinoda Y, Imai K. 1996. Effect of MUC1 mucin, an anti-adhesion molecule, on tumor cell growth. *Japanese journal of cancer research*, 87(5), pp.505–11.

Mangelsdorf DJ, Thummel C, Beato M, Herrlich P, Schütz G, Umesono K, Blumberg B, Kastner P, Mark M, Chambon P, Evans RM. 1995. The nuclear receptor superfamily: the second decade. *Cell*, 83(6), pp.835–9.

Mardon H, Grewal S, Mills K. 2007. Experimental models for investigating implantation of the human embryo. *Seminars in reproductive medicine*, 25(6), pp.410–7.

Margarit L, Gonzalez D, Lewis PD, Hopkins L, Davies C, Conlan RS, Joels L, White JO. 2009. L-selectin ligands in human endometrium: comparison of fertile and infertile subjects. *Human reproduction*, 24(11), pp.2767–77.

Margarit L, Taylor A, Roberts MH, Hopkins L, Davies C, Brenton AG, Conlan RS, Bunkheila A, Joels L, White JO, Gonzalez D.2010. MUC1 as a discriminator between endometrium from fertile and infertile patients with PCOS and endometriosis. *The Journal of clinical endocrinology and metabolism*, 95(12), pp.5320–9.

Martín JC, Jasper MJ, Valbuena D, Meseguer M, Remohí J, Pellicer A, Simón C. 2000. Increased adhesiveness in cultured endometrial-derived cells is related to the absence of moesin expression. *Biology of reproduction*, 63(5), pp.1370–6.

Martín-Sosa S, Martín MJ, Hueso P. 2002. The sialylated fraction of milk oligosaccharides is partially responsible for binding to enterotoxigenic and uropathogenic Escherichia coli human strains. *The Journal of nutrition*, 132(10), pp.3067–72.

Matthews J, Gustafsson JA. 2003. Estrogen signaling: a subtle balance between ER alpha and ER beta. *Molecular interventions*, 3(5), pp.281–292.

Maybin JA, Critchley HO. 2012. Steroid regulation of menstrual bleeding and endometrial repair. *Reviews in endocrine & metabolic disorders*, 13(4), pp.253–63.

McEver RP. 2002. Selectins: lectins that initiate cell adhesion under flow. *Current opinion in cell biology*, 14(5), pp.581–6.

Meng CX, Andersson KL, Bentin-Ley U, Gemzell-Danielsson K, Lalitkumar PG. 2009. Effect of levonorgestrel and mifepristone on endometrial receptivity markers in a three-dimensional human endometrial cell culture model. *Fertility and Sterility*, 91(1), pp.256–64.

Merkel R, Nassoy P, Leung A, Ritchie K, Evans E. 1999. Energy landscapes of receptor-ligand bonds explored with dynamic force spectroscopy. *Nature*, 397(6714), pp.50–3.

Meseguer M, Aplin JD, Caballero-Campo P, O'Connor JE, Martín JC, Remohí J, Pellicer A, Simón C 2001. Human endometrial mucin MUC1 is up-regulated by progesterone and down-regulated *in vitro* by the human blastocyst. *Biology of reproduction*, 64(2), pp.590–601.

Meseguer M, Pellicer A, Simón C. 1998. MUC1 and endometrial receptivity. *Molecular human reproduction*, 4(12), pp.1089–98.

Migneault I, Dartiguenave C, Bertrand MJ, Waldron KC. 2004. Glutaraldehyde: behavior in aqueous solution, reaction with proteins, and application to enzyme crosslinking. *Biotechniques*, 37(5), pp.790–6, 798–802.

Minas V, Loutradis D, Makrigiannakis A. 2005. Factors controlling blastocyst implantation. *Reproductive Biomedicine Online*, 10(2), pp.205–216.

Moniaux N, Escande F, Porchet N, Aubert JP, Batra SK. 2001. Structural organization and classification of the human mucin genes. *Frontiers in bioscience*, 1(6), pp.1192-206

Moreno-Herrero F, Colchero J, Gómez-Herrero J, Baró AM. 2004. Atomic force microscopy contact, tapping, and jumping modes for imaging biological samples in liquids. *Physical review E, statistical, nonlinear and soft matter physics*, 69(3), e.031915.

Morita S, Wiesendanger R, Meyer E, Reichling M, Barth C. 2002. *Noncontact Atomic Force Microscopy*, Springer books.

Mote PA, Balleine RL, McGowan EM, Clarke CL. 1999. Colocalization of progesterone receptors A and B by dual immunofluorescent histochemistry in human endometrium during the menstrual cycle. *The Journal of clinical endocrinology and metabolism*, 84(8), pp.2963–71.

Van Mourik MS, Macklon NS, Heijnen CJ. 2009. Embryonic implantation: cytokines, adhesion molecules, and immune cells in establishing an implantation environment. *Journal of leukocyte biology*, 85(1), pp.4–19.

Müller DJ, Fotiadis D, Scheuring S, Müller SA, Engel A. 1999. Electrostatically Balanced Subnanometer Imaging of Biological Specimens by Atomic Force Microscope. *Biophysical journal*, 76(2), pp.1101–1111.

Müller DJ, Krieg M, Alsteens D, Dufrêne YF. 2009. New frontiers in atomic force microscopy: analyzing interactions from single-molecules to cells. *Current opinion in biotechnology*, 20(1), pp.4–13.

Müller DJ, Dufrêne YF. 2011. Atomic force microscopy: a nanoscopic window on the cell surface. *Trends in cell biology*, 21(8), pp.461–9.

Müller DJ, Dufrêne YF. 2008. Atomic force microscopy as a multifunctional molecular toolbox in nanobiotechnology. *Nature nanotechnology*, 3(5), pp.261–9.

Müller DJ, Helenius J, Alsteens D, Dufrêne YF. 2009. Force probing surfaces of living cells to molecular resolution. *Nature chemical biology*, 5(6), pp.383–90.

Murphy CR. 2006. Understanding the apical surface markers of uterine receptivity Pinopods — or uterodomes ? *Human reproduction*, 15(12), pp.2451–2454.

Nardo LG, Sabatini L, Rai R, Nardo F. 2002. Pinopode expression during human implantation. *European journal of obstetrics & gynecology and reproductive biology*, 101(2), pp.104–108.

Nardulli AM, Greene GL, O'Malley BW, Katzenellenbogen BS. 1988. Regulation of progesterone receptor messenger ribonucleic acid and protein levels in MCF-7 cells by estradiol: analysis of estrogen's effect on progesterone receptor synthesis and degradation. *Endocrinology*, 122(3), pp.935–44.

Nejatbakhsh R, Kabir-Salmani M, Dimitriadis E, Hosseini A, Taheripanah R, Sadeghi Y, Akimoto Y, Iwashita M. 2012. Subcellular localization of L-selectin ligand in the endometrium implies a novel function for pinopodes in endometrial receptivity. *Reproductive biology and endocrinology*, 10(1), pp.1-9.

Nelson WJ, Dickinson DJ, Weis WI. 2013. Roles of cadherins and catenins in cell-cell adhesion and epithelial cell polarity. *Progress in molecular biology and translational science*, 116, pp.3–23.

Neubauer NL, Ward EC, Patel P, Lu Z, Lee I, Blok LJ, Hanifi-Moghaddam P, Schink J, Kim JJ. 2011. Progesterone receptor-B induction of BIRC3 protects endometrial cancer cells from AP1-59-mediated apoptosis. *Hormones & cancer*, 2(3), pp.170–81.

Neuman KC, Nagy A. 2008. Single-molecule force spectroscopy: optical tweezers, magnetic tweezers and atomic force microscopy. *Nature methods*, 5(6), pp.491–505.

Neveu N, Granger L, St-Michel P, Lavoie HB. 2007. Comparison of clomiphene citrate, metformin, or the combination of both for first-line ovulation induction and achievement of pregnancy in 154 women with polycystic ovary syndrome. *Fertility and Sterility*, 87(1), pp.113–120.

Niklaus AL, Aubuchon M, Zapantis G, Li P, Qian H, Isaac B, Kim MY, Adel G, Pollard JW, Santoro NF. 2007. Assessment of the proliferative status of epithelial cell types in the endometrium of young and menopausal transition women. *Human reproduction*, 22(6), pp.1778–1788.

Nilsson S, Gustafsson JA. 2002. Biological role of estrogen and estrogen receptors. *Critical reviews in biochemistry and molecular biology*, 37(1), pp.1–28.

Nishida M, Kasahara K, Kaneko M, Iwasaki H, Hayashi K. 1985. Establishment of a new human endometrial adenocarcinoma cell line, Ishikawa cells, containing estrogen and progesterone receptors. *Nihon Sanka Fujinka Gakkai Zasshi*, 37(7), pp.1103–11.

Nishida M. 2002. The Ishikawa cells from birth to the present. *Human cell*, 15(3), pp.104–17.

Norwitz ER, Schust DJ, Fisher SJ. 2001. Implantation and the survival of early pregnancy. *The New England journal of medicine*, 345(19), pp.1400–8.

Noy A. 2011. Force spectroscopy 101: how to design, perform, and analyze an AFM-based single molecule force spectroscopy experiment. *Current opinion in chemical biology*, 15(5), pp.710–18.

Oberyszyn TM, Conti CJ, Ross MS, Oberyszyn AS, Tober KL, Rackoff AI, Robertson FM. 1998. Beta2 integrin/ICAM-1 adhesion molecule interactions in cutaneous inflammation and tumor promotion. *Carcinogenesis*, 19(3), pp.445–55.

Oesterschulze E, Scholz W, Mihalcea C, Albert D, Sobisch B, Kulisch W. 1997. Fabrication of small diamond tips for scanning probe microscopy application. *Applied Physics Letters*, 70(4), pp.435–437.

Okayama H, Kumamoto K, Saitou K, Hayase S, Kofunato Y, Sato Y, Miyamoto K, Nakamura I, Ohki S, Koyama Y, Ishii Y, Takenoshita S. 2011. Ectopic expression of MECA-79 as a novel prognostic indicator in gastric cancer. *Cancer science*, 102(5), pp.1088–94.

Olive D, Schwartz, L. 1993. Endometriosis. *New England Journal of Medicine*, 328(24), pp.1759–1769.

Ozturk S, Demir R. 2010. Particular functions of estrogen and progesterone in establishment of uterine receptivity and embryo implantation. *Histology and histopathology*, 25(9), pp.1215–28.

Pablos JL, Santiago B, Tsay D, Singer MS, Palao G, Galindo M, Rosen SD. 2005. A HEV-restricted sulfotransferase is expressed in rheumatoid arthritis synovium and is induced by lymphotoxin-alpha/beta and TNF-alpha in cultured endothelial cells. *BMC immunology*, 7(6), pp.6.

Pafilis J, Batistatou A, Iliopoulou A, Tsanou E, Bakogiannis A, Dassopoulos G, Charalabopoulos K. 2007. Expression of adhesion molecules during normal pregnancy. *Cell and tissue research*, 329(7), pp.1–11.

Panaitescu D, Vuluga Z, Radovici C, Nicolae C. 2012. Morphological investigation of PP/nanosilica composites containing SEBS. *Polymer Testing*, 31(2), pp.355–365.

Panidis D, Tziomalos K, Papadakis E, Katsikis I. 2013. Infertility treatment in polycystic ovary syndrome: lifestyle interventions, medications and surgery. *Frontiers of hormone research*, 40, pp.128–41.

Pelinck MJ, Vogel NE, Arts EG, Simons AH, Heineman MJ, Hoek A. 2007. Cumulative pregnancy rates after a maximum of nine cycles of modified natural cycle IVF and analysis of patient drop-out: a cohort study. *Human reproduction*, 22(9), pp.2463–70.

Pellicer A, Rubio C, Vidal F, Mínguez Y, Giménez C, Egozcue J, Remohí J, Simón C. 1999. *In vitro* fertilization plus preimplantation genetic diagnosis in patients with recurrent miscarriage: an analysis of chromosome abnormalities in human preimplantation embryos. *Fertility and Sterility*, 71(6), pp.1033–9.

Perez BH, Gipson IK. 2008. Focus on Molecules: human mucin MUC16. *Experimental eye research*, 87(11), pp.400–1.

Perret E, Leung A, Feracci H, Evans E. 2004. Trans-bonded pairs of E-cadherin exhibit a remarkable hierarchy of mechanical strengths. *Proceedings of the National Academy of Biosciences of the United States of America*, 23(11), pp.16472-7.

Petersen A, Bentin-Ley U, Ravn V, Qvortrup K, Sørensen S, Islin H, Sjögren A, Mosselmann S, Hamberger L. 2005. The antiprogesterone Org 31710 inhibits human blastocyst-endometrial interactions *in vitro*. *Fertility and Sterility*, 83(4), pp.1255–1263.

Petz LN, Nardulli AM. 2000. Sp1 binding sites and an estrogen response element half-site are human progesterone receptor A promoter. *Molecular endocrinology*, 14(7), pp.972–985.

Pinho SS, Seruca R, Gärtner F, Yamaguchi Y, Gu J, Taniguchi N, Reis CA. 2011. Modulation of E-cadherin function and dysfunction by N-glycosylation. *Cellular and molecular life sciences*, 68(3), pp.1011–1020.

Pittenger B, Slade A, Berquand A. 2013. Application Note # 141: Toward quantitative nanomechanical measurements on live cells with PeakForce QNM. Bruker nano, pp.1–10.

Pletikapić G, Berquand A. 2012. Quantitative nanomechanical mapping of marine diatom in seawater using PeakForce tapping atomic force microscopy. *Journal of Phycology*, 48(1), pp.174–185.

Poncelet C, Leblanc M, Walker-Combrouze F, Soriano D, Feldmann G, Madelenat P, Scoazec JY, Daraï E. 2002. Expression of cadherins and CD44 isoforms in human endometrium and peritoneal endometriosis. *Acta obstetricia et gynecologica Scandinavica*, 81(3), pp.195–203.

Putman C, Van der Werf K, De Grooth B, Van Hulst N, Greve J. 1994. Tapping mode atomic force microscopy in liquid. *Applied Physics Letters*, 64(18), p.2454.

Quenby S, Anim-Somuah M, Kalumbi C, Farquharson R, Aplin JD. 2007. Different types of recurrent miscarriage are associated with varying patterns of adhesion molecule expression in endometrium. *Reproductive Biomedicine Online*, 14(2), pp.224–234.

Quenby S, Vince G, Farquharson R, Aplin J. 2002. Recurrent miscarriage: a defect in nature's quality control? *Human reproduction*, 17(8), pp.1959–1963.

Quinn C, Casper R. 2009. Pinopodes: a questionable role in endometrial receptivity. *Human reproduction update*, 15(2), pp.229–36.

Rahnama F, Thompson B, Steiner M, Shafiei F, Lobie PE, Mitchell MD. 2009. Epigenetic regulation of E-cadherin controls endometrial receptivity. *Endocrinology*, 150(3), pp.1466–72.

Rashid NA, Lalitkumar S, Lalitkumar PG, Gemzell-Danielsson K. 2011. Endometrial receptivity and human embryo implantation. *American journal of reproductive immunology*, 66(6), pp.23–30.

Razawi H, Kinlough CL, Staubach S, Poland PA, Rbaibi Y, Weisz OA, Hughey RP, Hanisch FG. 2013. Evidence for core 2 to core 1 O-glycan remodeling during the recycling of MUC1. *Glycobiology*, 23(8), pp.935–45.

Redwine DB. 2002. Was Sampson wrong? *Fertility and Sterility*, 78(10), pp.686–93.

Reshef E, Lei ZM, Rao CV, Pridham DD, Chegini N, Luborsky JL. 1990. The presence of gonadotropin receptors in nonpregnant human uterus, human placenta, fetal membranes, and decidua. *The Journal of clinical endocrinology and metabolism*, 70(2), pp.421–30.

Rief M, Oesterhelt F, Heymann B, Gaub HE. 1997. Single Molecule Force Spectroscopy on Polysaccharides by Atomic Force Microscopy. *Science*, 275(5304), pp.1295–7.

Riener C, Kienberger F, Hahn C, Buchinger G, Egwim I, Haselgrübler T, Ebner A, Romanin C, Klampfl C, Lackner B, Prinz H, Blaas D, Hinterdorfer P, Gruber H. 2003. Heterobifunctional crosslinkers for tethering single ligand molecules to scanning probes. *Analytica chimica acta*, 497(1-2), pp.101–114.

Riethmacher D, Brinkmann V, Birchmeier C. 1995. A targeted mutation in the mouse E-cadherin gene results in defective preimplantation development. *Proceedings of the National Academy of Sciences of the United States of America*, 92(1), pp.855–9.

Riva A, Tandler B, Ushiki T, Usai P, Isola R, Conti G, Loy F, L Hoppel C. 2010. Mitochondria of human Leydig cells as seen by high resolution scanning electron microscopy. *Archives of histology and cytology*, 73(1), pp.37–44.

Roduit C, van der Goot FG, De Los Rios P, Yersin A, Steiner P, Dietler G, Catsicas S, Lafont F, Kasas S. 2008. Elastic membrane heterogeneity of living cells revealed by stiff nanoscale membrane domains. *Biophysical journal*, 94(4), pp.1521–32.

Roduit C, Saha B, Alonso-Sarduy L, Volterra A, Dietler G, Kasas S. 2012. OpenFovea: open-source AFM data processing software. *Nature methods*, 9(8), pp.774–5.

Ros R, Schwesinger F, Anselmetti D, Kubon M, Schäfer R, Plückthun A, Tiefenauer L. 1998. Antigen binding forces of individually addressed single-chain Fv antibody molecules. *Proceedings of the National Academy of Sciences of the United States of America*, 95(13), pp.7402–5.

Rosen SD. 2004. Ligands for L-Selectin: homing, inflammation, and beyond. *Annual review of immunology*, 22(1), pp.129–156.

Sader JE, Sanelli JA, Adamson BD, Monty JP, Wei X, Crawford SA, Friend JR, Marusic I, Mulvaney P, Bieske EJ. 2012. Spring constant calibration of atomic force microscope cantilevers of arbitrary shape. *The review of scientific instruments*, 83(10), pp.103705.

Sakaguchi H, Fujimoto J, Aoki I, Tamaya T. 2003. Expression of estrogen receptor α and β in myometrium of premenopausal and postmenopausal women. *Steroids*, 68(1), pp.11–19.

Salilew-Wondim D, Schellander K, Hoelker M, Tesfaye D. 2012. Oviductal, endometrial and embryonic gene expression patterns as molecular clues for pregnancy establishment. *Animal reproduction science*, 134(9), pp.9–18.

Sampson, J. 1927. Metastatic or Embolic Endometriosis, due to the Menstrual Dissemination of Endometrial Tissue into the Venous Circulation. *The American journal of pathology*, 3(2), pp.93–110.

Sánchez F, Smitz, J. 2012. Molecular control of oogenesis. *Biochimica et biophysica acta*, 1822(12), pp.1896–912.

Sandal M, Benedetti F, Brucale M, Gomez-Casado A, Samorì B. 2009. Hooke: an open software platform for force spectroscopy. *Bioinformatics*, 25(11), pp.1428–30.

Satyaswaroop PG, Fleming H, Bressler RS, Gurpide E. 1978. Human endometrial cancer cell cultures for hormonal studies. *Cancer research*, 38(11), pp.4367–75.

Schindler AE, Campagnoli C, Druckmann R, Huber J, Pasqualini JR, Schweppe KW, Thijssen JH. 2008. Classification and pharmacology of progestins. *Maturitas*, 61(9-10), pp.171–80.

Schlafke S, Enders A. 1967. Cytological changes during cleavage and blastocyst formation in the rat. *Journal of anatomy*, 102, pp.13–32.

Shan Y, Huang J, Tan J, Gao G, Liu S, Wang H, Chen Y. 2012. The study of single anticancer peptides interacting with HeLa cell membranes by single molecule force spectroscopy. *Nanoscale*, 4(4), pp.1283–6.

Shirane, A. et al., 2012. Regulation of SIRT1 determines initial step of endometrial receptivity by controlling E-cadherin expression. *Biochemical and biophysical research communications*, 424(3), pp.604–10.

Shirane A, Wada-Hiraike O, Tanikawa M, Seiki T, Hiraike H, Miyamoto Y, Sone K, Hirano M, Oishi H, Oda K, Kawana K, Nakagawa S, Osuga Y, Fujii T, Yano T, Kozuma S, Taketani Y. 2013. Aberrant expression of E-cadherin and integrin β-1 in trophoblasts is associated with malignant gestational trophoblastic diseases. *International journal of gynecological cancer*, 23(4), pp.749–54.

Silberzan P, Leger L, Ausserre D, Benattar J. 1991. Silanation of Silica Surfaces. A New Method of Constructing Pure or Mixed Monolayers. *Langmuir*, 7(8), pp.1647–1651.

Silva Z, Tong Z, Cabral MG, Martins C, Castro R, Reis C, Trindade H, Konstantopoulos K, Videira PA. 2011. Sialyl Lewisx-dependent binding of human monocyte-derived dendritic cells to selectins. *Biochemical and biophysical research communications*, 409(3), pp.459–64.

Simons K, Vaz WL. 2004. Model systems, lipid rafts, and cell membranes. *Annual review of biophysics and biomolecular structure*, 33, pp.269–95.

Singh H, Nardo L, Kimber SJ, Aplin JD. 2010. Early stages of implantation as revealed by an *in vitro* model. *Reproduction*, 139(5), pp.905–14.

Slayden OD, Nayak NR, Burton KA, Chwalisz K, Cameron ST, Critchley HO, Baird DT, Brenner RM. 2001. Progesterone antagonists increase androgen receptor expression in the rhesus macaque and human endometrium. *Journal of clinical endocrinology and metabolism*, 86(6), pp.2668–2679.

Smith BA, Tolloczko B, Martin JG, Grütter P. 2005. Probing the viscoelastic behavior of cultured airway smooth muscle cells with atomic force microscopy: stiffening induced by contractile agonist. *Biophysical journal*, 88(4), pp.2994–3007.

Sneddon IN. 1965. The relation between load and penetration in the axisymmetric boussinesq problem for a punch of arbitrary profile. *International Journal of Engineering Science*, 3(1), pp.47–57.

So KH, Lee CL, Yeung WS, Lee KF. 2012. Glycodelin suppresses endometrial cell migration and invasion but stimulates spheroid attachment. *Reproductive biomedicine online*, 24(6), pp.639–45.

Song Y, Wang Q, Huang W, Xiao L, Shen L, Xu W. 2012. NFκB expression increases and CFTR and MUC1 expression decreases in the endometrium of infertile patients with hydrosalpinx: a comparative study. *Reproductive biology and endocrinology*, 10(1), pp.86.

Song Y, Bhushan B. 2008. Atomic force microscopy dynamic modes: modeling and applications. *Journal of Physics: Condensed Matter*, 20(22), pp.225012.

Stark M, Stark R, Heckl W, Guckenberger R. 2002. Inverting dynamic force microscopy: From signals to time-resolved interaction forces. *Proceedings of the National Academy of Sciences*, 99 (4), pp.8473–8478.

Fuhrmann A, Staunton JR, Nandakumar V, Banyai N, Davies PC, Ros R. 2011. AFM Stiffness Nanotomography of Normal, Metaplastic and Dysplastic Human Esophageal Cells. *Biophysical Journal*, 100(3), pp.190.

Steiner P, Alberi S, Kulangara K, Yersin A, Sarria JC, Regulier E, Kasas S, Dietler G, Muller D, Catsicas S, Hirling H. 2005. Interactions between NEEP21, GRIP1 and GluR2 regulate sorting and recycling of the glutamate receptor subunit GluR2. *The EMBO journal*, 24(8), pp.2873–84.

Stricker R, Eberhart R, Chevailler MC, Quinn FA, Bischof P, Stricker R. 2006. Establishment of detailed reference values for luteinizing hormone, follicle stimulating hormone, estradiol, and progesterone during different phases of the menstrual cycle on the Abbott ARCHITECT analyzer. *Clinical chemistry and laboratory medicine*, 44(7), pp.883–7.

Strott CA, Yoshimi T, Ross GT, Lipsett MB. 1969. Ovarian physiology: relationship between plasma LH and steroidogenesis by the follicle and corpus luteum; effect of HCG. *The Journal of clinical endocrinology and metabolism*, 29(9), pp.1157–67.

Strowitzki T, Germeyer A, Popovici R, von Wolff M. 2006. The human endometrium as a fertility-determining factor. *Human reproduction update*, 12(5), pp.617–30.

Sulchek TA, Friddle RW, Langry K, Lau EY, Albrecht H, Ratto TV, DeNardo SJ, Colvin ME, Noy A. 2005. Dynamic force spectroscopy of parallel individual

Mucin1-antibody bonds. *Proceedings of the National Academy of Sciences of the United States of America*, 102(46), pp.16638–43.

Sulchek T, Friddle RW, Noy A. 2006. Strength of multiple parallel biological bonds. *Biophysical journal*, 90(12), pp.4686–91.

Sundqvist J, Andersson KL, Scarselli G, Gemzell-Danielsson K, Lalitkumar PG. 2012. Expression of adhesion, attachment and invasion markers in eutopic and ectopic endometrium: a link to the aetiology of endometriosis. *Human reproduction*, 27(9), pp.2737–46.

Suresh S. 2007. Biomechanics and biophysics of cancer cells. *Acta biomaterialia*, 3(4), pp.413–38.

Surveyor GA, Gendler SJ, Pemberton L, Das SK, Chakraborty I, Julian J, Pimental RA, Wegner CC, Dey SK, Carson DD. 1995. Expression and steroid hormonal control of Muc-1 in the mouse uterus. *Endocrinology*, 136(8), pp.3639–3647.

Takano H, Kenseth JR, Wong SS, O'Brien JC, Porter MD. 1999. Chemical and biochemical analysis using scanning force microscopy. *Chemical reviews*, 99(10), pp.2845–90.

Tamayo J, Garca R. 1997. Effects of elastic and inelastic interactions on phase contrast images in tapping-mode scanning force microscopy. *Applied Physics Letters*, 71(16), pp.2394–2396.

Tamm-Rosenstein K, Simm J, Suhorutshenko M, Salumets A, Metsis M. 2013. Changes in the transcriptome of the human endometrial Ishikawa cancer cell line induced by estrogen, progesterone, tamoxifen, and mifepristone (RU486) as detected by RNA-sequencing. *PloS one*, 8(7), pe.68907.

Tangemann K, Bistrup A, Hemmerich S, Rosen SD. 1999. Sulfation of a high endothelial venule-expressed ligand for L-selectin. Effects on tethering and rolling of lymphocytes. *The Journal of experimental medicine*, 190(7), pp.935–42.

Tarantal AF, Hendrickx AG. 1988. Use of ultrasound for early pregnancy detection in the rhesus and cynomolgus macaque (Macaca mulatta and Macaca fascicularis). *Journal of medical primatology*, 17(2), pp.105–12.

Tarp MA, Clausen H. 2008. Mucin-type O-glycosylation and its potential use in drug and vaccine development. *Biochimica et biophysica acta*, 1780(3), pp.546–63.

Tedder TF, Penta AC, Levine HB, Freedman AS. 1990. Expression of the human leukocyte adhesion molecule, LAM1. Identity with the TQ1 and Leu-8 differentiation. *Journal of immunology*, pp.532–540.

Tedder T. 1995. The selectins: Cellular adhesion molecules. *The FASEB Journal*, 9(10), pp.866–873.

Teklenburg G, Macklon NS. 2009. Review: *in vitro* models for the study of early human embryo-endometrium interactions. *Reproductive sciences*, 16(9), pp.811–8.

Thathiah A, Blobel CP, Carson DD. 2003. Tumor necrosis factor-alpha converting enzyme/ADAM 17 mediates MUC1 shedding. *The Journal of biological chemistry*, 278(5), pp.3386–94.

Thathiah A, Carson DD. 2004. MT1-MMP mediates MUC1 shedding independent of TACE/ADAM17. *The Biochemical journal*, 382, pp.363–73.

Thathiah A, Carson DD. 2002. Mucins and blastocyst attachment. *Reviews in endocrine & metabolic disorders*, 3(2), pp.87–96.

Thie M, Röspel R, Dettmann W, Benoit M, Ludwig M, Gaub HE, Denker HW. 1998. Interactions between trophoblast and uterine epithelium: monitoring of adhesive forces. *Human reproduction*, 13(11), pp.3211–9.

Thie M, Denker HW. 2002. In vitro studies on endometrial adhesiveness for trophoblast: cellular dynamics in uterine epithelial cells. *Cells, tissues, organs*, 172(3), pp.237–52.

Thigpen JT, Brady MF, Alvarez RD, Adelson MD, Homesley HD, Manetta A, Soper JT, Given FT. 1999. Oral medroxyprogesterone acetate in the treatment of advanced or recurrent endometrial carcinoma: a dose-response study by the Gynecologic Oncology Group. *Journal of clinical oncology*, 17(6), pp.1736–44.

Thornton DJ, Rousseau K, McGuckin MA. 2008. Structure and function of the polymeric mucins in airways mucus. *Annual review of physiology*, 70, pp.459–86.

Tinel H, Denker HW, Thie M. 2000. Calcium influx in human uterine epithelial RL95-2 cells triggers adhesiveness for trophoblast-like cells. Model studies on signalling events during embryo implantation. *Molecular human reproduction*, 6(12), pp.1119–30.

Tjew SL, Brown KL, Kannagi R, Johnson P. 2005. Expression of N-acetylglucosamine 6-O-sulfotransferases (GlcNAc6STs)-1 and -4 in human monocytes: GlcNAc6ST-1 is implicated in the generation of the 6-sulfo N-acetyllactosamine/Lewis x epitope on CD44 and is induced by TNF-alpha. *Glycobiology*, 15(7), pp.7C–13C.

Toppila S, Paavonen T, Nieminen MS, Häyry P, Renkonen R. 1999. Endothelial L-selectin ligands are likely to recruit lymphocytes into rejecting human heart transplants. *The American journal of pathology*, 155(4), pp.1303–10.

Tranchida D, Kiflie Z, Piccarolo S. 2007. Atomic force microscope nanoindentations to reliably measure the young's modulus of soft matter. *Modern research and educational techniques in microscopy*, pp.737–746.

Trtik P, Kaufmann J, Volz U. 2012. On the use of peak-force tapping atomic force microscopy for quantification of the local elastic modulus in hardened cement paste. *Cement and concrete research*, 42(1), pp.215–221.

Tsang H, Cheung TY, Kodithuwakku SP, Chai J, Yeung WS, Wong CK, Lee KF. 2012. 2,3,7,8-Tetrachlorodibenzo-p-dioxin (TCDD) suppresses spheroids attachment on endometrial epithelial cells through the down-regulation of the Wnt-signaling pathway. *Reproductive toxicology*, 33(1), pp.60–6.

Tsapikouni T, Missirlis YF. 2011. P-selectin/ligand unbinding force measured with atomic force microscopy: comparison of two chemical protocols for the tethering of single molecules. *Journal of molecular recognition*, 24(5), pp.847–53.

Tsuji I, Ami K, Miyazaki A, Hujinami N, Hoshiai H. 2009. Benefit of Diagnostic Laparoscopy for Patients with Unexplained Infertility and Normal Hysterosalpingography Findings. *The Tohoku Journal of Experimental Medicine*, 219(1), pp.39–42.

Valles CS, Domínguez F. 2006. Embryo-endometrial interaction. *Chang Gung medical journal*, 29(1), pp.9–14.

Vegeto E, Shahbaz MM, Wen DX, Goldman ME, O'Malley BW, McDonnell DP. 1993. Human progesterone receptor A form is a cell- and promoter-specific repressor of human progesterone receptor B function. *Molecular endocrinology*, 7(10), pp.1244–55.

Velija-Ašimi Z. 2013. Evaluation of endocrine changes in women with the polycystic ovary syndrome during metformin treatment. *Bosnian journal of basic medical sciences*, 13(3), pp.180–5.

Vilella F, Ramirez L, Simón C. 2013. Lipidomics as an emerging tool to predict endometrial receptivity. *Fertility and Sterility*, 99(4), pp.1100–6.

Vinckier A, Heyvaert I, D'Hoore A, McKittrick T, Van Haesendonck C, Engelborghs Y, Hellemans L. 1995. Immobilizing and imaging microtubules by atomic force microscopy. *Ultramicroscopy*, 57(4), pp.337–43.

Wang B, Sheng JZ, He RH, Qian YL, Jin F, Huang HF. 2008. High expression of L-selectin ligand in secretory endometrium is associated with better endometrial receptivity and facilitates embryo implantation in human being. *American journal of reproductive immunology*, 60(2) pp.127–134.

Wang G, Zhang Y, Zhao Y, Yang G. 2004. Pull-in instability study of carbon nanotube tweezers under the influence of van der Waals forces. *Journal of Micromechanics and Microengineering*, 14(8), pp.1119–1125.

Wang H, Pilla F, Anderson S, Martínez-Escribano S, Herrer I, Moreno-Moya JM, Musti S, Bocca S, Oehninger S, Horcajadas JA. 2012. A novel model of human implantation: 3D endometrium-like culture system to study attachment of human trophoblast (Jar) cell spheroids. *Molecular human reproduction*, 18(1), pp.33–43.

Wang H, Bocca S, Anderson S, Yu L, Rhavi BS, Horcajadas J, Oehninger S. 2013. Sex steroids regulate epithelial-stromal cell cross talk and trophoblast attachment

invasion in a three-dimensional human endometrial culture system. *Tissue engineering. Part C, Methods*, 19(9), pp.676–87.

Wang H, Dey SK. 2006. Roadmap to embryo implantation: clues from mouse models. *Nature reviews. Genetics*, 7(3), pp.185–99.

Wang J, Armant D. 2002. Integrin-mediated adhesion and signaling during blastocyst implantation. *Cells, tissues, organs*, 172(3), pp.190–201.

Wang L, Chen T, Zhou X, Huang Q, Jin C. 2013. Atomic force microscopy observation of lipopolysaccharide-induced cardiomyocyte cytoskeleton reorganization. *Micron 51(8)*, pp.6–11.

Wang P, Dharmaraj N, Brayman MJ, Carson DD. 2010. Peroxisome proliferator-activated receptor gamma activation inhibits progesterone-stimulated human MUC1 expression. *Molecular endocrinology*, 24(7), pp.1368–79.

Weder G, Hendriks-Balk MC, Smajda R, Rimoldi D, Liley M, Heinzelmann H, Meister A, Mariotti A. 2013. Increased plasticity of the stiffness of melanoma cells correlates with their acquisition of metastatic properties. *Nanomedicine*, 10(1), pp.1–8.

Weisenhorn, 1993. Deformation and height anomaly of soft surfaces studied with an AFM. *Nanotechnology*, (4), pp.106–113.

Wen DX, Xu YF, Mais DE, Goldman ME, McDonnell DP. 1994. The A and B isoforms of the human progesterone receptor operate through distinct signaling pathways within target cells. *Molecular and cellular biology*, 14(12), pp.8356–64.

Wesseling J, van der Valk SW, Vos HL, Sonnenberg A, Hilkens J. 1995. Episialin (MUC1) overexpression inhibits integrin-mediated cell adhesion to extracellular matrix components. *The Journal of cell biology*, 129(1), pp.255–65.

Wierzbicki R, Købler C, Jensen MR, Lopacińska J, Schmidt MS, Skolimowski M, Abeille F, Qvortrup K, Mølhave K. 2013. Mapping the complex morphology of cell interactions with nanowire substrates using FIB-SEM. *PloS one*, 8(1), p.e53307.

Wolff EF, Vahidi N, Alford C, Richter K, Widra E. 2013. Influences on endometrial development during intrauterine insemination: clinical experience of 2,929 patients with unexplained infertility. *Fertility and Sterility*, 100(1), pp.194–9.

Wooding FB. 1992. Current topic: the synepitheliochorial placenta of ruminants: binucleate cell fusions and hormone production. *Placenta*, 13(2), pp.101–13.

Wooding FB. 1984. Role of binucleate cells in fetomaternal cell fusion at implantation in the sheep. *The American journal of anatomy*, 170(2), pp.233–50.

Wreschner DH, McGuckin MA, Williams SJ, Baruch A, Yoeli M, Ziv R, Okun L, Zaretsky J, Smorodinsky N, Keydar I, Neophytou P, Stacey M, Lin HH, Gordon S.

2002. Generation of ligand – receptor alliances by " SEA " module-mediated cleavage of membrane-associated mucin proteins. *Protein Science*, 11(3), pp.698–706.

Xiong T, Zhao Y, Hu D, Meng J, Wang R, Yang X, Ai J, Qian K, Zhang H. 2012. Administration of calcitonin promotes blastocyst implantation in mice by up-regulating integrin β3 expression in endometrial epithelial cells. *Human reproduction*, 27(12), pp.3540–51.

Xu B, Sun X, Li L, Wu L, Zhang A, Feng Y. 2012. Pinopodes, leukemia inhibitory factor, integrin-β3, and mucin-1 expression in the peri-implantation endometrium of women with unexplained recurrent pregnancy loss. *Fertility and Sterility*, 98(2), pp.389–395.

Xu M, Ma L, Bujalowski PJ, Qian F, Sutton RB, Oberhauser AF. 2013. Analysis of the REJ module of polycystin-1 using molecular modeling and force-spectroscopy techniques. *Journal of biophysics*, (online) p.525231.

Ye TM, Pang RT, Leung CO, Liu W, Yeung WS. 2012. Development and characterization of an endometrial tissue culture model for study of early implantation events. *Fertility and Sterility*, 98(6), pp.1581–9.

Yen S. 1977. Regulation of the hypothalamic--pituitary--ovarian axis in women. *Journal of reproduction and fertility*, 51(1), pp.181–91.

Yersin A, Hirling H, Steiner P, Magnin S, Regazzi R, Hüni B, Huguenot P, De los Rios P, Dietler G, Catsicas S, Kasas S. 2003. Interactions between synaptic vesicle fusion proteins explored by atomic force microscopy. *Proceedings of the National Academy of Sciences of the United States of America*, 100(15), pp.8736–41.

Yokokawa M, Takeyasu K, Yoshimura SH. 2008. Mechanical properties of plasma membrane and nuclear envelope measured by scanning probe microscope. *Journal of microscopy*, 232(10), pp.82–90.

Yolken RH, Peterson JA, Vonderfecht SL, Fouts ET, Midthun K, Newburg DS. 1992. Human milk mucin inhibits rotavirus replication and prevents experimental gastroenteritis. *The Journal of clinical investigation*, 90(5), pp.1984–91.

Yoshinaga K. 1988. Uterine receptivity for blastocyst implantation. *Annals of the New York academy of sciences*, 541, pp.424–31.

Young SL. 2013. Oestrogen and progesterone action on endometrium: a translational approach to understanding endometrial receptivity. *Reproductive biomedicine online*, 27(11), pp.497-505.

Yucha RW, Jost M, Rothstein D, Robertson N, Marcolongo MS. 2013. Quantifying the biomechanics of conception: L-selectin-mediated blastocyst implantation mechanics with engineered "trophospheres". *Tissue engineering. Part A*, 20(1-2), pp.189-96.

Zaretsky J, Wreschner DH, Hareuveni M, Tsarfaty I, Smorodinsky N, Horev J, Kotkes P, Weiss M, Lathe R, Dion A. 1990. Human epithelial tumor antigen cDNA sequences Differential splicing may generate multiple protein forms. *European journal of biochemistry*, 189(5), pp.463–473.

Zeitoun K, Takayama K, Sasano H, Suzuki T, Moghrabi N, Andersson S, Johns A, Meng L, Putman M, Carr B, Bulun SE. 1998. Deficient 17beta-hydroxysteroid dehydrogenase type 2 expression in endometriosis: failure to metabolize 17beta-estradiol. Journal of clinical endocrinology and metabolism, 83(12), pp.4474–4480.

Zhang D, Wei J, Wang J, Liu S, Wang X, Yan Q. 2011. Difucosylated oligosaccharide Lewis Y is contained within integrin αvβ3 on RL95-2 cells and required for endometrial receptivity. *Fertility and Sterility*, 95(4), pp.1446–51.

Zhang H, Honda Y, Takeoka S. 2013. Tapping-Mode AFM Study of Tip-Induced Polymer Deformation under Geometrical Confinement. *Langmuir*, 29(5), pp.1333–1339.

Zhang S, Lin H, Kong S, Wang S, Wang H, Wang H, Armant DR. 2013. Physiological and molecular determinants of embryo implantation. *Molecular aspects of medicine*, 34(5), pp.939-80.

Zhang X, Chen A, De Leon D, Li H, Noiri E, Moy VT, Goligorsky MS. 2004. Atomic force microscopy measurement of leukocyte-endothelial interaction. *American journal of physiology: Heart and circulatory physiology*, 286(1), pp.359–67.

Zhang X, Bogorin DF, Moy VT. 2004. Molecular basis of the dynamic strength of the sialyl Lewis X--selectin interaction. *Chemphyschem*, 5(2), pp.175–82.

Zhang, Y, Wang Y, Li Z, Huang Y, Li D. 2007. Snap-Through and Pull-In Instabilities of an Arch-Shaped Beam Under an Electrostatic Loading. *Microelectromechanical Systems, Journal of*, 16(3), pp.684–693.

Zhang Y, Zhao H, Zuo L. 2012. Contact dynamics of tapping mode atomic force microscopy. *Journal of Sound and Vibration*, 331(23), pp.5141–5152.

Zhong Q, Inniss D. 1993. Fractured polymer/silica fiber surface studied by tapping mode atomic force microscopy. *Surface Science Letters*, 290(1–2), pp.688 – 692.

Zimmermann G, Ackermann W, Alexander H. 2012. Expression and production of human chorionic gonadotropin (hCG) in the normal secretory endometrium: evidence of CGB7 and/or CGB6 beta hCG subunit gene expression. *Biology of reproduction*, 86(3), p.87.

Zimmermann JL, Nicolaus T, Neuert G, Blank K. 2010. Thiol-based, site-specific and covalent immobilization of biomolecules for single-molecule experiments. *Nature protocols*, 5(6), pp.975–85.